Research on deployment of modern nuclear reactors in the urban environment with emphasis on the *Molten Salt Reactor*

Materials Science and Engineering

TU Delft Department of Architectural Engineering + Technology
BK Bouwkunde

J.G. Emmen

Supervisors: Prof.dr.ir. J. Sietsma
Dr.ir. F.A. Veer
Dr.ir. V. Marques Pereira
Dr. R.M.J. Bokel

Department of Material Science and Engineering & Building Technology
Delft University of Technology

This dissertation is submitted for the degree of
Master of Science

3mE and BK

August 2022

Preface

This thesis was inspired by a fascination with nuclear energy, a controversial but remarkable technology. The finished product is the result of more than a year's worth of investigation into various nuclear energy-related fields. The presented work includes a description of the implementation of nuclear energy and its societal, economic, and engineering challenges, as well as in-depth research on the degradation of a Ni-based to be material used in generation IV molten salt reactors.

By offering a fair assessment of the technology as well as interesting sustainable possibilities, I sincerely hope that this thesis can help further de-stigmatize nuclear energy. The microstructural and mechanical material research on the MONICR alloy will provide additional information and insight into the material's thermal stability and behaviour. Consequently, contributing to the development of generation IV molten salt reactors. The research is being conducted in collaboration with the ENICKMA project.

This work is made possible by Delft University of Technology and Nuclear Research and Consultancy Group (NRG), providing both guidance, materials and facilities.

J.G. Emmen
Rotterdam, September 2022

Acknowledgements

I want to express my gratitude to a number of individuals who provided assistance with the writing of this master's thesis. They provided valuable advice throughout many stages of graduating and assisted in setting up a number of experiments and the thesis's framework. First of all, I want to thank Dr.ir. F.A. Veer and Prof.dr.ir. J. Sietsma, my Delft University of Technology supervisors. Graduating from two distinct scientific fields is a challenge that necessitates constant evaluation and flexibility, and this thesis would not be possible without their knowledge and expertise in a variety of scientific fields. I want to thank both in particular for their many insightful discussions on the science behind nuclear energy and its materials as well as their understanding of the societal challenges associated with the science. Second, I want to express my gratitude to Dr.ir. V. Marques Pereira for all of her assistance this past year. You not only offered excellent guidance and advice, but you also added fun to the project with the numerous discussions we had each week at the beginning of our meetings. I also want to express my sincere thanks to Mathilde Laot, Dr. R.M.J. Bokel and Kiki Naziris for their insightful comments and advice, which allowed me to concentrate on key issues and helped me specify many of the research objectives.

Additionally, I want to thank Kees Kwakernaak for all of his assistance and direction with the SEM. He not only assisted me in gathering the data but also provided to this project with interesting discussions about the subject. I also want to thank Sean Scott, Kevork Perez Bustos, Ton Riemslag, Ruud Hendrikx, and Hans Hofman for helping me set up my experiment in the lab and for supporting me throughout all of the lab work.

Finally, I want to express my most sincere appreciation to my friends, family, and, in particular, my boyfriend—the people who mean the most to me. You have all put up with my never-ending monologues about nuclear power and helped me get through this every so often stressful and difficult year. It's important to look back on the loving people in your life and, of course, to thank them for everything in a year marked by so many extremes.

Table of contents

List of figures

List of tables

Acronyms

2DS 2-Degree Scenario. 20

AFCR Advanced Fuel CANDU Reactor. 36

ANVS Authority for Nuclear Safety and Radiation Protection. 35, 36

AP1000 Advanced Passive Pressurised Water Reactor. 36–39

APR1400-EUR Advanced Power Reactor. 36–39

ASMR Advanced Small Modular Reactor. xiii, 26, 27, 36, 39–44, 53, 74, 99, 141, 145, 163

B2DS Beyond 2-Degree Scenario. 19, 20

BEI Backscatter Electron Image. xvi, xviii, 214, 223, 224, 229, 230, 232, 234–236, 243, 245, 246, 248, 249, 251, 252, 281, 306

BF Bright Field. 222

BWR Boiling Water Reactor. 34, 41, 43

CCS Carbon Capture and Storage. 13, 14, 16, 18, 62, 65

CDF Core Damage Frequency. 37, 38, 41, 43

CHP Combined Heat and Power. 87

DF Dark Field. 222

DIC Differential Interference Contrast. 222

dpa displacements per atom. 191, 199

EBSD Electron Backscatter Diffraction. xvi, xviii, 214, 223–225, 229, 231, 232, 244, 247, 251–258, 269, 281, 306

EDS Energy-Dispersive X-ray Spectroscopy. xvi–xviii, 223, 224, 229, 232, 247, 249, 250, 304, 305

EoL End-of-Life. 23, 53, 54, 94, 107, 118, 122, 126, 133, 140, 162–164, 177

EPMA Electron Probe Microanalysis. 224, 249, 280

EPR2 European Pressurised Rreactor 2. 26, 36–39, 98, 99, 162

EU European Union. 10, 13, 17–20, 22, 26, 29, 31, 38, 39, 49, 58, 64, 81, 95, 122

EUR European Utility Requirements. 35, 36, 39

EVOL Evaluation and Viability Of Liquid fuel fast reactor. 49

EZK Ministry of Economic Affairs and Climate Policy. 25, 36, 37, 41, 43

FNR Fast Neutron Reactor. 48

FOAK First-Of-A-Kind. xiii, 36–39, 41, 43, 44

GB Grain Boundary. 186, 189, 190, 196–198, 202, 203, 241, 243, 244, 249, 250, 254, 269, 271, 272, 276, 288, 289, 302

GCP Geometrically Close-Packed. 181, 185, 206, 239

GFR Gas-cooled Fast Reactor. 45, 46, 49, 307

GHG Greenhouse Gases. 9, 10, 12, 18, 26, 28, 52, 54, 61, 64, 65, 75, 81, 104, 112, 118, 121, 130, 139, 151

GIF Generation IV International Forum. 44

HAGB High-Angle Grain Boundary. 252, 256, 258, 270, 271, 276

HFR High Flux Reactor. 178

HG Heat Grid. 88

HT Heat Treatment. xviii, 214, 216, 217, 243, 247–252, 255, 256, 261, 266, 269–273, 275, 280, 306

IAEA International Atomic Energy Agency. 35

IEA International Energy Agency. xiii, 20, 295

IPCC Intergovernmental Panel on Climate Change. 9, 294

IPF Inverse Pole Figure. 231

LAGB Low-Angle Grain Boundary. 211, 232, 252, 254, 255, 258

LCA Life Cycle Assessment. 54, 73

LCOE Levelised Cost of Energy. 25

LFR Lead-cooled Fast Reactor. 45, 46, 48, 49, 307

LWR Light Water Reactor. 46, 47, 49

MRDH Rotterdam-The Hague metropolitan area. 2, 4, 54, 57–61, 64–66, 70–72, 78, 83, 86, 87, 117, 120, 138, 139, 156, 160, 161, 308

MSFR Molten Salt Fast Reactor. xiii, 47, 49–51, 194, 195, 307

MSR Molten Salt Reactor. 2, 4, 5, 34, 43, 45, 47–49, 133, 177–181, 183, 191, 194, 200, 210, 211, 216, 273, 274, 276, 279, 280, 307

NEA Nuclear Energy Agency. xvii, 38, 299

NRG Nuclear Research and Consultancy Group. iii, 178, 179, 211, 216, 275

NSSS Nuclear Steam Supply System. 41, 42

O&M Operational and Management. 2, 95

ODS Oxide Dispersion Strengthened. 180, 181

OM Optical Microscopy. 214, 222, 236

PHWR Pressurised Heavy Water Reactor. 36

PKA Primary Knock-on Atom. 192

PV Photovoltaic. 11, 13, 18–20, 22–24, 26, 28, 29, 52, 60, 65, 72–75, 77, 90, 94, 97, 101, 107, 122, 133, 163, 296, 300, 308

PWR Pressurized Water Reactor. 34, 36–38, 41–43

RED Radiation-Enhanced Diffusion. 194, 195, 199

REE Rare Earth Element. 19, 20

RIS Radiation-Induced Segregation. 198

RTS Reference Technology Scenario. 20

SAMOFAR Safety Assessment of the Molten Salt Fast Reactor. 49, 50

SCWR Supercritical Water-Cooled Reactors. 45, 47, 49, 307

SEI Secondary Electron Image. 214, 223, 224, 229, 235, 248

SEM Scanning Electron Microscope. xvi, 3, 5, 220, 223–225, 236, 243, 248, 250, 261, 269, 279

SFA Shear Fracture Appearance. 214, 218, 219, 262, 266, 270, 272, 275

SFR Sodium-cooled Fast Reactor. 45, 46, 48, 49, 307

SFT Stacking Fault Tetrahedra. 196, 290

SIA Self-Insterstitial Atom. 194, 198, 289

TCP Topologically Close-Packed. xvi, 3, 181, 183, 185, 206, 207, 210, 211, 239, 244–251, 269–276, 279

TEM Transmission Electron Microscopy. 280

VHTR Very High Temperature Reactor. 45, 46, 48, 49, 307

VVER-TOI Water-Water Energy Reactor. 36

WDS Wavelength-Dispersive Spectroscopy. 224

XRD X-Ray Diffraction. 3, 5, 214, 225, 229, 232, 242, 275

Nomenclature

Greek Symbols

α	Capture-to-fission cross section
η	Number of neutrons released per neutron absorbed

Chapter 1

Research focus

1.1 Problem statement

Modern scientific research is highly specialised and concentrated on specific aspects of the scientist's scientific field. However, when complex challenges arise, such as the sustainable energy transition, strong collaboration between scientific fields is required. Unfortunately, in many cases, these fields do not overlap, which causes communication and collaboration problems. As a result, research development is inefficient, and results are inconsistent. As a result, there is a schism between different scientific fields as well as between policymakers. Finally, this leads to less sustainable development.

1.1.1 Sector coupling

The connection between two academic worlds, the built environment and materials science and engineering, is the focus of this double master's thesis, allowing for the evaluation of a highly scientific technology that is little understood by professionals in the built environment, namely nuclear reactor technology. This is achieved by combining traditional research topics of both fields and creating an extensive research framework that is able to evaluate nuclear technology in both its technical and social implications. Part I of this research thesis goes into great detail about sector coupling.

1.2 Research abstract

1.2.1 Part I: Building Technology

Many important life cycle assessment elements are left out of current energy energy transition evaluation methods, making it impossible to conduct a neutral and long-term assessment of the highly complicated energy transition. Consequently, chosen strategies cannot truly ensure long-term sustainable development due to the emergence of new challenges and bottlenecks. As a result, the primary goal of this master's thesis is to investigate an alternative and extended assessment method

capable of re-evaluating the current energy strategy proposition, as well as its primary systems and other energy technologies.

This study focuses on the implementation of nuclear energy in densely populated urban areas, although this technology has been deemed unsustainable by many previous evaluation methods. Nonetheless, it is regarded as an interesting technology due to its numerous potential benefits and relatively high energy density. The Netherlands currently has three designated nuclear energy reactor sites, one of which is in the highly developed Rotterdam-The Hague metropolitan area (MRDH). This region is known for its limited land availability and flexibility, which makes the energy transition even more difficult. As a result, the area has been chosen as the thesis' primary research location. A well-founded comparison between various technologies deemed sustainable can be made by re-evaluating the proposed regional energy transition (RES). Both large-scale system transitions and individual technology studies can benefit from this approach.

The study focuses on determining the challenges, bottlenecks, and benefits of the energy transition. Several transition strategies, including the current proposal and various nuclear energy scenarios, are investigated to evaluate these key strategy parameters. A computational system analysis is performed per strategy to analyse the effects of a given energy system. Several important uncertainty factors that influence the outcome of energy systems, such as climate change and consumption behaviour trends, have been added to the python-based simulation. This research method enables a fair comparison of the advantages and disadvantages of various energy generation strategies and techniques. Finally, nuclear energy can be re-evaluated in a specific region.

The implementation of nuclear energy sources in the region is beneficial in several stages of the energy transition, according to the results of dynamic energy system simulation and evaluation. Both strong (multiple reactors) and light (single reactor) nuclear implementation in the region are viewed as more sustainable than the current transition strategy. The technology's high energy density allows for significant reductions in low energy-dense renewable sources, significantly reducing the required land for energy applications. Furthermore, the technology reduces transitional investment costs, Operational and Management (O&M) costs, and, as a result, energy prices. Furthermore, because of its low potential for new bottlenecks and challenges, energy affordability can be maintained after 2050, whereas renewable-focused strategies cannot guarantee this stability due to their reliance on external regions and thus global stability due to their relatively short operational lifetime.

1.2.2 Part II: Materials Science and Engineering

The goal of the current research is to evaluate a Ni-based structural candidate material under MSR operation conditions to aid in the research and development of Molten Salt Reactor (MSR). Due to their exceptional high-temperature properties and corrosion resistance, Hastelloy-like alloys are being considered for use as structural materials in a number of conceptual MSR designs. However, alloys

based on nickel are known to be vulnerable to thermal neutron radiation. Additionally, prolonged exposure to high temperatures causes gradual changes in the microstructure through thermally triggered microstructural processes like grain growth, phase changes, and precipitation. The High-Flux Reactor (HFR) in Petten, the Netherlands, houses the ENICKMA (Evaluation of NICKel-based MAterials) irradiation project, which was started with the intention of examining the degradation behaviour of six Ni-based alloys and one stainless steel under high-temperature neutron irradiation. The target fluences for the radiation are currently 1 x 2021 n·cm^{-2} for thermal neutrons and 3 x 1021 n·cm^{-2} for fast neutrons, and the temperatures range from 650 to 750°C. The irradiation will be completed by the end of 2022.

In this study, the impact of heat treatment on the microstructure and consequently on the mechanical properties of an un-irradiated Ni-based alloy (MONICR 77.4wt% Ni, 15.0wt% Mo, 5.9wt% Cr) is investigated. The alloy specimens were heated to 800°C in an air atmosphere for intervals ranging from 6 hours to 2,232 hours (3 months). Using electron microscopy (SEM), X-ray diffraction (XRD) and instrumented Charpy and indentation tests performed at room temperature, the alloy was characterised in both its as-received and heat-treated states. In the first 24 hours of thermal treatment, compared to the as-received condition, the heat treated specimens exhibit embrittlement and a decline in strength, leading to a loss in toughness. This period is followed by a partly recovery in toughness relative to the initial value, with measurement indicating mechanical stability after 2 weeks of thermal treatment.

The trends in strength, ductility and toughness indicate the importance of several microstructural mechanisms during thermal treatment. Qualitative observations showed the formation of intergranular jagged Topologically Close-Packed (TCP) precipitates during the first hours of thermal treatment at 800°C. The morphology of this phase promotes brittle fracture because of stress concentrations around the precipitate tips along the grain boundary, this mechanism dominates the observed decrease in toughness. Continued aging coarsens the precipitates and transforms the morphology to a more rounded shape, hence decreasing the intensity of stress concentrations around the precipitates and thus improving the ductility. Second, during the first 48 hours of thermal treatment grains grow by an average of 5 microns, annihilating boundaries in the process, decreasing the density of High-Angle Grain Boundaries and twin boundaries. The loss in twin density decreases the dislocation slip barrier density, which improves the strain hardening ability of the material during deformation, resulting in an increase in toughness. Both mechanisms control the mechanical behaviour during the recovery in toughness. Subsequent thermal exposure does not indicate further grain growth, suggesting that Zener pinning, by the intergranular precipitates, reduces grain boundary migration and creates stability in the alloy its mechanical behaviour. Additional precipitate coarsening is observed to have to have no effect on the toughness of the material but potential depletion of solid solution strengtheners Mo and Cr from the matrix can lead to strength reductions.

The findings of this study will be combined with the findings of the post-irradiation examination test campaign to forecast how these materials will perform over the long term.

1.3 Research outline

1.3.1 Part I: Building Technology

The Building Technology research thesis work is divided into six chapters (chapter 2-7). The first chapter, chapter 2, describes the complexities of the energy transition and its primary challenges, as well as background information on energy support systems and modern nuclear reactor technology. Chapter 3 provides a review of the current literature on the MRDH area's regional transition approach. The research objectives are presented at the end of this chapter. The methodology used to analyse potential energy system transitions is described in Chapter 4. The results of the dynamic simulation are presented in Chapter 5. These outcomes are compared, and each researched strategy's challenges, bottlenecks, and benefits are listed. Chapter 6 discusses these findings and provides an assessment of the experiment's projected correctness. Finally, chapter 7 summarises the main conclusions by returning to the research's main objective. This is followed by suggestions for future research on the subject.

1.3.2 Part II: Materials Science and Engineering

A Ni-based alloy that was characterised by poor brittle performance at high temperatures is the subject of the Materials Science and Engineering section of this research thesis, which is broken up into 5 chapters (chapters 8-12). These chapters discuss the challenges, the state of the research, and experimental work on the alloy.

By reviewing research literature, the first chapter, ch. 8, provides background information on the investigated topic: *embrittlement of a MSR-application Ni-Cr-Mo alloy during heat-treatment at elevated temperatures*. The challenges and specifications for MSR materials, the primary microstructural mechanisms that change the mechanical properties of Ni-based materials when subjected to high temperature thermal treatment, and the microstructural evolution of irradiated materials are all covered in this chapter. A general understanding of the microstructural evolution of MSR nuclear materials, with an emphasis on thermal treatment, is produced by combining these findings. The main conclusions and literature gap from this literature review are presented after this discussion. Finally, these are brought together to create the research goal that is studied and discussed in the experimental work of this study.

The focus on the research methodology and materials is covered in the following chapter, ch. 9. The as-received material is examined first, and then the experimental method resulting from the study's research objectives is covered. Along with background information on data processing of the test data, this chapter also includes brief descriptions of the instruments used. Finally, the chapter offers some techniques for estimating fundamental mechanical properties from test results that clarify some underlying mechanisms of the material's embrittlement.

The findings of the various experiments carried out during the embrittlement study are presented in the third chapter, ch. 10. The results of mechanical testing, computational phase equilibrium simulations, SEM microscopy images and measurements, and XRD measurements are all included in this chapter. In some cases, additional theoretical approximations are used to support the results. A brief description and discussion of the results, including any deviations, is given, followed by an assessment of the data's experimental validity.

The results chapter is followed by an extensive discussion chapter, ch. 11. The various findings are brought together in this chapter to establish a link between changes in mechanical behaviour and microstructural evolution. The discussion lays the groundwork for the key research findings and, as a result, the comprehension of the study's objective—the embrittlement problem of MONICR.

Finally, chapter 12 provides a brief summary of the research's key findings. Following this conclusion, recommendations for additional research on Ni-based alloys for MSR applications are made.

Part I

Building Technology: *Nuclear Energy Implementation*

Chapter 2

Background

The sustainable energy transition

2.1 Global warming

Following the 2021 Intergovernmental Panel on Climate Change (IPCC) report on climate change it became once again obvious that global warming is a result of human activities. The main contributor of global warming is the emission of Greenhouse Gases (GHG) which, in combination with other human activities and natural changes, warmed up the planet its surface temperature by 1.07°C in the last 150 year or so [1, A.1.3]. This rise in surface temperature resulted in warmer oceans that directly impact the arctic region as glaciers and ice sheets melt away, raising the sea level by 3.7mm per year (in combination with thermal expansion of sea water) in the last 15 years, while additionally lowering the ocean salinity [1, A.1.4-7 & A.4.3]. These changes affect many natural climate patterns, such as increasing the likelihood of extreme weather events globally. These events include extremes such as droughts, heatwaves, cyclones/hurricanes and heavy precipitation including increased flooding risk (for full list of climate change effects see appendix figure B.1) [1, A.3].

In all emission scenarios researched by IPCC [1, B.1] the earth will warm up between 1.5°C to 2.0°C with respect to the 20^{th} pre-industrial century (further referred as global warming), unless GHG emission are reduced drastically. For that reason many countries, including the Netherlands, signed the *Paris Climate Agreement* to ensure that global surface temperatures will not exceed the 2.0°C global warming limit to reduce further calamity. For the Netherlands this agreement resulted in a legislation named *Klimaatakkoord*, which states that the emission of GHG need to be nearly eliminated by 2050, while safeguarding the sustainable development goals of the United Nations [3]. The sustainable development goals of the United Nations are listed in figure 2.1.

2.2 Dutch energy strategy

Fig. 2.1 The 17 sustainable development goals to promote prosperity and protect the planet. Reprinted from United Nations [2].

Following the *Paris climate agreement* (2016) and the additional European Union (EU) its climate agreement *Fit for 55* package the Dutch government approved a climate strategy in 2019 for the coming 30 years to lower greenhouse gas emissions and limit the temperature increase related to global warming to less than 2°C. In this strategy, named *Klimaatakkoord*, the Dutch government set a couple of future conditions related to national emissions, with as final goal climate neutrality in 2050. To ensure this goal some additional conditions were set for 2030 [4; 5]. These conditions are:

2030

- 49-55% GHG-emissions compared to 1990
- 27% renewable electricity share in energy mix
- 906 PJ reduction in primary energy consumption (1990[1]: 2856 PJ, 2030: 1950 PJ)

2050

- 95% GHG-emissions compared to 1990
- 100% carbon neutral electricity production

To reach these ambitious goals the government proposed a variety of measures concerning five sectors; (1) the built environment, (2) mobility, (3) industry, (4) agriculture and land use, and (5) electricity. Their share on the Dutch emissions is illustrated in figure 2.2. This thesis mainly focuses on the three built environment related sectors, also referred to as the *greater built environment*, as these are most connected with the generation of energy in the Netherlands. These sectors are the built environment, neighbouring industry, agricultural greenhouses and the overarching electricity sector. The agricultural sector is not discussed in this section because the national strategy primarily focuses on other aspects of the sector in contrast to greenhouses. Nevertheless, the other sector is discussed briefly, due to its potential synergetic relation with surplus energy.

[1] Primary energy usage of 1990 [6].

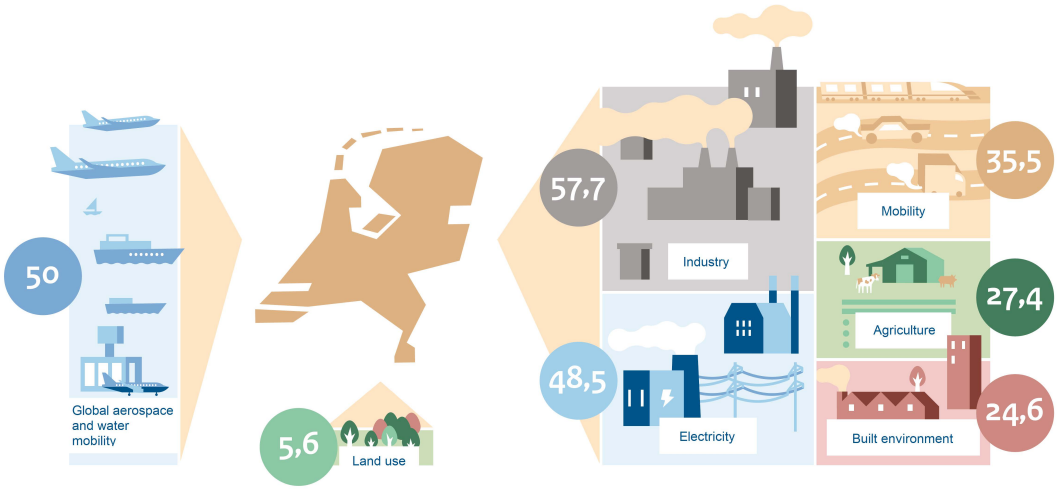

Fig. 2.2 Greenhouse gas emissions of the Netherlands (2017) per sector in Mton CO_2-equivalent. Reprinted and modified from Ministry of Economic Affairs and Climate Policy [5, p. 27].

2.2.1 Built environment

The reformed 2050 built environment envisioned by the Dutch government consists of several significant transitions to lower its total emissions. The most important being the reduction of *usage* related embodied carbon. Meaning all buildings in the Netherlands are required to reduce their energy demand to their fullest potential, while leftover demand is supplied with near-emissionless heat and electricity. The electricity demand can be supplied with local renewable energy from Photovoltaic (PV) solar panels on the roof or a carbon-free source somewhere else in the Netherlands or, to a lesser extend, even Europe. Yet, the remaining heat demand and supply can greatly differ from place to place.

Efficiency in heat generation plays a significant role, buildings located in high density urban neighbourhoods are most likely connected to a heat grid supplied with waste heat from nearby industry or sustainable heat sources, such as geothermal. Buildings located in more remote areas make use of small natural heat sources or covert their green electricity into heat by an electric heating systems [4, p. C1.1].

The 2030 goal is a built environment related emission reduction of 3.4 Mton CO_2-equivalent, resulting in a leftover heat demand of roughly 333 PJ. A 1 Mton reduction is required in the utility sector and for residential buildings 2.4 Mton is required. In 2050 these values need to be reduced even more to have a maximum emission of 5% compared to 1990 [4, p. C1].

To summarise the transition of the built environment, all potential energy sources and flows need to be mapped out, allowing for efficiency studies. Considering not only energy reduction and (infrastructure) optimisation but also economics and consequently energy cost neutrality. The energy mix of the built environment sector of 2019 is given in figure 2.3. It clearly shows the enormous heat

demand of the built environment, but also the potential to transform the system towards a less fossil fuel dependent supply.

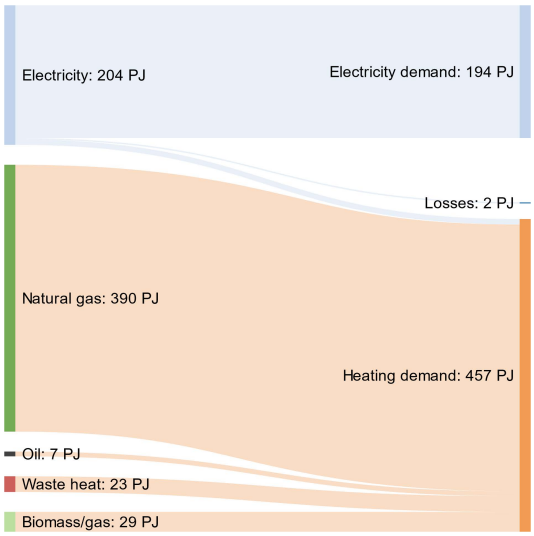

Fig. 2.3 Sankey diagram of the 2019 Dutch built environment sector energy mix. The diagram excludes non-energy resource usage. Data from Energie Beheer Nederland [7] was used to create this overview diagram.

2.2.2 Industry

The future of Dutch industry primarily focuses on synergy relations between industry clusters by the use of material, energy and 'waste' flows resulting in a more circular system. These symbiotic flows, when optimised, result in a significant reduction of required resources, hence lowering the total energy demand of the sector and its embodied GHG-emissions. Luckily, the most polluting industries are clustered in 5 areas in the Netherlands, hence allowing for extensive synergy connections with other industries. This connection translates in an extensive infrastructure network for different resources such as heat and chemicals in and around these industrial clusters. For example, heavy industry with high thermal processes can share its produced waste heat with less heat demanding industries nearby. Besides this new interconnected system, the industry transforms many low heat processes ($< 600°C$ [4, p. 172]) into electric processes, reducing their dependence on coal or natural gas. Processes dependent on higher temperatures still require some sort of combustion supported heating system to operate efficiently, for that reason low carbon fuels are used such as hydrogen produced from surplus electricity [4; 5].

In 2030 the industrial sector is expected to lower its emission share by 59% compared to 1990, a reduction of 14.3 Mton of CO_2-equivalent. Reductions in other sectors due to commensalistic relations with industry clusters do not account for emission reductions in the industry sector. Final emissions are expected to reduce to less than 5%, compared to 1990, in 2050 [4, p. C3].

All in all, clustered industry transforms into a symbiotic system, sharing chemicals, heat and many other resources. Additionally, when possible the industry electrifies to become less dependent on pol-

luting combustion processes and further exploits sustainable electricity sources. When electrification is not possible carbon neutral fuels are used. The energy mix of the built environment sector of 2019 is given in figure 2.4. Once again showing its dependence on heat supplied by many different fossil fuels. Nevertheless, it also illustrates the benefit of commensalistic connections between industries, considering the current waste heat input, supplying a quarter of the heat demand in this sector.

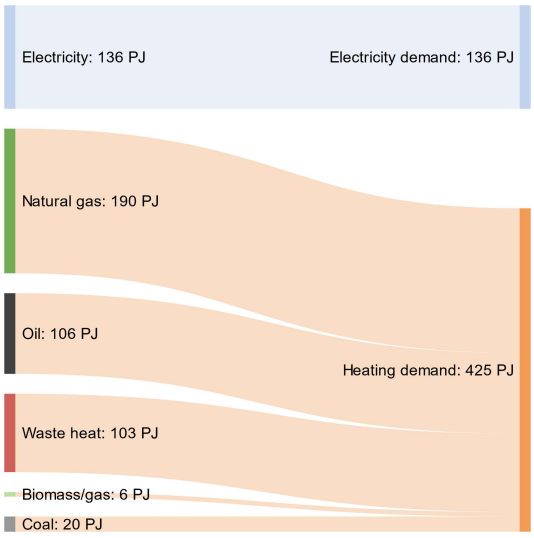

Fig. 2.4 Sankey diagram of the 2019 Dutch industrial sector energy mix. The diagram excludes non-energy resource usage. Data from Energie Beheer Nederland [7] was used to create this overview diagram.

2.2.3 Electricity

Electricity production, being the second most polluting sector in the Netherlands, fully transforms into a carbon neutral sector by 2050. Roofs will be used for PVs and wind turbines will be placed where possible, offshore and onshore. These sources are all very dependent on weather and therefore require grid stabilisers in the form of batteries, hydrogen loops and flexible smart grids. The last referring to a system that prioritises certain processes over another in case of shortages. Other, more constant, electricity sources include power plants using synthetic gas, biogas or fossil fuels with Carbon Capture and Storage (CCS) systems. Importing electricity from other EU countries is seen as a viable option to reduce risks of shortages [4, p. C5]. The addition of nuclear energy to this mix is not likely to happen before 2030, but is expected before the 2050 goal, following the inclusion of nuclear energy into the Dutch 2021 coalition agreement and the European green energy source list, the *EU taxonomy* [8; 9].

To fully decarbonise electricity production, the Netherlands set a goal for 2030 to reduce emissions to 20.2 Mton, a 28.3 Mton reduction from 2017. Current 2030 operating capacity (full load) ambitions go up to 84 TWh (302.4 PJ) of renewable sources, roughly 70% of the total electricity demand. Most of this electricity is produced offshore in wind parks [4; 5].

Currently, the most ambitious scenario for 2050 primarily focuses on wind energy and includes 54 GW of installed offshore wind turbines and 17 GW installed capacity onshore, totalling 239 TWh.

A maximum occupational value calculated by Kuijers *et al.* [10], including all realistic potential locations for future wind turbines.

2.3 Energy demand projections

The yearly published Climate and Energy Outlook (KEV) evaluates current progress and near-future projections regarding the Dutch energy transition. The 2021 outlook [11] projects a emission reduction of 38-48% by 2030, a bit below the required 49% and more ambitious 55% goals. The uncertainty relates to several aspects, such as weather conditions and expected technological/economical development.

With current progress it is expected that the Dutch electricity mix will contain a 75% share of renewables in 2030. Nevertheless, the share of sustainable heating will be drastically less, roughly 12%. Take into account that these figures include questionable sustainable sources such as biomass that still emit carbon-dioxide. This lack in progression is mainly related to the slow roll-out of a shared heat infrastructure between the built environment, greenhouses and industry. Moreover, the temporary use of additional natural gas as a replacement for more polluting energy sources such coal goes less smoothly due to the changing natural gas market and its extremely high prices, as of September 2021 [12]. Additionally, sustainable heat sources, such carbon-free hydrogen and biogas, still have a negligible supply compared to the total Dutch thermal energy demand. Ergo, shifting preferred energy sources back to the more polluting fossil fuels, negatively affecting the emission reduction progression [11].

Summarising, with current progression and legislation[2] the electricity demand of the Netherlands is expected to reach net-zero by 2050. However, the thermal energy demand still faces many challenges and problems as renewable electricity to hydrogen and biogas production are currently inadequate. Further implementation of complex synergetic energy networks can greatly enhance efficiency and reduce demand in all sectors. Nevertheless, a share of the thermal energy will still be dependent on fuels to reach adequate temperatures and efficiency levels if no other energy alternatives are added to the mix. Consequently, increasing the uncertainty that the proposed emission goals are met by 2050 with the current national strategy. Thus, making it evermore important to re-evaluate not only the current strategy, but also the bigger picture, namely the national energy mix with its supporting system.

2.4 Dutch energy mix

The Netherlands has a rather diverse and complex energy network that is dependent on several sources. In the current state a large share of the heat and electricity requirements are still met with carbon

[2]Current national legislation states that fossil fuels and biomass/gas combustion combined with CCS is considered a sustainable energy source.

emitting fossil fuels. An overview of the main energy sources/carriers is given in figure 2.5. The Sankey diagram illustrates the primary energy values and the connections to final consumption. Note that energy conversions happen several times in this system and some include losses. While there are losses related to heat generation, they are not included in this figure because of the primarily decentralised production of heat. This decentralisation results in a variety of energy conversion methods and consequently different efficiencies. For this reason only the primary energy values are of interest. The sector specific energy mix is given earlier in figure 2.3 (built environment) and 2.4 (industry). The energy mix of both agriculture/land-use and mobility are given in appendix figure B.8, as they are less relevant to this master thesis[3].

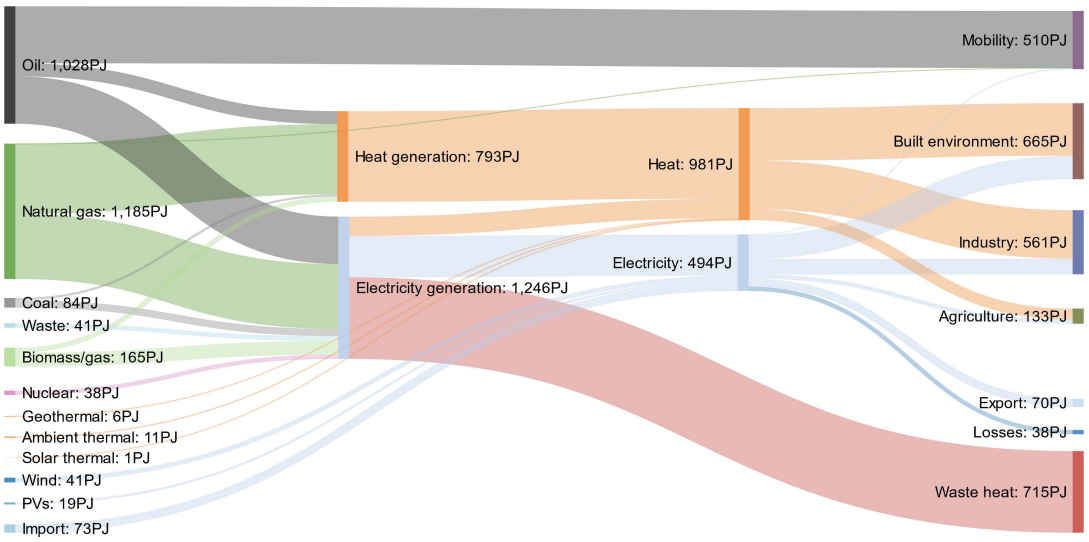

Fig. 2.5 Overview Sankey diagram of the 2019 Dutch energy mix for the primary sectors. The diagram excludes non-energy resource usage. A variety of databases, from Energie Beheer Nederland [7] and CBS [13; 14], were used to create this overview diagram.

Relating back to the energy goals of the Netherlands it makes sense to simplify the diagram above and decrease the input to 6 sources; fossil fuels, renewables, biomass/gas, waste, nuclear and the net import. The latter is included to show certain import/export dependence but is not discussed. Biomass and biogas are separated from the renewable group because these energy resources are not necessarily sustainable renewables. These resources can be produced in a variety of ways, meaning without strict government enforcement they can be produced in way that harms the environment, hence removing its potential to benefit the energy transition. Additionally, these sources still produce carbon emissions, and thus need to be captured and stored to be truly sustainable, this is the same for waste incineration. Nuclear energy is separated from the other groups because it is not seen as a renewable because it still requires fissile material that needs to be excavated. It is also not categorised as a fossil fuel as it is categorised as a nearly carbon-free source. The simplified overview is given in figure 2.6.

[3]The national agricultural energy mix is not comparable to the primarily greenhouse agriculture of the researched region.

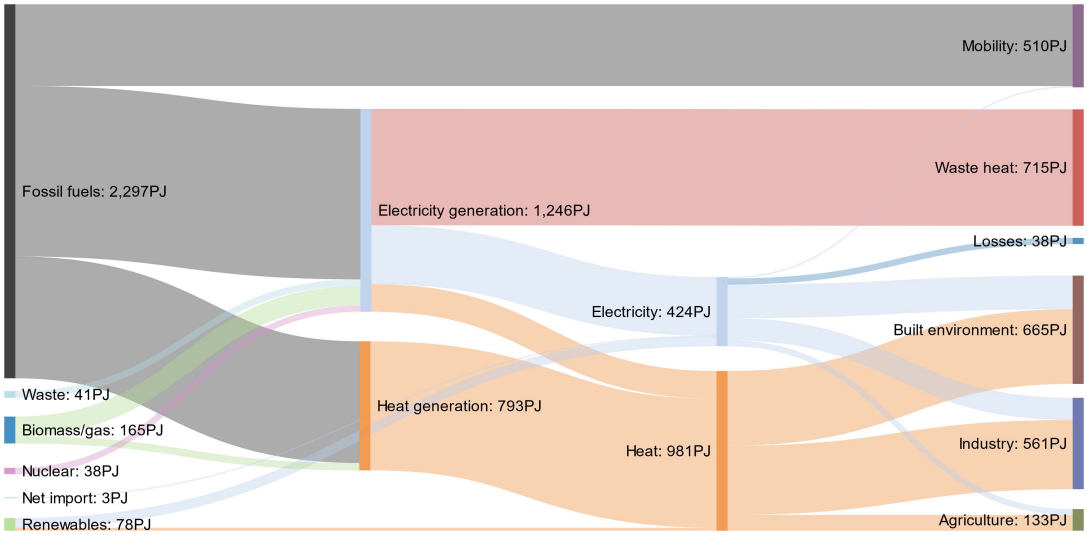

Fig. 2.6 Simplified overview Sankey diagram of the 2019 Dutch energy mix for the primary sectors. The diagram excludes non-energy resource usage. A variety of databases, from Energie Beheer Nederland [7] and CBS [13; 14], were used to create this overview diagram.

To summarise the current (2019) energy mix state of the Netherlands the primary energy sources are categorised into four groups; fossil fuels (non-renewable, CO_2-emitting), renewable fuels (renewable, CO_2-emitting), nuclear (non-renewable, CO_2-neutral) and renewables (renewable, CO_2-neutral). The list below shows their current energy share:

- Fossil fuels: 87.7%
- Renewable fuels: 7.9%
- Nuclear: 1.4%
- Renewables: 3.0%

When these figures are compared to the 2050 energy goal, namely a 95% carbon neutral energy mix, the Netherlands still has a long way to go. At its current state the sources produce a share of roughly 4.4% up to 9.6% of nearly carbon neutral energy. In which the uncertainty range is related to the ability to store carbon emissions of the renewable fuels. In the most ambitious 2030 scenario a Carbon Capture and Storage capacity of 5-11 Mton is expected [11, p. 14]. Yet, biomass (excluding biogas) incineration resulted in a 16.7 Mton CO_2 emission in 2019 [15], meaning between 30-66% could potentially be carbon neutral by 2030 if the biomass incineration does not increase.

All in all, it is clear that the Netherlands is still highly dependent on carbon emitting energy sources even when techniques such as CCS are added to the energy mix system.

2.4.1 Energy mix projections

Due to the complexity of energy the following projections all have a considerable range due to many uncertainties, such as political decisions, popular opinions and technological development. Most of these estimates are made for the near-future because several new energy projects are already approved or even under construction. Consequently, the estimates for the (near) future supply are more precise than those of the projected demand.

When comparing data from last several years it becomes clear that the primary energy demand in the Netherlands is reducing. In 1990 the primary energy use was 2,440 PJ excluding non-energy resources. At current rates the demand for 2030 is projected to be reduced to roughly 2,200 PJ excluding non-energy resources. Nevertheless, if the Netherlands invest more to improve energy efficiency it may reach the European guideline goal (32.5% energy reduction compared to 1990 in 2030), namely 1,647 PJ. These reductions are the result of synergy networks between different users, but also the enhanced efficiency resulting from modernised industrial processes and the greater built environment energy saving projects [11, ch. 4.1.2].

Another important transition is the electrification of the energy mix. In 2019 roughly 16% of the total primary energy supply was consumed as electricity. PBL [11, p. 99] estimates this share will increase to roughly 25% in 2030. For 2050 the predictions are still uncertain, but many different scenarios, such as the ones described in table 2.1, approximate a drastic increase in the electricity demand share up to 71% in 2050, due to both industrial electrification and increase in digital devices (digitalisation).

Last couple of years the capacity of renewables is growing steadily and the installed capacity is predicted to grow up to 4 times compared to 2019. The installed capacity estimates for 2050 have a large range, as many uncertainties, such as political decisions and popular opinions, can change the preferred energy sources drastically in this 30 year time span. Table 2.1 shows the key figures from the most recent and elaborate Dutch energy transition scenario studies, and the current to near-future installed capacities. The scenario's *regional, national, EU and international* compare different political approaches and their effect on the chosen sources, while *adapt and transform* describe the societal willingness to change our consumption behaviour, with transform representing a more anti-consumeristic society. At last the *realistic potential* scenario is given, this scenario describes the maximum installed capacity in the Netherlands based on land availability, including many limitations such as the built environment regulations and land-use related stakeholder challenges.

Table 2.1 Scenario overview of several potential strategies based on political decisions and societal willingness to change. Data given in this table is bundled from different references given under the *Source* row. The electricity generation row gives the predicted annual production values taking the full load hour efficiency, described by ENCO [16, p. 47], in mind; offshore wind 43%, onshore wind 24% and solar PV 10%. **Real production value of 2019.*

	2019	**2030**	**Regional**	**National**	**EU**	**International**	**Adapt**	**Transform**	**Realistic potential**
Solar PVs [GW]	7	25	125	106	42	38	99	89	102-167
Onshore wind [GW]	3.5	8	20	20	10	10	8	11	9-17
Offshore wind [GW]	1	11.5	31	52	30	28	33	58	36-54
Electricity generation [PJ]	62*	295	966	1,191	615	575	820	1,150	878-1,384
Primary energy reduction	-7%	5%	43%	32%	8%	5%	10%	31%	-
Electricity share (primary)	16%	25%	68%	69%	37%	35%	43%	71%	-
Source	*PBL [11] and CBS [17]*		*den Ouden* et al. *[18]*				*Scheepers* et al. *[19]*		*Kuijers* et al. *[10]*

The most ideal 2050 scenario would be a large reduction in primary energy consumption combined with a high share of electrification. This combination results in a minimum heat requirement which works beneficially with renewable energy sources as these techniques produce electricity directly, and therefore do not produce any waste heat during conversion. For this scenario the yearly primary energy requirement results in 1,684 PJ (excluding non-energy related resources) with an electricity demand of 1,195 PJ. From these figures it becomes obvious that many of the scenarios given in table 2.1 are not able to produce nearly enough to supply the electricity demand, making them dependent on import of electricity from other countries. The additionally 489 PJ heat requirement needs to come from other resources that produce little to none GHGs. To achieve the current 2050 goal, a 95% GHG-emission reduction, a 8.2 Mton CO_2-equivalent release is allowed. Without any CCS techniques this translates into an allowed combustion of 145 PJ worth of natural gas[4] and leaves a 344 PJ heat demand gap. When generating this heat with hydrogen an additional 491-688 PJ of electricity is required[5]. Resulting is a total electricity demand of at least 1,686 PJ, a value 22% higher than the maximum realistic potential calculated in the spatial research study conducted by Kuijers *et al.* [10] from Wageningen University & Research. Take in mind that these figures do not include the required energy for electricity storage and other grid stabilisation components. An overview of this extreme transition is given in figure 2.7.

It is important to comprehend the scale of this given transformation, as the system as a whole is required to change. Resulting in a renewable fleet growth of 1800% and a 100 times increase on electricity import from neighbouring countries, hence increasing the Dutch energy dependency. Therefore, it is important to discuss the addition of other sustainable energy sources to the future energy mix of the Netherlands. Ensuring the economical and innovative position of the Netherlands even well after the energy transition.

[4] 1 PJ of natural gas releases 0.0564 Mton CO_2-equivalent [20].

[5] Current hydrogen electrolysis processes have an efficiency between 50-70% [10, p. 154].

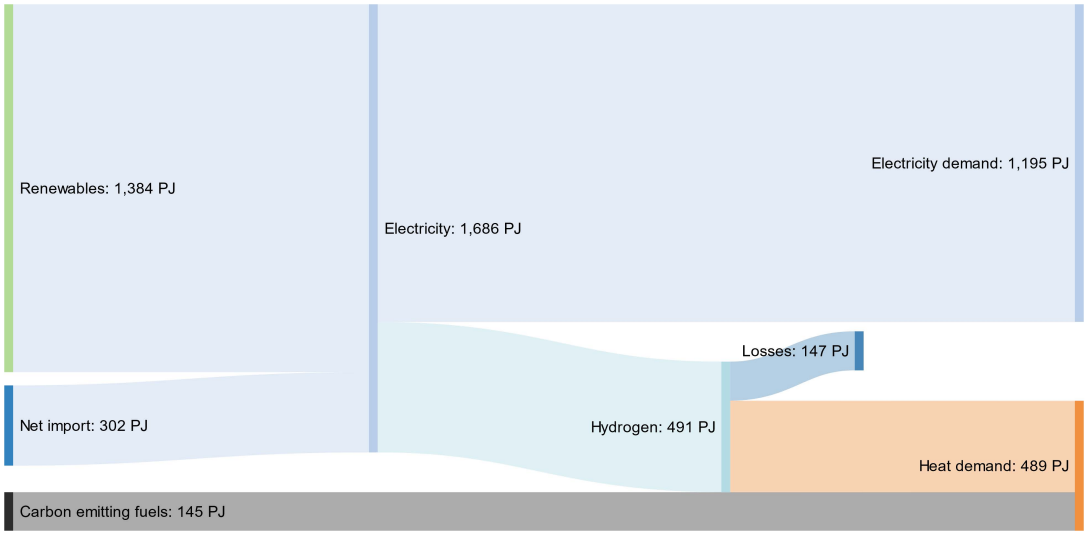

Fig. 2.7 Sankey diagram of the 'ideal' 2050 energy mix following current energy transition strategy of the Netherlands and the most optimal trends.

2.5 Renewable technology challenges

2.5.1 Material requirement

Unfortunately most renewables, and mostly solar PVs, wind turbines and their associated batteries, require substantially more minerals compared to the current fossil fuel market [21, p. 11]. Therefore, with the current energy transition approach (Beyond 2-Degree Scenario (B2DS)), 70% renewable energy sources in 2050, global demands in many elements will peak the coming 30 years. As a result Watari *et al.* [22] predicts that the material flow associated with the production of these required materials will be around 200-to-900% of current values just for the energy sector. As seen in figure 2.8, the overall global material demand is estimated to quadruple in the next 30 years if we want to limit global warming, a growth that is mainly caused by the implementation of renewables in developed countries. Such an increase in demand can result in various future material problems and challenges, potentially diminishing the sustainable character of the transition.

The most difficult challenges is meeting the increasing element demand used in these technologies. Most of the current used renewables, and other in-demand technologies, are dependent on a wide range of different elements [23, pp. 96-99; 24, p. 7], many of those belonging to the Rare Earth Element (REE) group [25, p. 7]. The scarcity of these elements in combination with the growing demand, as shown in figure 2.9 for several elements, can lead to many future supply risks and (political, social and economical) dependence for the Netherlands and European Union, but also many other non-REE producing countries, which could be a danger to the smooth transition from fossil to low-carbon energy, as prices are likely to increase [24, p.7]. Figure 2.10 shows the supply risk of some important

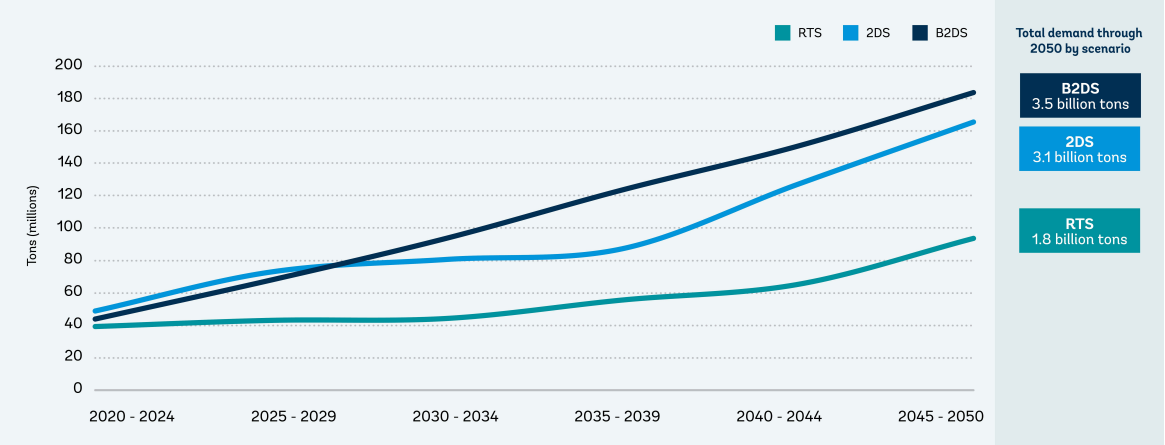

Fig. 2.8 Annual projected mineral demand up to 2050 for three different IEA scenarios: Beyond 2-Degree Scenario (B2DS), 2-Degree Scenario (2DS) and Reference Technology Scenario (RTS). Reprinted from Hund *et al.* [21, p. 11].

elements that are used in some key transition technologies. A full list of important elements in both solar PVs and wind turbines is given in appendix figure B.4.

Fig. 2.9 Global annual critical element demand for solar and wind energy during the energy transition, between 2020 and 2050, compared with annual production of these elements (2017 = 1). Reprinted from van Exter *et al.* [24, p. 9].

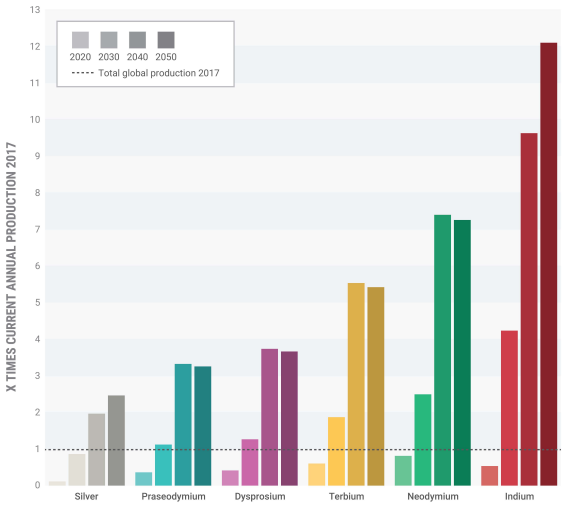

Most of these REEs are currently by-products of other mining activities, but with the drastic increase of renewables, such as PV and wind turbines, require the REE industry to immensely scale up in the foreseen future to meet the growing demand [27, p. 35]. Unfortunately, these minerals are not feasibly found within the European Union, therefore making the EU dependent on other countries [23, p. 14]. A full list of all critical elements for the EU is given in appendix figure B.5).

Sadly, scaling up industrial processes does not come without risks. Mining the required minerals can impact local ecosystems and affect human health in these regions as there are many hidden (by-product) material flows required for mineral extraction that can pollute the environment, hence

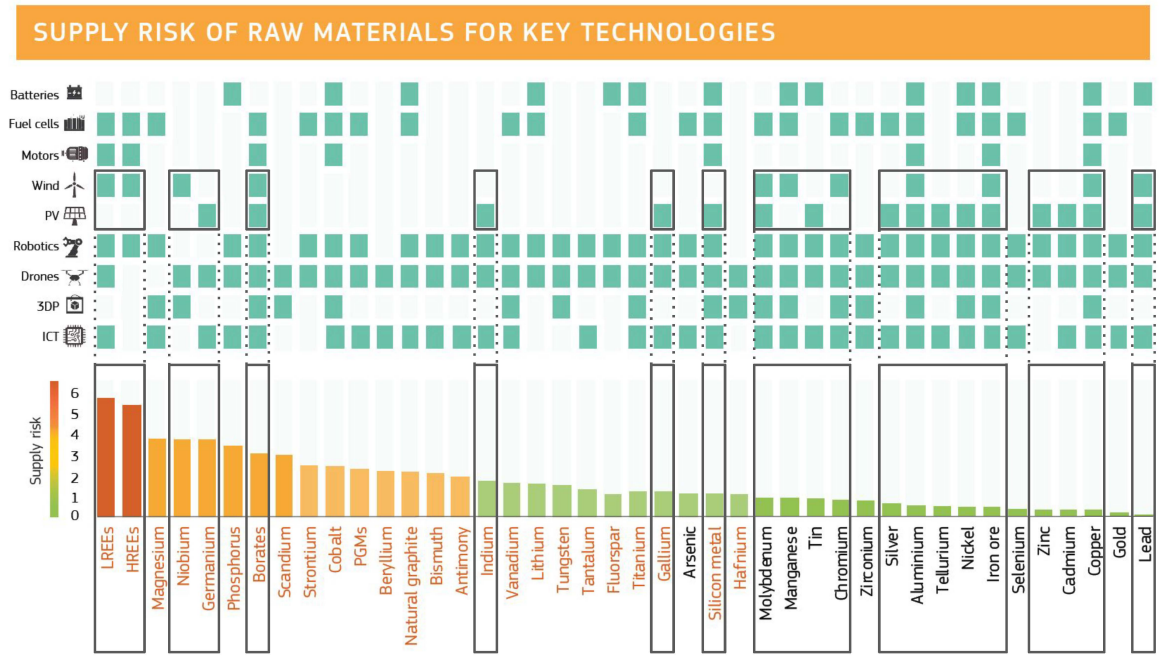

Fig. 2.10 Raw material usage and their supply risk of key technologies for the digital and green transition. Reprinted and modified from Joint Research Centre (JRC) [26].

affecting the greater sustainability goals described by the United Nations [22, p.100]. An example of such environmental degradation is the mining of cobalt (used in lithium-ion batteries) in the Congo, where the extraction resulted in heavy element contamination of the environment, as well as escalating ethical problems such as child labour. Which, in its turn, result in many health complications in these mining communities, but also result in crop failures and the reduction of wildlife [22, p. 100]. All weakening these vulnerable communities. For some of the critical elements the impact of extraction is already well known, making it possible to reduce its negative impact, while for minerals that are currently produced as a by-product the impact is uncertain.

Additionally, other problems arise when mining activities scale up, such as the degradation of ore grades as element concentrations and their locations in the earth its crust are a limiting factor [22, p. 92]. An example of this degradation is the decline in copper ore grade by 25% in the last 10 years [28]. Ores with lower grades result in a higher total material flow as more ore and energy is needed to produce the same amount of material, while also producing more mining waste and sometimes by-products [22, p. 95; 21, p. 104]. This degradation of ore quality can increasingly affect the cost and supply of these currently non-critical materials. Potentially making these elements critical in the near-future as a consequence of the current energy transition strategy.

For the Netherlands this means that if 2030 emission goals need to be met with its current strategy, a significant portion of the global element production is required to construct the needed renewable sources and their supporting systems. Only if solar panels and wind turbines (excluding required grid

batteries) are taken into account, the country requires roughly 1.8% of global neodymium production, 1.5% terbium, etc, for the coming years (other elements given in appendix figure B.6). Comparing these values with the energy share of the Netherlands globally, 0.51% [29], the renewable transition seems extremely difficult to achieve, making the current strategy less feasible and more prone to potential future threats and problems. Therefore, it is important to explore other low-carbon energy alternatives that require less (scarce) materials to produce a similar amount of energy.

2.5.2 End-of-Life complications

As described many renewables are required to produce our current demand in the Netherlands. Consequently, increasing the demand of a variety of different minerals, both critical and common. Normally such investments, related to great transformations, are not seen as a primary problem if these sources provide huge amounts of energy for an extensive operational lifetime (high economical potential). Yet, for many of the key technologies for a renewable energy system there lifetime can be problematic. Below a list is given of the technical operational lifetime for the most important technologies discussed in this thesis. These values are based on a 100% utilisation factor.

Technical operational lifetime

Energy sources

- Solar PVs: *20-25 years* [10; 16; 30]
- Offshore wind turbines: *25 years* [18; 30]
- Biomass and natural gas power plant: *30 years* [18; 30]
- Nuclear reactors: *60-80 years* [16; 18; 30]

Energy storage

- Hydrogen P2P plant: *10 years* [16; 18]
- Electrical batteries: *10 years* [30]

As seen, the operational lifetimes of every technologies greatly differ. With storage technologies having the shortest lifetime, followed by solar and wind renewable sources. Due to these shorter lifetimes many of the key elements in a renewable energy system require replacement every couple of decades. Due to these replacements the expected growth of waste materials from these sources is projected to drastically increase the coming decade. As illustrated in figure 2.11, the increase in Photovoltaic waste is the most considerable in the European Union. While theoretically a large share of this waste could be recycled[6] the majority of components cannot be feasibly extracted [31].

[6] PVs 95%, wind turbines 90% and batteries 100% [31].

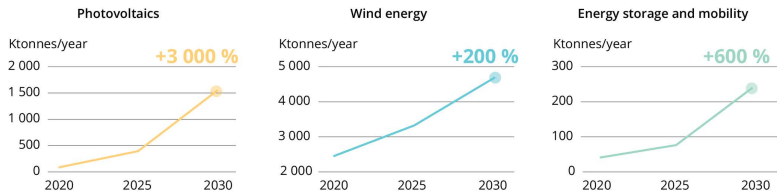

Fig. 2.11 Expected growth of waste materials generated by the clean-energy infrastructure in the coming 10 years. Reprinted from the European Environment Agency [31].

The primary problem regarding the recycling of these technologies is the way these technologies are manufactured. Complex components such as permanent magnets used in wind turbines and semiconductors used in PV cells are more difficult to recycle as these materials are layered or glued to other materials, making it increasingly difficult to recycle them without degrading their required high quality standards. Additional problems arise from material design decisions, as affordability is, in most cases, chosen over End-of-Life (EoL) processing feasibility. For example wind turbine blades a made with composite materials as this material allows for light weight and affordable blades. Unfortunately, due to the characteristic composition of these materials, they are very difficult to recycle.

These complexities result in high cost of recycling combined with significant energy and chemical requirements, if adequate recycling quality grades are to be preserved. These grades are necessary if the recycled product wants to be re-used in new solar PVs or wind turbines. Otherwise these material intensive components are downcycled, incinerated or deposed as landfill.

To conclude, due to the many challenges related to the recycling of these technologies the amount of waste from renewable technologies will accumulate. Without any extensive EoL strategies for these technologies the demand of these products will not decrease. Consequently, keeping the demand and production of the required virgin elements constantly high in the near-future. Further increasing the problems and challenges around material production emissions and element criticality, as discussed in section 2.5.1.

2.5.3 Electricity network instability and cost

One of the main challenges with the current energy transition strategy is the instability of renewable electricity production. While many other forms of energy sources deliver a constant amount of energy, referred to as a *base load*, many renewables do not as they are dependent on weather. With solar and wind dependent technologies being the most vulnerable to generation variations. Consequently destabilising the electricity grid, resulting in many inconsistencies and therefore creating new challenges regarding the electricity demand.

Figure 2.12 clearly illustrates these daily and monthly fluctuations. While yearly the production of electricity seems to be somewhat constant the day to day fluctuations greatly affect the supply and demand chain of electricity in the Netherlands. Our current grid is not able to handle these fluctuations as many of our sectors require a constant energy supply. This effect is most notable in the industrial sector that in many cases has the highest operational efficiency when industrial processes can operate

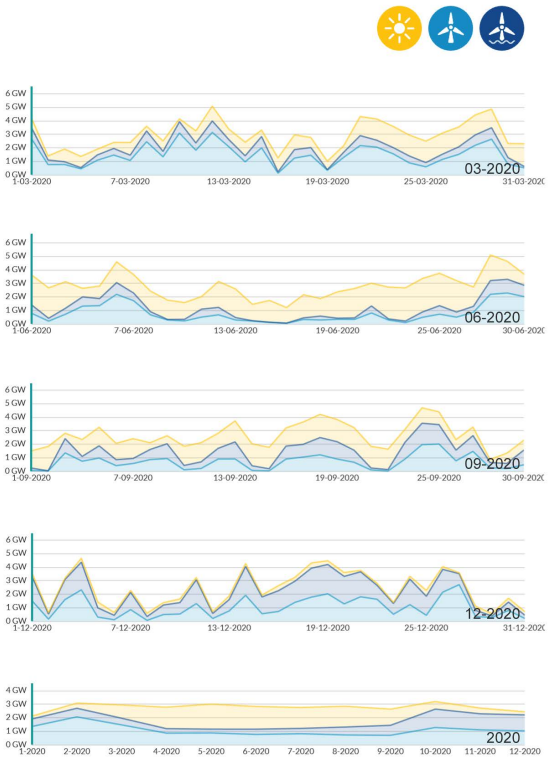

Fig. 2.12 Overview of renewable electricity production of wind and solar PVs, for the seasonal months March, June, September and December and the yearly overview of 2020. The graphs present the real production capacity. Retrieved from Energieopwek [32].

constantly 24 hours a day, 7 days a week. Meaning that a possible industrial plant shutdown due to shortages could result in a higher overall electricity demand. These fluctuations are amplified on hour to hour span as renewables on average produce less electricity during the night (visualised in appendix figure B.9). An increased renewables share results in the so-called *duck curve*, an hour dependent imbalance between in electricity production resulting from renewables that creates an imbalance. This imbalance is illustrated in figure 2.13.

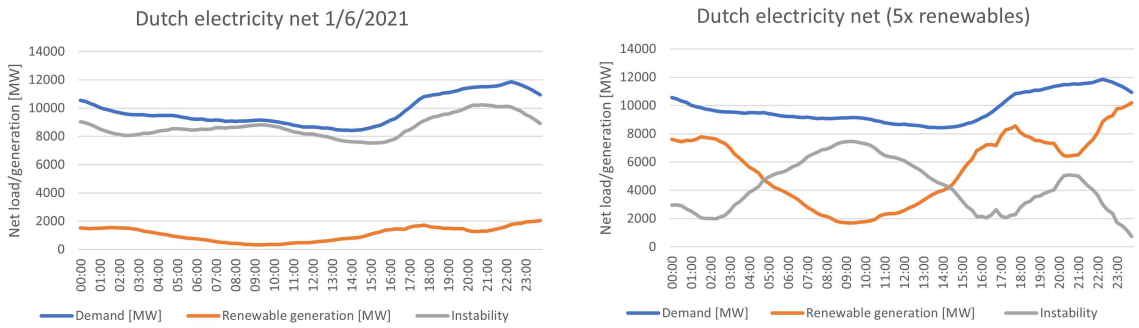

Fig. 2.13 Net instability as a result of daily demand fluctuations and renewable electricity generation fluctuations on the first of June 2021. (left) Real net instability, (right) amplified instability with 5 times more renewables in system. Data retrieved from ENTSO-E [33].

Additionally, the instability of electricity production translates into the requirement for a flexible electrical grid that is able to operate even under peak generation hours. Currently the Dutch electrical

grid has a flexible capacity of roughly 22 GW, but with the future energy mix this capacity needs to increase to around 24-27 GW in 2030 and roughly 44 GW in 2050, due to factors such as local peak loads and increasing distribution heterogeneity. Such increases in the electrical grid are extremely costly [34, p. 120, 139].

Grid stabilisation technologies

To stabilise a grid including renewables, and thus smoothening the duck curve imbalance, storage capacity is required. This capacity can come from several technologies such as electric batteries, synthetic fuels (including hydrogen) and natural batteries (e.g. gravity battery). All of these technologies are, at the required scale, very expensive and can cost multiples more than the construction and operation of renewable sources [16, ch. 5.5]. For example, the production (electricity-to-fuel) and conversion (fuel-to-electricity) of hydrogen enables time independent storage of energy, but when converted back to electricity loses 52-64% of the initial energy input as a result of production limitations and efficiencies [35, p. 64]. Additionally, it requires a substantial amount of land for the connected support infrastructure, conversion hubs and commercially available storage, this problem is similar to all current storage technologies. For this reason it is important to research alternative energy system strategies that potentially balance the grid with different flexible energy sources to potentially minimise total electricity cost and reduce the system its impact.

Levelised cost of renewables

One of the main incentives for industrial change is cost. For this reason it is important to compare the cost of different CO_2 neutral energy sources over their complete lifetime, this cost is referred to as Levelised Cost of Energy (LCOE) [EUR/MWh]. To compare these costs it is important to understand which factors influence the overall cost of a source, these factors are listed below, note this list includes system costs as these are significant for modern energy sources. The values shown in this section are results from the energy mix study from ENCO [16, ch. 4.3] commissioned by the Ministry of Economic Affairs and Climate Policy (EZK).

- Capital cost; total cost from application of power plant up to first moment of operation.
- Plant operating cost; fuel, waste, operation, maintenance (including future design modifications), insurance, taxes and final decommissioning fund.
- External cost; environmental and health related levies related to energy production.
- System cost; cost of energy source integration into the electricity system, e.g. energy storage for variable sources or cost of additional power lines.

In this comparison between variable renewable energy sources and nuclear multiple assumptions are made, a full list of assumptions can be found in appendix C.1. The most important assumption

is the technical lifetime of the sources, namely 25 years for the renewable sources (solar PVs and onshore/offshore wind) and 60 years for nuclear. It must be noted that the lifetime for assumption for nuclear is very conservative as current projected lifetime for new nuclear plants is estimated around 80 up to 120 years. The next assumption is the utilisation of the sources, which is set at 100%. Peaks and shortages due to variable production are stabilised by hydrogen battery systems. Figure 2.14 illustrates the estimated cost per MWh in the Netherlands for an energy mix with 50% renewables and its resulting additional cost of required storage capacity in the form of hydrogen in 2040 [16, ch. 5]. Both EPR2 and ASMR represent nuclear technologies and are further discussed in section 2.7.2-2.7.6.

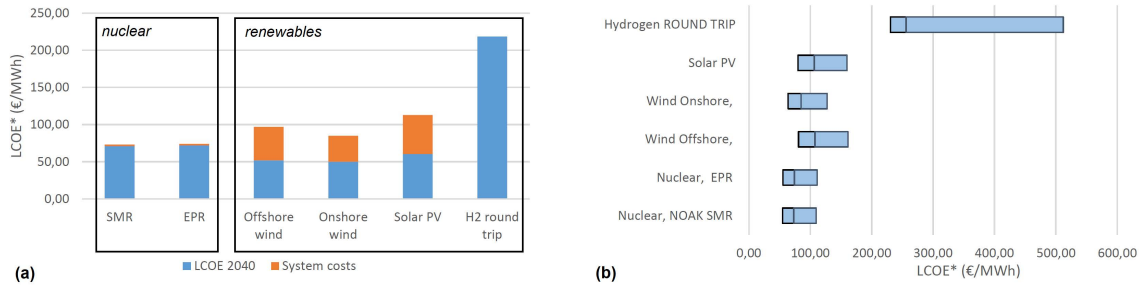

Fig. 2.14 The levelised cost of energy in the Netherlands (2040) for carbon neutral energy sources with a 50% renewables share and full utilisation including electricity storage as hydrogen (H2 round trip). Figure (a) represents the average estimated cost, (b) illustrates the uncertainty range. Reprinted and modified from ENCO [16, pp. 53-55].

The study concluded that alternative technologies known for their high cost, such as nuclear energy, when used in combination with renewables, become relatively more affordable compared to variable renewable sources. As system costs and electricity buffer requirements are almost negligible in technologies that provide constant output. In other words, the addition of such constant energy sources to the energy mix of a country such as the Netherlands could potentially result in a significant reduction in cost per energy unit, including all elements directly related to the energy system.

2.6 An alternative source: Nuclear energy

Due to the complexities of the energy challenges the European Union does not want to reject any form of GHG-free energy sources beforehand, and therefore carried out a research assessing the safety of nuclear energy to ensure its possible position in the energy mix of the EU. Possibly adding nuclear energy to the *EU taxonomy* list, giving the technology the environmentally sustainable label and consequently improving investor security. This label makes the energy source more interesting to investors, leading to an enhanced financial environment that is willing to provide more to the expensive nuclear power plant construction and nuclear energy research projects. The research conducted by the Joint Research Centre (JRC) [36] concluded that modern nuclear energy reactors and their related processes can be considered as a sustainable energy source that could contribute significantly to the energy transition objectives set by the EU.

In the last 50 years nuclear power plants became an important public debate as whether to continue the production of nuclear energy. After multiple nuclear accidents the world changed their view on the technology, as many find it to be unsafe for humanity [37, p. 9]. But when looking at the accidents themselves the World Nuclear Association [38] reported that only the Chernobyl disaster resulted in direct fatalities and serious human harm, while the usage of nuclear power also resulted in roughly 76 PWh of nearly carbon-free stable energy from 1971 to 2018. This avoided 63 gigatonnes of cumulative carbon dioxide emissions in this period [39, pp. 8-9], equaling an avoided 0.03°C of global warming [1, p. D.1.1] and preventing roughly 1.84 million air pollution-related deaths. Yet, all nuclear disasters combined caused an estimated 4,900 deaths, clearly illustrating the current stigma of the technology being harmful [40].

For modern reactors this stigma is even less coherent, as assessment of modern reactor technologies[7] found that these technologies have equal or magnitudes smaller impact on the environment and human health compared to other energy sources, including renewables, making them an interesting option for sustainable climate change mitigation strategies.

2.6.1 Advantages of nuclear energy

Stable, emissionless and energy dense

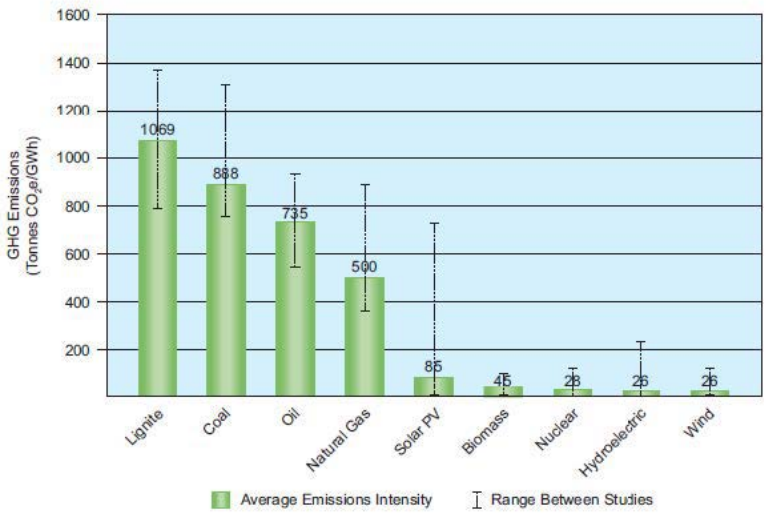

Fig. 2.15 Life cycle greenhouse gas emissions for several key energy source technologies. Based on a variety of studies. Reprinted from the Abousahl *et al.* [36].

Nuclear reactors, such as any fuel dependent energy source, are independent of external factors regarding their energy output. Therefore providing a stable output when provided with enough fissile material to sustain nuclear fission processes. One of the main benefits of nuclear fission is the high energetic potential of these reactions, releasing lots of energy without the production of

[7] Modern reactors are classified as; generation III+, Advanced Small Modular Reactor and expected generation IV reactors.

GHG-emissions and additionally only requiring little fuel. Thus, resulting in a high energy production per unit area value. Combined with an average lifetime of at least 60 years for modern reactors the resulting emission intensity of the energy source outperforms other technologies labeled as sustainable, as seen in figure 2.15 [36].

Geographical flexibility

In addition, many low-carbon energy sources are dependent on geography, as hydropower requires height differences, PV panels a sufficient amount of solar radiation and wind turbines perform more efficiently in specific topographies. These requirements make it more difficult for various regions and climates to transition to carbon-'free' energy. For the Netherlands specifically this means that some of these energy sources are not ideal. Solar power will be less efficient compared to more sunnier countries, as the full load efficiency are roughly 10% in the Netherlands. Consequently, meaning the Netherlands requires many more PVs to supply a significant amount of solar energy, hence resulting in a higher total material flow. The same goes for hydropower which is not feasible in most of the Netherlands due to its flat topography. While wind energy is a great candidate, as the country is known for its windy weather. Still, many regulations limit the placement of those turbines [41, p. 14], narrowing the theoretical power output as discussed in section 2.4. Nuclear power, however, is an energy source that is less dependent on geography. Most important geographical requirements are a low probability of extreme natural disasters, such as flooding and ground motion, and the accessibility to a reliable water source [42].

Material demand and environmental impact

As already discussed in 2.5.1, the energy transition comes with an enormous material demand that is mainly provided with virgin materials to maintain the technology standards. Resulting in further production emissions of GHGs that accumulate in our atmosphere and contribute to climate change. When comparing the predicted cumulative emissions as result virgin material production of six major energy transition elements per transition technology, see figure 2.16, nuclear energy stands out as it has a minimal emissions compared to the other sources. It is important to note that the data shown in this image represents a share of nuclear energy of roughly 24% while the renewables account for just 16% [43], favouring nuclear energy even more. One of the main reasons for this low cumulative emission value is the relatively long operational lifetime of nuclear reactors, as renewables have a lifetime of roughly 25 years while modern nuclear reactors last at least 60 years.

2.6.2 Disadvantages of nuclear energy

As with any technology nuclear reactors come with their own challenges and problems. Ergo, it is important to discuss the most limiting problems to understand the challanges of this energy source.

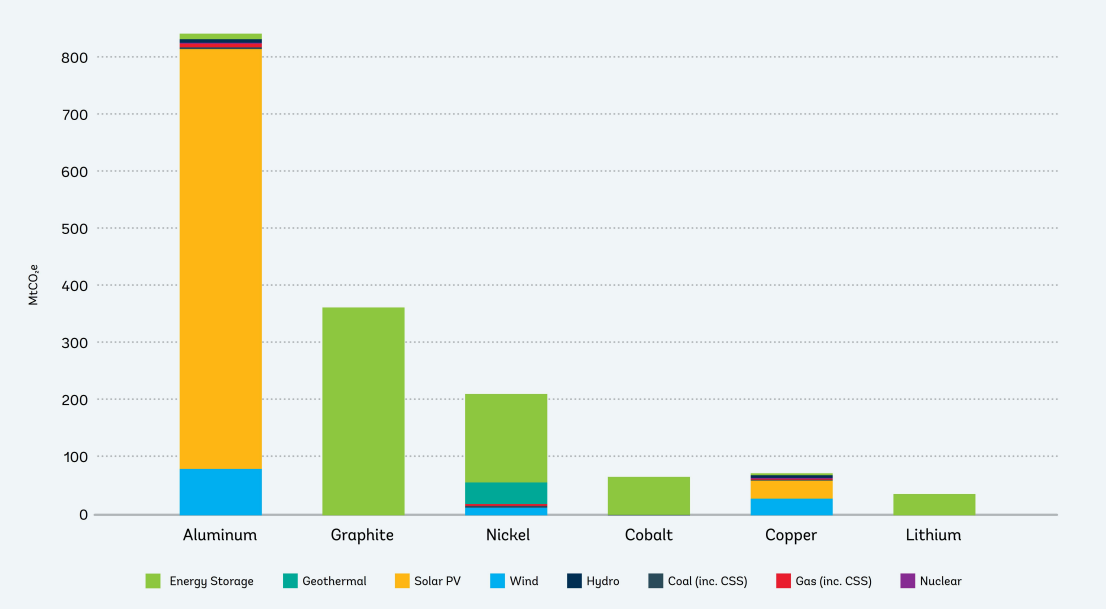

Fig. 2.16 The cumulative carbon dioxide equivalent emission potential from extraction and processing of the major six energy transition elements (excludes operation emissions). Solar PVs, wind and its supporting energy storage systems represent 15.6% of total energy share, while nuclear represents 23.7% [43]. Reprinted from Hund *et al.* [21, p. 11].

Radioactive waste

The main problem of nuclear energy is the production of radioactive waste that lasts for thousands of years. Radioactive isotopes are produced as a byproduct during fission reactions, but also during the production of fuel and re-processing of spent fuel. These isotopes are produced in all life cycle stages of the power plant. The majority of these waste products are labeled as low-to-intermediate level radioactive waste that requires storage for several decades in a cooled and ventilated space. When the isotopes have a very long half-life the waste is stored in stable geographical repositories such as old mines. Prolonged presence in these waste storage rooms can be harmful to our health. After a certain period, depending on the half-life of the waste isotopes, the radioactivity decreased enough to be labeled as safe again. At this point the waste can be recycled and re-used for other purposes. Only a minor fraction of the reactor waste consists of high level radioactive waste, which is separated from the other less dangerous waste. These isotopes are seen as extremely harmful as they produce high levels of radiation. For that reason they require many additional safety measures to be safely disposed and stored until it is safe to be recycled. Just as with the other waste the storage time depends on its half-life. For the transuranic isotopes such as plutonium this means providing safe storage for thousands of years. Currently several locations are allocated for this highly safeguarded storage in the EU. These locations include very stable deep geographical repositories in France and Sweden, but also the *COVRA* in the Netherlands. In combination with the many regulations around nuclear storage in the EU the long-term disposal of these isotopes is assessed as safe [36].

Additionally, the implementation of generation IV burner reactors could greatly reduce the negative impact of radioactive waste. These reactors are, because of their re-designed fuel cycle, able to 'burn' more actinides that normally do not have the possibility to fission. These isotopes are mainly transuranic and therefore the amount of waste combined with their long-term activity characteristics are significantly reduced. Resulting in a maximum high level radioactive waste storage of roughly 300 years for only a minor fraction of the current high level radioactive waste. The physics behind this ability are described in section 2.7.1.

Non-renewable: fuel dependence

It must be noted that renewable energy sources are all without fuel requirements, and thus have a very low amount of in-use operational material cost (only repairs and maintenance). Considering the current energy market, the extraction and processing of, mainly fossil, fuels require an immense amount of labour, chemicals, cost and energy. In 2014 the worldwide energy sector produced roughly 100,697 PJ out of coal alone [43], equaling roughly 5,000 Mt of bituminous coal[8] [43]. Such a mining industry can affect the environment considerably. Nuclear energy however, uses fertile or fissile isotopes that have an extremely high intrinsic energy potential of roughly 200 MeV per fission. This translates in an energy density of around 80 TJ/kg for pure uranium-235, uranium-238 and thorium-232[9]. Thus, when using nuclear (theoretical full fission) only 1260 tonnes of pure nuclear elements are required, a value drastically smaller than that of coal. However, in the case of uranium nuclear power this theoretical energy density is never reached as the fissile ^{235}U makes up only 0.7% of natural uranium and therefore needs to be enriched to become a fissile fuel. In addition, the solid fuel in the currently most used reactors only 'burn' up 4% of its potential energy due to fission product pollution [45]. Due to these complications 200 tonnes of natural uranium need to be mined to obtain only 1 tonne of fission energy [37, p. 15]. For thorium this works differently, as only one isotope of thorium is found in the earth its crust, namely ^{232}Th, making all of the naturally found thorium entirely fertile [46, p. 247]. Next to that, the most researched thorium reactors work with closed-cycle liquid fuel (a technology also possible for uranium reactors), making it possible to fission nearly all material [45, p. 308]. Therefore, the effective energy density of natural uranium is around 0.4 TJ/kg for most of the current in-use reactors or 10 TJ/kg for liquid fuel reactors, while that of thorium can be 80 TJ/kg if liquid fuel is used.

Yet, the dependence on non-renewable isotopes is not seen as a future risk as the reserves of uranium are still sufficient to provide energy for many generations. The amount of identified natural uranium is currently estimated at 6.15 Mton, while 35,328 tonnes are consumed annually. For thorium the reserves are even more favourable as 6.36 Mton of pure fertile thorium are currently identified, while current thorium consumption is nearly negligible [47; 48].

[8] Using an estimated heating value of 20 MJ/kg bituminous coal [44].

[9] Energy density=$\frac{\kappa_{fission}[\text{MeV/fission}]\cdot N_A[/\text{mol}]\cdot 1.60217\cdot^{-18}[\text{TJ/kg}]}{A[\text{g/mol}]\cdot 0.001[\text{kg/g}]}$

To conclude, due to the high energy density of nuclear fuel and the still widely available deposits of both natural uranium and thorium the non-renewable character of nuclear reactors is not seen as a feasible challenges for the coming generations. Due to both improvements in fuel efficiency and fission isotope alternatives.

Investment risk

Next to the non-renewable character and waste production of nuclear reactors, the cost is also seen as a leading disadvantage. Due to the complexity and high safety standards of nuclear power plants the construction time is extremely lengthy, with construction periods of over 10 years not being an exception. The risk of investing in these projects drastically increases as energy prices can change and societal opinions regarding nuclear energy can change in these significant periods. Therefore, it is important for reactor designs to reduce construction time and capital cost of their sources while providing affordable energy if they want to enhance their affordability with regard to other sustainable energy sources. The effects on cost are further discussed in section 2.7.

2.6.3 Nuclear Energy in the Netherlands

For the Netherlands this report and possible addition to the EU taxonomy list re-sparked the nuclear energy debate. The political cabinet *Rutte IV* (2021-2025) included nuclear energy in their coalition agreement, wanting to further investigate the feasibility of nuclear energy, support the construction of two new nuclear power plants and invest in nuclear research. The coalition budgeted 5 billion euros for these investments, resulting in an enhanced investment environment for new nuclear power plants [49].

Nevertheless, the Netherlands still have very strict regulations related to nuclear technologies that currently allow the deployment of nuclear reactors at specific locations. These locations are characterised by their ample availability of cooling water, distance to densely populated areas and only allow a minimal impact on vulnerable and important natural environments following a severe accident[10]. Note that these locations were agreed upon by the Dutch government in 1986 (*'Waarborgingsbeleid kernenergie'*) and therefore only considers generation I and II reactor requirements, the allocated locations are illustrated in figure 2.17. Current reactor technologies have vastly different specifications and requirements and therefore, most likely, allow for more viable locations.

Of the current three allocated nuclear reactor locations in the Netherlands, the *Eems* located in the northern province of Groningen, is seen as least viable due to the on-going energy crisis complications in the region. The province has provided a large amount of natural gas from its gas fields the last several decades. These activities have resulted in the emergence of many earthquakes in this region, resulting in significant damage of property. As little progress is made regarding these problems, the population of Groningen became very hesitant to house other energy sources that are currently seen as controversial [34, p. 145].

[10] Such as the potential to contaminate drinking water reservoirs with radioactive material.

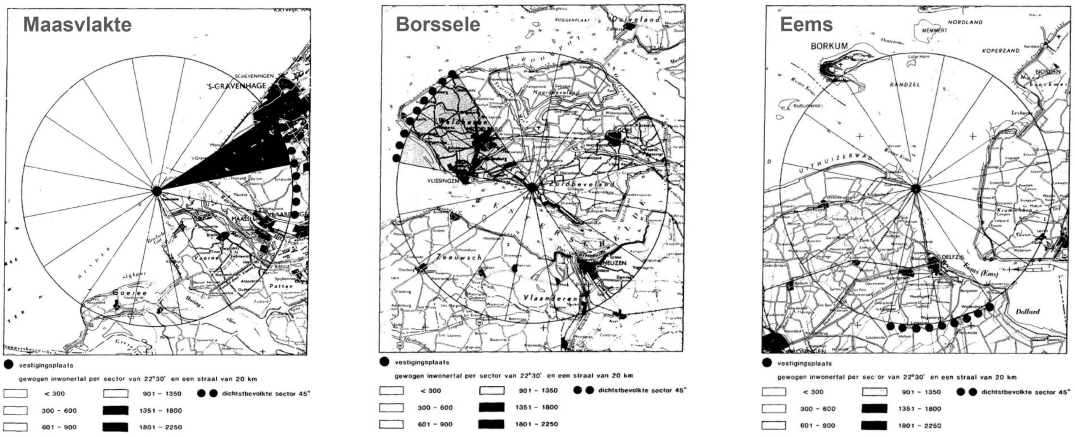

Fig. 2.17 The three approved locations for nuclear power plants in the Netherlands following the 'Waarborgingsbeleid kernenergie' agreement. Reprinted and modified from Ministry of Economic Affairs [50].

Borssele on the contrary, already houses the only nuclear power plant of the Netherlands. This resulted in a very positive attitude towards nuclear energy in the region, as the plant provided a stable amount of employment and economical potential to the province of Zeeland. The current power plant operator at Borssele, *EPZ*, already proposed a plan to construct two new generation III+ reactors that combined would generate 3 GW of electricity. With an estimated 90% operation time this would result in a stable annual output of 85 PJ, roughly the equivalent of 23 GW installed offshore wind turbines. It is estimated operation could start between 2033 and 2036 if licensing starts early next year [51].

Nevertheless, construction of more nuclear reactors could potentially benefit the energy mix of the Netherlands. For that reason it is interesting to research the implications of a nuclear reactor at the *Maasvlakte*, the final of three allocated locations. This location is of interest as it is located next to the logistics core of western Europe, the port of Rotterdam, and two major cities part of the metropolitan area named *Randstad*.

2.7 Modern nuclear reactor technology

2.7.1 The nuclear fuel cycle

Nuclear technology has been around for roughly 70 years, and many improvements have been made during this period. These improvements have focused on making modern reactors more safe, efficient and affordable, but also more diverse. This diversity in reactor design research has resulted in the development of alternative fuel cycles that enhance the many improvements of these modern reactors. With the most important alternative being the closed fuel cycle.

Closed fuel cycle Most of the nuclear reactors currently operating work with a so-called open fuel cycle. Meaning fissile isotopes enter the reactor for a certain time, transmuting a certain share of its content until the fission process is not feasible anymore. The final output is a spent fuel that is partly re-processed into new fuel and partly disposed as nuclear waste. This fuel cycle results in many logistic challenges and a non-optimal use of the fissile isotopes as a certain share is lost during the cycle without producing energy. A closed fuel cycle, oppositely, re-process the fuel isotopes on-site. Hence, recycling the isotopes repeatedly until nearly all fissile material has reacted and most of its inherent energy is released [46]. This process projects less logistical problems, but comes with its own technological challenges discussed in the following sections.

Thorium fuel Currently the most used nuclear fuel is enriched natural uranium (3-20% ^{235}U, rest ^{238}U), a fissile isotope containing fuel that can sustain a fission chain reaction as it produces 1-to-5 neutrons while requiring only one neutron [52]. The remaining fuel is made out of the fertile uranium-238 that can absorb one neutron and eventually turn into fissile plutonium-239 [$^{238}\mathrm{U}(n,\gamma+2\beta^-)^{239}\mathrm{Pu}$] which can further absorb neutrons and become unstable, resulting in the accumulation of minor actinides in the fuel waste with only a couple of neutron-absorption steps [52]. These minor actinides are responsible for most of the long-term radiotoxicity in the used fuel [53, p. 18] and some can, if filtered out of a closed fuel cycle, be used in the production of nuclear weapons [46, p. 68].

Fig. 2.18 Nuclear reaction chain possibilities for thorium-232 from fertile (^{232}Th) to fissile (^{233}U and ^{235}U) isotopes. The orange outline represents the fissile isotopes, the orange contour outlines a breeding ratio reducing reaction. Reprinted and modified from Nayak & Sehgal [53, p. 13].

By using fertile thorium as fuel a neutron first needs to be absorbed to transmute into fissile uranium-233 [$^{232}\mathrm{Th}(n,\gamma+2\beta^-)^{233}\mathrm{U}$]. The nuclear reaction chain is illustrated in figure 2.18. Due to the relatively low capture cross section and high, but comparable, fission cross section[11] of uranium-233 over a wide range in the neutron energy spectrum (compared to ^{235}U and ^{239}Pu), the probability of fissile capture increases significantly [53, p. 14]. This results in a relatively higher percentage of fissile reactions, while transmutation, for ^{233}U into protactinium-234, occurs less. Thus, as a result, improving the ratio of neutrons released to neutrons absorbed (η). This allows the fuel to maintain

[11] low capture- and high fission cross section equals a very low capture-to-fission cross section α.

breeding ($\eta > 2$) for even the thermal and resonance neutron energy range [37, p. 11; 53, pp. 14-15], as seen in figure 2.19.

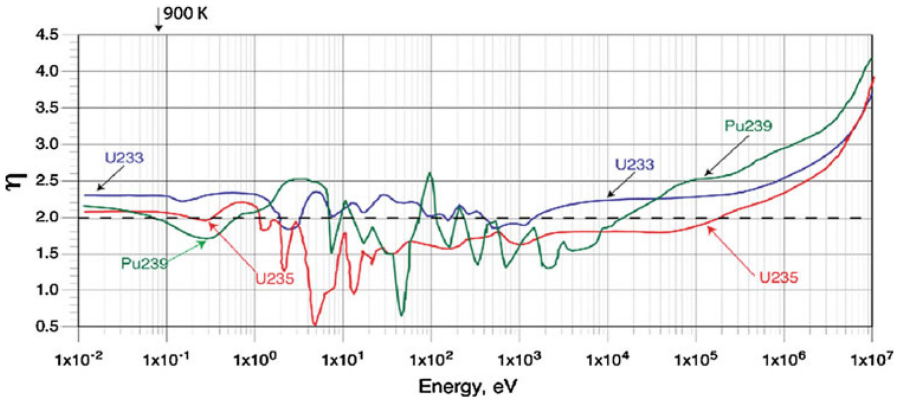

Fig. 2.19 Number of neutrons released per neutron absorbed ratio (η) for ^{233}U, ^{235}U and ^{239}Pu. Values above dashed line represent reactor core environments that continue breeding without external stimulants. Reprinted from Revol *et al.* [37, p. 12].

One of the advantages of thorium fuel is the reduced chance of producing plutonium and minor actinides as it requires many more neutron captures and thus transmutations, compared to ^{238}U, before these long-term radiotoxic isotopes are formed [53, p. 15; 37, p. 34 & 103]. In combination with the closed fuel cycle the actinoids in the fuel are able to further transmute into more stable elements, reducing waste drastically compared to the once-through solid fuel systems [46, p. 8]. With the thorium MSR 83% of the fission products will be stable in 10 years, 17% in roughly 300 years and only 0.01% will be the major actinide plutonium. For uranium only 3.7% of the enriched uranium will fission, leaving 96.3% of enriched uranium that needs to be disposed as nuclear waste. The remaining part that undergoes fission, leaves roughly 23% of plutonium, an extremely long-term radioactive waste with a half-life of over 24,000 years [45, p. 308; 34, p. 41]. Hence, making long-term storage of spent enriched uranium-235 fuel way more difficult.

While thorium still produces actinides such as plutonium the share of fissile isotopes is drastically lower, resulting in a spent fuel that is rendered inadequate for nuclear weapons [37, p. 34] as roughly 10 kg of nearly pure plutonium-239 is required per warhead [54]. Therefore, making thorium an excellent replacement from current uranium fuel designs.

2.7.2 Generation III+ reactors

The current nuclear power plant fleet mainly consists of generation II, and even some generation I, Pressurized Water Reactor (PWR) and Boiling Water Reactor (BWR) designs that depend on outdated technology. Ergo, having an increased severe accident risk, compared to these newer technologies. Severe accidents could potentially be of a similar scale to the Chernobyl and Fukushima nuclear power plant meltdowns [55, p. 8; 56, ch. 2].

Fortunately, in the 1980s and 1990s another generation of nuclear reactors was designed, namely the generation III designs, or also commonly referred to as *advanced reactors*. These reactors are all evolutions on the previous generation, but include additional safety systems, such as passive safety mechanisms. Reducing the dependence on electronic safety systems, such as backup pumps, during a defective system event. Additionally, these designs have an enhanced overall efficiency in fuel usage, waste production and thermal efficiency of the power plant. Another feature of these reactors are their standardised designs, reducing the required approval time for a reactor significantly as the design has already been certified for compliance with the European Utility Requirements (EUR) and, specifically for the Netherlands, Authority for Nuclear Safety and Radiation Protection (ANVS) [57, ch. 7].

Even while these reactor designs are already between 20-40 years old, they still are of great interest as their technologies have been updated over time. After the Fukushima nuclear power plant accident in 2011 the safety systems of these gen-III reactors has been further refined to make them even safer. These reactors are commonly referred to as gen-III+ reactors. Additionally, the designs have also been adjusted to the new energy market, meaning they do not only deliver a base load (constant) output, but also have the possibility to adjust their energy production significantly in a minute-to-hour time frame. Thus, when renewables produce enough electricity the load of the reactor can be reduced, consequently reducing electric grid problems. Or the reactor is able to produce heat for industrial applications or be adjusted for hydrogen production. This flexibility requirement is listed in the EUR, meaning all approved gen-III+ reactors have this ability. The final feature of this generation is the extended operational lifetime of at least 60 years and being extendable up to 120 years [57, ch. 7]. Generation III+ reactor technologies are interesting and promising alternatives to the current nuclear reactor fleet[12] by reason they diminish some of the commonly discussed challenges of nuclear power.

The most important feature of these reactors are the utilization of passive safety elements that make the reactor safety system inherently safer. Such systems use inherent material properties and natural phenomena to its fullest extend, enabling backup elements that automatically activate when temperature increases or during a vessel depressurisation event [57, ch. 7; 56, appx. B; 34, p. 42]. To summarise all the advanced reactor technology (gen-III+) features the required behaviour is listed below. The list is a combination of the specific European Utility Requirements and the general International Atomic Energy Agency (IAEA) requirements described by Kerlin & Upadhyaya [56], Kadak [58], and Zohuri & McDaniel [59].

- Standardised and simplified design, allowing for easier operation, reduced capital cost, reduced construction time and easier permit procedures
- Operation lifetime of around 60 years
- Increased fuel efficiency and less waste compared to gen-II
- Reduced severe accident risks by additional active safety systems
- Use of passive safety systems, allowing for a 3 day *grace period* [13]

[12] The term fleet is used to describe the collection of nuclear power plants in a region.

[13] A grace period is a term describing the period in which a reactor core safety and stability is ensured.

- *Core catcher* to mitigate radioactive material release after a severe accident
- Flexible energy output adjustment (minute-to-hour time frame)

Many of the generation III reactor designs have been updated throughout the past decade to comply with the post-Fukushima European Utility Requirements. These reactor designs are referred to as generation III+. As earlier mentioned, the designs do not only have to follow the EUR, but also possible national requirements. In the Netherlands the Authority for Nuclear Safety and Radiation Protection, in compliance with the Dutch government, set additional requirements to reactor safety standards, making reactor licensing more complex and time consuming. For this reason many Dutch and also other European market players advocate for further European, or even global, standardisation of these requirements. All to simplify the permit procedure and press the high costs of nuclear investments. In addition, the Netherlands does not evaluate reactor design safety beforehand, meaning design licensing will happen next to location evaluation, increasing permit process time significantly. Nevertheless, the ANVS does accept *proof of safety* documentation from other reactor design and construction applications from other countries, in order to accelerate the licensing process. They do, however, have a preference for European countries and to a lesser extend the United States. Current estimations around the licensing period are between 3 to 5 years in the Netherlands [34, ch. 3].

Next to these safety requirements listed by the EUR organisation and the ANVS, the Dutch Ministry of Economic Affairs and Climate Policy (EZK) also excludes some reactor designs for near-future construction. Designs from Russia and China are currently seen as disfavoured alternatives due to a variety of mainly dependence related concerns, both political and economical. Additionally, the Dutch government strongly focuses on proven reactor designs that are already being built. This allows for better capital investment estimates and reduces the risk that is mainly connected to First-Of-A-Kind (FOAK) reactors [34, ch. 1].

Leading gen-III+ reactor designs for the European market that currently comply with the European Utility Requirements are listed in table 2.2. Note that not all of these reactor designs are seen as viable options for the Netherlands. Hence, only the reactor designs selected by the EZK will be discussed in this section. Other large generation III+ designs of interest will not be discussed in this paper, because these designs still come with to many risks for near-future Dutch nuclear fleet development.

Table 2.2 Generation III+ reactor designs for the European market in a commercialised or operational stage. EZK stands for Ministry of Economic Affairs and Climate Policy. This table excludes Chinese reactors, generation III reactors and advanced ASMRs. Acronyms 'Y' and 'N' stand for yes and no respectively. Data in this table comes from KPMG [34], Kerlin & Upadhyaya [56], International Atomic Energy Agency (IAEA) [60] and Kadak [58].

Design name	Producer	Country	Reactor technology	Selected by EZK	Operational
European Pressurised Rreactor 2 (EPR2)	EDF group	France	PWR	**Y**	N
Advanced Passive Pressurised Water Reactor (AP1000)	Westinghouse	USA	PWR	**Y**	N
Advanced Power Reactor (APR1400-EUR)	KEPCO	South Korea	PWR	**Y**	Y
Water-Water Energy Reactor (VVER-TOI)	Rosatom	Russia	PWR	N	Y
Advanced Fuel CANDU Reactor (AFCR)	SNC Lavalin	Canada	PHWR	N	N

When comparing all the different reactor designs given in table 2.2, it is clear only three out of five possible gen-III+ designs are of direct interest following EZK advice, namely the European Pressurised Rreactor 2, the Westinghouse AP1000 design and the APR1400-EUR system. All of these designs already have several reactors under construction or even operational.

European Pressurised Rreactor 2 (EPR2)

The EPR2 is a large reactor design, designed by the French EDF group, that is able to produce 1,660 MW of electricity (gross) with a thermal efficiency around 37%. It is a direct evolution of the generation II Pressurized Water Reactor that improves the inherent safety of the reactor in a robust manner. While the design is based on a more standardised generation II reactor it still has significant construction cost barriers due to all additional safety implementations. These new systems allow for an extremely safe design with a Core Damage Frequency (CDF)[14] of around $5 \cdot 10^{-7}$ [58, pp. 31-32; 60].

Pre-Fukushima, 4 reactors were under construction, two in China, one in Finland and one in France. During construction both European reactors have been updated to the new post-Fukushima standards and, ergo, are referred to as *new model* EPRs, the Chinese reactors did not. The new model is named EPR2. In 2018 two EPR2 FOAK reactors of this upgraded model started construction. These reactors are named *Hinkley Point C1/2* and are located in the United Kingdom. The construction cost of these twin reactors is estimated around 26 billion EUR, or 8,122 EUR/kW. Construction time of these FOAK reactors is currently estimated at 8 years [34, ch. 2].

While construction has not yet been finished at Hinkley Point, another twin EPR2 reactor, *Sizewell C*, is already proposed in the UK. These reactors will most likely start construction before 2024. Hinkley point C is projected to be fully operational in June 2026.

Advanced passive reactor (AP1000)

The AP1000, an evolution on the second generation PWRs, is produced by the American company Westinghouse. The reactor has a gross electric output of roughly 1120 MW with a thermal efficiency of 33%. While the EPR2 is mainly a traditional gen-II PWR with many additional safety features, the AP1000 is full overhaul of the safety design. As the name already implies it fully depends on passive and natural safety systems, hence does not require any electrical input to function. This passive system results in a CDF of around $2.4 \cdot 10^{-7}$, or around half the risk of the previously discussed EPR2 design. Additionally, these passive systems greatly reduce the amount of required and complex safety components (e.g. 35% fewer pumps). These design specific modifications result in a simplified design that allows for faster construction and lower cost. The final feature of the reactor is its modular design, allowing for factory component manufacturing, hence further reducing capital costs [58, pp. 24-26; 56, appx. B.5.1; 60].

[14] The CDF value represents the chance of severe core damage per year-reactor. Hence a CDF value of 10^{-5} means one event of severe core damage is expected once every 100,000 years per reactor.

Of the post-Fukushima design two reactors, *Vogtle 3/4*, are currently under construction in the United States. Construction started in 2013 and is expected to finish in late 2021, resulting in a FOAK construction time of 8 years [34, p. 45]. Westinghouse predicts that the construction period can be lowered to 3 years when prefabrication processes are fully developed [58, pp. 24-26]. Construction cost of these reactors is estimated at 18 billion EUR, or 7,118 EUR/kW [34, ch. 2].

Advanced power reactor APR1400-EUR

The last selected reactor design is the Advanced Power Reactor (APR1400-EUR), engineered by the Korean *KEPCO* (Korea Electric Power Corporation). Similar to the EPR2, the design of the APR1400-EUR is a less innovative evolution of the gen-II PWRs. The electrical output of the reactor is estimated around 1,400 MW with a thermal efficiency of 35%. Just as the EPR2 the reactor relies on several independent active emergency safeguards with passive supporting systems, allowing for a very safe design with a CDF of 10^{-6}. All these different systems do increase cost and construction time significantly [58, pp. 29-30; 60].

Three of these power plants are currently under construction in South Korea and the United Arab Emirates, resulting in plenty of building expertise. All of these power plants are designed with quadruple reactors. Construction time for these FOAK reactors is currently estimated at 8 years [34, ch. 2] with a cost of around 22 billion EUR or 4,089 EUR/kW [61].

2.7.3 Generation III+ reactor comparison

Comparing all of the discussed third generation reactor technologies is rather difficult as they all have specific pros and cons. The most obvious being construction cost and time, while *proof of concept* comparisons are more complex. A general comparison overview is given in table 2.3.

Table 2.3 Generation III+ reactor technology comparison of discussed designs. Acronyms 'Y' and 'N' stand for yes and no respectively.**Includes both operational and under construction reactors. **The construction time and cost are given as a range following post-FOAK reactor assumptions given by KPMG [34].*

Design name	Amount of reactors*	Construction time** [years]	Construction cost** [EUR/kW]	Core damage frequency	Passive design	Built in Europe
EPR2	4	6-8	4,873-5,848	$5 \cdot 10^{-7}$	N	Y
AP1000	2	3-8	4,271-5,125	$2.4 \cdot 10^{-7}$	Y	N
APR1400-EUR	12	6-8	2,453-2,944	10^{-6}.	N	N

Note that the construction cost and time are calculated from the FOAK reactor estimations and a reduction factor described by KPMG [34, p. 9 & 16]. The cost reduction is estimated to be around 28-40%. Higher reductions (closer to 40%) are expected when FOAK reactors are built within the EU or UK (*European atomic energy community*), or to a lesser extend member countries of the Nuclear Energy Agency (NEA). Projects out of the NEA scope have a smaller effect on the reduction as less knowledge is shared. Appendix figure B.7 shows a map of all Nuclear Energy Agency member states. Construction time is predicted to lower with roughly 2 years, as less construction interventions are

required compared to FOAK reactors. The manufacturer of the AP1000 expects this period to reduce even more to 3 years when prefabrication processes are fully set up.

When looking at the amount of reactors per power plant the economic factor plays an important role. EPR2 and AP1000 are both optimised as twin reactors, meaning their total electrical output is in the range of 2,000-3,000 MW, while the APR1400-EUR is designed as a quadruple reactor that produces around 5,600 MW. The latter, possibly faces many implementation challenges as it can be non-compatible to the electric grid infrastructure capacity, hence requiring very expensive additional grid infrastructure to support this high electricity output of the reactor. The Dutch grid will have poor compatibility as it has a maximum capacity of between 2,500-6,500 MWe [34, p. 139]. Therefore, with current infrastructure and demand the APR1400-EUR seems redundant as a quadruple reactor for the Netherlands as similar complications connected to renewables arise.

Costwise the EPR2 and AP1000 are both roughly similar, yet AP1000 clearly stands out with its passive safety systems, and consequently its overall core safety. Nevertheless, with current construction and operational information the European EPR2 is seen as the most feasible option for third generation nuclear power in the Netherlands. Reasoning for this decision are the deep understanding of this design within the European Union and the constructional expertise created in both the UK and France, consequently smoothening the construction- and licensing processes. Nonetheless, the AP1000 could become a dominant European player in the near-future when it can proof its extensive modularity and ambitious 3-year construction time goals that could transform the investment climate for nuclear power drastically.

2.7.4 Advanced small modular reactors (ASMR)

As discussed previously the construction and permit period of nuclear power plants can be a long haul. Such extended time periods can greatly affect the cost of such power plants, as technology keeps advancing and public opinions change, consequently changing permit requirements, hence forcing new implementations, and delaying the construction. A study conducted by CATF [55] estimates that every additional construction year results in an added cost of around 175 to 450 EUR/kW in the United States, as seen in figure 2.20. The additional costs are expected to be higher in EU member states as the EUR maintains a stricter requirement framework. For this reason the construction of smaller modular reactors could be a beneficial alternative, solving those construction cost related problems.

Although, large nuclear power plants have the benefit of *economy of scale*, meaning that efficiency increases with reactor size and consequently output, they are not cost friendly in a short-term. Large scale power plants often have problems with prefabrication as less reactors are built, making their designs, in many cases, less standardised. Smaller reactors, also referred to as an Advanced Small Modular Reactor (ASMR), do not necessarily have this problem since their reduced energy output allows them be used in a more flexible manner. Possibly resulting in a increased demand for these

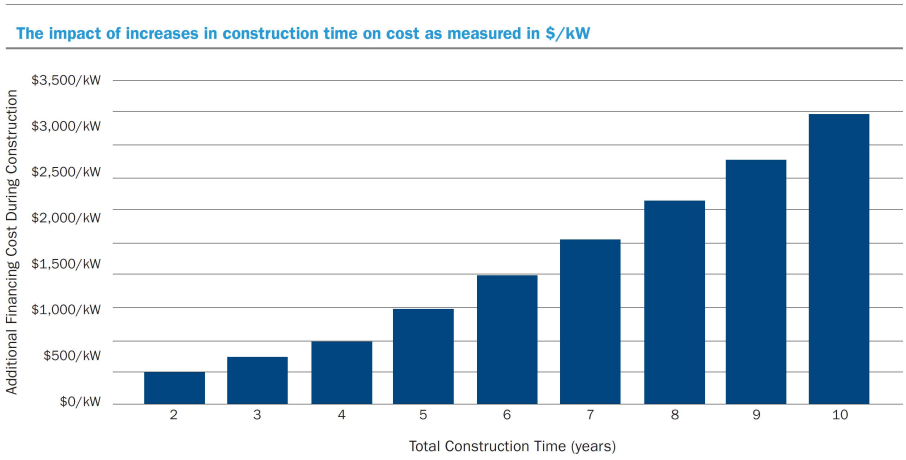

Fig. 2.20 Impact of increased construction time on the cost per kW in the US. Reprinted from CATF [55, p. 17].

reactors, ergo, allowing for extensive prefabrication processes and pushing prices down [59, ch. 3.8; 56, B.7].

Because these ASMRs are designed to have a lower energy output, with a maximum of 300 MWe[15], their core volume can be reduced drastically compared to their larger counterparts. These size reductions are very beneficial as they allow the design to be simplified, reducing the amount of necessary support systems. Additionally, as the core size shrinks more components can be placed in the pressure vessel, allowing for integral reactor designs that clearly perform better in a safety point of view, considering everything is contained in just one vessel. But even non-integral ASMR designs have a more efficient passive safety system as cooling systems perform better when core size decreases. This all allows for more standardisation, simplification and even full off-site prefabrication in the case of integral designs, hence lowering the required construction time to roughly 3 to 5 years in the Netherlands. Consequently, these changes in reactor design greatly benefit the overall cost of the small power plant [57, pp. 71-73; 56, B.7; 34, pp. 54-58; 55, ch. 4].

Additionally, due to the benefits of a reduced size and output the reactors can be placed in a more flexible manner as the spatial requirements such as water consumption are drastically reduced. This flexibility can be strategically be used to replace coal power plants (that have similar energy outputs), providing carbon-free energy without adding new infrastructure. Additionally, small heat grids could be developed around these reactors, optimising energy use even in less urban areas. To allow for such a strategy a new nuclear allocation assessment framework, specifically for ASMRs, needs to be developed.

Currently, several companies are developing Advanced Small Modular Reactor that are based on proven gen-III+ reactor technology, but also more innovative generation IV technologies. Roughly 10 of these concepts are already in an advanced development stage (licensing, under construction or

[15]MWe stands for electrical power.

operational), meaning commercialisation and governmental certification is only a couple of years away. Six of these reactors[16] are classified as generation III+ reactors and are all water cooled design. The other four designs are classified as IVth generation[17]. Nevertheless, the operational gen-IV ASMRs are both test reactors ($<$ 25 MWe) built in the late 90s up to early 2000s, for that reason they are excluded as they were not designed to be commercialised, yet. Of these ASMRs many are designed in China and Russia, just as before these reactors are out of the scope of this thesis due to decisions made by the Ministry of Economic Affairs and Climate Policy. Some other reactors that are operational or under construction will be excluded because they are research test reactors. Other designs that are still in their design phase are excluded in this thesis. This does not mean these designs are not suitable or feasible in the Netherlands, but currently too little is known about these reactors. All reactors currently in development are discussed by the IAEA [62] in *Advances in Small Modular Reactor Technology Developments*. To following reactor designs are currently seen as the most feasible and commercially ready designs for the near-future.

NuScale [62, pp. 89-92] The NuScale gen-III+ reactor is designed to be extremely modular, a single NuScale power plant is able to house up to 12 reactors, allowing for lots of flexibility. It is designed by the US based NuScale Power. The most important aspect of their design is the use of a fully factory fabricated integral PWR vessel that contains the entire Nuclear Steam Supply System (NSSS), hence enhancing safety and economics drastically.

It uses both passive and active safety systems to ensure sufficient safety throughout its lifetime. The reactor refuelling is conducted once every 2 years with low enriched uranium (<5% ^{235}U) pellets.

BWRX-300 [62, pp. 93-96] The Japanese and American BWRX-300 is the only advanced ASMR design that evolved from the Boiling Water Reactor. This generation III+ reactor designed by GE Hitachi incorporates a fully passive safety and natural circulation system. Consequently making this reactor extremely safe with a CDF of $< 10^{-7}$, but also economically interesting, as less complex and costly support systems are required. Cost of this reactor is estimated to be similar to that of natural gas power plants, these reactor cost around 950 EUR/kW in the United States [63].

The plant uses very low enriched uranium (3.40%) pellets that require to be refuelled every 12 to 24 months.

SMART [62, pp. 53-56] SMART is a generation III+ evolution reactor of the PWR with an integral pressure vessel containing the NSSS. It is designed by KAERI and K.A.CARE from the Republic of Korea and the Kingdom of Saudi Arabia respectively. The power plant only includes one reactor, meaning a fraction of the year the plant will be down for maintenance or refuelling work, consequently diminishing the energy output. The power plant is estimated to cost around 5,300-6,200 EUR/kW for a non-FOAK reactor.

[16] 1 operational (Russia), 1 under construction (Argentine) and 4 in licensing phase.
[17] 2 operational (Japan and China), 1 under construction (China) and the last is currently licensed.

The reactor uses both passive and active safety systems to simplify the design and improve economics. Additionally, the reactor is specifically designed to use seawater as coolant. This allows for easy implementation without many modifications if used in a coastal area. The core requires to be refuelled every 30 months with low enriched uranium pellets.

UK SMR [62, pp. 85-88] The generation III+ UK SMR designed by Rolls-Royce has a different reactor approach to the other ASMRs as it works with a 3-loop steam generator system supported by a small PWR reactor. This setup allows for flexibility, modularity and efficiency. Costs are estimated to be around 4,790 EUR/kW when prefabrication is rolled out [64].

Just as most of the reactors, the UK SMR uses both active and passive safety systems to ensure an extremely low core damage frequency of $< 10^{-7}$. Similar to the other PWR ASMRs the reactor requires refuelling of low enriched uranium pellets every 18 to 24 months.

NUWARD [62, pp. 37-40] The generation III+ NUWARD reactor is a design by the French EDF group. It is an small modular evolution on the traditional PWR technique with additional safety systems and a full integral reactor vessel. A NUWARD power plant is designed to have two reactors that allow for some seasonal flexibility and a permanent base load during maintenance.

The integral reactor pressure vessel houses all the main components of the NSSS. This design allows for extensive in-factory production. The reactor vessel is fully submerged in an underground water wall that works as a passive heat sink that cools the vessel for over 3 days without active cooling, consequently passively improving safety significantly. The reactor uses low enriched uranium (ceramic UO_2) and requires refuelling of half of the core rods every 2 years.

IMSR [62, pp. 243-246] The IMSR is the only generation IV design, it is an evolution from the original molten salt reactor experiment of the Oak Ridge National Laboratory. The reactor vessel is designed to be fully manufactured in a factory, containing everything the reactor requires, hence being a fully sealed integrated vessel. By fabricating everything off-site it requires no operator intervention during operation, meaning safety risks are significantly reduced. The vessel is delivered to power plants every 7 years were it will replace the 7 year old vessel. For this reason no additional refuelling is required. Nevertheless, feasibility of this design is highly dependent on the manufacturing scale.

Just as all other systems the IMSR runs on low enriched uranium, but in this reactor it is dissolved into the molten salt. Other fuel types, such as the thorium/uranium cycle are possible but are planned to be implemented in a later stage.

Due to these design choices the reactor has a very high safety standard. As described in section 2.7.6 the molten salt technology is inherently safe, nevertheless the reactor will include additional active safety systems to ensure safety as less is known about these systems.

2.7.5 ASMR comparison

All these reactor designs have vastly different concepts as they are all designed for specific needs, making it quite complex to compare them. To give some sort of overview their main specifications are summarised in table 2.4.

Table 2.4 Overview of the different Advanced Small Modular Reactor designs that are in their post-design stage. Data labeled as '-' stands for unknown value. Data given in this table comes from *Advances in Small Modular Reactor Technology Developments* by IAEA [62]. **Site footprint is assumed to be 20 times larger than plant footprint. **Rough early price estimation of EDF.*

	NuScale	BWRX-300	SMART	UK SMR	NUWARD	IMSR
Country of origin	US	US & Japan	Korea & Saudi Arabia	UK	France	Canada
Design company	NuScale Power	GE Hitachi	KAERI & K.A.CARE	Rolls-Royce	EDF	Terrestrial Energy
Reactor type	Integral PWR	BWR	Integral PWR	3-loop PWR	Integral PWR	MSR
Circulation type	Natural	Natural	Forced (active)	Forced (active)	Forced (active)	Forced (active)
Fuel cycle	Once-through cycle	Once-through cycle	Once-through cycle	Once-through cycle	Once-through cycle	Closed fuel cycle
Safety system type	Active and passive	Fully passive	Active and passive	Active and passive	Active and passive	Active and passive
Coolant	Light-water	Light-water	Light-water	Light-water	Light-water	Fluoride salt
Operating temperature [°C]	321	287	322	327	307	700
Operating Pressure [MPa]	13.8	7.2	15	15.5	15	<0.4
Electrical output [MWe]	12x 60	280	107	443	2x 170	195
Thermal efficiency [%]	30.0	32.2	29.3	34.7	31.5	44.3
Fuel cycle length [months]	24	12-24	30	18-24	24	84
Site footprint [m^2]	140,000	168,000*	90,000	40,000	>70,000*	45,000
Design life [years]	60	60	60	60	60	56 (8 replacements)
Core Damage Frequency	$3.5 \cdot 10^{-10}$ [65]	$< 10^{-7}$	$< 5 \cdot 10^{-7}$ [66]	$< 10^{-7}$	-	-
Construction cost [EUR/kW]	3,190 [65]	950	5,300-6,200	4,790	5,882**	< 4,540 [67]

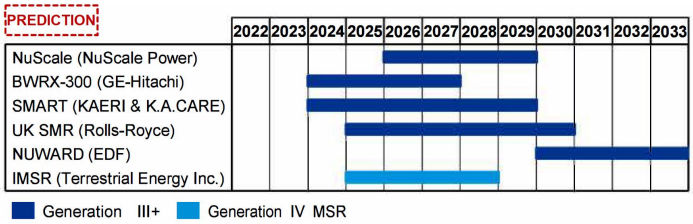

Fig. 2.21 Predicted construction timeline of the most interesting Advanced Small Modular Reactor III+ and IV designs. Reprinted, modified and translated from KPMG [34, p. 59].

In general the start to operation period for new nuclear power plants is significantly shorter for ASMRs than regular sized reactors, due to construction time. The licensing period, however, is equal for both types of generation III+ reactors, namely 3 to 5 years. Yet, the licensing framework of the ASMR still requires many modifications as they do not fit into the large reactor framework. A 4-10 year period is predicted for these modifications [34, p. 96].

However, following the same logic as described before, the EZK does not favour a FOAK reactor and therefore prefers to wait until a design is proven and operational before deciding on a technology

and eventually government investment. For that reason the KPMG [34] estimated that generation III+ ASMR licensing applications can be reviewed between 2027 and 2033 in the Netherlands.

For generation IV ASMRs the permit process is expected to take roughly 15 years in the Netherlands as the licensing framework needs to be fully redone because of the different technology. But even after the framework is finalised the licensing process is still expected to take roughly 10 years when operational gen-IV ASMRs are limited. Meaning the application processes could start somewhere between 2035 and 2040 at the earliest [34, pp. 93-96]. Figure 2.22 by KPMG [34] illustrates the predicted timeline for when the licensing framework is completed for the given technologies, and thus when commercial licensing application can be submitted.

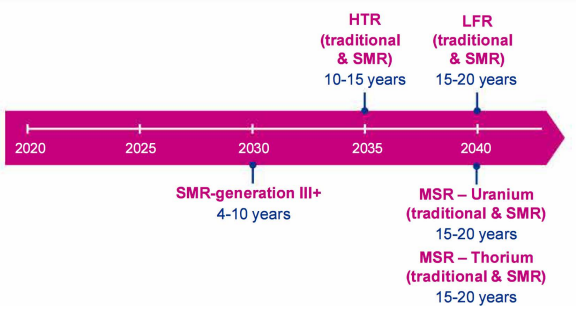

Fig. 2.22 Predicted finish date and process time for licensing framework preparations for a variety of generation III+ and IV advanced small modular reactor techniques. Reprinted and translated from KPMG [34, p. 96].

Finally, figure 2.21 illustrates the predicted timeline for the FOAK reactors of these ASMR designs. The construction time of these FOAK reactors is estimated between 4 and 6 years. All of these reactors are expected to be operational before the Netherlands is able to review their commercialisation permits. Note that the generation IV reactor is based on new technology and therefore requires additional reviews before it can be licensed.

To conclude, lower investment risk, construction time and increased flexibility, scalability and safety make the Advanced Small Modular Reactor an interesting alternative to larger nuclear power plants. Their flexibility allows for easy replacement of polluting fossil fuel and biomass power plants, without straining the current electric infrastructure. Although, construction of these reactors is not expected to start before 2030 in the Netherlands.

2.7.6 Generation IV reactors

As the quest for clean energy is rapidly gaining importance so has the interest in the by the GIF selected IVth-generation nuclear reactor concepts. Currently many different designs are proposed, all part of the gen-IV nuclear reactors[18]. The selected concepts are summarised in table 2.5.

[18]Generation IV reactors are bound to a set of goals such as minimised waste, economic feasibility, excellent safety and reliability and proliferation resistance [68, p. 38].

Table 2.5 Generation IV nuclear systems. Reprinted and modified from Pioro [68, pp. 37-54]. Additional fuel and core power density data can be found at appendix C.1 table C.1.

System	Neutron spectrum	Coolant	Outlet temperature [°C]	Fuel cycle	Size [MW_{el}]	Gross efficiency [%]
Very High Temperature Reactor (VHTR)	Thermal	Helium	900-1000	Open	250-300	≥55
Gas-cooled Fast Reactor (GFR)	Fast	Helium	850	Closed	1200	≥50
Sodium-cooled Fast Reactor (SFR)	Fast	Sodium	500-550	Closed	50-1500	40
Lead-cooled Fast Reactor (LFR)	Fast	Lead	480-570	Closed	20-1200	41-43
Molten Salt Reactor (MSR)	Thermal-fast	Fluoride salts	700-800	Closed	1000	50
Supercritical Water-Cooled Reactors (SCWR)	Thermal-fast	Water	510-625	Open & Closed	300-1500	45-50

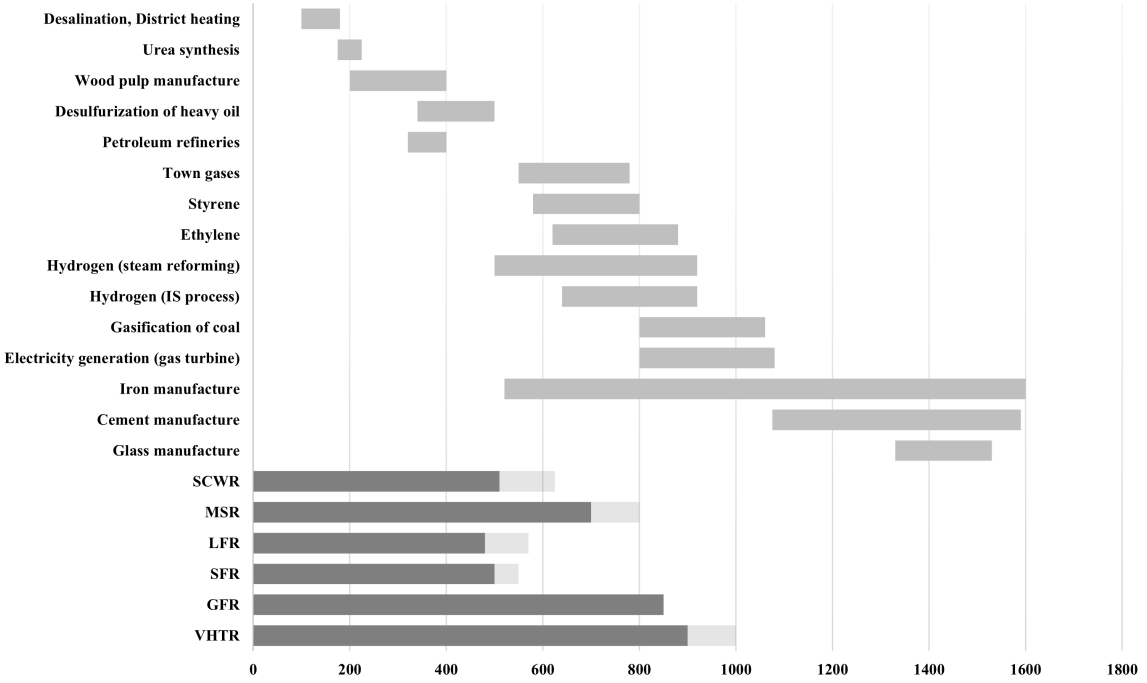

Fig. 2.23 High temperature industrial thermochemical applications. Reprinted and modified from Generation IV International Forum (GIF) [69, p. 90].

Very High Temperature Reactor (VHTR) [68, p. 42]

The VHTR is a thermal neutron spectrum reactor with a core outlet temperature of around 900°C which allows the reactor to produce electricity, hydrogen and support many more industrial processes (requires indirect heat cycle), see figure 2.23. As a generation IV reactor the system is inherently safe and relatively low cost. The system supports modular construction design, which can significantly lower investment risk and overall cost.

The reactor operates under an open, once-through, solid fuel cycle of low-enriched uranium-235, but can also burn other fuels such as thorium or plutonium, making it a more versatile and thus feasible

concept. Due to the open fuel cycle the burning efficiency will be relatively low compared to the closed fuel cycle, thus requiring more fuel, while generating a higher amount of waste. Making the VHTR a less appealing option for the green energy transition.

Gas-cooled Fast Reactor (GFR) [68, pp. 43-44]

The GFR is a fast spectrum reactor operating at very high temperatures of roughly 850°C. Due to the high temperature the indirect heat cycle allows for many industrial thermochemical applications, as seen in figure 2.23. The system works with a close solid fuel cycle that makes it possible, in combination with the fast neutrons, to minimise waste and optimise the fuel burning efficiency. For solid fuel these efficiency rates are relatively high. The closed *solid* fuel cycle does require a separate reprocessing facility. The technology does however, come with severe safety issues regarding the low thermal inertia of the reactor core, which can induce a sudden and swift heat-up when cooling methods fail [70, p. 19], leading to a core meltdown.

Sodium-cooled Fast Reactor (SFR) [68, pp. 44-46]

The SFR, similar to the GFR, is a closed-cycle solid fuel fast neutron reactor. Allowing for the minimisation of waste products and a relatively high fuel efficiency. The liquid sodium, which is used as the coolant, allows for a low coolant volume due to its favorable power density and low pressure operation. Resulting in reduced cost and improved plant safety. The major downside however, is the extreme chemical reactivity of the sodium with oxygen and water. If these chemicals come in contact a *sodium fire* develops, creating acute safety risks such as a meltdown due to possible coolant problems [70, p. 34]. However, when the reactor vessel, and thus the sodium, is correctly sealed the oxygen-free environment will prevent corrosion. With the reactor core operating between 500-550°C thermal industrial processes are less efficient or not even possible, see figure 2.23. The thermal efficiency[19] at these operating temperatures is relatively low, at roughly 40%, compared to other gen-IV, and high temperature, reactors.

Lead-cooled Fast Reactor (LFR) [68, pp. 46-47]

Just as the previous two reactors the LFR is a closed-cycle solid fuel fast neutron reactor, thus being a relatively fuel efficient and a minor waste producer. The reactor operates at a low pressures and temperatures between 480-570°C, resulting in a relatively low gross efficiency and less thermochemical possibilities, see figure 2.23. Like the VHTR, the reactor can operate with alternative fuel cycles such as thorium and allows for the burning of spent LWR fuel (actinides). The main drawback of the system are the coolant properties, resulting in high rates of corrosion and erosion of structural core parts. Additionally, problems such as creep are increased due to the high coolant density complicate

[19] The gross/thermal efficiency describes the conversion efficiency of thermal to mechanical energy.

the technology. The low opacity of the lead also poses a problem as it makes fuel handling and in-core monitoring/inspection rather difficult [70, p. 23].

Molten Salt Reactor (MSR) [68, pp. 47-49]

The MSR, a closed-cycle *liquid* fuel thermal-to-fast neutron reactor, is able to efficiently burn fuel as the liquid fuel is reprocessed on-site, making it possible to theoretically use all fuel minimising radiotoxic nuclear waste (non-proliferation) without requiring a solid fuel reprocessing facility. The system allows the use of many different fuel cycles between the thermal and fast neutron spectrum, such as the traditional uranium-235 cycle, but also the thorium-uranium cycle, allowing for fuel optimisation per power plant location. The coolant, molten fluorides and liquid fuel, operate under low pressures (atmospheric) and high temperatures, while also being optical transparent. This allows for easy inspection and monitoring of the reactor core. Another benefit of the MSR is the inherent, and full passive, safety as the reactor has very favourable void reactivity and negative temperature coefficients [70, p. 29]. Currently, due to research limitations, the main challenge is the reactor materialisation. High temperatures between 700-800°C in combination with the molten salt reactivity and the neutron interactions result in early lifetime failure, making the reactor less feasible (reactor downtime).

The Molten Salt Fast Reactor is seen as the most promising design as it is able to burn actinides produced from the fuel but also from spent LWR fuel and waste, due to its fast neutron environment.

Supercritical Water-Cooled Reactors (SCWR)

The SCWR is a high-pressure, high-temperature (up to 1500°C) solid open or closed fuel cycle reactor. Due to these conditions the coolant becomes single-phased, meaning a boiling crisis[20] is not possible [70, pp. 40-41]. Overheating of the fuel cladding and large neutronic variations due to density varieties are still possible, consequently decreasing its inherent safety. The system is able to work on the thermal and fast neutron spectrum and mixtures of thorium-oxides and plutonium fuel are possible, enabling the consideration between economics, fuel availability and fuel efficiency. The technology is based on current Light Water Reactor (LWR), lowering the capital cost of the system drastically. However, when the core gets damaged and cooling systems do not work properly[21] severe accidents are still possible due to the reactor system.

2.7.7 Generation IV reactor comparison

Generation IV reactor safety [71, pp. 2-8, 163–184 & 190]

Due to many years of experience, nuclear reactor technology safety greatly increased with the use of safeguard systems and passive protection mechanisms. But as a result to natural disasters and

[20] A boiling crisis causes the reactor core surface material to weaken or even melt, reducing mechanical performance drastically.

[21] As the reactor is not inherently and passively safe.

human interference these systems are able to fail, resulting in possible disasters. For that reason an inherent passive safety mechanisms is desired for generation IV reactors. Unfortunately, of the gen-IV concepts only the Molten Salt Reactor safety system is inherently passive. All other concepts rely on the many added passive safeguard systems that greatly reduce calamity risk.

These reactors are all depended on solid fuel particles or pellets that, when cracked due to overheating, release radioactive gases that can greatly pollute the environment when released into the atmosphere. Next to that, the cladding includes zirconium, that, in combination with enormous heat (during loss-of-coolant) and steam, can form hydrogen gas. This gas, if in contact with air, can combust and cause an explosion that damages the reactor and its safety mechanisms. These hydrogen explosions can only occur when water is used as coolant or when steam can leak into the core. The Very High Temperature Reactor and Lead-cooled Fast Reactor are both prone to these accidents.

The Sodium-cooled Fast Reactor, which uses the chemical active sodium as a coolant, is susceptible to sodium fires when it comes in contact with air or water. Normally this risk is prevented by fully sealing the reactor, but human mistakes and/or natural disasters can lead to leakage and thus aggressive fires, damaging the reactor and its safety systems.

The use of graphite moderators, such as in the VHTR, that can produce graphite dust overtime. This dust is highly flammable and can explode, again resulting in possible damage to the reactor and its related safety systems.

All these accidents can lead to a loss of coolant material and reduced coolant flow or pressure, causing an uncontrollable overheating of the *solid* fuel. When the fuel reaches its melting temperature it will start forming a magma called corium. This fissile liquid is able to melt through the reactor vessel and enter the reactor containment while still releasing massive amounts of heat.

The Molten Salt Reactor does not face these problems as its safety system is inherently passive due to the use a very chemically stable fluoride coolant with liquid fuel. It does however require the addition of a fuel salt drainage system that, in the case of a reactor system shutdown, drains the fissile fuel to a sub-critical storage tank that overtime slows down the fission reactions. This prevents overheating of the reactor core and thus protecting the reactor from severe damage.

Generation IV reactor comparison

It is clear from inherent safety mechanisms that the Molten Salt Reactor is superior to the other gen-IV concepts because of the fuel and coolant properties. Additionally, the ability of on-site fuel reprocessing enables the fuel to almost entirely fission, hence reducing the amount of required fuel and also reduces waste generation [72]. While the solid closed-cycle reactors require the fuel to be handled and reprocessed somewhere else, adding to reactor design complexity. Regarding the neutron environment, the Fast Neutron Reactors in combination with fuel recycling (closed cycle) are on the long run more sustainable, as they are able to burn minor actinides formed during fission reactions, as

well as from spent LWR fuel, thus reducing long-term radioactive lifetime of the reactor fuel waste [72].

Table 2.6 Generation IV nuclear system comparison based on inherent safety, fuel efficiency and flexibility, proliferation (nuclear weapons) possibility and gross efficiency. The factors are rated less, neutral or better: -/○/+, relative to the gen-IV reactor goals set by Pioro [68, p. 38].
**more research required to quantify inherent safety of concept.*

System	Fuel efficiency	Fuel flexibility	Inherent passive safety	Non-proliferation	Gross efficiency
Very High Temperature Reactor (VHTR)	-	+	○	-	+
Gas-cooled Fast Reactor (GFR)	○	-	-	○	+
Sodium-cooled Fast Reactor (SFR)	○	○	○	○	-
Lead-cooled Fast Reactor (LFR)	○	-	-	○	-
Molten Salt Reactor (MSR)	+	+	+	+	○
Supercritical Water-Cooled Reactors (SCWR)	○	-	○*	○	○

Table 2.6 gives an overview and reactor comparison of the most important factors set by Pioro [68] nuclear reactor systems. Because of all these advantages of a MSR the EU selected the concept as one of their main research projects [73] to explore the technology and analyse its ability to play a role in the green energy transition. Unfortunately, the MSR still has a couple of issues that cut down on reactor lifetime, making the technology currently less feasible.

For the Molten Salt Fast Reactor these issues are amplified due to the combination of high temperatures, neutron interaction and the corrosive environment caused by the molten salt. All resulting in severe material damage around the reactor core, over time weakening the structural components of the reactor vessel, thus requiring more inspections, maintenance and eventually replacements. Nevertheless, due to the benefits described the European nuclear research program started working on a project named Evaluation and Viability Of Liquid fuel fast reactor (EVOL), a thorium fueled Molten Salt Fast Reactor (MSFR), lead by Prof. Elsa Merle-Lucotte and Delft University of Technology, as they believe these reactors can be the final answer to nuclear energy.

All the generation IV reactors are still in their conceptual research stage. Meaning these reactors require additional research before the European Union certifies the designs, making them unlikely candidates for near-future (<2040) power plants.

Molten Salt Fast Reactor (MSFR)

The European EVOL project resulted in a concept reactor by the Safety Assessment of the Molten Salt Fast Reactor (SAMOFAR) project, a Molten Salt Fast Reactor (MSFR). As seen in figure 2.24 and 2.26, the reactor containment consists of two main segments. Namely, the *critical* [22] reactor vessel including the core, the main intermediate fuel cycle and its gas processing system. Second, a *sub-critical* [23] chamber that houses the emergency draining system. The reactor, with outlet temperatures

[22] Reactor chamber that can sustain fission reactors, thus being critical.
[23] Reactor space that cannot sustain a fission reaction.

between 700-800°C, is in figure 2.24 connected to an indirect Brayton power cycle. Other generator cycles are also possible.

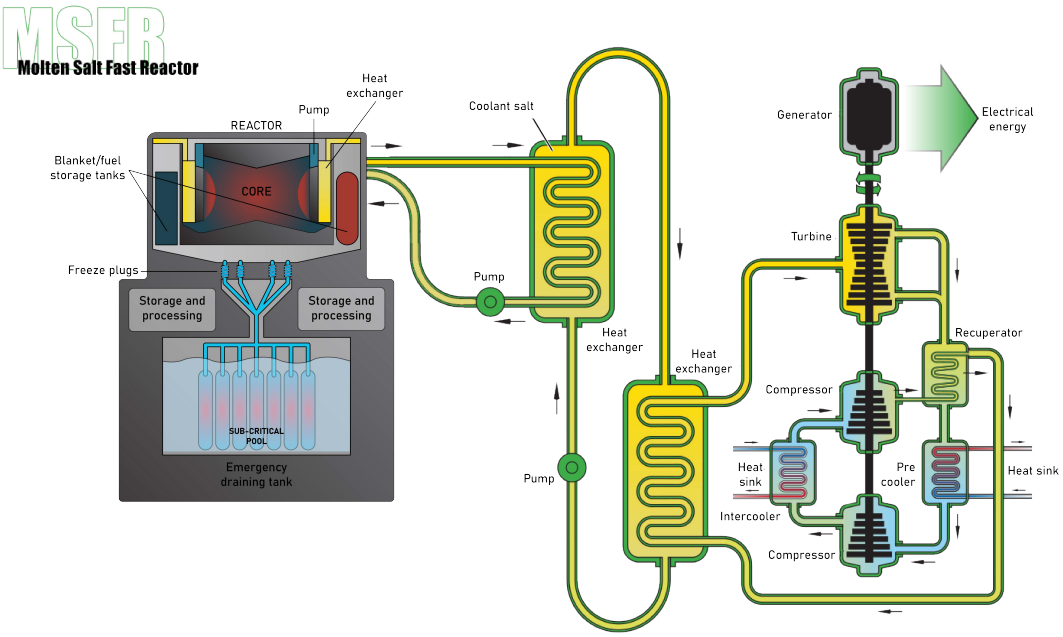

Fig. 2.24 Schematic diagram of the Molten Salt Fast Reactor. Generator cycle, right, reprinted and from Pioro [68, p. 48]. Reactor containment and emergency pool, left, based on SAMOFAR [74].

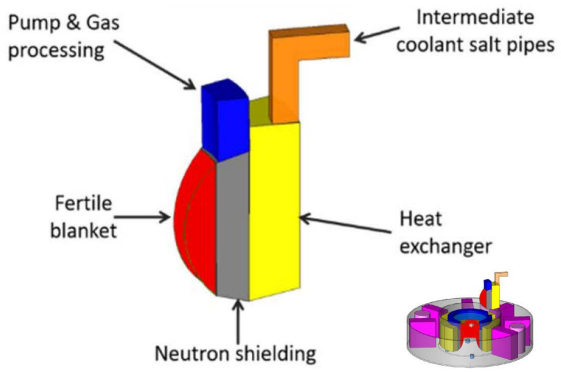

Fig. 2.25 Components of the modular reactor sector surrounding the fission chamber. Reprinted from Merle, E. [75, p. 23].

The core of the reactor is very different from all other reactor concepts due to the liquid fuel. The absence of control rods and neutron moderators allows for a more compact core design that supports constant fuel circulation from heat exchanger to the fission chamber and back. As seen in figure 2.26 the reactor core is surrounded by 16 sectors that house the main reactor components. The modularity of these components makes it easier and cheaper to maintain and, if necessary, replace elements when damaged, all to reduce the leakage risk [75, p. 77]. The sector is made out of 4 segments as seen in figure 2.25, namely the fertile blanket, an intermediate heat exchanger connected to coolant salt pipes, neutron shielding between the fertile blanket and the heat exchanger and a section for the fuel pump with the gas processing equipment. The heat exchanger is also connected to a temporary fuel storage, by a routine-draining siphon, for controlled fuel storage up to a few weeks, to allow reactor vessel maintenance. The same goes for the fertile blanket that has

its own storage tanks [75, p. 23 & 48]. The final components, that is connected to the routine-draining siphon system and the core, are the emergency-draining openings with a freeze plug that melt in case of core overheating. When melted the molten salt fuel liquid will flow into a collector under the reactor vessel and drain the liquid towards the emergency draining vessel, a sub-critical storage pool containing cooling rods and storage tanks, slowing and eventually stopping the fission reactions. When reactions cease the fuel will cool down and ultimately solidify. When problems related to the overheating are fixed the fuel can be melted again by external heating, thus recovering the fuel [75, p. 24].

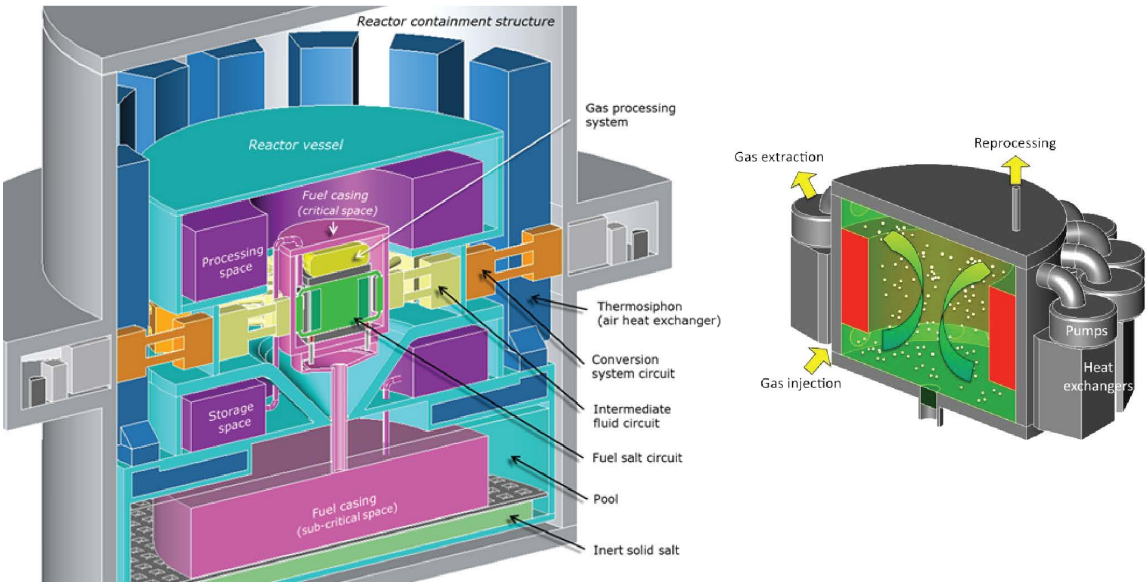

Fig. 2.26 (left) Schematic layout of the Molten Salt Fast Reactor containment. (right) Schematic diagram of the MSFR core. Reprinted from SAMOFAR [74].

The core of the reactor consists of two liquid circuits supporting the fission reactions, namely the fertile blanket circuit and the intermediate fluid circuit. The fertile blanket improves the breeding ratio of the core while also acting as a reflector and neutron shield, protecting the other core components such as the heat exchanger. The blanket contains 77.5 mol% LiF (lithium fluoride) and 22.5 mol% ThF_4 (thorium tetrafluoride), that, when the reactor is active, gradually transmutes into $^{233}UF_4$ (uranium-233 tetrafluoride). This liquid uranium-233 is extracted, stored and/or moved to the fissile fuel, thus maintaining its non-fissile character. Due to these reactions some fissile products will be generated in the blanket, making it of importance to process the salt, extracting the fissile products, add new thorium salt and cool the liquid [76, p. 4].

The intermediate (fissile) fluid circuit, the molten salt that circulates from the central fission cavity to the heat exchanger and back, is subject to constant reprocessing of the fuel. Initially, the fissile load consists of a mixture of different fluoride salts, including thorium and fissile isotopes[24] [75, p. 14], but overtime these isotopes transmute and eventually form many fission products that poison the fuel,

[24]The addition of additional transuranic elements is also possible.

resulting in a lower breeding ratio, thus reprocessing is required. In the core an on-line gas processing system constantly removes insoluble fission products out of the fuel, while roughly 40 L/day of intermediate fuel is subtracted from the loop to undergo off-line reprocessing in a separate space outside of the reactor vessel, see figure 2.26 and 2.27. There the soluble fission products are removed from the molten salt fuel, while other elements such as lithium, thorium, uranium and fluoride will be added to maintain the most efficient molten salt composition [76, p. 23; 75, pp. 57-58].

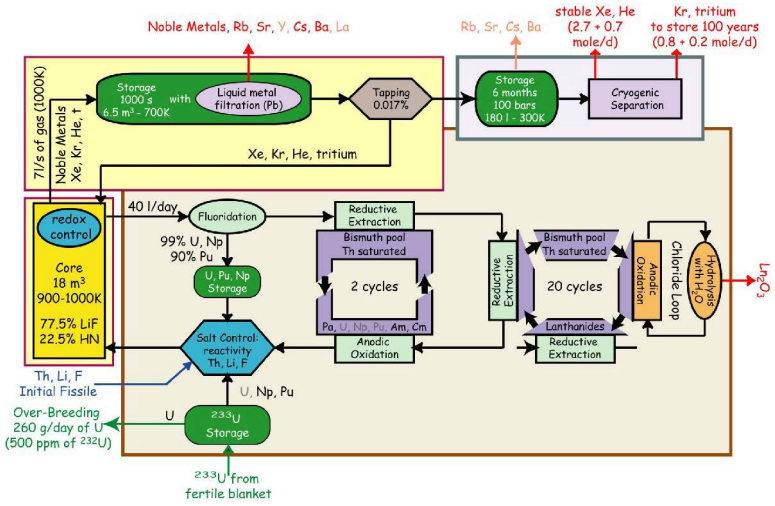

Fig. 2.27 Schematic off-site fissile molten salt fuel control and reprocessing cycle steps. Reprinted from Merle, E. [75, p. 58].

2.8 Summary

As a result of the *Klimaatakkoord* the Netherlands is exploring methods and strategies to nearly abolish its GHG-emissions by 2050 to reduce global warming with its catastrophic consequences. The energy sector, being the most polluting sector, has the highest priority to transition because of its current dependence on fossil fuels, primarily natural gas and coal.

Nevertheless, transitioning towards a more sustainable energy system is not an easy task. Many different sectors that are key to the Dutch economy are dependent on the current energy system. This makes them exceptionally susceptible to changes as this can drive up cost and disturb the current continuity. The latter of which is significantly reduced with the replacement of renewable electricity sources such as wind turbines and solar PVs, due to their weather reliant character of electricity generation. Therefore, requiring additional support systems to smoothen variations in the electricity supply. These additions are increased infrastructure capacity, conversion stations and energy storage systems, all coming with their own material requirement and costs. Furthermore, a major renewable electricity share correspondingly results in an extensive material requirement as the current used techniques, wind and solar, are low energy dense electricity sources. Meaning many turbines and panels are required to generate a notable share of the Dutch energy demand, further increasing the cost per power unit.

These mainly material and cost related complications demonstrate the necessity of additional alternative energy sources to reduce energy cost. Consequently, easing the energy transition and transforming it into a system that is beneficial for all.

Ergo, addition of nuclear energy to the Dutch energy mix could be a valuable substitute to other more cost demanding techniques. Nevertheless, many energy transition related visions do not include nuclear power as there are many fears for nuclear disasters and radioactive waste, but also the capital cost and related investment risks. Many of these studies, however, do not include fair energy source comparisons. Material requirements, EoL scenarios and system costs for both energy source and support infrastructure are left out in most cases. Hence, making the investigation towards sustainable energy systems less complete.

The study conducted by *ENCO* concluded that the addition of nuclear energy could play a key role in reducing the cost per power unit in the Netherlands as this energy source itself requires little additional infrastructure and has the potential to lower the required support systems for weather dependent renewables. While this study only focuses on cost, it does show the importance of such poorly studied comparisons.

In spite of these possible benefits of nuclear energy to the energy system, the majority of the current global nuclear reactor float still consists of decades old generation II reactors. These reactors are mainly outdated designs that in most cases perform inefficiently and do not meet modern nuclear safety standards. Hence, making them unfit for accurate comparisons to other sustainable energy sources as nuclear technology has advanced significantly.

These technological advancements resulted in new reactor designs, namely generation III+/IV reactors and the Advanced Small Modular Reactor designs. Some of the generation III+ reactors are already commercialised and constructed in several parts of the world, including Europe, hence slowly renewing the nuclear float and consequently improving specifics required for comparison to other modern energy sources.

Of all these new technologies the most matured reactor designs for the modern market are the generation III+ designs. Many of these designs are already operational or under construction in developed countries. This makes these designs interesting for near-future implementation (2030-2035) as they could be operational in less than 10 years. These designs are evolutions of the older generation II designs but are more efficient and multiples safer. Nevertheless, most designs are still reliant on active safety systems.

After 2030 the ASMR reactor designs will be ready for deployment. These reactors will allow more flexibility for complex energy systems because of their smaller size, capacity and lower capital cost. Combined with their enhanced safety and in many cases even passive systems they are seen as a potential beneficial addition to support the 2050 emission goals.

At last the generation IV reactors, designs known for their high fuel efficiency, low waste production and extremely high safety systems, are expected to be commercialised somewhat after

2040. For this reason they are not seen as potential designs to combat climate change before 2050, but due to their many expected benefits are seen as a great replacement for older reactors closing after 2050.

2.9 Conclusion

The transition towards a sustainable energy mix requires many transformations and new system elements, as the transition is of an immense scale. Yet, the energy transition is not only about reducing Greenhouse Gases emissions, but also concerns other goals to guarantee a development that is both beneficial for the society and planet altogether. The sustainable development goals essential to a sustainable transformation of the energy system are given in figure 2.28.

Fig. 2.28 The sustainable development goals related to the energy transition in the Netherlands. Reprinted from United Nations [2].

For that reason, it is of importance to assess technologies as being part of an *energy system*. Not only focussing on the direct effects of energy production technologies, but rather at the complete system including infrastructure and other required support components. In combination with an extensive Life Cycle Assessment (LCA) other more indirect effects, such as the End-of-Life impact and material challenges, can significantly reshape the sustainable character of certain technologies. For that reason, it is important to re-evaluate technologies that have been labeled as unsustainable previously, as these sources have the potential ability to accelerate a sustainable energy transition.

The transition away from fossil fuels and its implications for the Netherlands are examined in this research thesis. Because of the numerous potential benefits of incorporating nuclear reactors into Dutch energy systems, with special emphasis on the area surrounding the *Maasvlakte*. The surrounding area is known as the Rotterdam-The Hague metropolitan area (MRDH), and it is regarded as the most interesting of all allocated areas for additional nuclear implementation. This thesis will re-evaluate nuclear energy's potential by incorporating previously overlooked elements in many energy transition strategies. Therefore, re-assessing both the direct and indirect consequences of certain technologies. As a result, a well-founded comparison between various technologies deemed

sustainable for the energy transition of this specific region is possible. This can be applied to both large-scale system transitions and power plant transformation studies[25].

[25]Example: Transformation of the Onyx coal power plant into a nuclear power plant.

Chapter 3

Literature review

Rotterdam–The Hague metropolitan area (MRDH)

The Rotterdam-The Hague metropolitan area, or also known as MRDH, is a large cluster of municipalities in the province of Zuid-Holland. This area is known for its high population density, greenhouse clusters and the big heavy industrial cluster around the port of Rotterdam. The area houses 2.4 million people and 128 thousand companies and institutions, all of them demand requiring heat and electricity [35, p. 6]. The total final energy consumption of the MRDH district equals 17.4% of the total Dutch energy consumption and 14.4% of the national CO_2-equivalent emissions [77].

To achieve the goals set by the Dutch government the MRDH needs to contribute to these ambitions. For this specific region these goals translate into a very complicated challenge as land is scarce and over 1/3 of the land is categorised as the greater built environment. Making the implementation of renewable sources difficult as these techniques require a substantial amount of land, not only for production but also for energy conversion hubs, additional infrastructure and storage. Therefore, a set of requirement criteria for the energy system was made to ensure a sustainable and feasible energy transition, the list is given below [35, pp. 34-35]:

- Long- and short term reliability and resilience (network stability to prevent shortages)
- Affordability of total energy cost (including support systems, see section 2.5.3)
- Constancy to ensure consumer and supplier trust and enhance investment environment (network stability)
- Financial support from the government (subsidies, insurance, etc)
- Sufficient labour market to support, maintain and construct energy related systems
- Equality in energy related costs (political debate)

This set of criteria clearly reflects the same factors that could be linked to the strengths, weaknesses, opportunities and threats of this region, as given in the list below:

Strengths

- Logistic center of EU: Port of Rotterdam
- Presence of strong innovative industrial cluster
- Developed built environment including heat grids

Weaknesses

- High energy demand from built environment, greenhouses and industry
- Scarcity of available land

Opportunities

- Synergic sector cooperation with energy flows
- Strong technological investment climate from industry

Threats

- Energy transition feasibility
- Affordability of energy

3.1 Energy transition strategies

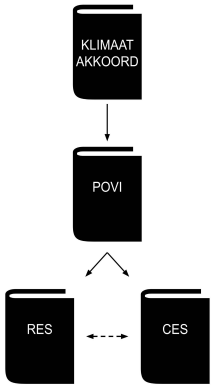

Fig. 3.1 Energy transition strategies per government level.

The energy transition vision of the Rotterdam-The Hague metropolitan area consists of two separate strategies, namely that of the industrial cluster *port of Rotterdam* and the regional *MRDH* strategy including all other areas, the latter is referred to as *RES*. The approaches are split because of the vastly different stakeholder situation. Both strategies describe aspired system integration between the industry cluster and the built environment. This thesis will further elaborate on this synthesis.

To guarantee a sustainable transition for both the environment and people the province of South Holland (*POVI*) created an assessment framework for energy transition policies. This assessment priority list includes both future ambitions and safeguards. The most important elements of this framework related to the energy system described in this thesis are listed below [78]:

Ambitions:

- Support innovation in region
- Enhance employment development
- Improves ecosystem diversity
- Enhance human health

Requirements:

- Lowers CO_2-emissions
- Possibility to easily integrate in current system

- None-to-little fresh water consumption
- Limited noise pollution 'emissions'
- Does not degrade water and environment quality
- Does not reduce quality of heritage sites

3.1.1 Regional Energy Strategy (RES)

The ambitions and strategy of the MRDH are described in the regional energy strategy (RES) for the MRDH region. To quantify the required changes in the transition the RES split their approach into four system groups, namely; heat, electricity, fuels and the energy system. With the last being the infrastructural link that connects the other groups together.

Heat The most important measure to accelerate the transition is to lower the heat demand by renovating and insulating the built environment and greenhouses. These measures are predicted to lower the heat demand by 20% and 30% with respect to 1990 respectively. These improvements are expected to be completed before 2030 [78, p. 15].

Yet, to account for the remaining heat demand the region has the possibility to use a more efficient heat system. Because of the unique urban and industrial character of the region the possibilities for an extensive collective heat network are seen as essential to the sustainability transition. These heat grids are able to provide heat from central sources towards neighbourhoods and greenhouses. This system centralises the production of heat and therefore is able to improve efficiency and economics.

Historically the region already has multiple detached heat grids ranging from small to large scale networks and (very) low to high temperature systems [79]. For this reason the region is especially suitable for extension and large scale attachments. The municipalities are visualising a heat roundabout connected to the port of Rotterdam that provides waste heat from industrial processes, but also from various economically feasible renewable heat sources. The network would extend from the port to Rotterdam up to Leiden and provide heat to the built environment and the surrounding greenhouse clusters, as illustrated in figure 3.2. If connection to this grid is not possible a sustainable fuel alternative is used to locally generate heat, such a fuel could be bio- or synthetic gas [35, ch. 3].

Electricity Since many heat related processes are converted to electrical systems the demand of electricity is predicted to grow steadily over the years. In the built environment the usage of smart technologies, digitalisation, heat pumps and cooling systems will outweigh the electricity savings by efficiency improvements, all in all resulting in an increasing electricity demand of 1% per year, equaling roughly 15% by 2030. Additionally, in industry this electrification is expected for most processes under 600°C that do not have access to a heat grid [11, p. 144; 18, p. 66].

Regarding electricity system the regional strategy focus intensifies the assessment framework of energy sources given by the province on multiple aspects, ensuring a resilient and sustainable transition. First, the electric source cannot reduce the environmental quality of an area, prioritising

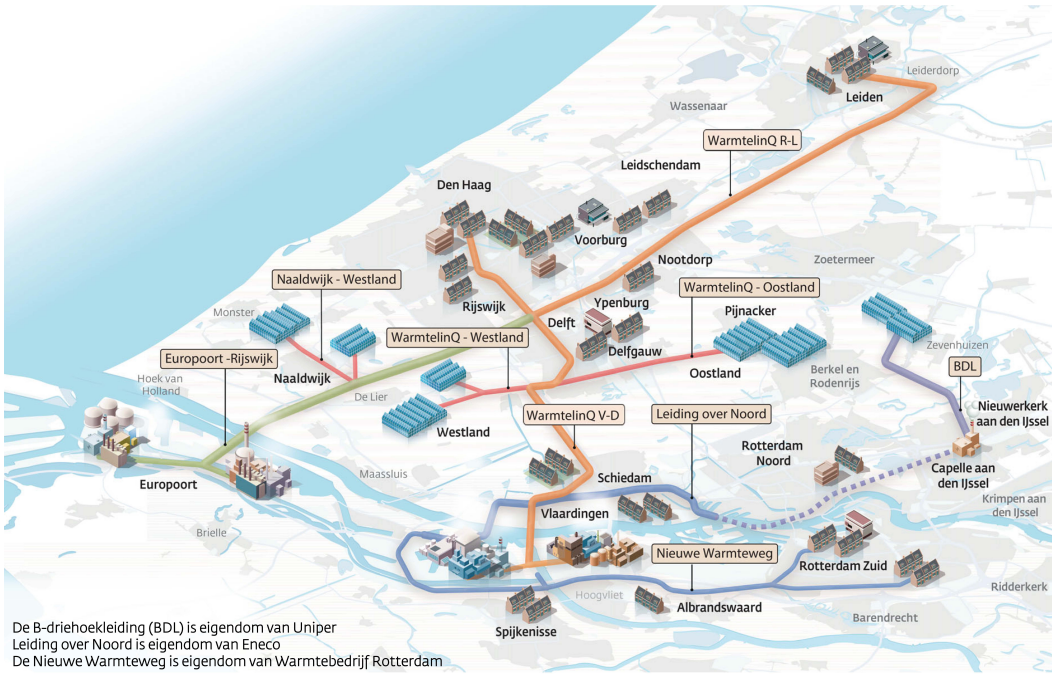

Fig. 3.2 Overview of the current and proposed heat grid of South Holland. Blue lines illustrate the current heat network, red represent proposed and likely future connections to the grid, green and orange lines are the main proposed network. Reprinted and translated from Gasunie [80, p. 70].

conservation of scarce quality spaces in the area. Secondly, the source is required to feasibly co-exist with the current land function and retain the quality of surrounding ecosystems and guarantee public safety. Third, the capacity of the source needs to balance out the social cost, meaning implementation cannot prevail over the objections of the public. Last, the effect on the electric grid needs to be taken into account, including capacity, stability and flexibility [35, ch. 4].

Due to this stricter assessment framework and the characteristics of the region the production of electricity with renewables is heavily limited. For this reason many of the suggested electricity sources focus primarily on solar PVs in the built environment, with roughly 40% of the roofs being suitable for PVs. The addition of new wind turbines and solar fields is limited in the area and for that reason only contributes a little. The total renewables potential is estimated at roughly 2.8-3.2 TWh (10.1-11.5 PJ) [35, ch. 4].

Fuels Currently the port of Rotterdam is the main import/export hub of energy carrying fuels in Europe. This focus will be maintained but will shift from fossil fuels towards sustainable fuels, such as bio- and synthetic fuels. In the MRDH this approach results in the construction a large-scale network for hydrogen, reinforcing the region to become the hydrogen fuel hub of northwestern Europe. In addition, several hydrogen and waste fermentation plants will produce a small amount of these fuels for local use. Hydrogen will eventually be produced by electrolysers using electricity generated from offshore wind turbines or other green sources. Due to the size limitations of the Rotterdam-The Hague

metropolitan area it is expected that the region cannot be self-sustaining and therefore will require the import of these green fuels. Nonetheless, the region wants to be characterised by innovation in sustainable fuels [35, ch. 5].

Energy system The region fully focuses on a smart system in which energy is used in the most efficient manner. This implies the integration of different sectors present in the region into one cooperative system. For example allowing the distribution of waste products such as heat to parties that can use these resources. Additionally, flexibility will play a key role in the supply and demand chain of electricity. The implementation of a smart grid aims to lower the demand during shortages by the use of smart devices and electricity priority per consumer, hence increasing grid stability and decreasing electricity cost for flexible consumers [35, ch. 6].

Due to the land limitations of the region, import of energy is seen as necessary, hence creating additional energy related dependencies in the future.

3.1.2 Port of Rotterdam: Cluster Energy Strategy (CES)

In the coming years the port of Rotterdam is going to transform into a modern industrial cluster that embraces circularity of material flows (including waste), heat, energy carriers and chemicals. Changing the heavy industry sources from fossil resources towards more sustainable alternatives. This circularity is possible because of the open networks between different industry and sectors nearby, allowing for synergetic relations, improving both efficiency and process economics. These changes result in a drastic decrease of GHG-emissions [81].

The 2050 ambition described above is a goal set by the port of Rotterdam to be able to meet climate goals while also assure its strong global market position. Currently the harbour and its surrounding industrial cluster are seen as the import and export hub of energy carrying resources in Europe. These resources, mainly raw oil, are refined and processed into a variety of fuels and chemicals that are required in our society. Nevertheless, these vital resources come with a cost as they primarily contain carbons that are emitted as CO_2 somewhere in their product lifetime[1]. These changes are important to achieve the national emission goals as in 2016 the industrial processes of the Rotterdam/Moerdijk cluster[2] emitted 26% of the total national industry related CO_2 emissions [77]. This master thesis will only focus on the Rotterdam-The Hague metropolitan area part of the Rotterdam/Moerdijk industrial cluster to give a finer synergetic strategy to the energy region (RES). Compared to the full size of the industrial cluster the Rotterdam share uses the lion's share of energy.

The industrial cluster work group illustrated their 2050 vision in figure 3.3. The images show the changing energy and material flows following the energy transition. The 2050 flow chart clearly indicates the industry cluster preference for electrification together with hydrogen heat. While energy sources focus on primarily offshore wind turbines and the more conservative sources biomass and

[1] from production to combustion or waste disposal

[2] The Rotterdam/Moerdijk industrial cluster refers to all industrial clusters around the Maas delta.

natural gas including CCS (in image CCUS). The estimated demand of 180 PJ offshore wind turbine electricity converts to roughly an installed capacity of 13 GW, or a quarter of the realistic maximum potential for wind turbines on the North Sea. The electrification of industrial heat processes has reached it full potential by 2050, using electric heating for all processes below 600°, if enough electricity is produced.

Regardless the main focus of the port of Rotterdam will be the transformation to the infrastructural hydrogen hub of northwestern Europe, replacing its current role as fossil fuel hub. This strategy will ensure the current strategical hub function during the energy transition of the coming years. Securing the economical, logistical and innovative impact on the Netherlands [82].

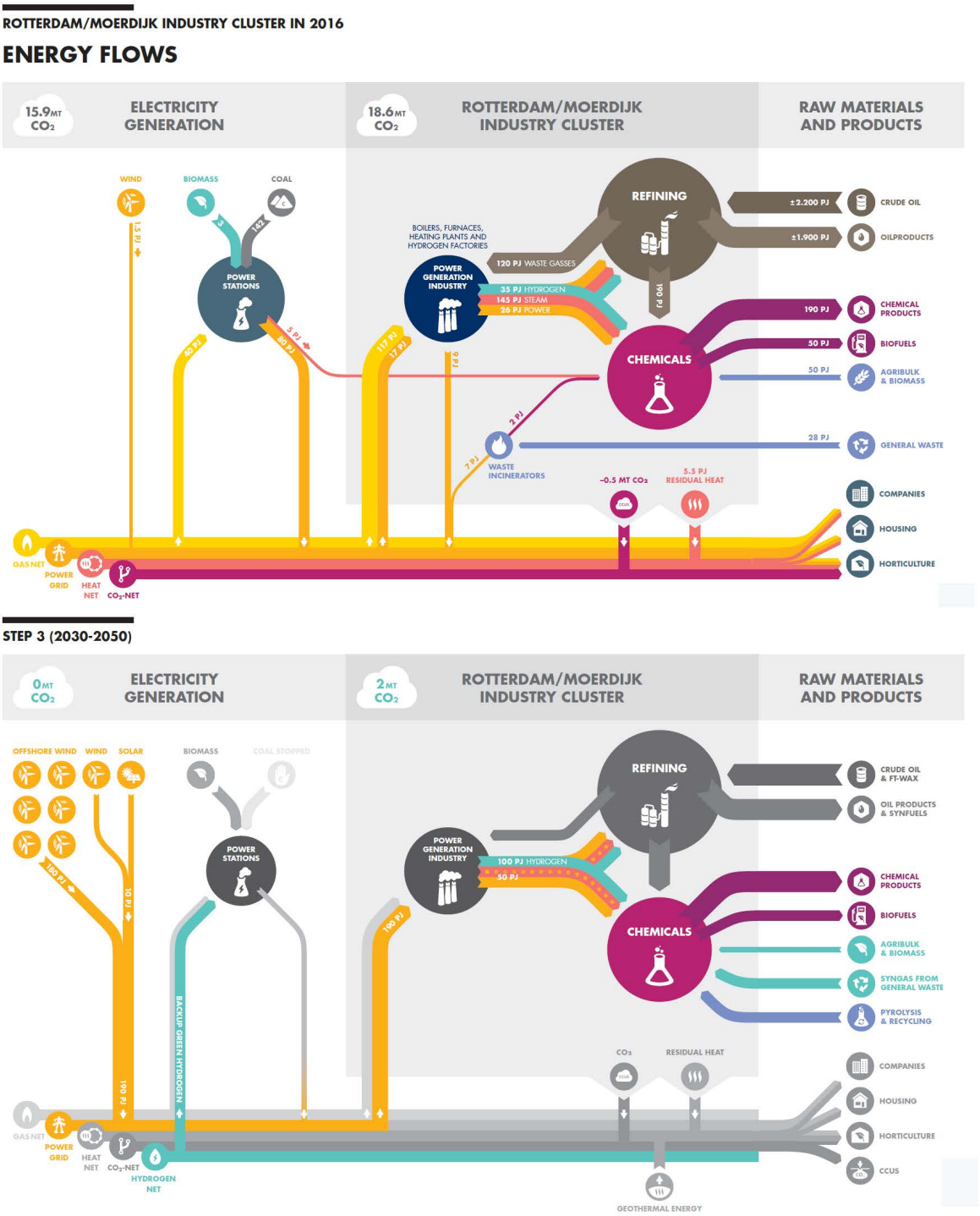

Fig. 3.3 Energy flow diagram for the industrial cluster Rotterdam/Moerdijk in 2016 (top) and 2050 (bottom). Reprinted from Rotterdam-Moerdijk industry cluster work group [83].

Following the industrial cluster's energy strategy and the projects currently under construction, it is possible to assume future trends for the input and output flows. These predictions for the coming years

up to 2030 are estimated by CES Rotterdam-Moerdijk [82] (1-2) and PBL Netherlands Environmental Assessment Agency [81, p. 25] (3). The projections are listed below:

1. Installed hydrogen production capacity:
   (a) 2030: total capacity 400MW, producing 0.092 Mt H_2/year (11 PJ)
   (b) 2050: total capacity 1510MW, producing 0.35 Mt H_2/year (42 PJ)
2. No electrification before 2030
3. Annual energy savings of 0.5 %

3.2 Reflecting back to national interests

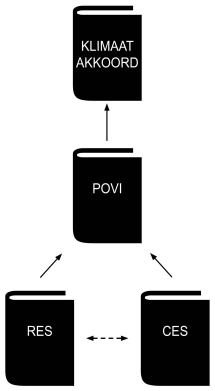

Fig. 3.4 Energy transition strategies per government level.

The discussed strategies and goals are all influential on the researched region, yet priority greatly differs. Following the climate goals of the European Union and the Dutch government some strict conditions are set for the years 2030 and 2050. With the help of these strategies the ambitions are translated to a more detailed strategy that leads to these desired reductions. In general all the discussed strategies, ambitions and visions are complementary and face similar challenges. Nevertheless, when comparing the detailed goals set by these approaches more complications appear.

The approach of the Dutch energy transition focuses on a layered transition program with the national energy transition strategy (*Klimaatakkoord*) seen as its guideline and the RES and CES as regional input. This approach, however, does result in some friction between the different strategies, creating uncertainties and overlapping resource demands. Considering the unique and complex characteristics of the researched region these problems seem to amplify.

As discussed in section 2.2 the future Dutch energy mix is required to transition into an effective and sustainable supply and demand chain. However, due to the many limitations related to land management the Netherlands is not able to produce all the energy required to sustain its requirements. Even in the most ideal scenarios the country would be dependent on import of sustainable energy and polluting fossil fuels. So if the Netherlands desires to transform into a sustainable energy hub it becomes essential to rethink the current strategy and further research alternatives that would benefit the future Dutch society.

This problem is only amplified when looking at the Rotterdam-The Hague metropolitan area as land is even scarcer and only little space is available for future energy development. The densely populated region combined with its heavy industry cluster account for a considerable amount of the national primary energy demand and GHG-emissions. This specific energy situation makes the MRDH region very dependent on other (neighbouring) areas as it could never be self-sustaining with

current renewable technology. For that reason, both the RES and CES, point at the potential offshore wind capacity on the neighbouring North Sea. With the industry cluster even suggesting a quarter of the total realistic potential of offshore wind to be appointed to its industry. Consequently reducing potential energy sources for other sectors in the Netherlands.

Such a dependence on renewables uncovers many new complications for the region. With an increasing share of PVs and wind turbines in the energy mix the instability of the electrical grid amplifies. These resulting variations are disastrous for many energy consuming processes that require a base load. Such a transition requires expansion of the current electricity infrastructure, but also demands other support systems such as energy storage hubs. All requiring many resources and space, hence increasing costs.

To reduce these grid variations the industrial cluster proposes extensive use of biomass/gas and natural gas to produce and supply a more stable amount of heat and electricity, as these sources are able to generate energy in a more flexible manner, being independent on weather. Additionally, leaving the industry with a smaller electrification assignment as heat can be produced in a more conservative fashion. These energy sources, however, do produce GHG-emissions and thus require the implementation of costly Carbon Capture and Storage technology.

To conclude, individually these strategies portray a roughly feasible strategy, yet when combined it becomes clear not all ambitions overlap. Add their similar dependencies on potential locations for new sustainable energy sources and these transition strategies turn out to be more and more unrealistic. All in all making it important to research alternative carbon-free energy systems that have the ability to reduce these mutual dependencies due to fewer spatial demands, and therefore increase the practicability of the transition. Considering the energy density of nuclear energy and the scarcity of space in the MRDH region the implementation of modern nuclear reactors seems to be a potentially beneficial addition to the currently proposed energy strategy on both national and regional levels. Additional, benefits of such an inclusion could be the enhancement of the strengths of the region by taking advantage of the unmistakable possibilities in the region without disregarding the preferences of the industry and built environment. Transforming the regional system into an network that makes most use of the high calorific values of energy sources.

3.3 Conclusion

As previously stated, it is critical to re-evaluate energy production technologies in order to assess current energy transition strategies. To re-evaluate these technologies, an extended assessment framework must be developed, which includes the elements that were previously overlooked, as discussed in chapter 1. This extended framework, as shown in figure 3.5, determines both the impact of strategy implementation and the feasibility of the transition while safeguarding the sustainable development criteria.

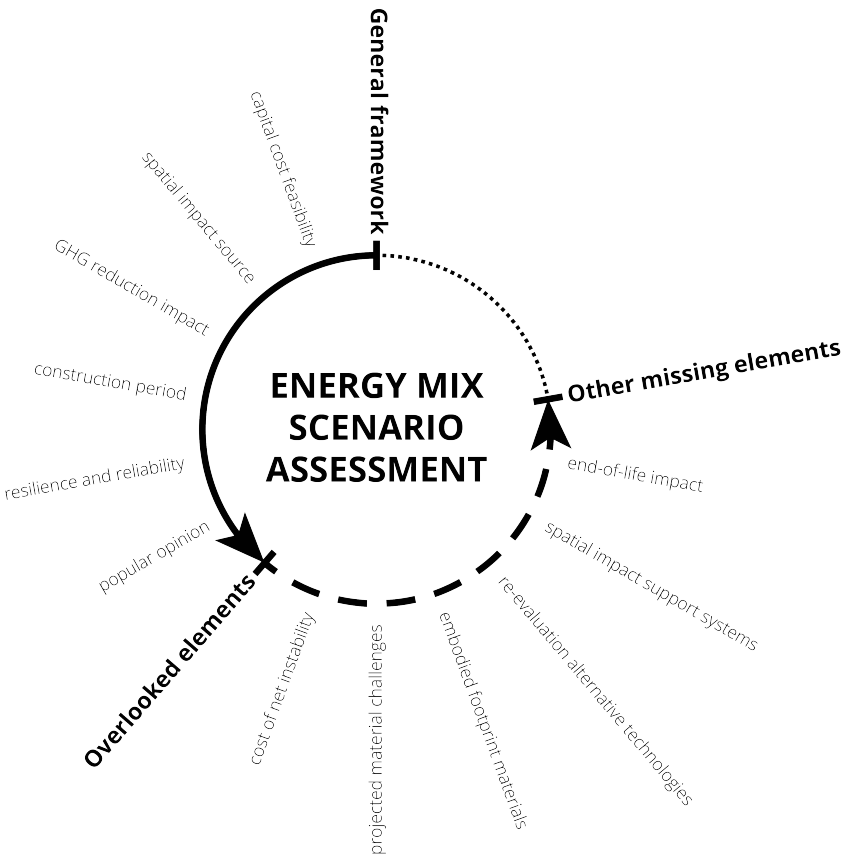

Fig. 3.5 Illustration of the overlooked assessment elements in current energy mix scenario assessment studies.

However, in order to properly assess these transition strategies, it is necessary to consider the impact of these strategies at both the regional and national levels. Transitions of this magnitude are exceptionally complicated, as the strategies can vary depending on the research location. As a result, a variety of approaches must be investigated in order to achieve the larger goal of a sustainable transition that benefits all sectors and stakeholders in a variety of ways. To do so, it's critical to re-evaluate the energy mix strategy on a regular basis, taking into account both regional and global ambitions and requirements, as shown in figure 3.6.

The Rotterdam-The Hague metropolitan area is seen as an interesting region for re-evaluation of nuclear energy due to its interesting *SWOT*[3] characteristics and the fact that construction of a nuclear power plant is currently permitted by law on the *Maasvlakte*. Re-evaluation of energy production techniques, combined with evaluation of new and improved energy flows, can help to provide an unbiased long-term viability study on the challenge of achieving a sustainable energy transition. By expanding the currently used assessment framework, this objective assessment can be achieved.

[3]SWOT: Strength, Weaknesses, Opportunities and Threats.

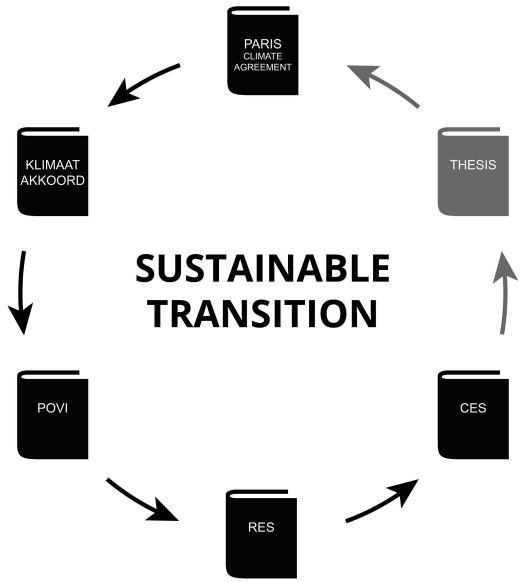

Fig. 3.6 Schematic illustration of the missing link between the different government level strategies.

3.4 Research objectives

The literature review and background chapter show that current evaluation methods do not allow for a neutral and long-term assessment of the extremely complex energy transition strategies. As a result, the primary goal of this master's thesis is to investigate an alternative assessment method for re-evaluating nuclear energy, a promising and widely discussed energy source in the energy transition. A research question is developed to investigate this objective.

Research question: *'To what extent can modern nuclear reactors benefit the future of the Rotterdam-The Hague metropolitan area sustainable transition and energy mix compared to other energy sources classified as sustainable?'*

To answer the research question raised above, various sub-objectives are investigated using the discussed assessment framework. These sub-goals are listed below.

1. Determine the current proposed energy transition strategy's challenges, bottlenecks, and benefits.
2. Investigate the integration of various nuclear energy scenarios, including the use of the sustainable assessment method.
3. Compare the benefits and drawbacks of various energy generation strategies and their associated techniques.

Chapter 4

Methodology

A dynamic and intelligent system analysis

4.1 Research method framework

To obtain a truly unbiased energy mix assessment, the energy system must be simulated in a near-real time and dynamic model. As previously stated, the implementation of renewable energy production technologies is causing the energy system to become more weather-dependent, resulting in a fluctuating energy imbalance. Because the weather is constantly changing, it is difficult to simulate the short-term imbalance between energy consumption and generation because weather data is limited to specific time intervals. Nonetheless, for a fair assessment of each scenario, it is critical to include these short-term fluctuations as well as long-term imbalances, as these have a significant impact on the requirements for supporting systems, as discussed in section 2.5.3.

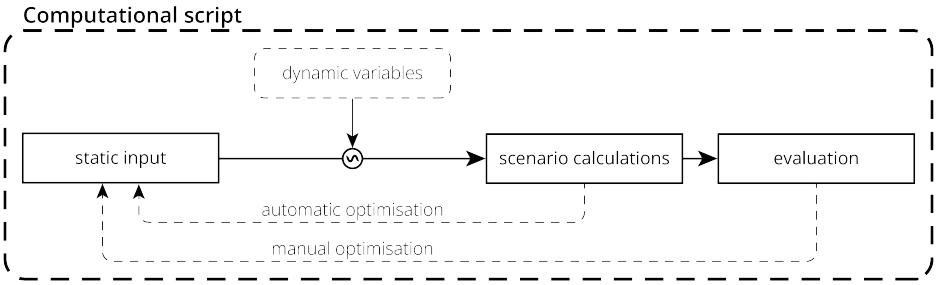

Fig. 4.1 Overview of simulation assessment tool and its section division methodology.

The assessment model script is divided into four major sections, as shown in figure 4.1. First is the *static input* which described the current and projected energy mix conditions, the reference scenario, quantification of assessment elements and the weather data. The second section discusses the *dynamic variables* that describes the uncertain behaviour of trends described as static input. Third,

the *scenario calculation* are discussed. Describing the system calculation methods for energy mix imbalance per time interval, the required supporting infrastructure on a yearly basis, and the impact of the transition scenario strategy. At last, the *scenario evaluation* section describes the assessment method. This final step allows for the investigation of all mentioned sub-objectives.

4.2 Static input

The scenario conditions are an important set of constants for the simulation. These are the baseline conditions, which correspond to the region's current energy production mix. This system serves as a starting point for evaluating various energy transition strategies. It is also used as a reference point for the other simulation calculations. Referencing simulation data is critical to ensuring output quality, particularly from renewable sources.

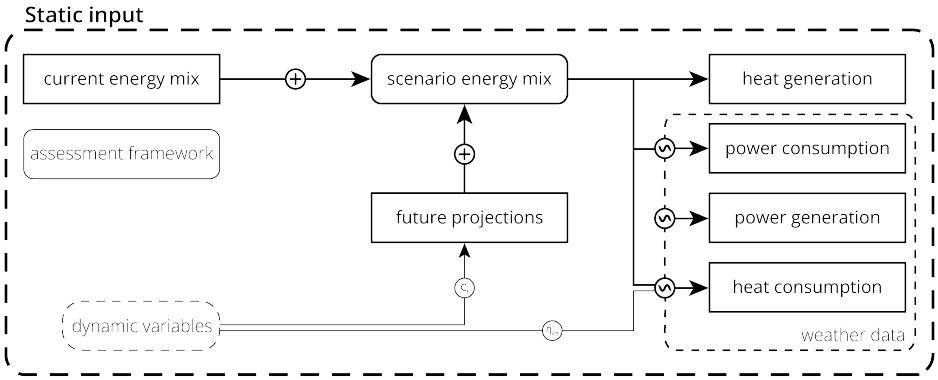

Fig. 4.2 Overview of the static input methodology of the script.

4.2.1 Current energy mix

Energy consumption

To allow for accurate future projections, the Rotterdam-The Hague metropolitan area energy consumption is divided into the various discussed sectors. Because the data for energy consumption in 2020 is not comparable to previous years due to the COVID pandemic, the data for 2019 will be used as a reference year. Table 4.1 summarises the yearly consumption of these sectors.

Table 4.1 Energy demand per sector of interest corresponding for the year 2019*. **Due to the COVID pandemic MRDH regional energy values of 2019 are chosen as a reliable simulation start year.* Energy consumption data is retrieved from Ministry of Infrastructure and Water Management [77].

2019*	**Industry**		**Built Environment**		**Agriculture**	
	heat	*electricity*	*heat*	*electricity*	*heat*	*electricity*
Consumption [PJ]	139.19	17.23	80.44	28.59	54.49	6.07
[TWh]	38.66	4.79	22.34	7.94	15.14	1.69

Hourly consumption data, on the other hand, is required to truly simulate the energy system. For heating (q [MW]) and electricity (P [MW]), this information is retrieved in different ways. Data from ENTSO-E [33] will be used to calculate hourly electricity consumption. This information can be divided into two categories: constant load and variable load. The electricity demand of the industry classifies as a constant load, meaning it is assumed that the electricity demand from industry does not fluctuate. The built environment, on the other hand, is constantly changing as a result of human activity. Agricultural electricity usage is primarily during the hours of darkness, because of greenhouse productivity and its dependence on solar irradiation.

Hourly heat consumption rates are calculated using the same method. Industry is seen as a constant consumer, similar to its electricity demand, while the built environment and the agricultural sector are consumers when both the temperature, wind and solar irradiation fall below acceptable levels. The combined effect between temperature and wind has the greatest impact on heat demand of these two factors and are therefore only used in these heating calculations.

To calculate heating demand, the effective temperature method from KNMI [84] is used. This effective temperature, T_{eff} [°C], is calculated following equation 4.1. The variables represent; outside temperature [°C]; average wind speed at surface, v [m/s].

$$T_{eff} = T - \left(\frac{2 \cdot v}{3}\right) \tag{4.1}$$

This effective temperature is calculated hourly and per day. If this average effective temperature is below 14°C for both day and hour averages, heating in both the built environment and agriculture are assumed. The amount of heating is depended on the deviation from the 14°C tipping point, this fluctuation is calculated hourly. During the nightly hours the heating values of the built environment are assumed to be cut in half (23.00-07.00). These reductions are commonly seen in the Netherlands because of the lower required temperature during sleep.

Energy generation

The current energy mix is divided into three categories: renewable, non-renewable, and import. The first category, renewable, has for electricity generation the same generation capacity as the previously

discussed *reference point* scenario. The information about non-renewable production is retrieved from the Netherlands Enterprise Agency (RVO) [85] database, which also includes information about capacity, full-load hours and fuel cycles. In this version of the outage rate of generation facilities is ignored due to time limitations. All technologies are therefore assumed to be functional at their theoretical maximum, hence ignoring both planned and forced outages. The last category, import, is equal to the yearly sum of generated electricity and consumption. This classification is used to describe dependence of analysed scenarios.

Heat generation was not yet discussed. This data is retrieved from the Stuurgroep Energiestrategie regio Rotterdam Den Haag [35] database. It includes geothermal heat, solar heat, (air source) heat pumps and industrial waste recovery. These values are summarised in table 4.2. In the simulation the local thermal heating systems are not connected to the several heat grids.

Table 4.2 Heat generation in the MRDH region in 2020, excluding private boilers. **Local heating represents both (air source) heat pumps and solar heating. **AVI stands for both biomass and waste incineration.* Energy generation data is retrieved from Stuurgroep Energiestrategie regio Rotterdam Den Haag [35].

	Geothermal	**Industrial waste**	**Local***	**Natural gas**	**AVI****	**Electric**
2020 [PJ]	3.0	0.7	2.5	2.8	2.7	0.2
[GWh]	833.33	194.44	694.44	777.78	750.00	55.56

Reference point

To ensure the accuracy of the data, the calculated values from the simulation are compared to the actual output of a given reference year between 2010 and 2020. In this thesis, actual net renewable electricity production in 2020 will be compared with the baseline scenario that includes installed renewable capacity in that year. For both PV-panels and onshore wind turbines the MRDH region is used as a reference point. Offshore wind turbines are excluded due to their limited installed regional capacity in 2020. The real net electricity output and installed capacity are retrieved from the Ministry of Infrastructure and Water Management [77] databank, see table 4.3.

The baseline scenario for the system check is based on the installed capacity as shown in table 4.3. However, capacity is not the only factor influencing electricity output per MW installed capacity. The technical specifications of the model also has an impact on performance. As a result, installed capacity is separated by model share; this information is gathered from information sheets provided by both energy producers and local governments. Appendix C.2 contains a complete list of the wind turbine technologies that are included. Unfortunately, information about PV-panel models is not stored in an open-source database. Therefore, multiple reference crystalline solar panels are used (see Appendix C.4). The chosen panels are regarded as high quality standards during that period. As a result, the output values for solar power are expected to deviate more from the actual electricity output of PV-panels in 2020. Due to this uncertainty the PVGIS tool from Joint Research Centre [86] is used as an additional reference check for solar power generation.

Table 4.3 Renewable installed capacity and historical production data. Reprinted from Ministry of Infrastructure and Water Management [77] databank.

Renewable source	Year	Installed capacity [MW]	Normalised net output [PJ]
Onshore wind turbines	2020	258	2365
PV-panels	2010	7.5	19
	2011	9.4	28
	2012	15.6	39
	2013	33.0	78
	2014	55.6	141
	2015	82.2	217
	2016	113.9	306
	2017	159.2	430
	2018	241.0	727
	2019	367.5	1019
	2020	498.6	1534

The use of an efficiency reduction factor corrects all deviations resulting from the reference point simulation.Rather than including the complex environmental factors themselves, this factor corrects the simulation by reducing the real output. Solar panel positioning and dust for PV-panels, as well as the turbine wake-effect for wind power, are common renewable reduction factors. Because only limited historical data was available for the wind power reduction simulation, the pre-2020 turbines were averaged and simplified into a reference model that was corrected to the 2020 deviation factor.

4.2.2 Assessment framework

Several factors must be considered in order to fully comprehend the implications of specific technologies within an energy mix. These elements can be used to describe both direct and indirect effects. A proper Life Cycle Assessment (LCA) can be made when these elements are assessed in relation to the energy mix over a given time period. In general, more assessment elements lead to a more accurate assessment of the energy mix. Nonetheless, due to time constraints, a selection of key elements is chosen after the conclusion of Chapter 2. The described values measured in MWh are corrected to the produced heat of each given technology[1]. Table 4.4 contains a summary of all the data. In the case of nuclear energy, more specific distinctions are made based on reactor model, see table 4.5. Only the models indicated in bold font are included in the described experiment. For both combustion plants and small modular reactors, the construction time for new plants is set at 5 years. For generation III+ and IV nuclear reactors, an 8-year construction period is assumed.

Quantification of assessment elements

1. Lifetime; The lifetime of the technology is an important factor as it influences the LCA of a given technology. The technical operational lifetime discussed in section 2.5.2 are used.

[1]Described in given literature; capacity factor and electricity generation efficiency.

Table 4.4 Quantified evaluation framework for each included technology. Data is retrieved from the various sources listed in this section. Missing data is indicated with a dash. **Construction data on natural gas corresponds to high calorific gas combustion plants.*

Technology	Lifetime [year]	Direct cost [M EUR/MW]	Indirect cost [EUR/MWh]	Spatial footprint [MW/km^2]	Direct emissions [kg CO_{2-eq}/MWh]	Indirect emissions [t CO_{2-eq}/MW]	Fuel demand [MWh/t]	Chemical waste [cm^3/MWh]
PV	25	1.6230	21.29	0.0643	0	5394.00	0	3.79
Onshore wind	25	2.2713	12.95	19.80	0	495.33	0	2.02
Offshore wind	25	4.3051	23.49	7.20	0	1,125.75	0	2.02
Natural gas*	30	0.9107	7.76	6,020.0	203.76	4,980.67	13.10	2.89
Biomass	30	1.2451	21.06	558.28	394.56	2,723.80	4.28	1.13
Coal	30	0.9670	14.88	558.28	338.40	10,982.02	8.06	4.42
Nuclear	60	1.9627	4.00	3,954.0	0	174.86	438,638.74	0.24
Alkaline	10	0.5	0	16,719.5	0	-	33.32	-
PEM	10	1.1	0	16,719.5	0	-	33.32	-
SOEC	10	2.8	0	16,719.5	0	-	33.32	-
Li-ion battery	10	0.339	0	2,000	0	44.1696	0	-

Technology	Radioactive waste [cm^3/MWh]	Water pollution [kg DCB_{-eq}/MWh]	Biodiversity reduction [PDFm2a/MWh]	Spatial nuisance [-]	Employment Employment [fte/MW]	Innovation potential [fte/MW]	Human health risk [μDALY/Mwh]	Fuel cost [EUR/MWh]
PV	0.04	10.00	0.29	4	1.17	6.70	392.31	0
Onshore wind	0	56.00	0.10	5	0.51	4.70	123.08	0
Offshore wind	0	56.00	0.10	3	1.28	15.60	123.08	0
Natural gas*	0	1.30	0.81	3	0.21	0.93	355.00	36.25
Biomass	0.10	0.74	3.12	3	2.28	2.90	414.62	115.17
Coal	0.03	0.74	3.12	3	1.72	5.40	414.62	14.88
Nuclear	4.09	0	0.05	3	2.20	1.30	35.54	7.93
Alkaline	-	-	-	1	1.2	1.35	-	-
PEM	-	-	-	1	1.2	1.35	-	-
SOEC	-	-	-	1	1.2	1.35	-	-
Li-ion battery	-	-	-	1	0.2	1.35	-	-

Table 4.5 Quantified evaluation framework for each included nuclear model. Data is summarised from section 2.7.2-2.7.6. The cost of post-FOAK reactors is reduced by 40% for generation IV reactors and 28% for small modular reactors. Cost on the generation III+ reactors are more available therefore original estimates are given.

Model	Generation	Thermal capacity [MW]	Thermal efficiency [%]	Outlet temperature [°C]	FOAK cost [M EUR/MW]	Post-FOAK cost [M EUR/MW]	Spatial footprint [MW/km^2]	Fuel efficiency [%]	Waste production [%]
EPR2	III+	4,500	37.0	313	3.00514	2.16376	3,954	100	100
AP1000	III+	3,200	33.0	303	2.34894	1.69125	3,954	100	100
APR1400-EUR	III+	3,983	35.0	307	1.43115	1.0304	3,954	100	100
MSR	IV	1,000	50.0	700	3.27113	1.96268	3,954	3.7	10.0
VHTR	IV	545	55.0	900	3.27113	1.96268	3,954	100	100
SFR	IV	2,500	40.0	500	3.27113	1.96268	3,954	3.7	10.0
SCWR	IV	2,200	45.0	510	3.27113	1.96268	3,954	100	100
Nuscale	ASMR	200	30.0	321	1.32917	0.957	17,142.9	100	100
BWRX-300	ASMR	870	32.2	287	0.424861	0.3059	5,178.57	100	100
SMART	ASMR	365	29.3	322	2.52306	1.8166	4,055.56	100	100
UK SMR	ASMR	1275	34.7	327	2.30851	1.66213	31,875	100	100
NUWARD	ASMR	540	31.5	307	2.57337	1.85283	7,714.29	100	100
IMSR	ASMR	440	44.3	700	2.79336	2.01122	9,777.78	3.7	10.0

2. Direct cost; Capital-, maintenance-, decommissioning- and operation costs are seen as direct investments. These costs are required even when the technology is not operational at maximum capacity. The values for direct cost for energy generation technologies are retrieved from the report '*Projected Costs of Generating Electricity*' by International Energy Agency (IEA [30]. For storage technologies information is retrieved from IEA [87]. The cost of battery parks are reduced from the original given value as these large orders are proven to be more cost efficient. The cost is based on the *Hornsdale* and *Victoria Big* battery parks in Australia. All values are expressed as cost per installed capacity; million euros per MW.

3. Indirect cost; The indirect costs are a combination of emission taxes and fuel-, and waste management costs. This data is retrieved from International Energy Agency (IEA [30]. The cost of both fuel for coal and natural gas are seen as manual input due to the strong price fluctuations of the past years. A reference price is always given, this price is retrieved from the Trading Economics database [88; 89][2]. Indirect cost is measured in euros per MWh. All given prices are from pre-covid year 2019 to ensure a normal price curve (not affected by global problems such as war and pandemics).

4. Spatial footprint; The direct spatial implication of the discussed technologies are based on a variety of documents. For wind turbines the spatial footprint is based on a study by Enevoldsen & Jacobson [90]. The spatial footprint of PV-panels is based on data from Kuijers *et al.* [10]. The spatial footprint of biofuel and natural gas are based on GIS calculations performed in *QGIS*. Several regional power plants; Onyx, MPP3, Enecogen, Maasenergie and Rijmond energie were used to find an applicable average. The spatial density of nuclear energy was based on the footprint of three young reactors, namely; Hinkley point C, Olkiluoto 3 and Taishan 1-2. For storage technologies a similar method was used based on reference projects because of limited information. All electrolyser technologies are based on the Shell hydrogen project in the port of Rotterdam. While the battery technology was based on the Hornsdale power reserve in Australia. All these values are expressed as installed capacity per square kilometer [MW/km^2].

5. Direct GHG-emissions; Combustion, fuel manufacturing, waste storage and transport all result in direct emission of greenhouse gases. The values were retrieved from the report '*Life Cycle Assessment of Electricity Generation Options*' by UNECE [91] in combination with the standard carbon dioxide-equivalent emission factors set by the Netherlands Enterprise Agency [92]. The values are given as kilograms of carbon dioxide-equivalent per MWh produced [kg CO_2-eq/MWh].

6. Indirect GHG-emissions; Emissions from construction, maintenance and decommissioning are classified as indirect pollution. These values are present even without the technology operating. Similar to direct emissions these figures are directly retrieved from UNECE [91]. Sadly, due to limited information the electrolysers are excluded as no viable information was found. The values are given as tonnes of carbon dioxide-equivalent per MW installed technology capacity [t CO_2-eq/MW].

7. Fuel demand; For the different energy production technologies the fuel demand per MWh can be calculated by the inverse of the lower heating value (LHV) [93]. For newly built generation III+ nuclear reactors this information is retrieved from World Nuclear [94]. Fuel demand is measured in MWh per tonne [MWh/t].

[2]The price of coal is given as USD/t, live exchange rates are used. 1 tonne of coal equals 8.141 MWh of energy.

8. Chemical waste; During operation the different generation techniques produce chemical waste. This waste is measured in cubic centimeter MWh [cm^3/MWh]. The values are retrieved from Abousahl *et al.* [36].

9. Radioactive waste; Some of the generation techniques produce radioactive waste as a by-product from electricity or heat generation. This waste is measured in cubic centimeter MWh [cm^3/MWh]. The values are retrieved from Abousahl *et al.* [36].

10. Construction material demand; During the construction of these technologies many materials are required. As discussed in section 2.5.1, many of these elements are classified as critical to the European Union. This material criticality is translated into potential future supply risks. Element specific data per MW installed capacity is retrieved from multiple sources [95; 96; 97; 98; 99; 100]. Elements with little to no future supply risk are not taken into account. All values are given as tonnes per installed technology capacity [t/MW].

11. Water pollution; the impact of a technology on the surrounding water is based on the ecotoxity of both freshwater and marine environments discussed by Abousahl *et al.* [36]. The values are given as kilograms 1,4-dichlorobenzene-equivalent per MWh [kg DCB-eq/MWh]. This topic is not covered for storage technologies due to limited information.

12. Biodiversity reduction; Similar to water pollution, losses in flora and fauna are based on the report published by Abousahl *et al.* [36]. The values are expressed in potentially disappeared fraction of species on a square meter earth surface during one year per MWh [PDFm^2a/MWh]. This topic is not covered for storage technologies due to limited information.

13. Spatial nuisance; When a technology is used in an urban setting, it can cause a spatial nuisance in the built environment. This nuisance is a subjective indicator based on the required land area, the size of the technology, and its ability to be integrated into the landscape.

14. Employment; All the discussed technologies have a positive effect on employment in the region. This employment is a combination of construction and operational jobs. The given values are based on Czako [101], and are expressed as yearly full-time (fte) per MW installed technology [fte/MW·y].

15. Innovation potential; Similar to employment the innovation capacity can be derived from Czako [101]. This value is based on the number of manufacturing jobs associated with the technology and is expressed in yearly full-time equivalent (fte) per MW installed technology [fte/MW·y].

16. Human health risk; At last a human health indication is made to compare the technologies on their direct and indirect effects on human health. These values are extracted from the Abousahl *et al.* [36] report. The element is measured in disability adjusted life years per MWh [μDALY/MWh].

4.2.3 Weather data

The importance of weather-related fluctuations in energy consumption and generation in our current energy system cannot be oversimplified. Temperature, wind speed, and solar irradiation all have a direct impact on the system, both locally and nationally. As a result, precise spatial data is required. Furthermore, because weather is a constantly changing phenomenon, the time interval of the data is critical. Ergo, a short time interval is preferred under the conditions of qualitatively weather data.

A 60 minute interval was chosen for this experimental study due to the quality, spatial precision, and historical characteristics of the weather data provided by the hourly *ERA5* database. A 30km grid and a large collection of different climate variables distinguish ERA5 from other open-source databases. This data is available for different atmospheric levels above land and ocean. Local climate change trends can be assumed because the data set spans 1979 to the present [102].

Variables extracted from the database are; 10m wind speed (u-and v-component), 100m wind speed (u-and v-component), mean sea pressure, sea surface temperature, 2m temperature, 2m dew point temperature, surface pressure, surface solar radiation downwards, and surface thermal radiation downwards. All of these parameters are used to calculate various important renewable energy-production and consumption variables.

Solar energy Calculating the near real-time electricity generation of PV-panels requires the *surface solar radiation downwards* variable, G [J/m^2]. This value represents the sum of both direct and diffuse solar radiation that reaches the earth's surface. Because solar radiation values constantly change the ERA5 model presents the accumulated amount of solar radiation ($J/m^2 = Wh/m^2$). To allow for solar power calculations this value needs to be divided by 3,600 to convert from accumulated energy to wattage.

Next, PV-panel model constants are required. These are the solar panel efficiency, η_{eff}; external environment losses, η_{loss}; mean PV-cell performance degradation losses, η_{degr}; module temperature losses, η_{temp}; and the total PV-cell area, A_{PV} [m^2]. With all these values the electric output of the combined panels can be calculated, P_{PV} [Wh], see equation 4.2. The electricity output is capped at the maximum capacity of the panel model.

$$P_{PV}(t) = G(t) \cdot \eta_{eff} \cdot (1 - \eta_{loss}) \cdot (1 - \eta_{degr}) \cdot (1 - \eta_{temp}) \cdot A_{PV}/3600 \tag{4.2}$$

The majority of the above-mentioned constants are related to the model specifications. External environmental losses, on the other hand, are treated as a fixed constant because they vary by location, panel position and external factors such as dirt. This value is calculated with the use of the reference

point simulation discussed earlier. The PVGIS tool from JRC predicts this value to be around $\eta_{loss} = 15.8\%$ for the MRDH region [86].

The performance degradation losses are calculated with the given technical data. This trend is assumed to be linear and follow the values given in appendix table C.4. At last the performance loss as a function of module temperature is calculated following the mathematical Faiman methodology. The module efficiency loss due to temperature increases (β [%/°C]) is given as a constant in the technical specifications of every model, therefore only the estimated module temperature needs to be calculated. The Faiman method describes a fairly accurate mathematical estimate that takes three variables and one constant into account, namely; ambient temperature T_a [°C], wind velocity at surface v [m/s], downwards surface solar radiation G [J/m^2], and the module transmittance value $\tau\alpha$ [W/m^{2}K]. When the module is above the *nominal module operating temperature* of 25°C performance will decrease gradually. The Faiman correlation for the module temperature, T_m, is reprinted from [103] and given in equation 4.3 and 4.4.

$$T_m(T_a, G, v) = T_a + \frac{\tau\alpha \cdot G}{30.02 + 6.28 \cdot v} \tag{4.3}$$

$$\eta_{temp}(T_m) = \begin{cases} (T_m - 25) \cdot \beta & \text{, if } T_m > 25°\text{C} \\ 1 & \text{, if } T_m \leq 25°\text{C} \end{cases} \tag{4.4}$$

As mentioned before, the electricity consumption of the agricultural sector is primarily driven by the usage of grow lights in greenhouses. For that reason, the electricity consumption can be seen as a function of downwards solar irradiation, G. In general lamps in these greenhouses are automatically activated when solar irradiation is below a certain limit. Following the report on greenhouse lighting by Hemming *et al.* [104] the lights are activated when the photon count per square meter second is below 92 $\mu mol/m^2 s$, or 29.98 W/m^2 of downwards solar radiation when taking the average greenhouse glass transmission (90%) into account.

The hourly electricity consumption, P_{Agri} [MW], for the agricultural sector can now be calculated following equation 4.5. In the equation $\sum t_y$ [hours] describes the total amount of hours in a given year and $\sum P_{agri}(y)$ [MWh] the total amount of electricity consumption of the sector in that year.

$$P_{Agri}(t, y) = \begin{cases} \dfrac{\sum t_y(y)}{\sum P_{agri}(y)} & \text{, if G} < 29.98 \text{ W/m}^2 \\ 0 & \text{, if G} \geq 29.98 \text{ W/m}^2 \end{cases} \tag{4.5}$$

Wind energy Calculating the mean hourly electricity output of wind turbines, P_{wind} [MWh], requires a bunch of additional calculations. As seen in the electricity generation equation 4.6, four variables are required; air density at wind turbine hub height (≈100m), ρ_{air}; normalised wind speed, $v_{norm,wind}$ [m/s]; wind turbine blade radius, r_{blade} [m] [kg/m^3]; and the turbine conversion efficiency, η_{eff} [%] [105]. The power output of the turbine is limited by the maximum capacity given per model.

$$P_{wind}(t) = v_{norm,wind}(t)^3 \cdot \frac{\pi \cdot r_{blade}^2}{2} \cdot \rho_{air} \cdot \eta_{eff}\ 10^6 \tag{4.6}$$

The last two variables, efficiency and radius, are both related to wind turbines. The rotor blade radius is well documented for various turbine models. This data has been taken from Lucas Bauer [106]. Regrettably, information on model efficiency is scarce. As a result, the reference point simulation is required to estimate the conversion efficiency factor for both land- and sea-turbine models. Wind turbines have a maximum efficiency of around 59 percent, which is known as the *Betz limit* [107].

The normalised wind speed is a combination of the real wind speed at a height of 100 meters above sea level and turbine model-specific wind speed parameters. Equation 4.7 is used to calculate the real wind speed from the u- and v-components. The cut-in and cut-out speeds, which are model-specific values, are then considered. The operational wind speed range of the turbines is represented by these values, which were also retrieved from the wind turbine data base [106]. The turbine will not produce electricity if the wind speed is below the cut-in speed, and if the wind speed is above the cut-out speed, the winds are too strong, forcing the turbine to stop. As a result, no electricity is generated.

$$v_{wind} = \sqrt{(u_{wind})^2 + (v_{wind})^2} \tag{4.7}$$

At last the air density at the wind turbine hub altitude needs to be calculated from the given weather variables. For this calculation a bunch of parameters are needed, namely: dew point temperature at 100m, $T_{dew,100m}$ [°C]; 100m altitude temperature, T_{100m} [°C]; and the 100m altitude pressure, P_{100m} [Pa]. The pressure is directly retrieved from the ERA5 database.

Surface temperatures from the ERA5 database are used to calculate both temperatures at the given altitude. In the troposphere (altitudes up to 11km) both the dew point- and environmental temperature decrease as a function of height and the lapse rate constant. The lapse rate, Γ [°C/m], is for both temperatures different due to different atmospheric parameters. Following the atmospheric standards the lapse rates are; $\Gamma_{dew} = -0.002$ and $\Gamma_{env} = -0.00649$ [108]. Equation 4.8 describes the relation between altitude, h [m], and temperature [°C] [105].

$$T_{altitude}(h) = T_{2m} - \Gamma \cdot (h - 2) \tag{4.8}$$

The partial vapour pressure, P_v [Pa], and the vapour saturation pressure, E_s or P_s [Pa], are calculated next. Both of these values can be calculated using the temperatures listed above, following the Herman Wobus' polynomial approximation. The Herman Wobus vapour pressure approximation is shown in equation 4.9, Vej [105, p.3-2] is the source of the equation. The partial vapour pressure is calculated using the dew point temperature as an input. The vapour saturation pressure is calculated using the ambient temperature. Dividing the partial vapour pressure by the vapour saturation pressure gives us the relative humidity, RH [%].

$$P(T) = \frac{e_{s0}}{p(T)^8} \cdot 100 \tag{4.9}$$
$$p(T) = c_0 + T(c_1 + T(c_2 + T(c_3 + T(c_4 + T(c_4 + T(c_5 + T(c_6 + T(c_7 + T(c_8 + T \cdot c_9)))))))))$$
$$e_{s0} = 6.1078$$

$$c_0 = 0.99999683 \cdot 10^{0} \qquad c_1 = -0.90826951 \cdot 10^{-2} \qquad c_2 = 0.78736169 \cdot 10^{-4}$$
$$c_3 = -0.61117958 \cdot 10^{-6} \qquad c_4 = 0.43884187 \cdot 10^{-8} \qquad c_5 = -0.29883885 \cdot 10^{-10}$$
$$c_6 = 0.21874425 \cdot 10^{-12} \qquad c_7 = -0.17892321 \cdot 10^{-14} \qquad c_8 = 0.11112018 \cdot 10^{-16}$$
$$c_9 = -0.30994571 \cdot 10^{-19}$$

At last the air density, ρ_{air} [kg/m^3], can be calculated by following equation 4.10. The equation uses the following variables and constants: atmospheric pressure at 100m, P_{100m} [Pa]; partial vapour pressure, P_v [Pa]; ambient temperature at 100m, T_{100m} [K]; specific gas constant for dry air, $R_d = 287.05$ [J/(kgK); and specific gas constant for water vapour, $R_v = 461.495$ [J/(kgK)].

$$\rho_{air} = \frac{P_d(T_{100m})}{R_d \cdot T_{100m}} + \frac{P_v(T_{100m})}{R_v \cdot T_{100m}} = \frac{P_{100m} - P_v(T_{100m})}{R_d \cdot T_{100m}} + \frac{P_v(T_{100m})}{R_v \cdot T_{100m}} \tag{4.10}$$

Heat consumption The effective temperature is used to calculate the hourly heat consumption, as shown in equation 4.1. The ambient surface temperature is converted to degrees Celsius, and the wind speed is calculated in the same way as in equation 4.7. After calculating the effective temperature hourly, a heating factor can be calculated to estimate variable heat consumption.

The data is first used to determine the minimum effective temperature value. This value can be used to create a temperature range between the minimum and the effective temperature heating threshold ($T_{eff}^{threshold} = 14$). This range is normalised to a 0 to 1 scale, O [-], with effective temperature values nearing 1 and vice versa. After that, all of these values are added together. The hourly heat consumption per sector can be calculated using equation 4.11, $q_i^{var,sector}$ [MW]. A value at a specific time interval is represented by the symbol i. The variable $q_{var,sector}$ represents a sector's variable heat consumption.

$$q_i^{var,sector}(t) = \frac{O_i(t)}{\sum_{n=1}^{len(i)} O_i(t)} \cdot q_{var,sector} \tag{4.11}$$

4.2.4 Scenario projections

To investigate the long-term implications of a given energy mix strategy, two 'milestone' years are set: 2035 and 2050. The year 2035 was chosen because of the thesis's focus on nuclear energy. As described in sections 2.7.2 and 2.6, the first new nuclear reactors could be operational in 2035. Meaning, by that time, all of the discussed energy production technologies could be built and operational. The year 2050 was chosen because it is regarded as the deadline for energy transition in both the Paris Agreement and the Klimaatakkoord. By this year, the energy transition will be nearly complete, and the Dutch energy system must meet EU regulations on GHG-emissions, as described in section 2.2.

Conditions for the simulation can be set based on various estimates and projections of the Netherlands' future energy consumption. Predicted trends and assumptions discussed in chapters 2 and 3 have resulted in these conditions. For that reason, it's important to remember that the future consumption scenarios described are estimates that could differ significantly depending on the energy transition strategy chosen by society, government and industry. Table 4.6 summarizes these projections.

	2019 [PJ]	**2035** [PJ]	**2050a** [PJ]	**2050b** [PJ]
Industry				
heat	139.2	140.9	105.8	24.3
electricity	17.2	22.0	50.3	131.3
Built Environment				
heat	80.4	69.7	72.0	-
electricity	28.6	36.2	50.3	-
Agriculture				
heat	54.5	36.5	36.5	-
electricity	6.1	6.9	6.9	-

Table 4.6 Energy demand projections per sector of interest, corresponding with the projected and assumed trends between 2020 and 2050. Sector energy consumption values are retrieved from table 4.1. 2050 is split in two projections, a and b. These are related to a intermediate- (a) and high (b) industrial electrification scenario.

Scenario implementation behaviour: *trendlines*

Multiple simplifications are used in the following paragraphs to describe projected trends. The projected estimates in each of the discussed categories are reduced to an equation that fits these trends. These equations have been fine-tuned to a day-to-day refinement. The electrification and energy efficiency trends in the discussed sectors are more difficult to predict due to their reliance on transitional drive. As a result, more assumptions based on proposed strategies will be made.

Due to the many differences in trend development, 5 different growth relations are used. These relations are shortly described by the characteristics [109]. Variables used in these equations are; time t in days; unit conversion factor γ; starting point y_0; 2050 end point y_m; lag time k; horizontal translation a; growth rate r. Note that some functions use a more complicated variable for time, as shown in equation 4.17. This factor is used to elongate the function to its usable length. All of

the time function equations discussed in the following paragraph begin on January 1, 2020 ($t = 0$). Electrification, energy efficiency, and heat production and distribution efficiency are discussed through these trends. At last an integration success rate coefficient is added, C_f. When this coefficient is equal to 1 (standard), the trends progress at projected rate, however, when the value is increased these trends behave in a delayed manner.

- *Quadratic growth (eq. 4.12)*: constant growth rate, increasing/decreasing over time.
- *Sigmoidal growth (eq. 4.15)*: exponential growth rate with flattening towards final plateau.
- *Developed Sigmoidal growth (eq. 4.16)*: translated Sigmoidal curve starting at highest rate.
- *Logistic growth (eq. 4.13)*: translated Sigmoidal curve, faster rate development
- *Gompertz growth (eq. 4.14)*: similar to Logistic curve, however at low y it develops fast and at high y it develops more slowly.

$$y_{quadratic}(t) = (1+r)^t \cdot \gamma \tag{4.12}$$

$$y_{logistic}(t) = \frac{y_m \cdot y_0}{(y_m - y_0) \cdot \exp[-k \cdot x] + y_0} \cdot \gamma \tag{4.13}$$

$$y_{Gompertz}(t) = y_m \cdot \left(\frac{y_0}{y_m}\right)^{(\exp[-k \cdot x])} \cdot \gamma \tag{4.14}$$

$$y_{Sigmoid}(t) = \frac{y_m}{1 + \exp[a - k \cdot x]} \cdot \gamma \tag{4.15}$$

$$y_{Sigmoid,developed}(t) = \left(\frac{2 \cdot y_m}{1 + \exp[a - k \cdot x]} - y_m\right) \cdot \gamma \tag{4.16}$$

$$x(t) = \frac{30t}{10958 \cdot C_f} \tag{4.17}$$

To correctly predict the described trends the trendlines will be computed following the given input; trendline, starting value (y_0), 2050 maximum value (y_m), time span in years (t_s), and a deviation margin (σ). With this information the lag time, k, can correctly be estimated, due to the behaviour of the curves a post-2050 limit, y_{max} is calculated. For logistic trends the values are calculated following equation 4.18 and 4.19, while the Gompertz values are derived from 4.20 and 4.21.

$$k = \frac{\log\left(\frac{\sigma \cdot y_0}{(1-\sigma)\cdot y_m - (1-\sigma)\cdot y_0}\right)}{t_s} \tag{4.18}$$

$$y_{max} = \frac{y_m \cdot y_0 \exp\left[-t_s \cdot k\right] - y_m \cdot y_0}{y_m \exp\left[-t_s \cdot k\right] - y_0} \tag{4.19}$$

$$k = \frac{\log\left(\frac{1-\sigma}{\left(\frac{y_0}{y_m}\right)}\right)}{t_s} \tag{4.20}$$

$$y_{max} = \left(\frac{y_m}{y_0 \cdot \exp\left[-t_s \cdot k\right]}\right)^{\left[\frac{1}{1-\exp\left[-t_s \cdot k\right]}\right]} \tag{4.21}$$

Consumption projections

Population trends Population plays a significant role in energy consumption. On a MRDH-scale population changes relate directly to energy consumption for both the built environment and industry. The increase in built environment is explained by the growing amount of houses, shops and offices, while for industry the workforce capacity is likely to increase. Because these increases are not included in the other discussed trends this increase is added to the energy consumption in the region. Projections made by CBS [110] estimate the population increase per every 5 years up to 2050. These numbers are used to create a logarithmic trendline that can forecast monthly population growth. The trendline begins in 2020 and continues until 2050, following the CBS trend. The trend becomes less certain after 2050. Nonetheless, due to the logarithmic trend visible in the CBS data, the trendline is seen as viable even after 2050. Equation 4.22 describes the logarithmic population growth factor of the region in the coming years. Symbols in the equation stand for; population growth factor at time d, C_P [-] and number of days after 2020, t [days]. In the equation the increased population is divided by the 2019 population that equals 2365.8 thousand people [111]. Because of the COVID-19 pandemic's energy reduction in 2020 and 2021, energy consumption data from 2019 is used. Therefore, 2019 is set as the baseline.

$$C_{pop.}(t) = \frac{165.74 \cdot ln\left(\frac{6t}{10958} + 1\right) + 2391.5}{2365.8} \tag{4.22}$$

As shown in equation 4.23, the population growth factor is used to describe the change in total energy consumption for both industry and the built environment, resulting in new energy consumption.

$$E_t = E_{2020} \cdot C_{pop.}(t) \tag{4.23}$$

Industry Because of innovations and system optimisation, the industrial sector's energy consumption (both heat and electricity) is expected to decrease. As discussed in sector 3.1.2, the sector is expected to reduce its total energy consumption by improving its energy efficiency by 0.5% annually after 2020 ($r = -0.005$). This trend is described by a quadratic growth equation 4.12. With the given values this results in equation 4.24, where $C_{eff}^{Industry}$ [%] stands for the industry energy demand coefficient.

$$C_{eff}^{Industry}(t) = \left(1 - \frac{0.005}{365.25}\right)^{x} \tag{4.24}$$

Additionally, significant electrification of the industrial sector is expected after 2030, as described in section 3.1.2. The industry is classified into three groups, namely low-, intermediate- and high-temperature processes. Due to efficiency constraints, low-heat processes are more likely to electrify, whereas high-temperature processes will continue to rely on high-calorific fuels. Unfortunately, because there is no industrial process data in an open-source database, assumptions must be made. As a result, non-heavy industry in the area is classified as low-temperature, refinery industry is classified as intermediate-temperature, and chemical industry is classified as high-temperature. Additionally, it is assumed that heavy industry generates their own energy on-site. This assumption allows for qualification of the share between the different industry categories. Data on the on-site industrial heat generation was retrieved from Netherlands Enterprise Agency (RVO) [85] and listed below:

- Low temperature industry (< 300): 23%
- Intermediate temperature industry ($300 \leq T < 600$): 60%
- High temperature industry (≥ 600): 17%

Due to the uncertainty of the industrial energy transition two scenarios are set at 2050. Situation 2050a describes full electrification of the low temperature industry only, while 2050b describes electrification of both low-and intermediate temperature industries. The electrification coefficient, $C_{el}^{industry}$ [%], is the share of industrial heat demand that electrifies. The electrification trend is described by a Sigmoid function because many historical transitions follow this trendline [112]. Equation 4.15 describes the predicted trend on a day-to-day basis. Variable values are; $k = 0.5$, $y_m = 0.23$ or $y_m = 0.83$ (depending on scenario a or b), and $a = 10.5$. No unit conversion is required, therefore $\gamma = 1$.

$$C_{el}^{Industry}(t) = \frac{y_m}{1 + \exp[10.5 - 0.5 \cdot t]} \tag{4.25}$$

As shown in equation 4.26, the electrification coefficient, combined with the population growth factor (eq. 4.22) and industrial energy efficiency (eq. 4.24), are used to calculate the industry electricity demand coefficient $C_P^{Industry}$ [%]. This value represents the consumption change relative to days after 2020. Δ is the energy share difference between heat and electricity for the industry sector. Following table 4.1 Δ equals the share of heat divided by the share of electricity, $\Delta = \frac{121.96}{17.23}$.

$$C_P^{Industry}(t) = \left(1 + \Delta \cdot C_{el}^{Industry}(t)\right) \cdot C_{eff}^{Industry}(t) \cdot C_{pop.}(t) \tag{4.26}$$

The same steps are followed to obtain the heat demand coefficient for the industry, $C_q^{Industry}$ [%]. This relation is described in equation 4.27.

$$C_q^{Industry}(t) = \left(1 - C_{el}^{Industry}(t)\right) \cdot C_{eff}^{Industry}(t) \cdot C_{pop.}(t) \tag{4.27}$$

Built environment Similarly to the industrial sector, energy efficiency (only heat) increases are to be expected for the built environment in the coming decade. Renovations in the areas of insulation, more energy-efficient installations, and electrification have resulted in these increases. As discussed in section 3.1.1, the heat demand of the sector is expected to decrease by 20% relative to 1990. the sector's heat demand is expected to decrease by 20% compared to 1990. Because heat consumption increased by 2.5 percent from 1990 to 2020, a relative reduction of 22 percent is expected between 2020 and 2030 International Energy Agency [29].

Demand reductions are assumed to stabilize after 2030 due to the many uncertainties. A Sigmoid-like trendline is expected, just as it was with industrial electrification. This trend, on the other hand, began around 1990, indicating that the trend's slope is already well developed in 2020. For that reason the developed Sigmoid-curve is chosen (eq. 4.16). The discussed projections result in trendline equation 4.28. $C_{q,eff}$ [%] symbolises the heat efficiency coefficient. Variable values are; $k = 0.5$, $y_m = 0.22$, and $a = 0$.

$$C_{q,eff}^{BuiltEnv.}(t) = 1 - \left(\frac{2 \cdot 0.22}{1 + \exp\left[-0.5 \cdot t\right]} - 0.22\right) \tag{4.28}$$

As shown in equation 4.29, the energy efficiency coefficient can be used to calculate the heat demand coefficient, $C_q^{BuiltEnv.}$ [%], for the built environment.

$$C_q^{BuiltEnv.}(t) = C_{q,eff}^{BuiltEnv.}(t) \cdot C_{pop.}(t) \tag{4.29}$$

The built environment is also expected to be further electrified for a variety of reasons. The demand for electricity is expected to rise as a result of both digitalisation and the electrification of heating systems. The electrification trend in the built environment has already begun and is expected to continue even after 2050. However, projections for the period after 2050 are too speculative. As a result, no additional electrification is assumed after 2050 in this thesis. As discussed in section 3.1.1, an annual increase of 1% in electricity consumption is expected. Therefore, an quadratic growth curve can be used (eq. 4.12). The growth rate is divided by the corrected (leap years) days a year.

The electrification trend, $C_{el}^{BuiltEnv.}$ [%], is described by equation 4.30.

$$C_{el}^{BuiltEnv.}(t) = \begin{cases} \left(1+\frac{0.01}{365.25}\right)^{t} & \text{, if } 0 < t \leq 10958 \\ \left(1+\frac{0.01}{365.25}\right)^{10958} & \text{, if t > 10958} \end{cases} \tag{4.30}$$

As shown in equation 4.31, the electrification coefficient, combined with the population growth factor, can be used to calculate the built environment electricity demand coefficient $C_P^{BuiltEnv.}$ [%]. This value represents the consumption change relative to days after 2020.

$$C_P^{BuiltEnv.}(t) = C_{el}^{BuiltEnv.}(t) \cdot C_{pop.}(t) \tag{4.31}$$

Agriculture No electrification is assumed due to a lack of literature on the projected electrification of the agricultural sector. These assumptions are supported by the fact that the greenhouse sector, in particular, is already highly digitalised. Furthermore, no increase in energy demand is expected because there is little to no room for expansion in the MRDH region.

Despite the above, significant reductions in heat demand are expected as a result of considerable insulation efforts. s mentioned in section 3.1.1, demand is expected to fall by 30% compared to 1990. hen you add in the 5% increase in heat consumption between 1990 and 2020, you get a reduction of 33% between 2020 and 2030 International Energy Agency [29] ue to the many uncertainties, the decrease is expected to stabilize after 2030, similar to the built environment.

Just as with the electrification and energy efficiency efforts the trend is assumed to follow a Sigmoid curve. Analysing the greenhouse's fuel for heat consumption in the past decades, the primary kind of agriculture in the region, confirmed this assumption [113]. The trend started in 2020 with significant improvements the first decade, before flattening out. Therefore, a developed Sigmoid-trend is chosen (eq. 4.16). The discussed conditions resulted in the heat efficiency coefficient $C_{q,eff}^{Agri}$ [%] equation 4.32. Variable values used are; $k = 0.5$, $y_m = 0.33$ and $a = 0$.

$$C_{q,eff}^{Agri}(t) = 1 - \left(\frac{2 \cdot 0.33}{1+\exp\left[-0.5 \cdot t\right]} - 0.33\right) \tag{4.32}$$

As shown in equation 4.33, the energy efficiency coefficient can be used to calculate the heat demand coefficient, C_q^{Agri}.

$$C_q^{Agri}(t) = C_{q,eff}(t) \tag{4.33}$$

Heat network and local heat production projections

The RES [35] describes an ambitious heat network with many renewable heat sources. These sources include waste heat from nearby industry, geothermal heat extraction, local geothermal heat storage, (air source) heat pumps and solar heating. The projections of this renewable heat system are summarised

in table 4.7. The heat network only covers the low temperature demanding sectors, namely agriculture and the built environment.

Currently the heat network of the MRDH region is limited to some neighbourhoods in the Rotterdam and the Hague periphery. This network is supplied with, primarily, heat from Combined Heat and Power (CHP), waste/biomass incineration (AVI) and centralised heating plants [80]. These energy stations are mainly fueled by natural gas and biomass/waste. Combined all different sources in the network provide 9.4 PJ of heat yearly (total production, 7.1 PJ delivered) [114]. Therefore roughly 39% of the heat comes from sustainable sources in 2020.

Table 4.7 Heat generation in the MRDH region between 2020 and 2050. **Heat loss due to transport and distribution, 4% and 30% respectively in 2020.* Projections are retrieved from Stuurgroep Energiestrategie regio Rotterdam Den Haag [35] and Segers *et al.* [114].

	Total [PJ]	**Geothermal** [PJ]	**Industrial waste** [PJ]	**Natural gas** [PJ]	**AVI** [PJ]	**Electric** [PJ]	**Heat loss*** [%]
2020	9.4	3.0	0.7	2.8	2.7	0.2	34
2030	25.8	8.0	17.8	-	-	-	29
2050	49.6	18.6	31.0	0	0	-	24

In the coming decades, up to 2050, the RES ambitions are to provide 32.8 PJ of heat by a connected heat grid. Additionally, 18.9 PJ will be provided in small grids by local heat sources. These sources do not lose as much heat during transport and are therefore more efficient. The projection for local heat sources is described in table 4.8.

Table 4.8 Local renewable heat generation projections in the MRDH region between 2020 and 2050. Local heating sources include (air source) heat pumps and solar heating. Energy generation data is retrieved from Stuurgroep Energiestrategie regio Rotterdam Den Haag [35].

	2020	**2030**	**2050**
Local heating [PJ]	2.5	5.6	18.9
Distribution losses [%]	30	26	22

All these projections can be formed into trendlines that estimate the heat grid capacity (total), generation per source and heat loss factor per day after 2020 ($t = 0$). Due to simplifications these trendlines deviate slightly from the above mentioned values. To match units in the following calculation steps a conversion factor is used, converting petajoule to GWh per day (see equation 4.34).

$$\gamma_1 = \frac{10^9}{365.25 \cdot 3600} \tag{4.34}$$

Both heat grid capacity and geothermal heat generation were found to best fit the logistic growth curve. The other trends; distribution losses, natural gas-, AVI- and waste heat, all fit the Gompertz curve best. The variables and quantities are summarised in table 4.9. The lag time, post-2050 limit and

calculated following the method described earlier. A time span of 30 years was used. For both natural gas and AVI a lag time value of 0.05 was used[3]. The electric heat, Q_{el}, is left blank intentionally as this heat source will absorb capacity shortages, as shown in equation 4.35.

Variable	HG capacity Q_{HG}	Geothermal Q_{Geo}	Industrial waste Q_{Ind}	Natural gas Q_{Gas}	AVI Q_{AVI}	Heat loss $\bar{\eta}$
σ [%]	5	5	1	-	-	1
y_0 [PJ]	9.4	3.0	0.7	2.8	2.7	34
y_m [PJ]	49.6	18.6	31.0	0	0	24

Table 4.9 Heat grid projection trend variables for 2020 and after. Variables are used in equations 4.13 and 4.14.

$$Q_{el}(t) = Q_{HG}(t) - \sum (Q_{Geo}(t) + Q_{Ind}(t) + Q_{Gas}(t) + Q_{AVI}(t)) \tag{4.35}$$

Unfortunately, the local renewable heat production, Q_{local}, does not fit in any of the discussed growth trends. For this reason, a polynomial trendline is chosen. This trendline is based on the three values given in table 4.8. This resulted in equation 4.36.

$$Q_{local}(t) = (0.01183333 \cdot t^2 + 0.19166667 \cdot t + y_0) \cdot \gamma_1 \tag{4.36}$$

The trendlines of both the heat grid and the local heating projections are seen as constant for all scenarios to simplify the simulation. Nevertheless, a heat grid implementation factor can be used to reduce the maximum capacity the proposed heat grid.

Storage projections

With the increased use of renewable, and thus fluctuating, energy sources, the demand for energy mix smoothing support systems grows. Storage technologies enable the short- and long-term storage of energy, allowing extreme peaks in both consumption and generation to be reduced, resulting in a more efficient energy system. In the energy simulation described here, two systems are used: batteries and hydrogen electrolysers.

Batteries Industrial-scale lithium-ion batteries are used as a short-term power storage technology in this computational model. Because battery models vary greatly, the technical specifications of a popular model, namely the Samsung UL9540A lithium-ion cell platforms, were used in the calculations below. This model has a C-rate of $c = 0.5$, which means it can charge and discharge half of its total storage capacity in an hour. It is assumed that the average battery state of health is 90%, $\eta_{SoH} = 0.9$ [115]. A standard round-trip efficiency of $\eta_{rt} = 0.95$ is assumed, resulting in the

[3] Due to their reduction towards 0 a 2050 value of 0.001 was used.

maximum short-term storage output power, $P^{max}_{sts,in}$ [MW], see equation 4.37. P_{cap} represents the total hourly capacity of the battery system.

$$P^{max}_{sts,in}(t) = c \cdot P_{cap} \cdot \eta_{SoH} \cdot \eta_{rt} \tag{4.37}$$

The battery capacity is determined by the scenario's hourly battery coverage. The scenarios described in this thesis cover the weekly averaged daily electricity fluctuations. This average is calculated by subtracting the total daily power surplus from the shortage. A construction threshold of 122 days is set to ensure battery usage efficiency. Construction of new battery parks is thus permitted only if the average storage capacity potential has increased significantly over the previous one-third of a year.

Hydrogen electrolysers Storing synthetically produced fuels are viewed as a viable option for long-term energy storage, with hydrogen being viewed as the most interesting option in the Netherlands following the strategies described in chapters 2 and 3.

Currently, there are three types of hydrogen production methods from electricity, namely: polymer electrolyte membrane- (PEM), alkaline-, and solid oxide cell (SOEC) electrolysers. All of these electrolysers are able to produce hydrogen for long-term storage from electricity, albeit with different efficiencies. The PEM electrolyser is also able to be used as short-term electricity storage, due to its fast variable 'charge/discharge' rate when used as a fuel cell. The produced hydrogen can be used in an industrial boiler to produce heat, standard efficiency boiler $\eta_b = 0.9$, or be used in a power station, standard fuel-to-power efficiency $\eta_{FtP} = 0.65$.

To calculate the round-trip efficiency of these electrolysers the standard low heating value of a normal cubic meter of hydrogen gas was used, $LHV = 3.00$ [kWh/Nm^3]. The results are given in table 4.10.

Table 4.10 The average round-trip electrolyser performance for the discussed electrolyser technologies. **Data on SOEC retrieved from Ghezel-Ayagh [116].*

Electrolyser	**Power consumption [117]** [kWh/Nm^3]	**R-T efficiency heat** [%]	**R-T efficiency electricity** [%]
Alkaline	4.1	47.6	65.9
PEM	4.5	43.3	60.0
SOEC	3.6*	54.2	75.0

Because of regional constraints, hydrogen will be used as a fuel in thermal applications such as the high temperature industry. This ensures that the high calorific gas is used efficiently. Alkaline electrolysers will be used in all scenarios because they are already widely proposed in the regional industrial cluster. The installation of these hydrogen production facilities will follow a Gompertz growth curve as the construction of the first facilities have already been started in the past couple of years. The total capacity at 2050 is set as a scenario parameter.

Generation projections

Renewable electricity production In the coming decades a steady increase of renewables is expected in the region. For that reason this growth of renewables is described by one of the growth curves mentioned above. All simulated scenarios are expected to follow these curves. PV-panel and onshore wind turbine capacity growth will be described by a Gompertz curve, as this group is already well established and is expected to grow at a high rate the coming years. Offshore wind, on the other hand, is expected to follow a logistics curve as the growth peak for that group is expected in the coming decade.

Renewables are expected to grow steadily in the region over the next few decades. As a result, the growth of renewables is described by one of the previously mentioned growth curves. These curves are expected to be followed by all simulated scenarios. As PV-panels and onshore wind turbines are already well established and expected to grow rapidly in the coming years, the capacity growth will be described by a Gompertz curve. Offshore wind, on the other hand, is expected to witness the fastest growth in the coming decade, hence following a logistics curve.

Naturally, these renewables need to be replaced every 25 years, as discussed in section 2.5. Because a fair share of PV-panels and wind turbines already have been built these technologies need to be replaced in the coming decades. Installed capacity data from the Ministry of Infrastructure and Water Management [77] was used to calculate the yearly installed capacity. After 25 years this capacity requires replacement.

Non-renewable energy production The region is home to a wide range of different combustion plants. These plants generate both heat and power and use a variety of fuels, including coal and biomass, natural gas, hydrogen, and even chemical byproducts of the regional oil industry. As previously stated, the average lifetime of combustion plants is around 30 years; however, due to the high proportion of industrial boilers, the lifetime of pre-2000 has been extended up to 2030 because too little information about the expected decommissioning dates of these facilities is known. Furthermore, according to the national Dutch energy strategy, all biomass and coal combustion plants are expected to close by the end of 2030. Similarly, after 2020 only the construction of new high-energy gas and nuclear plants is permitted. Additionally, when available, hydrogen gas will be the preferred fuel for the gas combustion facilities.

When combustion plants overproduce energy, their output is reduced to balance the demand. These savings are incorporated into all calculations. This plant capacity reduction is based on a scenario parameter and is ordered hierarchically. This parameter specifies whether cost savings or emission reductions are preferred. Unless otherwise specified, cost savings are preferred over emission reductions in general.

4.3 Dynamic variables

A dynamic input, or variables, are used to assess a range of uncertainties. This type of input enables the simulation of a set of scenarios under various predetermined conditions. Due to time constraints, this thesis will concentrate on two dynamic aspects: projected trendline progression and climate change projections.

Trendline progression As previously stated, a set of conditions is changing over the analysed time period of 2020-2050 and beyond. In an ideal world, all of these trends would behave as currently predicted; however, many uncertainties, such as willingness, economic crisis, or political wars, could have a significant impact on these trends. As a result, the coefficient for integration success rate, C_f, is added to the computational script. When the coefficient is set to one, the trend follows the expected pattern. When the coefficient is increased, however, the trend slows and transition efforts are postponed. Three different integration success rates, namely 1.0, 1.15, and 1.3, are used for a thorough investigation of scenario impact. These coefficients correspond to a 4.5 and 9-year delay, respectively, relative to the on-schedule rate.

Because the heat grid and new local heating technologies are treated separately, this success coefficient has no effect on their implementation. Despite the fact that these elements will face numerous challenges due to a lack of economic stimulants, societal determination, and land law issues, the integration rate, η_{int}, and capacity will be set at 1, implying that no delays will be considered. This decision is made to ensure qualitative rather than quantitative results.

Climate change projections

Multiple projections are used in the simulation due to the many future uncertainties caused by climate change. SSP1-1.9, SSP1-2.9, SSP2-4.5, SSP3-7.0, and SSP5-8.5 scenarios are included, ranging from the least to the most global warming in the coming decades. The projections are retrieved from the World Bank Group [118] and include relative monthly projected temperature and relative humidity changes. Both are important for the energy consumption and generation projections.

To generate climate change adapted weather years after 2021, a year at random between 2001 and 2021 is chosen for each successive year. This chosen year is compared to the relative base year used in the World Bank Group's climate projections, and the temperature and relative humidity are updated. The post-2021 years are chosen at random and according to a randomness seed. To provide extensive trend information, 5 different seeds are used to generate 5 different weather projection scenarios.

All of these projections are used in different energy mix calculations. When analysing the data, these random projections are combined with the climate scenarios to generate an uncertainty range, which includes a maximum, average, and minimum value based on all projections.

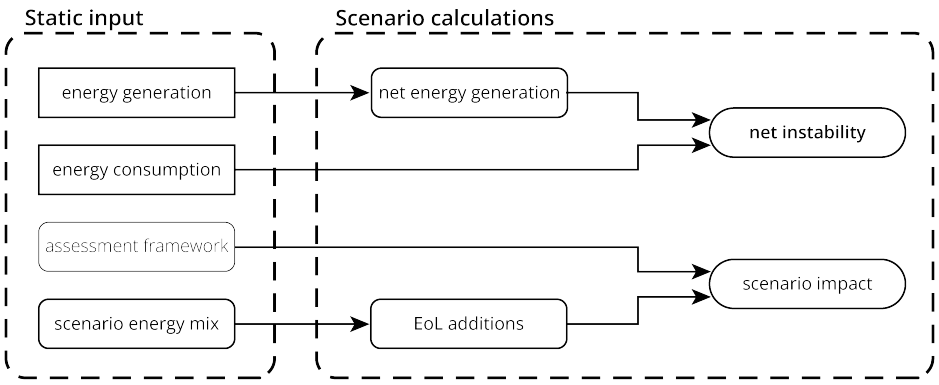

Fig. 4.3 Overview of the scenario calculation methodology of the script.

4.4 Scenario calculations

4.4.1 Net energy balance

The net stability can be calculated when the energy mix for a given time, t [days], is known. This stability is determined by the balance of energy production and consumption at any given time. Because power and heat have different dependencies, their net stability is described separately.

In order to accurately calculate the stability, storage facilities must be included. When the energy system overproduces power, the excess energy is stored in both short- and long-term storage technologies. In the simulation only the power surplus and its storage potential are calculated. The storage of surplus heat is expected to be occurring locally and is therefore already included in the local heating projections.

Short-term electricity storage, such as batteries, can provide electricity at a set rate instantly. As a result, the system's instability peaks are smoothed. Long-term storage, on the other hand, requires more time to store energy because (e.g.) hydrogen must be produced before becoming available for the net again. Due to the high cost of hydrogen production, and conversion efficiency challenges, in the region it is assumed that batteries provide electricity during a power shortage, while hydrogen is only used as a fuel for thermal applications such as high temperature industry. Equation 4.38 and 4.39 describe the power or heat imbalance per time interval, $P_{imbalance}$ $q_{imbalance}$ [MW]. Other variables are: net power or heat supply, $P_{net,in}$ or $q_{net,in}$ [MW]; short-term storage power supply, $P_{sts,in}$ [MW]; long-term storage power and heat supply, $P_{lts,in}$ or $q_{lts,in}$ [MW]; and the sum of the total electricity or heat consumption at that hourly interval, $P_{consumption}$ or $q_{consumption}$ [MW]. Note that the script automatically depletes the short-term storage before importing additional electricity. When the power imbalance is positive short-term storage is filled before hydrogen is produced. Hydrogen storage capacities are not limited in the simulation.

$$P_{imbalance}(t) = P_{net,in}(t) - \sum P_{consumption}(t) \tag{4.38a}$$
$$q_{imbalance}(t) = q_{net,in}(t) - \sum q_{consumption}(t) \tag{4.38b}$$

$$P_{imbalance}(t) + P_{sts,in}(t) + P_{import}(t) = 0 \tag{4.39a}$$
$$q_{imbalance}(t) + q_{lts,in}(t) = 0 \tag{4.39b}$$

Distribution losses

The strong reliance on renewable electricity production in the future energy mix results in an increased amount of distribution losses. These losses are a result of the conversion between direct current (DC) power (generated by solar panels) and alternating current (AC), the European standard. All other electricity power plants in the Netherlands directly generate AC power.Even though wind turbines generate alternating current (AC), a portion of the generated electricity is lost during distribution because offshore wind parks are located far from consumers. As a result, to reduce sea-cable distance losses, AC power from these parks is converted to DC current. Nonetheless, two conversions between the various current types are required. For these conversions an inverter is used, resulting in the electricity losses. In general, high quality inverters are used for power generation technologies. These inverters have an average efficiency of $\eta_{inverter} = 94.9\%$ [119].

Furthermore, the electricity net exhibit losses from AC cables and voltage converters. All the different types of AC transmission cables and converters have different losses, yet when summed the average electricity loss of the entire net is around 4% in the Netherlands [120]. For that reason, the total amount of produced electricity is multiplied by the net efficiency, $\eta_{net} = 96.0\%$, before being delivered to the electricity consumers.

At last, the losses due to long-distance DC transmission from offshore sea cables are included. These cables are known as HVDC-interconnection cables, or high voltage direct current cables, and have an average transmission loss of 4.3% per 1000km ($\vartheta_{HVDC} = 4.3 \cdot 10^{-5}$), or with an efficiency of $\eta_{HVDC}(d) = 1 - \vartheta_{HVDC} \cdot \sum d$ [121]. In which $\sum d$ equals the sum of all offshore cables in kilometers. Due to the distance between offshore wind park and coastal net connection these losses are seen as significant enough to be included. Data on the wind park size and locations, as well as sea cabling are retrieved from the Ministry of Infrastructure and Water Management [122; 123], see appendix C.5.

When all of these loss factors and production outputs are added together, the net power supply, $P_{net,in}$ [MW], can be calculated using equation 4.40. The power outputs of different electricity generation technologies are symbolised with $P_{technology}$. P_{plant} describes the power output for nuclear, biomass/gas, coal and natural gas.

$$P_{net,in}(t,d) = \left(\left(P_{offshore} \cdot \eta_{HVDC}(d) \cdot \eta_{inverter} + P_{PV}\right) \cdot \eta_{inverter} + P_{onshore} + \sum P_{plant}\right) \cdot \eta_{net} \quad (4.40)$$

4.4.2 Scenario impact

Assessment calculations

The energy mix composition, consumption, and production must all be considered when calculating the implications of a given scenario. When combined with the assessment framework described in section 4.2.2, the direct and indirect consequences for the period 2020-2050 can be calculated. These consequences are categorised as; End-of-Life implications, fuel dependency (focus on natural gas), material requirement increases, operational effects and technology construction implications.

Data on the construction date, decommissioning date, and operational capacity are stored in order to calculate these effects. Many assessment elements, such as operational effects, fuel dependency, and construction cost, can thus be found directly as a function of the given assessment database.

End-of-Life predictions and yearly installed capacity requirements

Every year, new wind turbines, PV-panels, and other energy-production technologies are added to the energy mix, and old ones are phased out. This results in both a demand and End-of-Life waste. For both pre- and post-2020 energy systems, the lifetime of all given technologies is taken into account in order to calculate these values. As a result, the amount of End-of-Life (EoL) products per year can be calculated, expressed as installed capacity P_{EoL} [MW]. Combined with the required installed capacity per year the added amount of installed capacity can be calculated per technology, following equation 4.41.

$$P_{added}(t_y) = \Delta P^{installed}_{technology}(t_y - t_{y-1}) + P_{EoL}(t_y) \quad (4.41)$$

Material requirement calculations

The material requirement of the transition strategy is more difficult to estimate as only little information is freely accessible. Nevertheless, a rough indication is made. Using the construction data and the material demand per technology, a rough estimate for all different raw materials can be made (including all major metals, minerals and pure elements).

To begin, Eurostat [124] data was obtained in order to model the relative raw material flow in the Netherlands. The data is divided into two categories: metallic and non-metallic materials. This data

shows the Netherlands' raw material consumption share in relation to the rest of the EU. To correct for the RES region the region's industrial production share was assumed to be 26 percent (based on the industry pollution share). Second, [96; 97] is used to obtain the total yearly material demand for all of the EU's major materials. This consumption data has been adjusted to reflect the RES region's share. Finally, the total material demand determined by the scenario construction data is added to the corrected RES material share data. Now the material dependency factor can be calculated by dividing it by the current known RES share (2019 data).

The material intensity factor is also used to approximate the criticality trends associated with the energy transition strategy. The intensity factor is multiplied by the data from the original critical raw material graph obtained from Joint Research Centre (JRC) [26]. As it is only a very rough indication, the newly formed graph is limited to a maximum economic importance and supply risk score of 10.0.

4.5 Scenario evaluation

To assess the different scenarios' sustainability performance, all calculated assessment data will be compared. The elements are graphed as a function of time in order to investigate potential trends and relationships between technology implementation and installed/operating capacity. The uncertainty range will be plotted whenever possible. The graphed elements are listed below. Note that the reference scenario results will be used to determine he various challenges and bottlenecks of the currently proposed transition strategy. The other described strategy simulations will be used to investigate the effect of nuclear energy integration.

1. Non-renewable plant timeline
2. Total installed power- (hourly) and simulated capacity (yearly)
3. Total installed heat- (hourly) and simulated capacity (yearly)
4. Assessment element projections as a function of time and operating capacity (yearly);
   (a) Biodiversity reduction
   (b) Direct emissions
   (c) Fuel demand
   (d) Fuel cost
   (e) O&M cost
   (f) Power import cost
   (g) Total indirect costs
   (h) Human health risk
   (i) Chemical waste
   (j) Radioactive waste
   (k) Water pollution
5. Renewable (support-)technology End-of-Life projections (yearly and accumulated)
6. Energy transition strategy implications as function of time and installed capacity

(a) Yearly direct cost
(b) Total spatial footprint
(c) Spatial nuisance
(d) Employment
(e) Innovation potential

7. Material requirement increase factor
8. Critical raw material projection trends
9. Fuel demand trend over time (natural gas)

4.5.1 Energy transition strategy totals

The assessment figures are calculated for all investigated scenarios under various dynamic conditions, resulting in a set of comparable matrices and graphs. These scenarios are then stored in a database. When a variety of scenarios are simulated, the resulting values can be converted into indicators. These indicators describe the total accumulated emissions, chemical waste, radioactive waste and total transition cost (2020-2050). To compare the different outcomes the reference scenario is used as a baseline and given a indication value of 3 for every discussed element. All calculated scenarios are not given a rating between 1 and 5 depending on their behaviour. The values are given in a radar/polar diagram to allow for rapid evaluation and comparison. Of the included elements total cost, emissions and spatial footprint are seen as the most important.

The final radar graph comparison is used to assess the advantages and risks of the various strategies and their associated technology focus. Consequently, substantiating the third research sub-objective.

4.6 Simulation scenario parameters

The computational simulation includes multiple input variables to allow for extensive and flexible energy transition scenario/strategy research. Because of the focus of this research, some of these parameters are fixed because they do affect the long-term effects of the energy transition to a lesser extent. All of the scenario related parameters are listed below:

1. Solar power, onshore- and offshore turbine projections:
   (a) total capacity in 2050 [MW]
   (b) model type (fixed: see appendix C.3 and C.4)
2. Short-term daily electric storage coverage [%] (fixed: 100%) (see 4.2.4 - batteries)
3. Electrolyser projections:
   (a) total capacity in 2050* [MW]
   (b) technology type; *alkaline, PEM or SOEC* (fixed: 'alkaline')

4. Heavy polluter (coal and biomass) stop after 2030 (fixed: 'yes')
5. Manually planned power or thermal plants
6. Heat grid implementation factor, η_{int} (fixed: 1.0)
7. Combustion plant fuel type reduction hierarchy (fixed: 'cost')

During the experimental work, all general simulation parameters remain constant. These options include the number of random seeds (weather projections), the climate projection scenarios included, success rate coefficient values (set at 1.0, 1.15 and 1.30), fuel cost and hourly electricity prices (retrieved from ENTSO-E [33]). Both fuel and electricity cost are required to be stable and unaffected by rare global economic events, for that reason stable year 2019 was chosen.

4.6.1 Reference scenario

The reference scenario chosen in the simulation represents the ambitious strategies discussed in chapter 3 and the RES [35]. The reference scenario closely corresponds to the energy-related topics discussed in the policy documentation, including additions, trends, and changes. As a result, the described trends do not always follow the expected trend behaviour as discussed in section 4.2.4. These deviating trends are described separately. Additionally, when common growth curves fail to describe the proposed capacity milestones, a polynomial is used.

In the reference scenario the amount of PV-panels grows from 498.6 MW-peak installed to 946.8 MW-peak in 2030 and eventually in 2050 to 2363.6 MW-peak. In 2050, an installed capacity of 14 GW for offshore wind turbines is proposed. While an increase in installed capacity of 282.5 MW for onshore wind turbines is expected from 2020 to 2030, in the RES strategy, this value stabilizes after 2030 and does not significantly increase further. These figures, like the predicted conditions, are fitted into trendlines. As shown in equation 4.42, a second order polynomial was chosen to compute the installed PV-panel capacity, $P_{PV}^{installed}$. For both onshore and offshore wind turbines the logistic curve describes the goals best. To calculate the corresponding lag time and true maximum value the current and projected capacity were given. For offshore wind these values are $y_0 = 129.0$ [MW] and $y_m = 14000$ [MW], and for onshore wind $y_0 = 256.8$ [MW] and $y_m = 781.1$ [MW]. The mathematical derivation of both lag time and y_{max}, described in the trendline section, with an 5% post-2050 deviation were used and resulted in a lag time and post-2050 capacity of of k=0.263, k=0.406, y_{max}=14778 and y_{max}=825.7, for offshore and onshore wind respectively.

$$P_{PV}^{installed}(t) = 0.72555939 \cdot t_y^2 - 43.26874330 \cdot t + y_0 \tag{4.42}$$

$$P_{Offshore}^{installed}(t) = \frac{y_{max} \cdot 129}{(y_{max} - 129) \cdot \exp[-k \cdot t] + 129} \tag{4.43}$$

$$P_{Onshore}^{installed}(t) = \frac{y_{max} \cdot 256.8}{(y_{max} - 256.8) \cdot \exp[-k \cdot t] + 256.8} \tag{4.44}$$

In terms of the other parameters, the scenario does not deviate from any of the trendlines described. In 2050, the electrolyser capacity is set at 1510 MW. This scenario includes no additional planned plants, implying that all thermal shortages will be met by new high calorific gas combustion plants, while electricity shortages will be covered by imports. Following current regional projections, the combustion plant reduction order is set at 'cost' efficiency.

4.6.2 Alternative scenarios

Two scenarios are researched in order to clearly investigate the impact of nuclear implementation in the region's energy system. Both of the scenarios proposed describe possible paths for a nuclear-assisted energy transition. Nonetheless, due to the wide range of modern nuclear reactor technology, both scenarios will be focussing on a different energy system functionality, such as power or thermal focused. The scenarios, ranging from light to heavy implementation in a successive manner, are described below.

Scenario 1

The first scenario will be used to investigate the potential of early nuclear power implementation in the region's energy transition. Primarily emphasising on the effects of replacing the low density energy sources present in the proposed strategy (reference scenario) with high density nuclear production facilities.

This scenario is the most similar to the previous reference scenario. However, a twin European Pressurised Rreactor 2 (EPR2) power plant will be built as soon as possible in relation to the start year 2020. (early 2030). In this scenario, the nuclear reactor will be located on the Maasvlakte, resulting in realistic short-term commercial licensing. All other parameters are similar to the reference scenario

The amount of renewables can be reduced without causing power shortages due to the addition of 3,350 MW of electrical capacity beginning in 2030. The optimal amount of renewables is calculated automatically as a function of the expected power surplus. The reduction amount for total 2050

renewable capacity is limited to 75%, so minor growth is always possible and expected. The most efficient renewables will be reduced last.

Scenario 2

Second, during the transitional period between 2036 and 2050, the potential benefits of additional multiple small modular reactors is investigated. Because of their inherent flexibility, these reactors allow for widespread integration of both power and thermal nuclear plants in the region. Consequently, rather than hydrogen combustion or electrification, the effects of providing intermediate industrial heat by nuclear reactors are being studied. Furthermore, information on the long-term implications of a strong transitional focus on nuclear energy will be provided.

Similar to the first scenario the following strategy included the construction of a twin EPR2 reactor and the optimised reduction of renewables. Yet, small modular reactor technologies are included after the year 2036, the estimated operational year for ASMR reactors in the Netherlands. To ensure a strong representation of these reactors, the old industrial boiler float that most likely needs to be replaced before 2030 is given a 7-year lifetime extension.

The reactors in this scenario are focused on carbonising the region's thermal energy system. As a result, both industry and the heat grid benefit from intermediate and low temperature heat. These reactors will be built in place of new gas combustion plants. Because most ASMR designs have a low outlet temperature, the high temperature heat will be covered by hydrogen. As a result, the hydrogen capacity is adjusted to meet this demand.

Chapter 5

Results

5.1 Pre-2020 renewable performance corrections

The renewable share built before 2020 will be corrected to real historical generation data to ensure accurate simulation results. PV panels and onshore wind turbines have been simulated using the methodology described in Section 1. A performance efficiency per model can be calculated using the installed capacity in one of the given historical years. Unfortunately, due to a lack of construction information on onshore wind turbines, the pre-2020 models are grouped and averaged. Following the set of four reference models, a more elaborate distinction can be made for solar power.

Solar power

This performance loss in solar panels is primarily due to deviating panel models in the region's PV share, as many of the panels are of lower quality than the reference models. Other factors influencing performance include solar panel positioning and dust accumulation. The resulting additional performance loss is summarised in table 5.1.

All of the resulting values are close to the PVGIS tool projections, 84.2%, from Joint Research Centre [86], therefore the calculated values are seen as realistic. The high performance of the later year ranges is most likely due to the construction of many high quality panels in that period, combined with efficient panel positioning.

The projected panel model is given a performance loss aligned with the PVGIS tool projections.

Table 5.1 Reference PV-panel performance corrections calculated from the reference point simulation.

PV-model	Construction period	Correction performance [%]
LG255S1K-G3	≤ 2013	84.35
LG280S1K-L4	$2013 < y \leq 2016$	73.95
LG330N1C-A5	$2016 < y \leq 2017$	92.15
LG365Q1C-V5	$2017 < y \leq 2019$	92.35

Wind power

Only onshore wind turbines are corrected for wind power because no offshore wind park generation data is available. As a result, the performance is aligned to that of onshore turbines. To calculate the performance of existing wind turbines, the production of an averaged turbine model was simulated (see appendix C.2). The resulting turbine efficiency factor was 43.04%. This value is regarded as reliable due to its close resemblance to the standard engineering range of wind turbine conversion efficiencies of 35-45 percent.

Projection turbines in the simulation are given the same value as the current average.

5.2 Reference scenario

The reference scenario results are divided into two categories: scenario A, low industrial heat electrification efforts, and scenario B, extensive low- and intermediate heat electrification efforts. This section will go over the potential challenges, bottlenecks and benefits. Discussing primarily on scenario B because of its closest resemblances to the original proposed energy strategy for the region. Scenario A will only be used to further investigate potential bottlenecks if the industry fails to electrify its intermediate temperature industry.

5.2.1 Transition strategy overview

As a result of the scenario input parameters, a large transition between combustion plants is expected in the early 2030s. This shift toward gas-only plants is being driven by the desire to eliminate coal and biomass combustion, as well as the anticipated renovation of many old industrial facilities. No significant reduction in heat consumption is expected because many electrification efforts are planned after this period.

Figure 5.1 gives an overview of the predicted combustion plant facilities in the region in the coming decades. It becomes clear from these images that a large float of gas-fired thermal plants will operate in the region for a period up to 2060s. If the industrial cluster manages to electrify both low- and intermediate-heat industrial facilities, new thermal combustion facilities will be reduced by 2% by the mid-2030s.

Heat production and consumption

Because of the float of old industrial boilers, most thermal combustion facilities must be replaced just before industrial electrification develops to significant levels. As a result, when electrification scenario A occurs, the installed capacity will be used quite efficiently, whereas in scenario B, a large proportion of the newly built facilities will be inactive, as shown in figures 5.2 and 5.3.

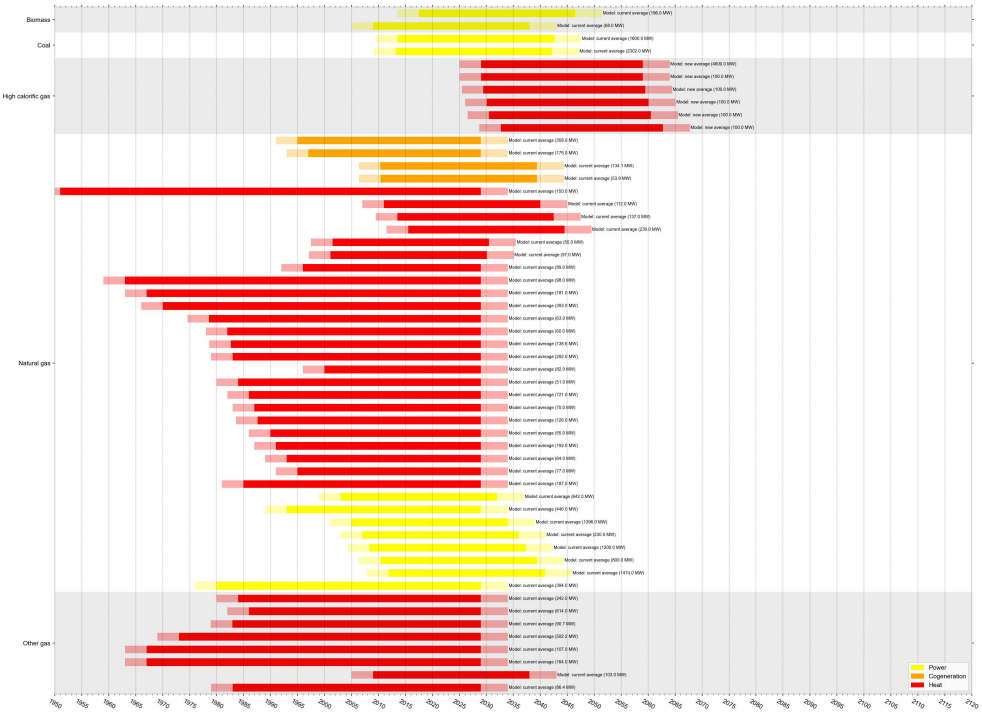

(a)

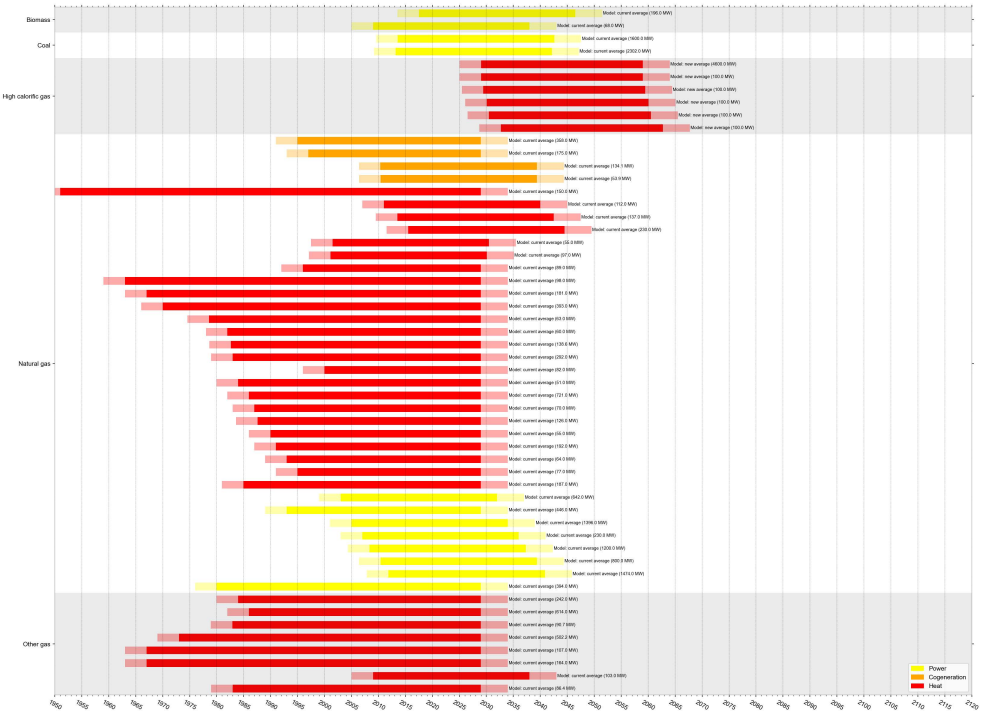

(b)

Fig. 5.1 Overview of the non-renewable energy plants over time in the reference scenario. The plants are classified by their output energy- and fuel type. (a) electrification scenario A, (b) electrification scenario B.

The projected electrification and consumption behaviour trends have only a minor impact on low temperature heat demand. The ambitious reductions discussed in the national energy transition strategy due to energy efficiency efforts are noticeable in the first decade, but after the 2030s population growth takes over, increasing the low heat demand once more. As a result, many more energy-saving efforts are required before the national government's reduction targets can be met.

Nonetheless, the implementation of a large-scale heat grid in the region significantly reduces the region's reliance on natural gas. In the early 2020s, natural gas consumption was around 130 PJ per year, but by 2050, this figure had dropped to around 80 PJ for low temperature heat.

In electrification scenario B, the share of intermediate heat production and consumption will decrease between 2045 and 2050, as expected. This massive drop in demand translates into a decline in natural gas demand for this group, implying that a large portion of the remaining high temperature heat can be produced by hydrogen, leaving only a small yearly natural gas fraction of 10 PJ in 2050. Unfortunately, if electrification efforts do not go as planned, demand for natural gas fuel will remain high, as scenario A only produces 20 PJ hydrogen per year. This leaves an annual gap of 85 PJ, which is filled by the combustion of polluting natural gas.

It can be stated that, under the current transition strategy, electrification of low- and intermediate-temperature industries is considered necessary if the region wants to significantly reduce its GHG emissions. Even in the best-case scenario, B, natural gas combustion balances at around 90 PJ in 2050, while in the worst-case scenario, A, demand remains as high as 165 PJ (relative to the 220 PJ in 2020).

Furthermore, in order to completely decouple the region's thermal energy demand from natural gas, hydrogen production and/or imports must increase significantly. The first requires a large number of additional electrolysers and electricity sources to obtain a reliable source of hydrogen. Therefore, the region is expected to become more reliant on other hydrogen sources outside of the region, consequently increasing the region's dependence on import.

Power production and consumption

For the power production and consumption other trends are clearly visible, as seen in figure 5.4. Following the strategy of the RES region renewables fully take over the electricity production in the region. Growing to a total installed capacity of more than 16 GW. This amount of renewables is projected to generate up to 33 TWh per year in 2050, enough almost enough to power scenario A with only minor industrial electrification. While the share of fossil fuels stays significant for another two decades it will decline over time when little electrification is happening. However, due to the variable output of these sources roughly 10 percent of the consumed energy will eventually be imported from other regions.

However, in electrification scenario B, this prospect is less favourable. Industry consumes a lot more electricity, resulting in a significant increase in power demand after 2035. Even with a large

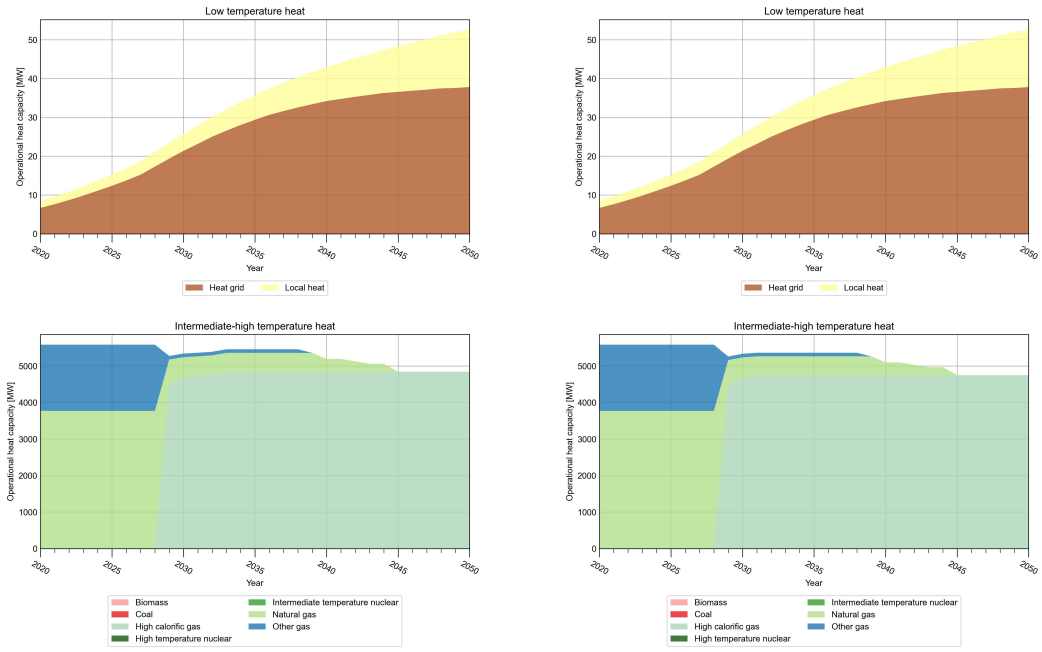

(a) **(b)**

Fig. 5.2 Overview of the heat production capacity per fuel type at low, intermediate, and high temperatures for the reference scenario. (a) electrification scenario A, (b) electrification scenario B.

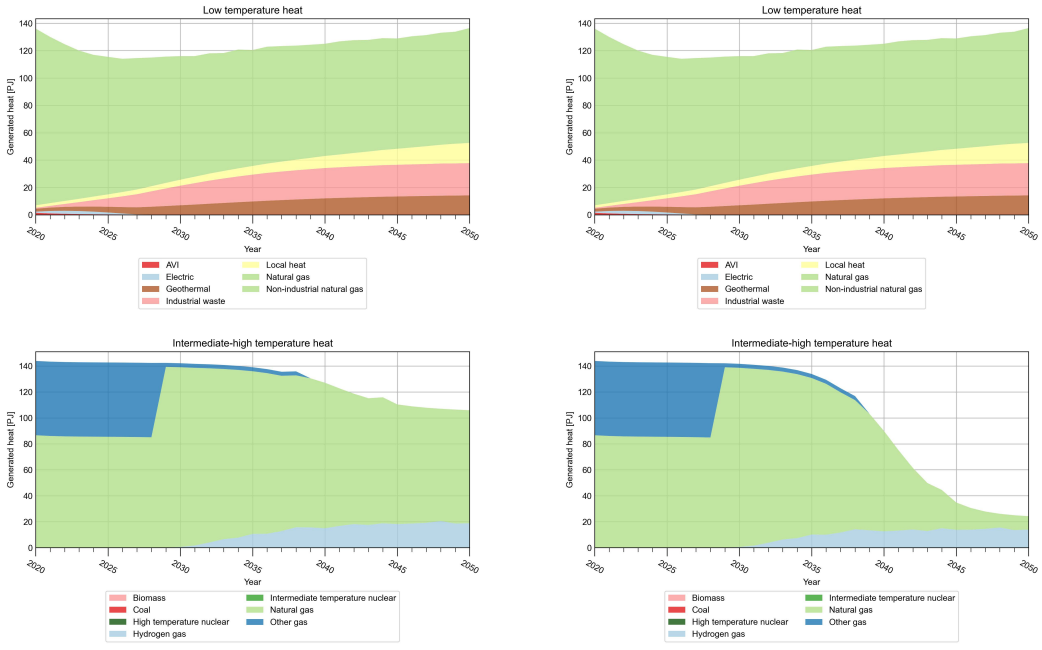

(a) **(b)**

Fig. 5.3 Heat related energy balance including heat production by fuel type at low, intermediate, and high temperatures for the reference scenario. (a) electrification scenario A, (b) electrification scenario B.

number of renewable sources, this demand cannot be met without an increase in both fossil fuel combustion in the late 2030s and early 2040s, as well as a relatively large increase in electricity import to around 20%. This reliance on imported electricity may have a significant impact on the scenario's feasibility, as electricity prices in times of scarcity are far from stable in a region powered by renewables.

Overall, even with a high proportion of renewables, the proposed transition will present numerous challenges, potentially making the current strategy overly reliant on other regions. The primary challenges for the given strategy are the continued reliance on fossil fuels into the late 2030s, as well as the above mentioned dependence on imports.

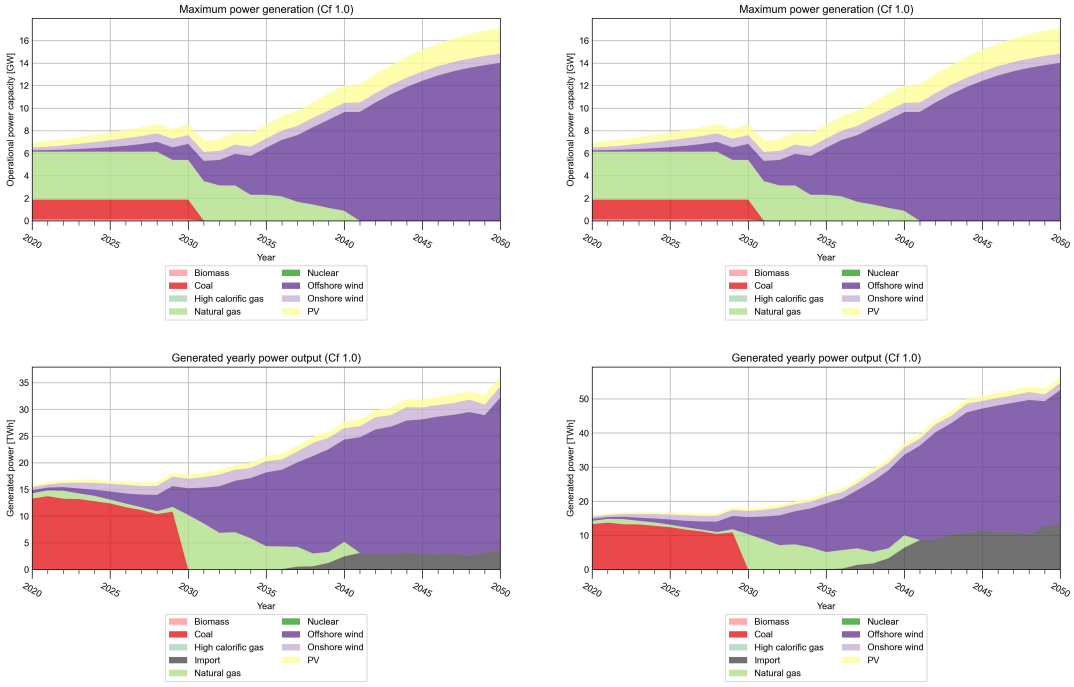

(a) **(b)**

Fig. 5.4 Maximum installed power capacity and simulated electricity balance including power production by fuel and technology type. (a) electrification scenario A, (b) electrification scenario B.

5.2.2 Assessment life cycle results

The images in figures 5.5 and 5.6 show that strategy can mitigate many of the negative consequences of energy production. Direct greenhouse gas emissions, biodiversity loss, human health risk, chemical waste, radioactive waste, and fuel demand and cost are all expected to fall steadily in the coming decades as more environmentally friendly energy sources are constructed. These improvements are most significant for an energy system that is primarily powered by electricity rather than heat, as

shown in projections scenario B. The most notable improvements are in direct emissions, biodiversity reductions, and human health risks, with annual reductions of 14-19 megatons CO_2-eq, 110-125 million PDF/m^2 and 13-22 thousand adjusted life years, respectively.

Another advantage of the simulated energy mix is that it reduces yearly indirect costs. These costs include fuel, operational and management expenses, and power imports. These reductions are almost immediately noticeable and will stabilise in the 2040s at around 3.5 and 3 billion euros per year, respectively, in scenarios A and B. These annual savings of 500 to 900 million euros have the potential to lower energy prices over time. Yet, the error margin of this trendline is very large, making this projection very uncertain.

Unfortunately, some negative trends are predicted for the current transition strategy. Construction of primarily offshore wind turbines is expected to increase water pollution by a factor of ten by 2050, potentially causing issues with regional water quality.

As previously discussed, when generation sources become less reliable due to weather dependencies, reliance on imported electricity will increase significantly. If electricity becomes less stable in the near future, these costs could skyrocket, making the strategy less affordable in the long run.

5.2.3 End-of-life projections

A significant amount of replacements are expected due to the large number of renewable energy sources and their support systems in the described transition strategy. Resulting from the relatively short operational lifespan of 10 to 25 years for storage systems and generation technologies respectively. Figures 5.7 and 5.8 clearly depict this projection, as the period after 2040 is heavily characterised by renewable energy replacements. Because there are currently no commercially available recycle techniques, this massive amount of End-of-Life (EoL) material is likely to accumulate over time.

This accumulation of EoL material could pose significant regional waste storage challenges in both electrification scenarios. With hazardous PV-panel waste expected to exceed 3.5 million panels by 2050, and unrecyclable turbine composites and permanent magnets expected to total more than 800 turbines. This waste heap will continue to grow at a rate comparable to that of the 2045-2050 period after 2050.

Lithium ion batteries and End-of-Life electrolysers are two other relatively new waste sources. These waste flows are also expected to steadily increase over time if no recycling facilities capable of handling this waste are built. Because higher power demand translates into a larger share of battery storage, the accumulation of batteries is expected to be higher in the electrification scenario.

5.2.4 Energy strategy implications

Figures 5.9 and 5.10 give an overview of the implications of the strategy related to construction cost, spatial requirements, employment (both direct and indirect) and construction emissions.

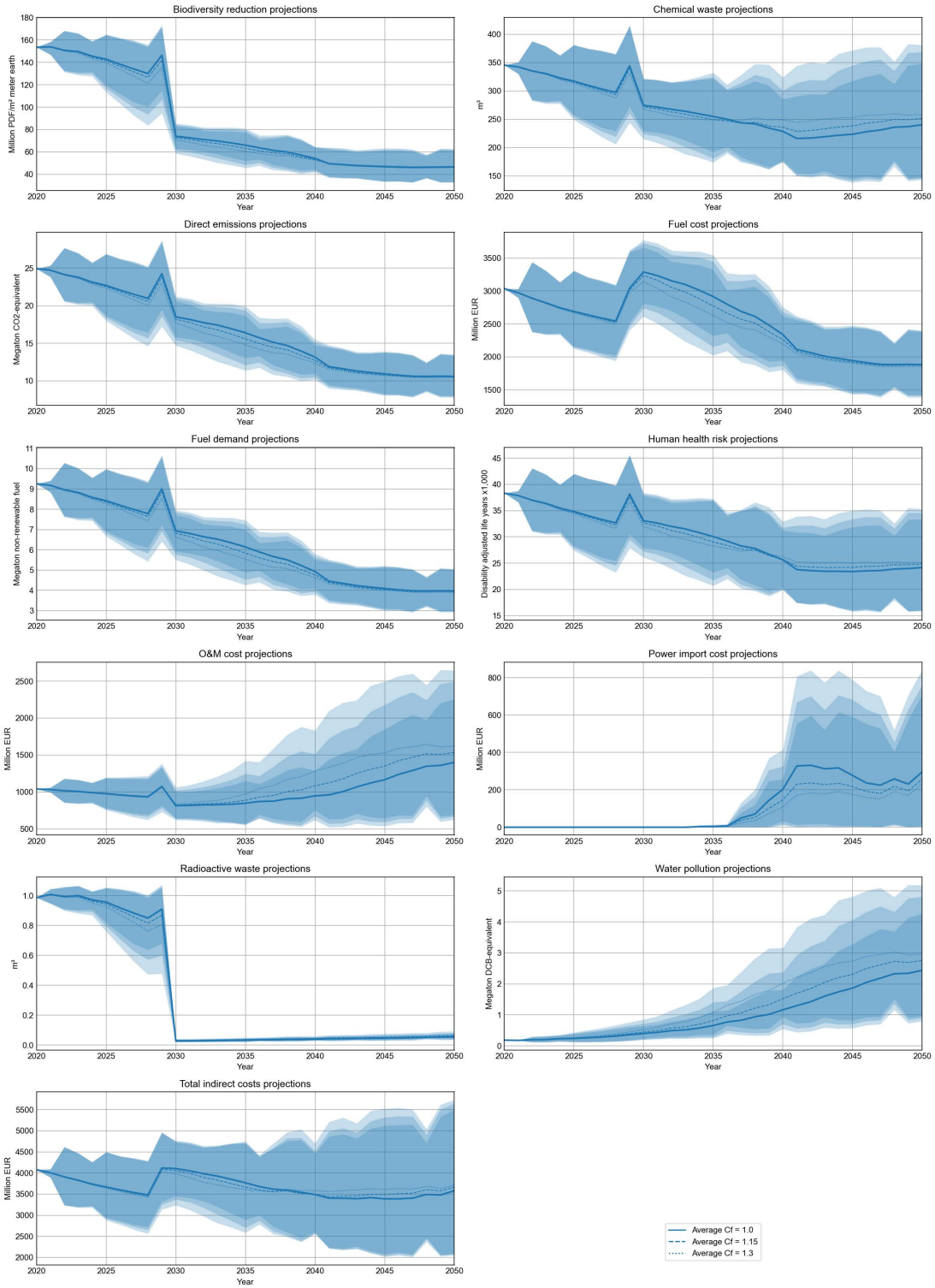

Fig. 5.5 Overview of the yearly projected operational effects following from the assessment framework. The graphs represent reference scenario A. The plotted area represents the uncertainty range for all included climate scenarios. Transparent areas are classified as unlikely extremes.

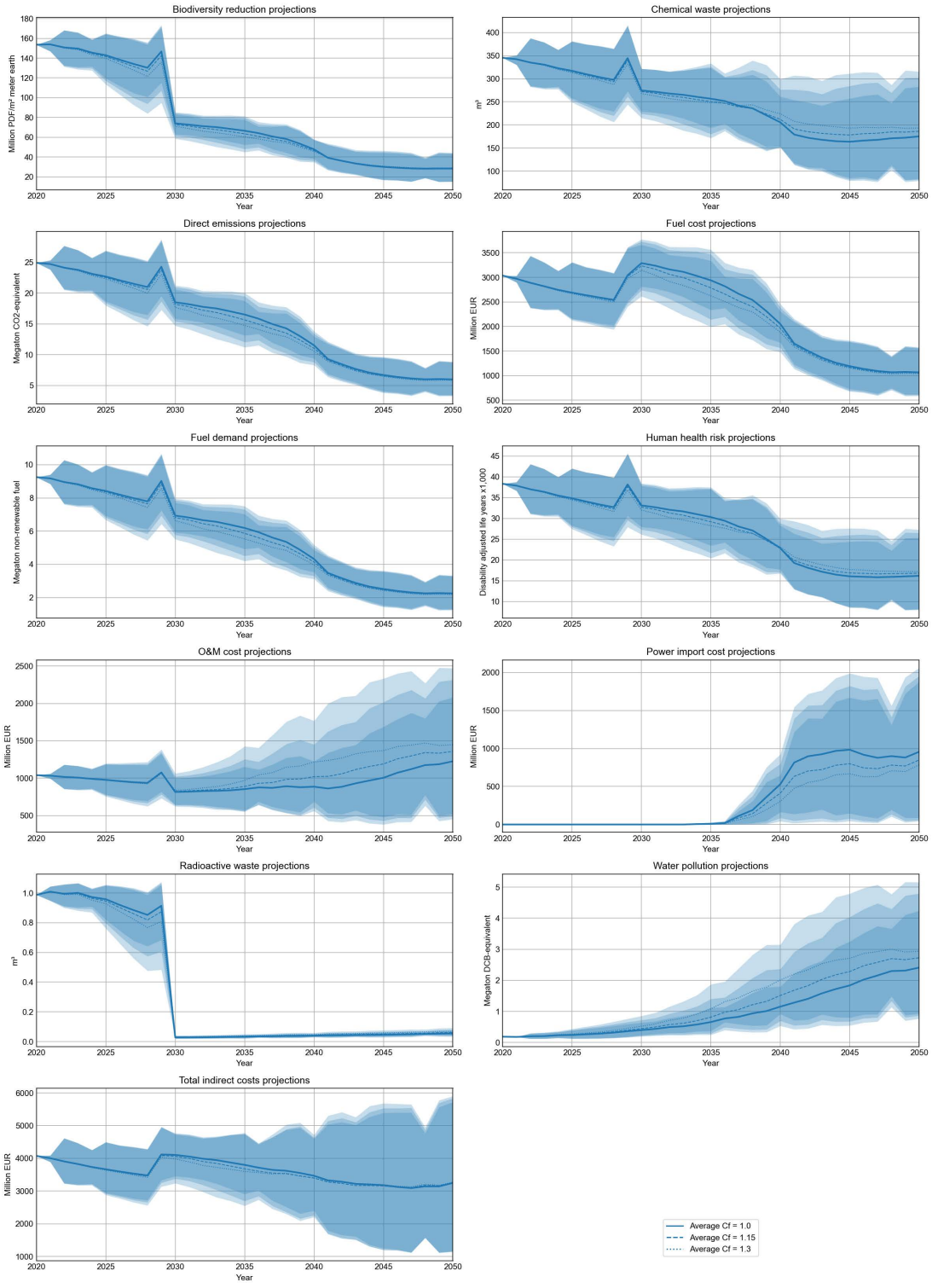

Fig. 5.6 Overview of the yearly projected operational effects following from the assessment framework. The graphs represent reference scenario B. The plotted area represents the uncertainty range for all included climate scenarios. Transparent areas are classified as unlikely extremes.

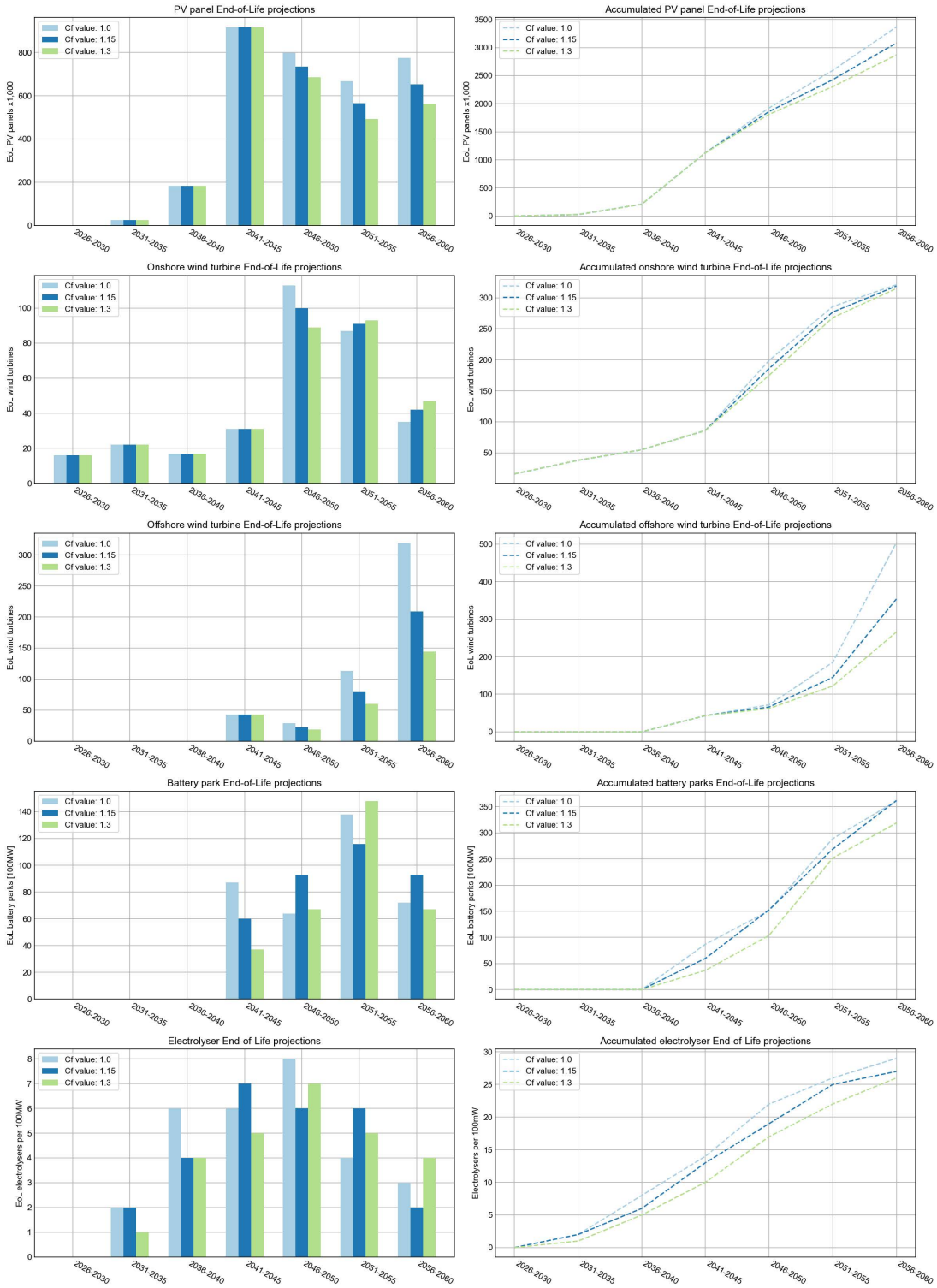

Fig. 5.7 Simulated projections of the End-of-Life renewable technology waste flow. The graphs represent reference scenario A.

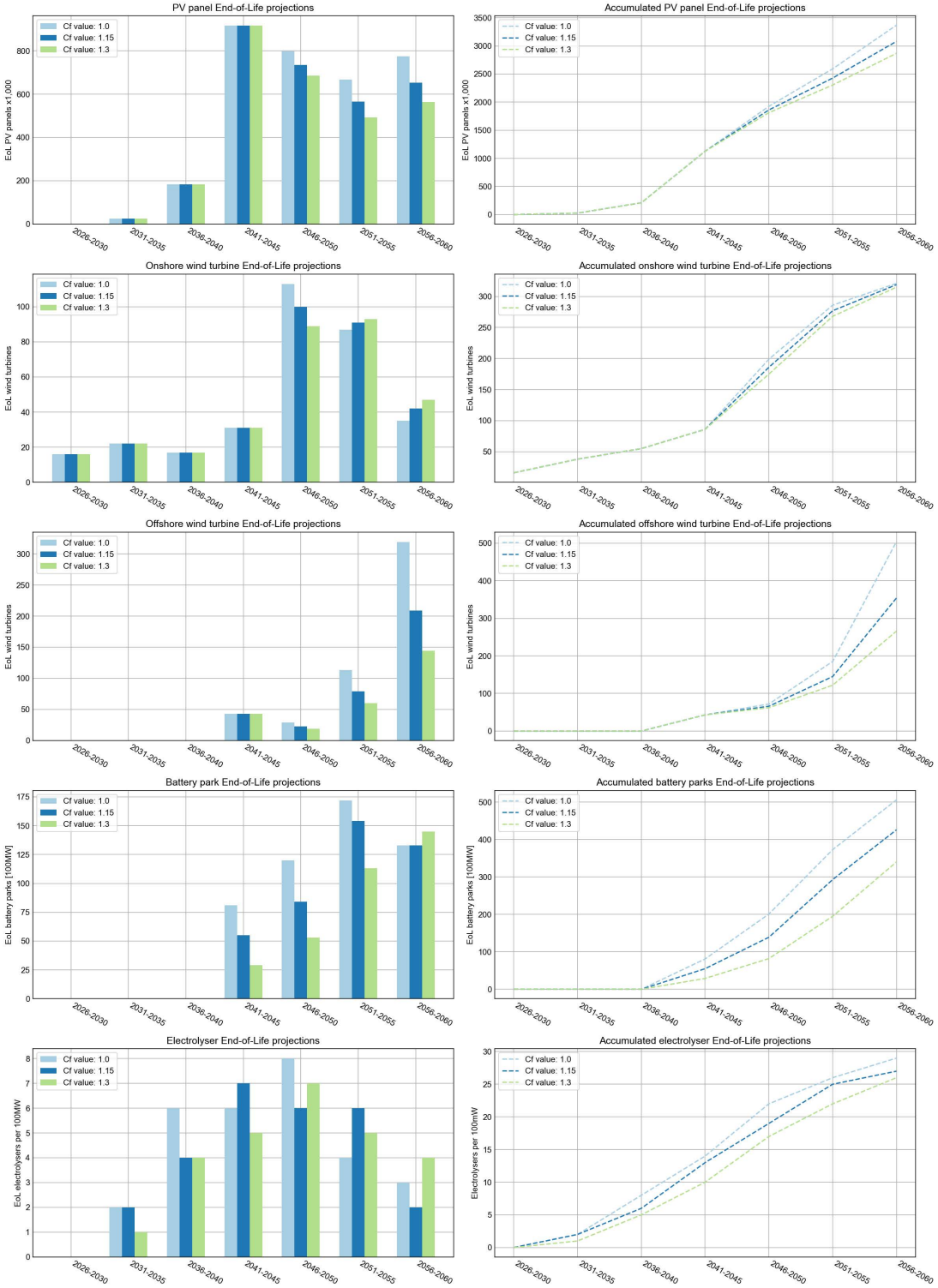

Fig. 5.8 Simulated projections of the End-of-Life renewable technology waste flow. The graphs represent reference scenario B.

The direct cost graph clearly shows that both electrification scenarios require massive investment. The strategy will cost the region 105.7-110.4 billion euros (scenarios A and B, respectively) over a 30-year transition period, or an average of 3.5-3.7 billion euros per year. For scenario B, with a population of 2.4 million people, this equated to a yearly investment of 1,540 euros per person. When the indirect cost of the strategy is factored in, this cost rises to 2,940 EUR/person for scenario A and 2,840 EUR/person for scenario B. This equates to about 8% of gross regional value product per citizen.

Additional to the cost, the construction of these technologies will release GHG-emissions into the atmosphere. For both scenarios this equals 169 megatonnes of additional CO2-equivalent emissions.

The enormous spatial footprint of the new energy system, which will grow from 50 square kilometres to 2,080 square kilometres, 107 km^2 of which will be on land, is another implication of the high renewable share. This means that roughly 8.6% of the land in the region will be used in some capacity for electricity generation or storage. Such a share of land means that the landscape of the region would drastically change in the coming decades. Transforming the current built environment into a energy-focused landscape.

Finally, there is a positive trend in terms of job opportunities. Old employers, such as the fossil fuel industry, will make way for new jobs, primarily in generation technology maintenance. There is also a significant opportunity for the development of a new industry centred on renewables. Potential industries include the manufacturing, engineering, and design of the technologies, with offshore wind turbines being the most promising. The further electrified scenario B performs significantly better in terms of both direct employment and innovation potential. This is primarily due to the increased number of battery parks.

5.2.5 Material requirements

The transition would have a massive impact on demand in comparison to the current regional material flow, as illustrated in figures 5.11a and 5.12a. Elements used primarily in wind turbines are seeing a significant increase in demand, sometimes up to 600 times the current demand (dysprosium). This material consumption is expected to remain high after 2050 due to the replacement of old panels, turbines, and batteries if recycling of these technologies does not take hold. Relative to scenario A, lithium demand is higher in scenario B due to additional battery parks.

The criticality of certain material groups is expected to rise as a result of increased material demand. Figures 5.11b and 5.12b show that many of the currently critical materials are expected to become even more scarce in the European market. As a result, their cost is likely to increase as a function of this scarcity. Currently non-critical materials; nickel, cadmium, manganese, molybdenum and tellurium and likely to be added to the critical raw materials list of the European Union in the coming decades.

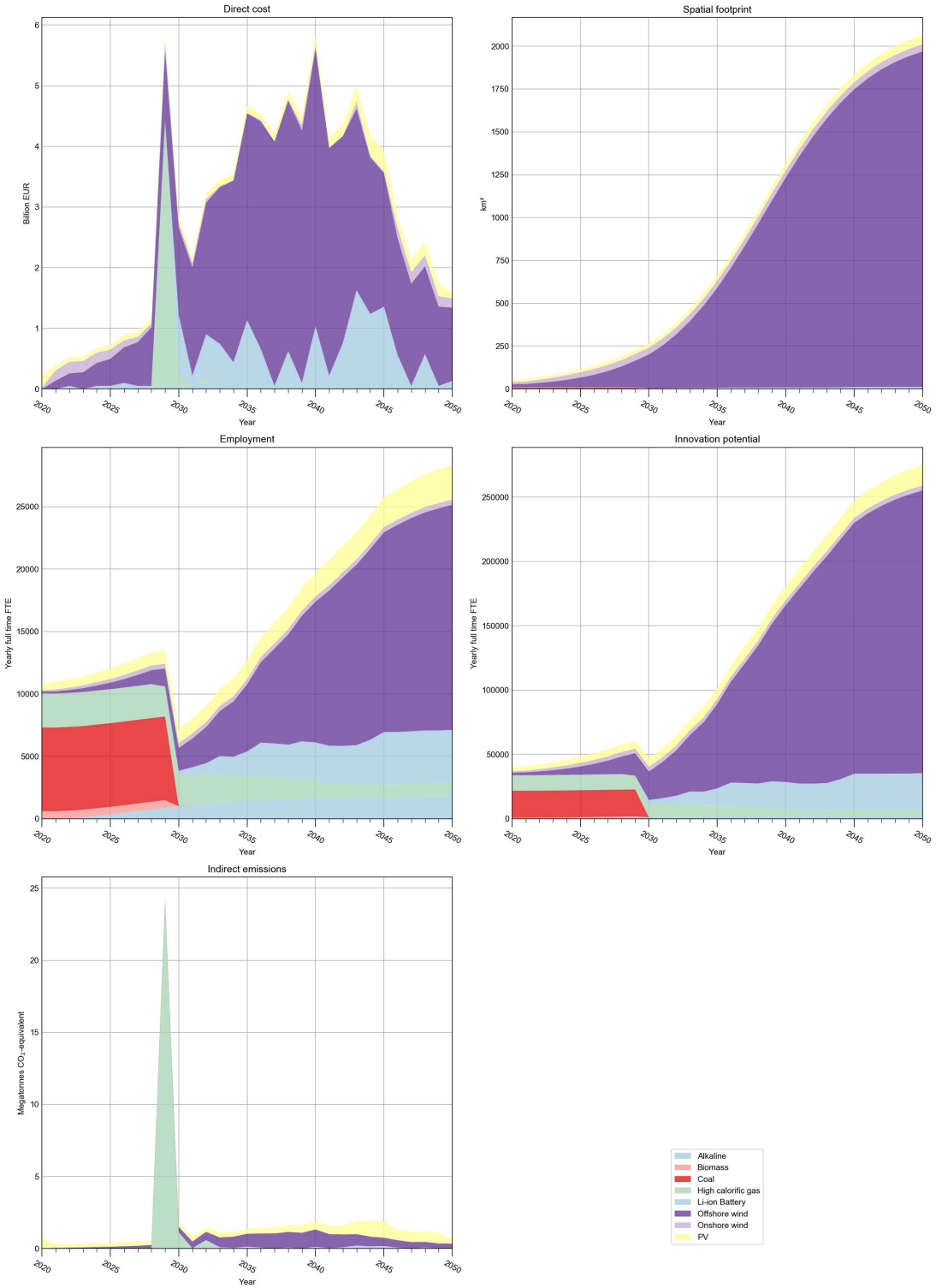

Fig. 5.9 Overview of the projected implications resulting from the energy strategy scenario. The graphs represent reference scenario A under standard projection conditions.

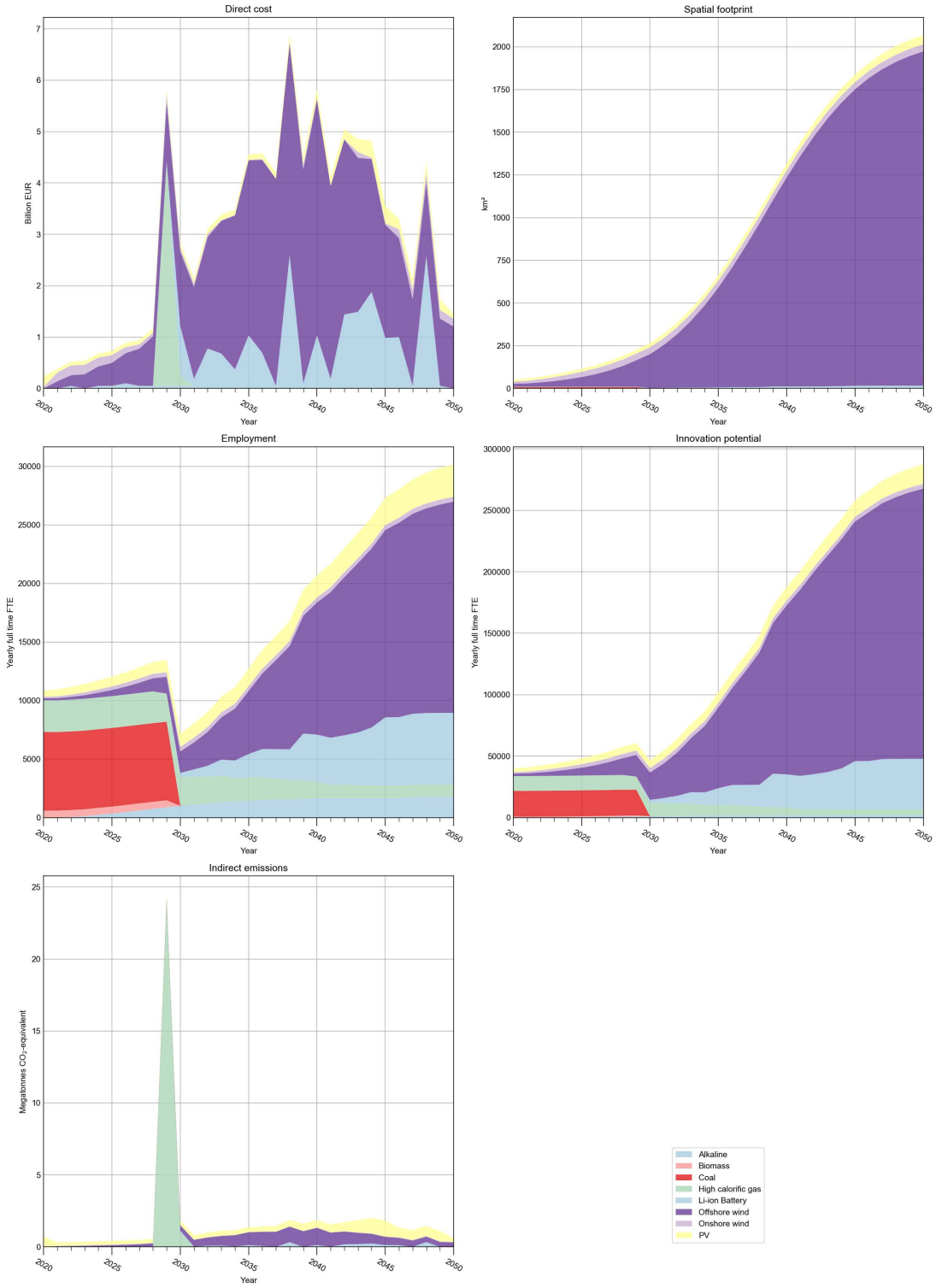

Fig. 5.10 Overview of the projected implications resulting from the energy strategy scenario. The graphs represent reference scenario B under standard projection conditions.

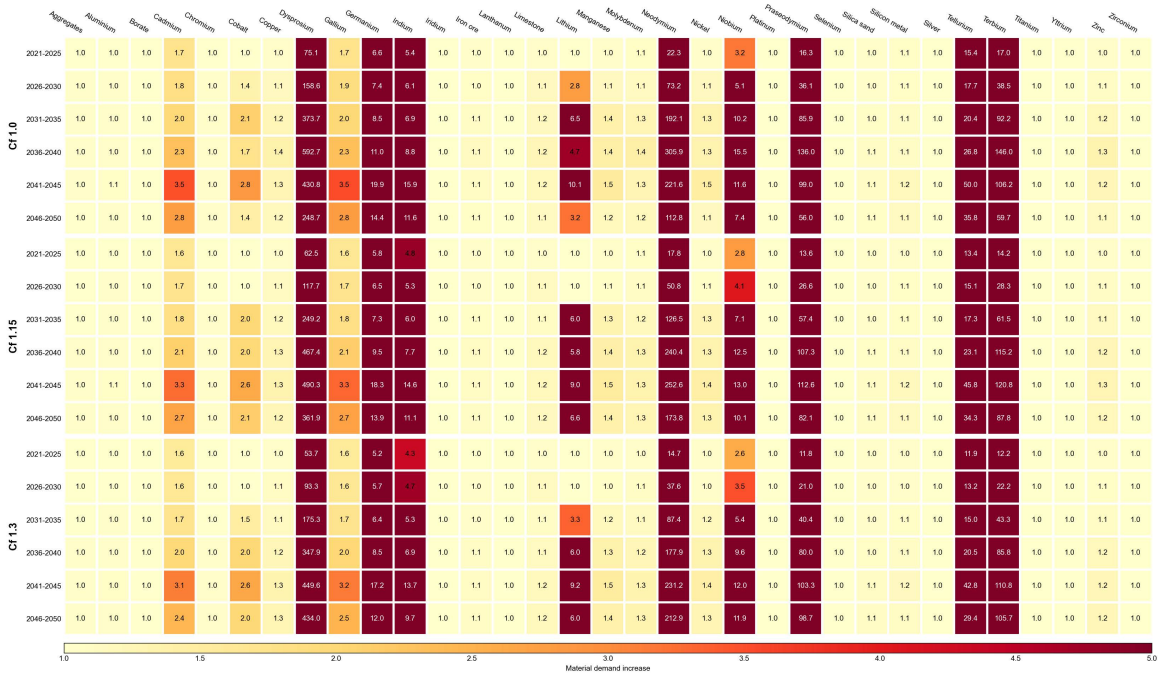

(a)

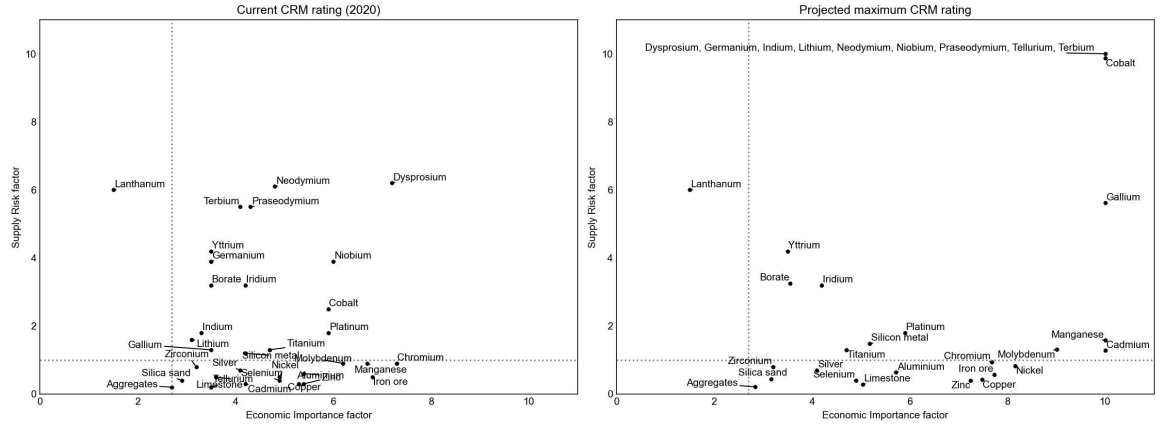

(b)

Fig. 5.11 Overview of the major materials in the European Union and the projected requirement intensification. The graphs represent reference scenario A. (a) material demand increases, (b) current critical raw material plot (left) and the estimated trend behaviour (right) for standard trend projections (Cf=1.0).

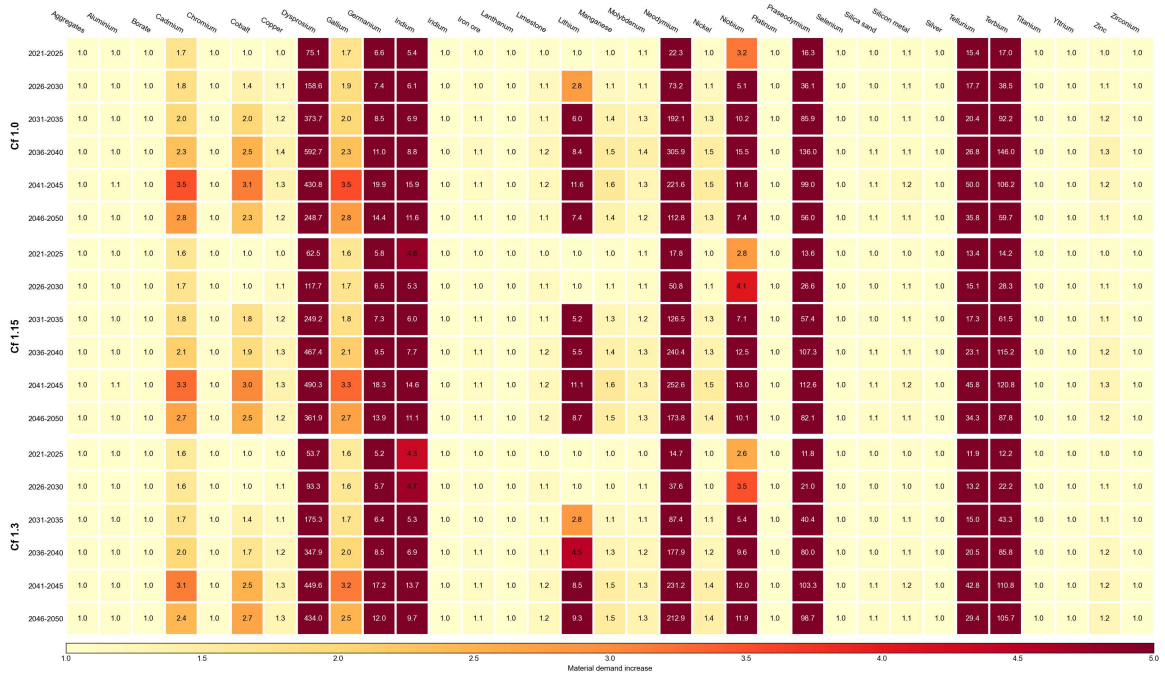

(a)

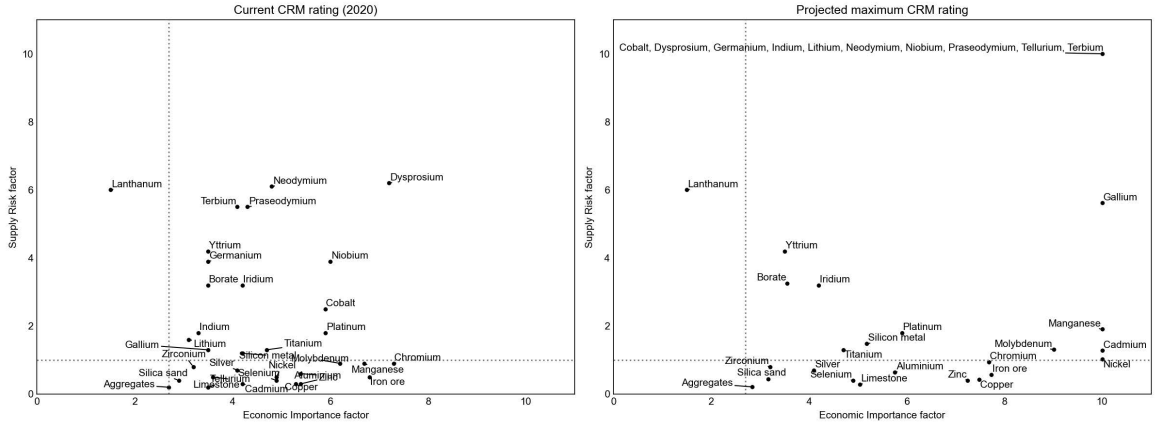

(b)

Fig. 5.12 Overview of the major materials in the European Union and the projected requirement intensification. The graphs represent reference scenario B. (a) material demand increases, (b) current critical raw material plot (left) and the estimated trend behaviour (right) for standard trend projections (Cf=1.0).

5.2.6 Natural gas demand projections

Finally, both electrification scenarios are expected to reduce natural gas consumption. This reduction will not only reduce regional emissions, but will also reduce the region's reliance on external natural gas providers. In 2050, this reduction is expected to fall to a daily average of 11 thousand tonnes of natural gas for scenario A and 6,000 tonnes for scenario B. The majority of demand will be generated by residential and greenhouse boilers.

In 2050, scenario A will consume 3.6 million tonnes of natural gas per year, while scenario B will consume 1.95 million tonnes. In comparison to Groningen's gas extraction (6.44 million tonnes per year [125]), these figures represent 55.9 percent and 30.3 percent of total extraction volume, respectively.

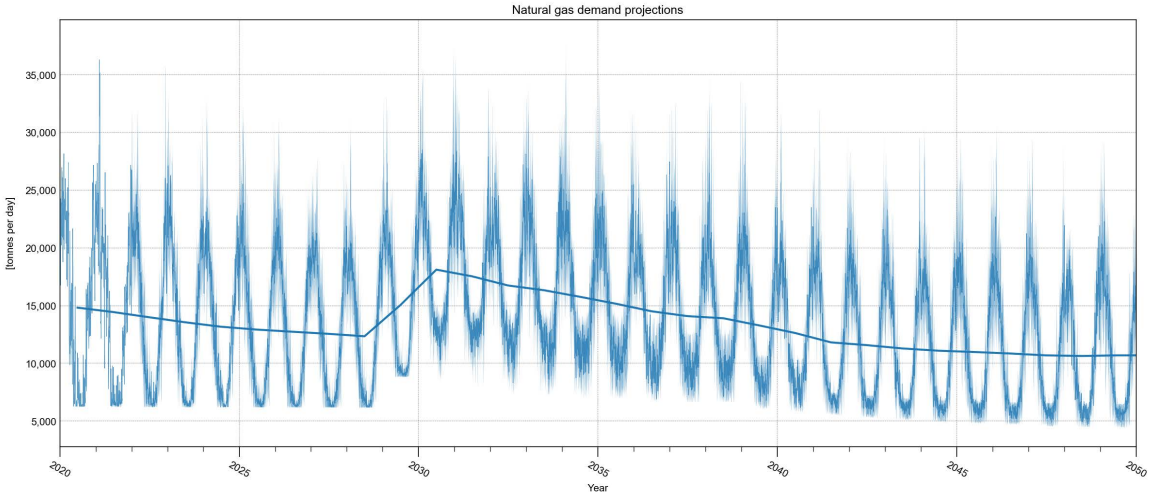

(a)

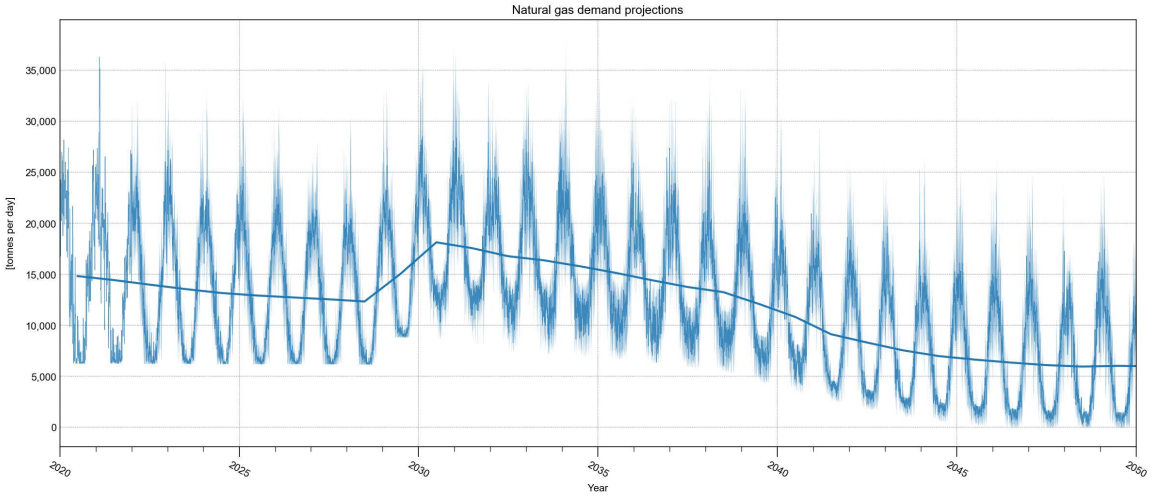

(b)

Fig. 5.13 Projections for daily natural gas demand in the MRDH region for the reference scenario under standard conditions. (a) electrification scenario A, (b) electrification scenario B.

5.2.7 Sub-scenario

Slight adjustments to the reference scenario are made to better understand the effects of energy buffers and the technology growth curves. The following results represent the reference sub-scenario (electrification B) with no battery systems, half the hydrogen capacity and normal expected growth curves. The growth curves are similar to the other scenarios.

Due to these changes some effects were expected. Because of the lower technology requirement the critical material demand decreases for a selection of elements mainly used in batteries, namely; lithium, manganese, nickel, copper and cobalt (see figure 5.14). These technology dependence reductions are also clearly visible in the EoL predictions, as seen in figure 5.15. Due to the normal growth curves taken into account the EoL is assumed to be more stable over time. Next, as seen in figure 5.16, the direct cost of the system transition is significantly lowered and more balanced when less storage facilities are constructed.

Negative side effects resulting from a decrease in net power stability was expected. Nevertheless, the effects were projected to be not that severe. Power import rates and consequently indirect operational costs are increasing slightly, around 8%. Additionally, a slight increase in natural gas consumption, chemical waste production, human health risk and GHG-emissions are projected. At last, when electricity and fuel import costs do not increase relative to the simulation stable year, the sub-scenario will result in lower overall costs per year with a rough decrease of 3% relative to the reference scenario.

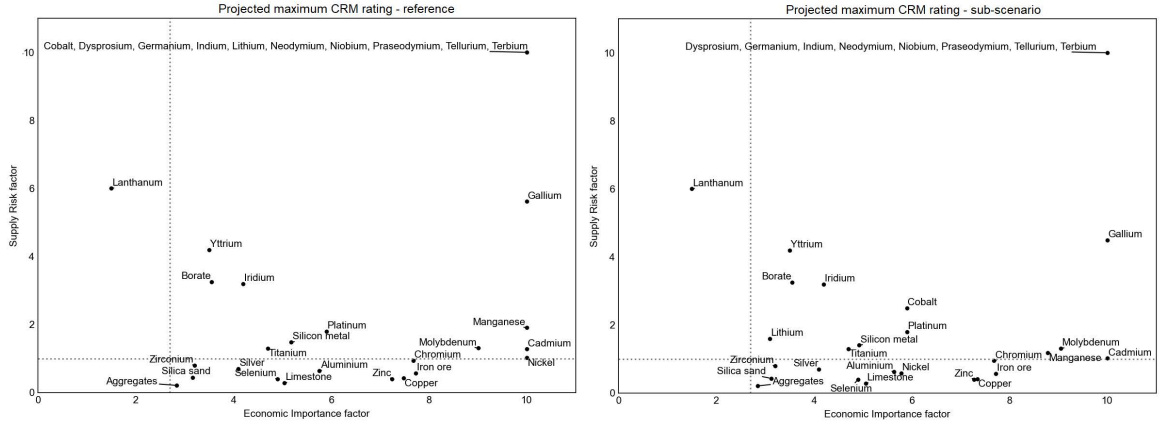

Fig. 5.14 Overview of the major materials in the European Union and the projected requirement intensification. The graphs represent the critical raw material plots for; (left) reference scenario B, and (right) reference sub-scenario B. The plots compare the estimated criticality in 2050 with a standard trend projections (Cf=1.0).

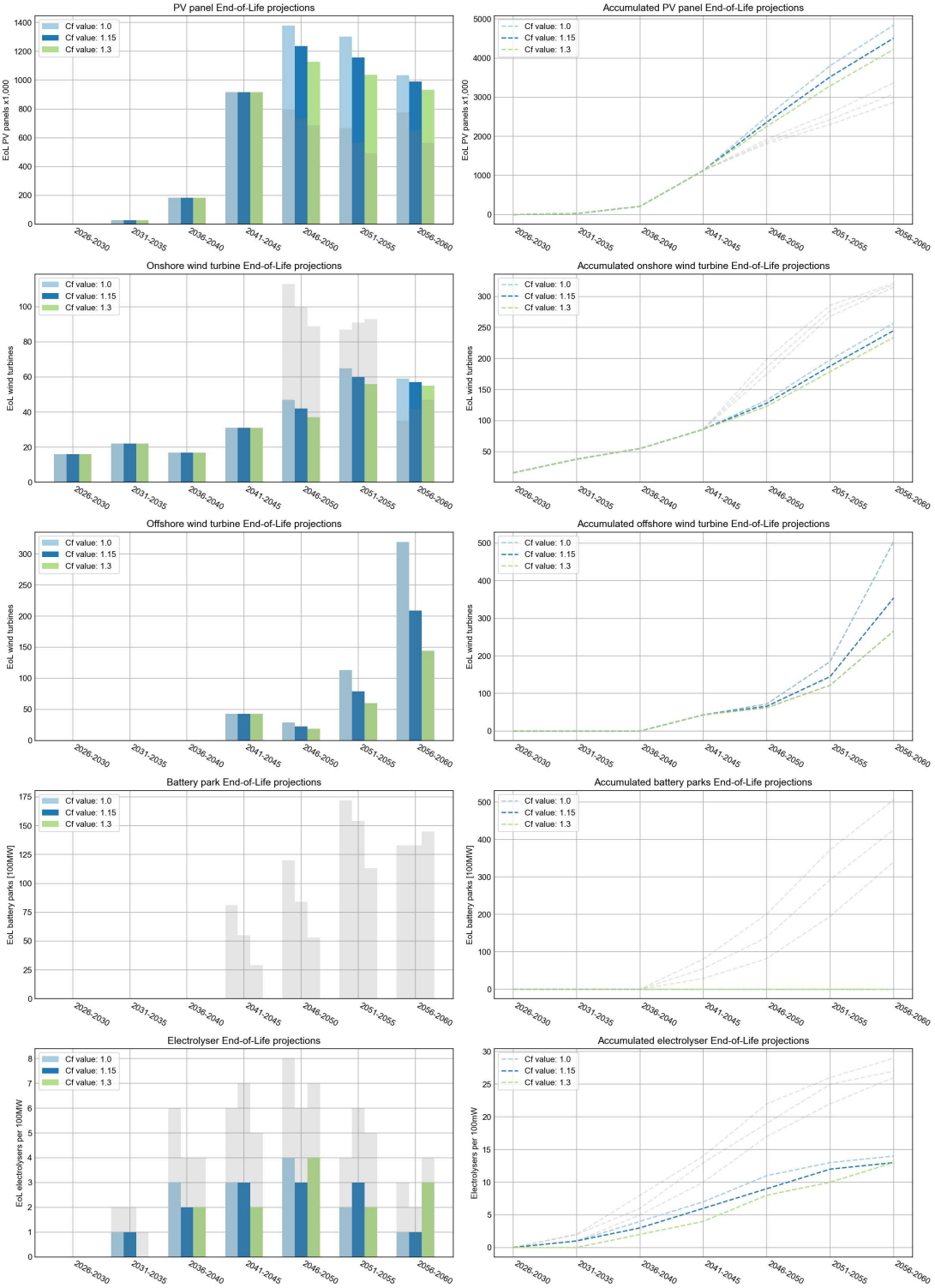

Fig. 5.15 Simulated projections of the End-of-Life renewable technology waste flow. The graphs represent reference sub-scenario with electrification B.

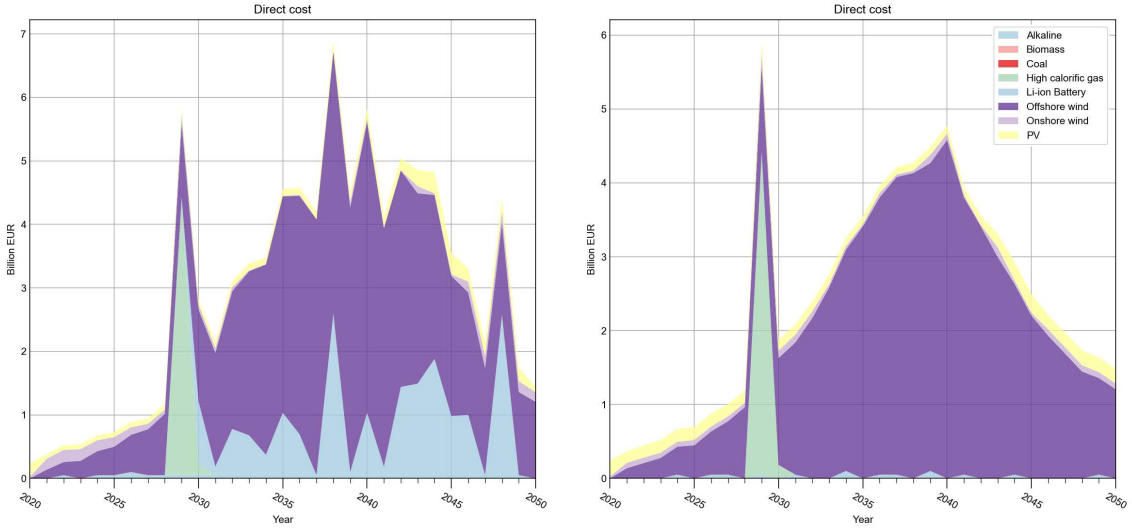

Fig. 5.16 Overview of the direct energy system transition cost for both the reference and sub-reference scenario. The graphs represent; (left) reference scenario with electrification B, (right) reference sub-scenario with electrification B.

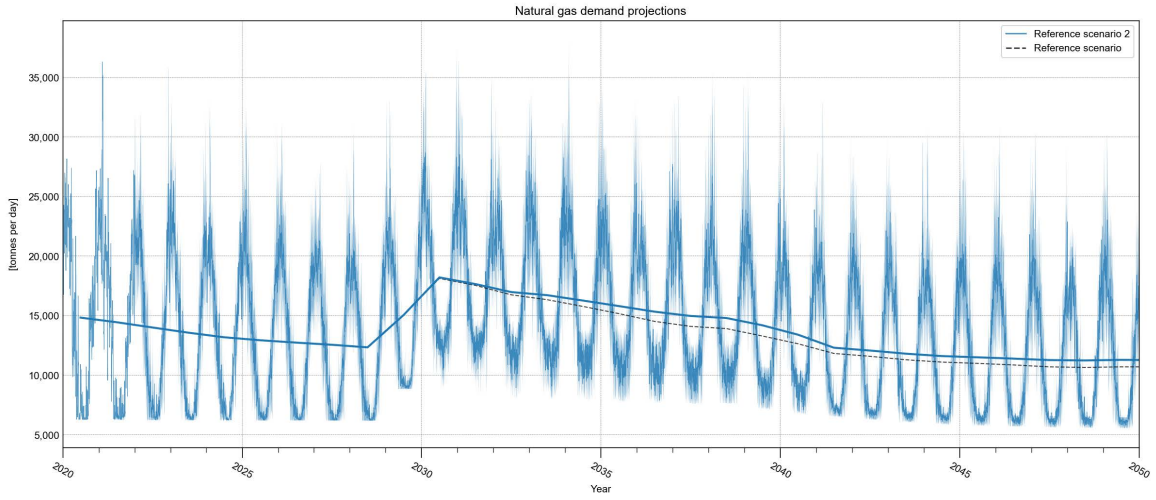

Fig. 5.17 Projections for daily natural gas demand in the MRDH region for the reference sub-scenario under standard conditions, electrification scenario A.

5.2.8 Conclusion

Following the international, national, and regional energy transition ambitions and goals, a set of benefits, challenges, and potential bottlenecks resulting from simulation projection results can be provided for this reference scenario.

Fig. 5.18 Performance overview of the two reference strategies relative to all researched scenarios. Values range from worst (1) to best (5). The grey area represents the reference scenario.

General outcome The main goal of the energy transition is to reduce GHG-emissions to reduce global warming. For that reason, the energy transition strategy is required to cut emissions by 95% relative to 1990 at the end of the transition. This translates into a maximum regional emission of 1.6 megatons of carbon-dioxide equivalent per year in 2050.

The current proposed strategy, with its high proportion of renewable technologies, has the potential to reduce direct emissions to around 6 Mton per year by 2050 if both low- and intermediate-temperature industries electrify. This is primarily due to the limited implementation of heat grids in both the built environment and the agricultural sector.

Advantages The primary advantage of the current proposed strategy is the anticipated increase in regional job opportunities. Even in the low industrial electrification scenario, the strategy would create more than twice as many jobs in the energy sector as before the transition. Furthermore, the incorporation of these renewable sources would create numerous opportunities for the formation of new innovation industries in the region, potentially creating many more high skill jobs if developed.

Second, the strategy's implementation is expected to significantly improve human health risks and biodiversity diversity. Hence, many of the regional goals for the transition strategy have been met.

Challenges The spatial footprint of the given strategy is very large due to the high share of low energy density technologies. Due to the scarcity of land in the region, many technologies that are

perceived as a spatial nuisance are likely to dominate the region's skyline, potentially reducing societal willingness for all the proposed transition elements. With projections predicting a 40% coverage on land, the built environment will undoubtedly evolve into an energy-focused landscape.

The regional requirement to prevent water quality degradation is another challenge arising from the strategy results. According to projections, the construction of many wind turbines, both onshore and offshore, will degrade water quality in all simulated scenarios. This development may have long-term consequences for the region's vulnerable aquatic ecosystem.

Bottlenecks The accumulation of electronic EoL material has the potential to significantly reduce the sustainability of the currently proposed strategy. The high proportion of low energy density technologies with relatively short operational lifetimes will almost certainly result in a large flow of commercially unattractive materials for recycling. Wind turbine rotor blade composites are difficult to recycle and currently have little value. Other more valuable components, such as permanent magnets, lithium batteries and layered PV cells, are extremely difficult to recycle without a significant amount of energy and chemicals. If done in a sustainable manner, this could make disposal of these products very expensive.

Another potential bottleneck is the high demand for materials for all the necessary facilities. If renewable technology recycling rates remain low in the coming years, already scarce materials may become even more valuable. Because the strategy is heavily reliant on high-tech electronics, the cost of new batteries, electrolysers, solar panels, and wind turbines may skyrocket in the near future, as many of the required materials are already listed as critical raw materials in the EU. As a consequence, maintaining the energy system post-2050 could become prohibitively expensive.

At last, because of the many fluctuating energy production sources net stability is decreasing significantly. As a result, energy imports will become increasingly important in the coming decades. The reliance on imports is not always a bad thing, but it makes ensuring affordable energy more difficult. This energy affordability, when combined with the high transition investment cost of approximately 110 billion euros over the next three decades, could be disastrous to the regional economy and the sustainable goals and ambitions.

Additional findings Multiple negative side effects result from the supporting storage systems described in the scenario, while power stability is preserved. However, if power and fuel prices remain stable relative to 2019, a large reduction in storage facilities will only slightly reduce scenario performance while relaxing critical material demand and limiting electronic EoL waste flows. If costs rise, as they did in late 2021 and early 2022, the additional benefits will not outweigh the increase in total annual energy costs.

5.3 Scenario 1

Multiple energy transition strategies were proposed to investigate the integration of nuclear energy in the region's energy mix. The first of these looks into the possibility of building a single large-scale generation III+ reactor on the Maasvlakte. Results of the transition strategy are discussed in this section.

5.3.1 Transition strategy overview

Figure 5.19 depict an overview of the region's combustion plants and nuclear facilities over the next decade. Because only the addition of a twin nuclear power plant is proposed, no deviations from the reference scenario are observed for the thermal plants.

Heat production and consumption

Because of the aforementioned reason, there is no difference in heat production capacity in this power-focused scenario. However, an interesting difference can be seen when comparing the heat production and consumption graph, figure 5.20. The current electrolysers in the region are expected to have higher output rates due to the addition of a very stable power source. This is reflected in both electrification scenarios A and B having a higher hydrogen share than the reference scenario. In addition to an increase in hydrogen combustion, hydrogen usage is expected to begin in the early 2030s at nearly full capacity. As a result, during the energy transition period, natural gas consumption will be significantly reduced.

Power production and consumption

The difference with the relative scenario becomes more informative when comparing power consumption and generation trends. As shown in figure 5.21, the addition of a large nuclear power plant, combined with a reduction in the share of renewables, significantly smooths the maximum power generation capacity trend. After 2040, the power generation mix will have stabilised and will consist primarily of nuclear energy (roughly one-third of total capacity) and offshore wind.

Between 2030 and 2040, there will be a noticeable increase in electricity generation and consumption. The electrolysers can operate at full capacity due to the stable source of power provided by the nuclear reactor.

Second, the implementation of a nuclear facility drastically reduces the share of fossil fuels that remained high in the reference scenario. Following the reactor's operational start date, a negligible amount of natural gas is used to provide power in the region.

Lastly, despite its lower renewable capacity, scenario 1 reduces its reliance on imported electricity significantly. The yearly import dependence is projected to be around 8 PJ in 2050 (scenario B), while it was closer to 12 PJ in the reference scenario. Furthermore, import does not begin to develop until

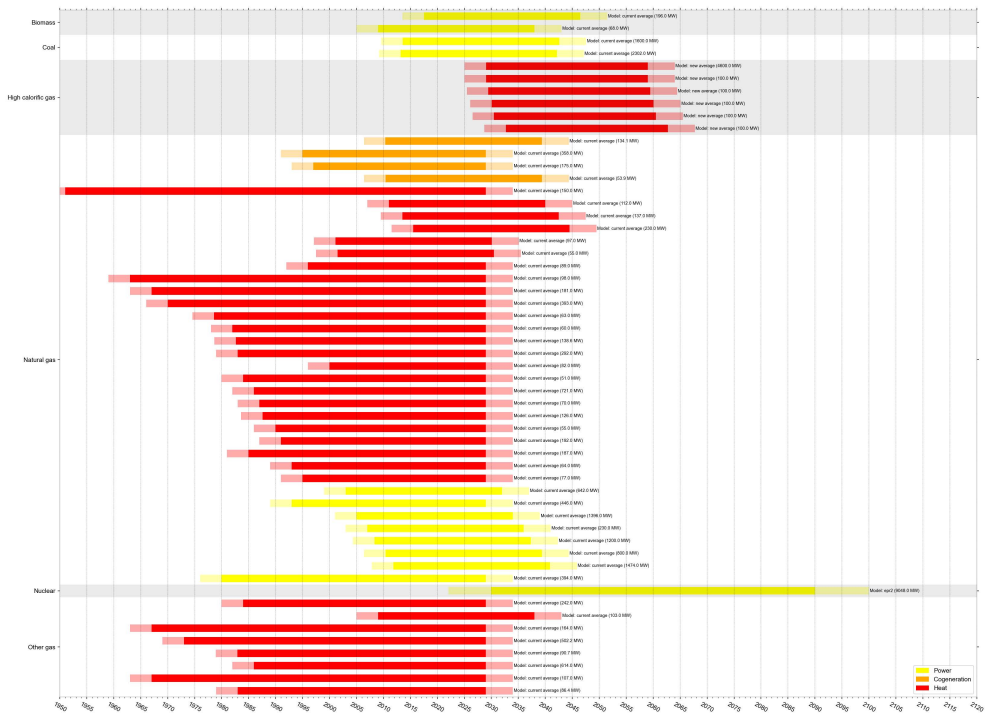

(a)

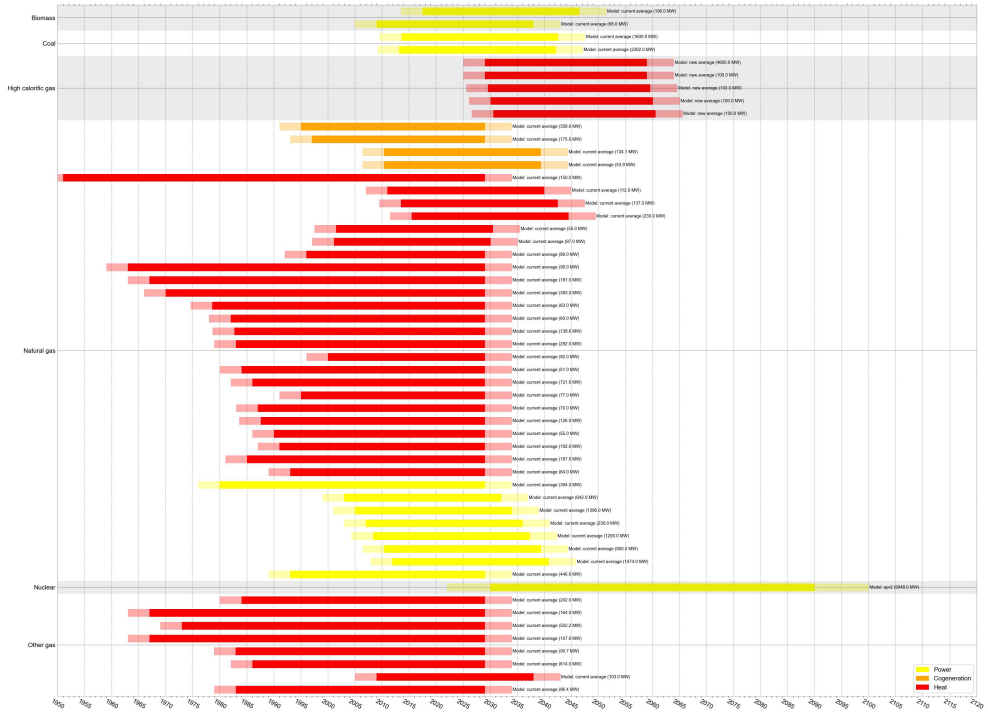

(b)

Fig. 5.19 Overview of the non-renewable energy plants over time in scenario 1. The plants are classified by their output energy- and fuel type. (a) electrification scenario A, (b) electrification scenario B.

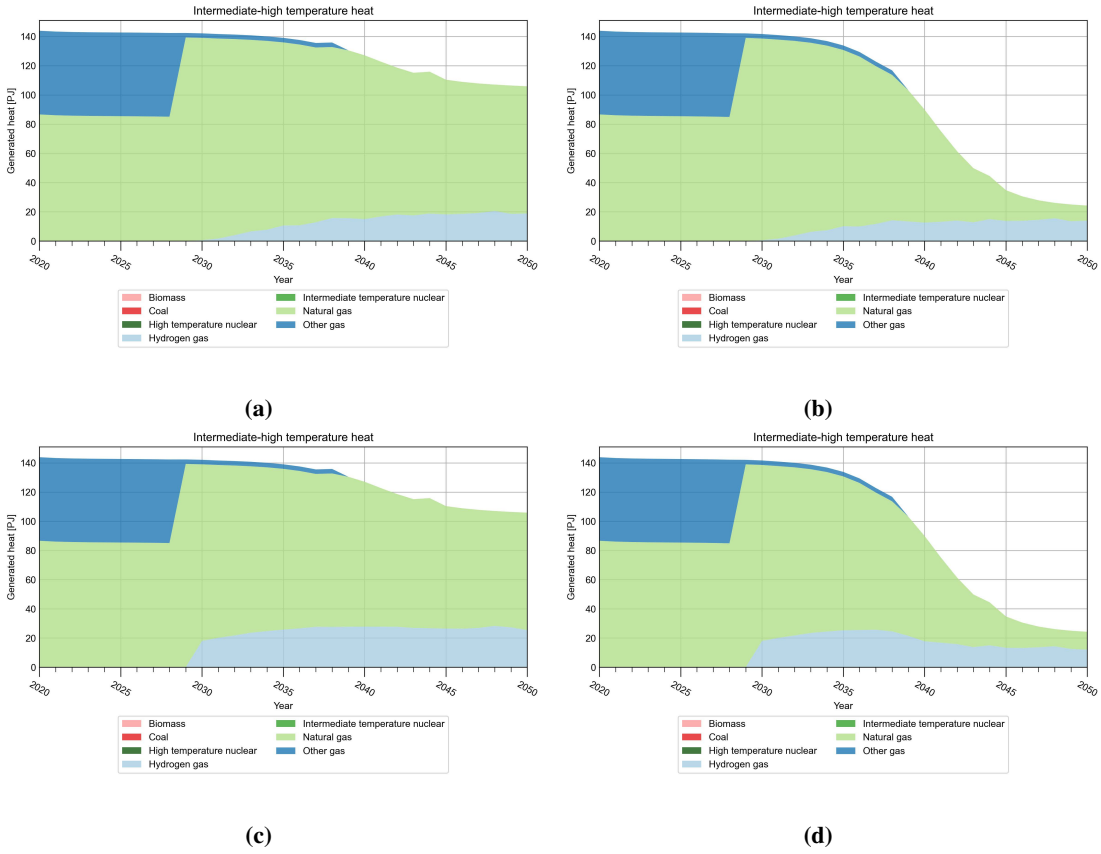

Fig. 5.20 Heat related energy balance including heat production by fuel type at low, intermediate, and high temperatures for scenario 1 (c-d). (a) reference scenario A, (b) reference scenario B, (c) electrification scenario A, (d) electrification scenario B.

well after 2040. In the long run, the construction of a new nuclear power reactor in the late 2030s could help prevent any type of import. The reliance on imports is already completely eliminated in the electrification scenario A.

5.3.2 Assessment life cycle results

In the following graphs, a grey scale is used to easily compare the operational effects of the reference scenario with the current strategy. The areas and lines depicted in this shade of grey represent the outcomes of the reference strategy.

For both the electrification scenarios the strategy behaves somewhat similar for many of the assessed elements, as seen in figures 5.22 and 5.23. Yet, the most evident difference is seen for chemical- and radioactive waste and water pollution. As expected the production of radioactive waste will significantly increase after the construction of the power plant.

After 2030, an annual maximum of 300 cubic metres of radioactive waste (scenario B) is produced. Approximately 96 percent of this waste can be recycled into new nuclear fuel, leaving approximately 11.1 m^3 of actual radioactive waste. A quarter of this waste is classified as high-level waste, with the remainder classified as low-to-intermediate waste. These figures translate into a storage capacity per decade of 84.5 m^3 for low-to-intermediate level waste and 25.5 m^3 for high level waste. When stored at COVRA, a new high-level storage facility must be built sometime after 2050. COVRA currently stores 110.1 cubic metres of high-level radioactive waste and 35,301 cubic metres of low-to-intermediate waste [126].

The strategy is assumed to perform significantly better than the reference strategy for chemical waste and water pollution values. Chemical waste production is reduced by approximately 40 cubic metres under electrification scenario A, and by approximately 25 m^3 under scenario B. The values for water pollution projections are reduced by more than half, reducing the strategy's potential to heavily pollute the region's water bodies.

At last, there is a noticeable decrease in total indirect projection costs, reducing the uncertainty from approximately 3 billion euros per year to 1.5 billion euros. As a result, this strategy is more likely to provide more affordable energy both during and after the transition period. Annual costs for both electrification scenarios are expected to fall by 1 billion euros in the first decade. These savings are primarily the result of lower operating and management costs, as well as less reliance on imported power.

5.3.3 End-of-life projections

The reference strategy's significant accumulation of EoL electronic waste from old solar panels, wind turbines, and lithium batteries was one of its major bottlenecks. As shown in figures 5.24 and 5.25, the replacement of renewables with nuclear power results in a significant reduction in EoL waste.

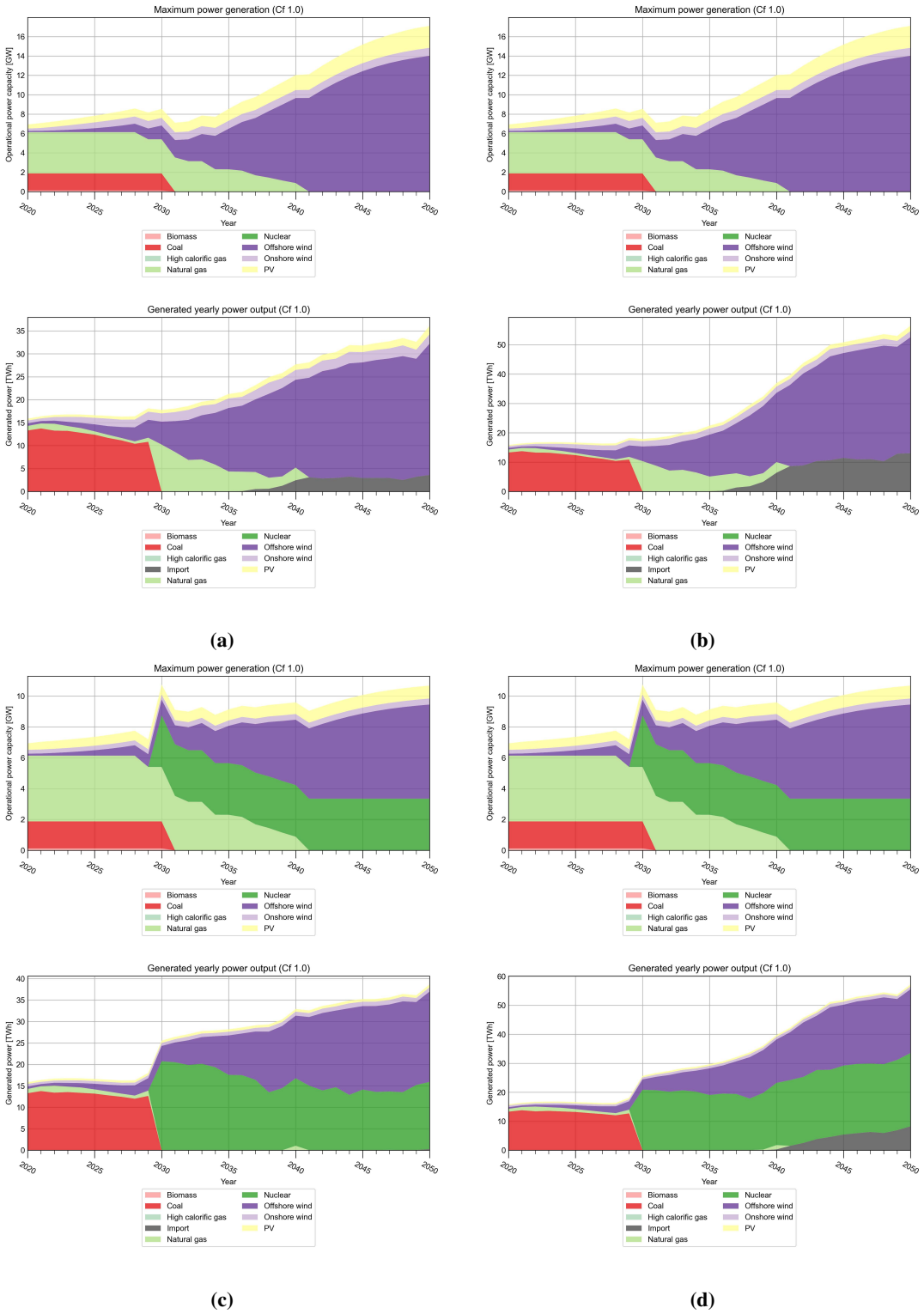

Fig. 5.21 Maximum installed power capacity and simulated electricity balance including power production by fuel and technology type for strategy scenario 1 (c-d). (a) reference scenario A, (b) reference scenario B, (c) electrification scenario A, (d) electrification scenario B.

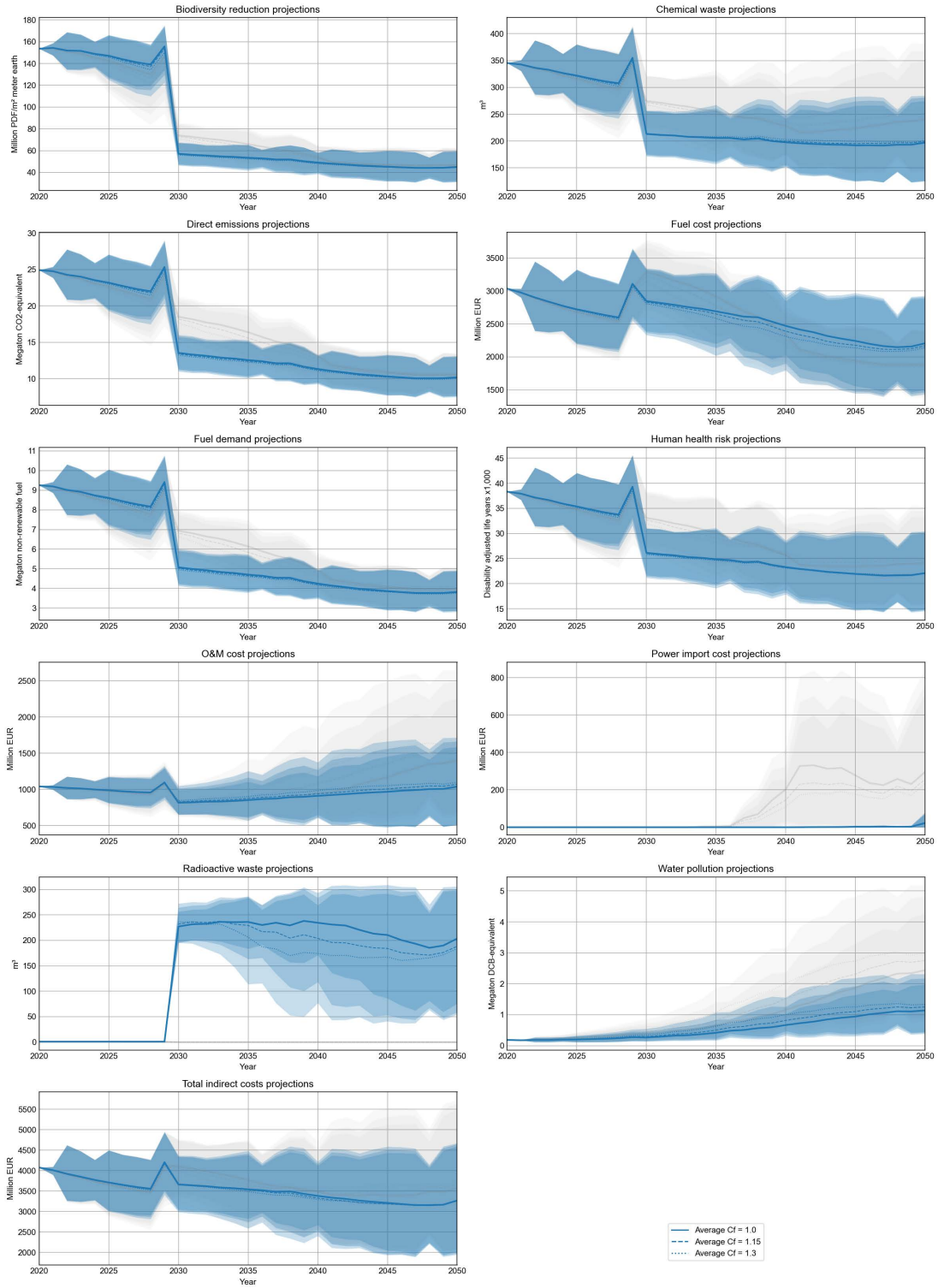

Fig. 5.22 Overview of the yearly projected operational effects following from the assessment framework. The graphs represent scenario 1 A. The plotted area represents the uncertainty range for all included climate scenarios. Transparent areas are classified as unlikely extremes.

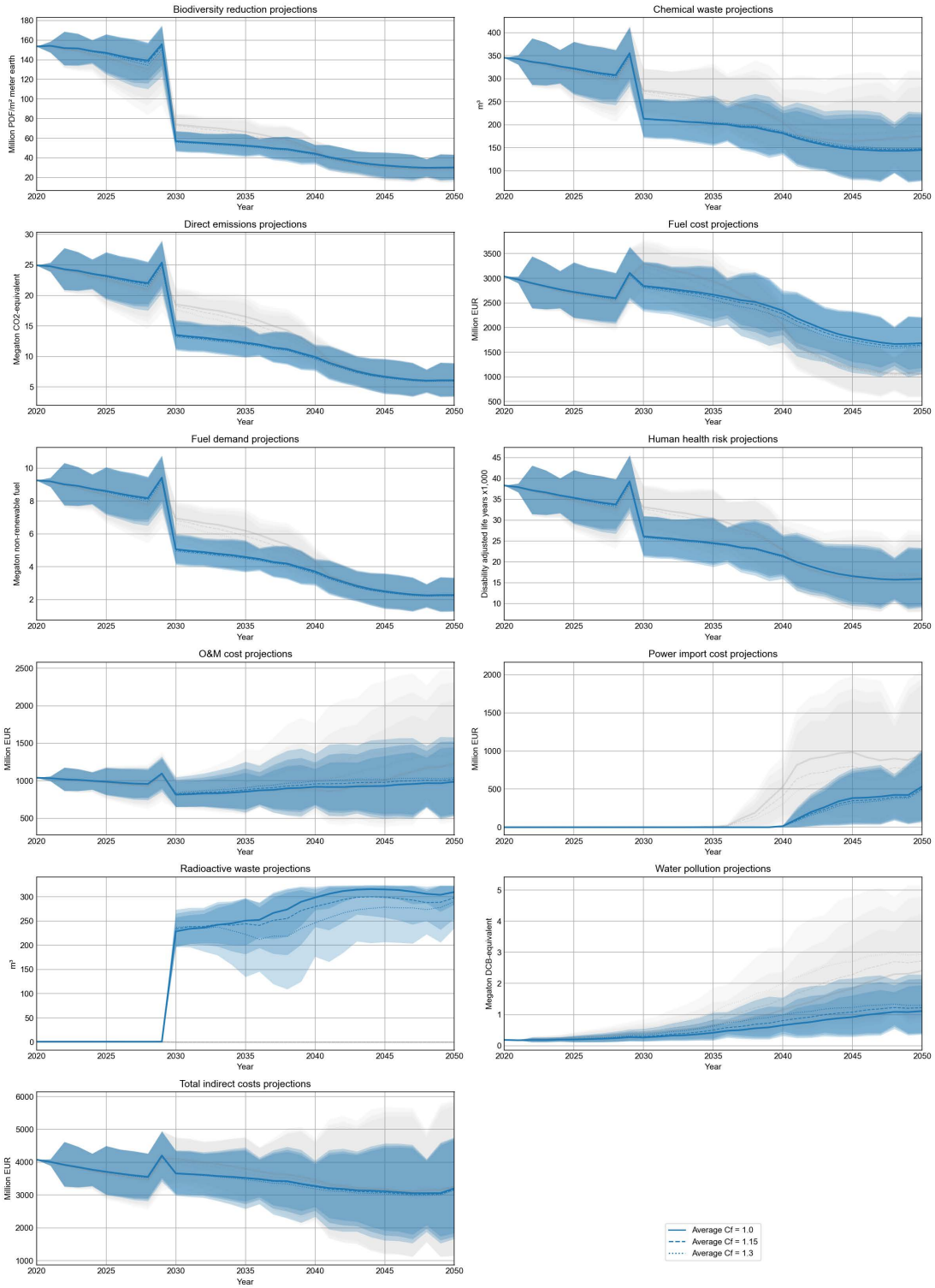

Fig. 5.23 Overview of the yearly projected operational effects following from the assessment framework. The graphs represent scenario 1 B. The plotted area represents the uncertainty range for all included climate scenarios. Transparent areas are classified as unlikely extremes.

This reduction is so significant that 150,000 fewer solar panels are accumulated over time, while EoL wind turbine count is expected to be reduced by 400 turbines.

Because of the nuclear strategy's higher net stability, less short-term electricity storage systems are required. In comparison to the reference scenario, electrification scenario A results in a reduction of approximately 100 accumulated battery parks in 2050. In electrification scenario B, almost all battery systems are obsolete, resulting in a battery park accumulation of slightly more than 100 in 2050. A value that is five times less than the reference scenario.

5.3.4 Energy strategy implications

Because of the high costs associated, the construction of a large generation III+ nuclear power plant twin will necessitate significant investment. Figures 5.26 and 5.27 show a sharp peak for 2030, the year the reactor goes online. This peak, however, will be smaller in reality because investment costs will be spread out over time. Currently, an 8-year construction timeframe is being considered. When investment costs are divided by construction years, a yearly investment of 3.4 billion is retained for 2022-2030. While this is still a significant investment, it will not significantly raise transition strategy prices because investment in renewable technologies has decreased significantly as well. The total transition investment cost for electrification scenario A is expected to be 71.96 billion euros. Costs for scenario B are estimated to be even lower, at around 68.04 billion euros over the three decades studied. A 35% reduction in direct costs compared to the reference energy transition. When investment costs and indirect costs are factored in, the total yearly energy cost per person will range between 2,245 EUR/person (scenario B) and 2,363 EUR/person (scenario A). Values are approximately 600 euros less than the reference scenario's projected total cost. The annual cost per person is 6.5 percent of the gross regional value product per citizen. While the uncertainty margins for indirect costs remain very high, savings relative to the reference strategy are likely.

GHG-emissions, like investment cost, are significantly less compared to the reference strategy. Due to the reduction energy storage systems and renewables the indirect emission is estimated to be reduced by 127.5 megatonnes of carbon-dioxide equivalents. A construction emission of 41.5 Mton remains.

The effects of renewable reductions in this strategy are even more visible in the spatial footprint projections. While the reference strategy uses 2,080 km^2 for energy generation and storage, the nuclear strategy uses only 900 km^2. This reduction is primarily due to the transition from low-energy density generation technologies to very dense energy generation facilities. When comparing only land coverage, the strategy occupies approximately 50 square kilometres, or 3.9% of the region's land, a 12-fold reduction from the reference strategy values. Furthermore, between 2020 and 2050, only 25 km^2 of additional energy space is required, reducing the search for energy producing acceptable locations by 450 square kilometres.

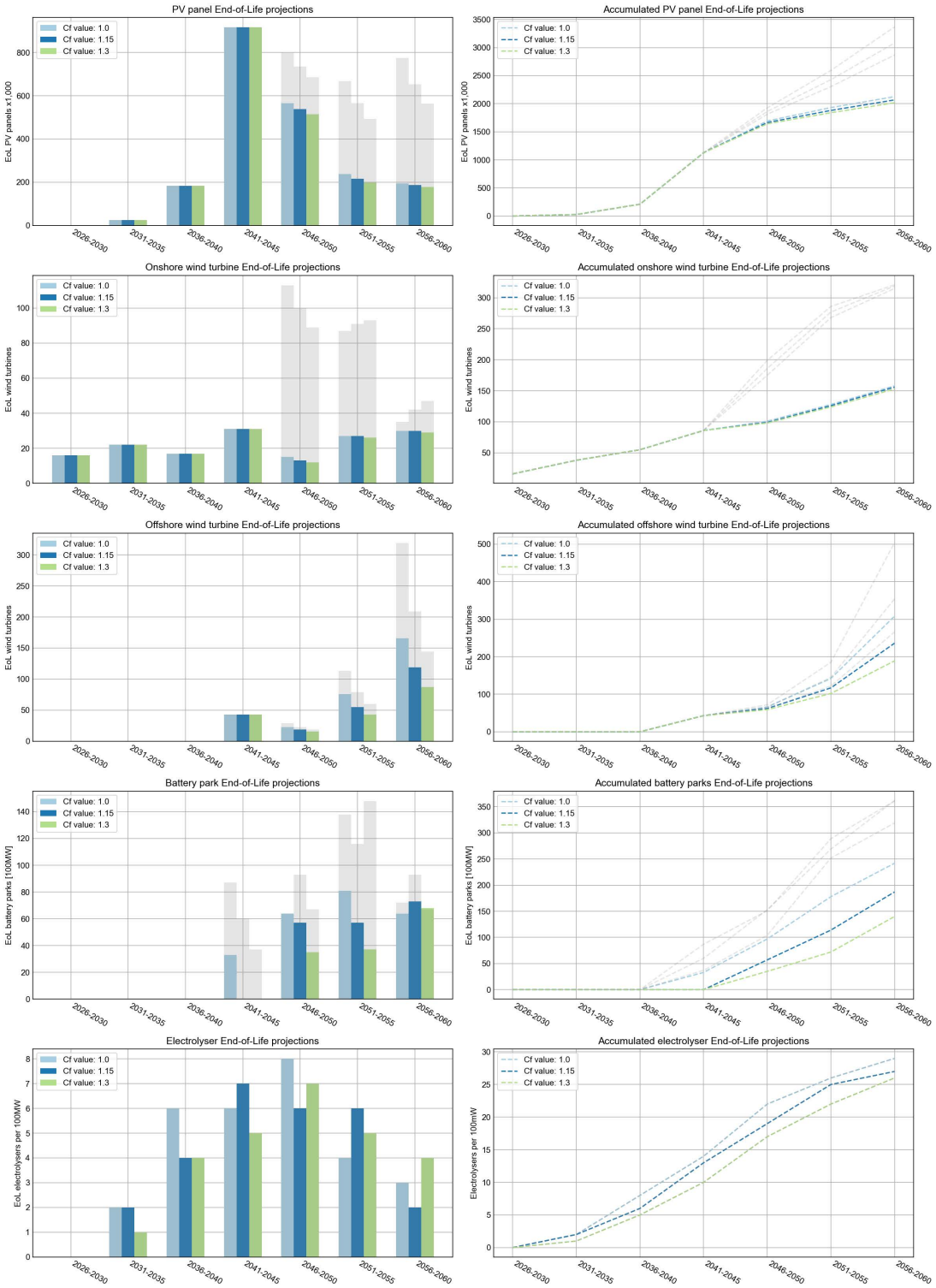

Fig. 5.24 Simulated projections of the End-of-Life renewable technology waste flow. The graphs represent scenario 1 A.

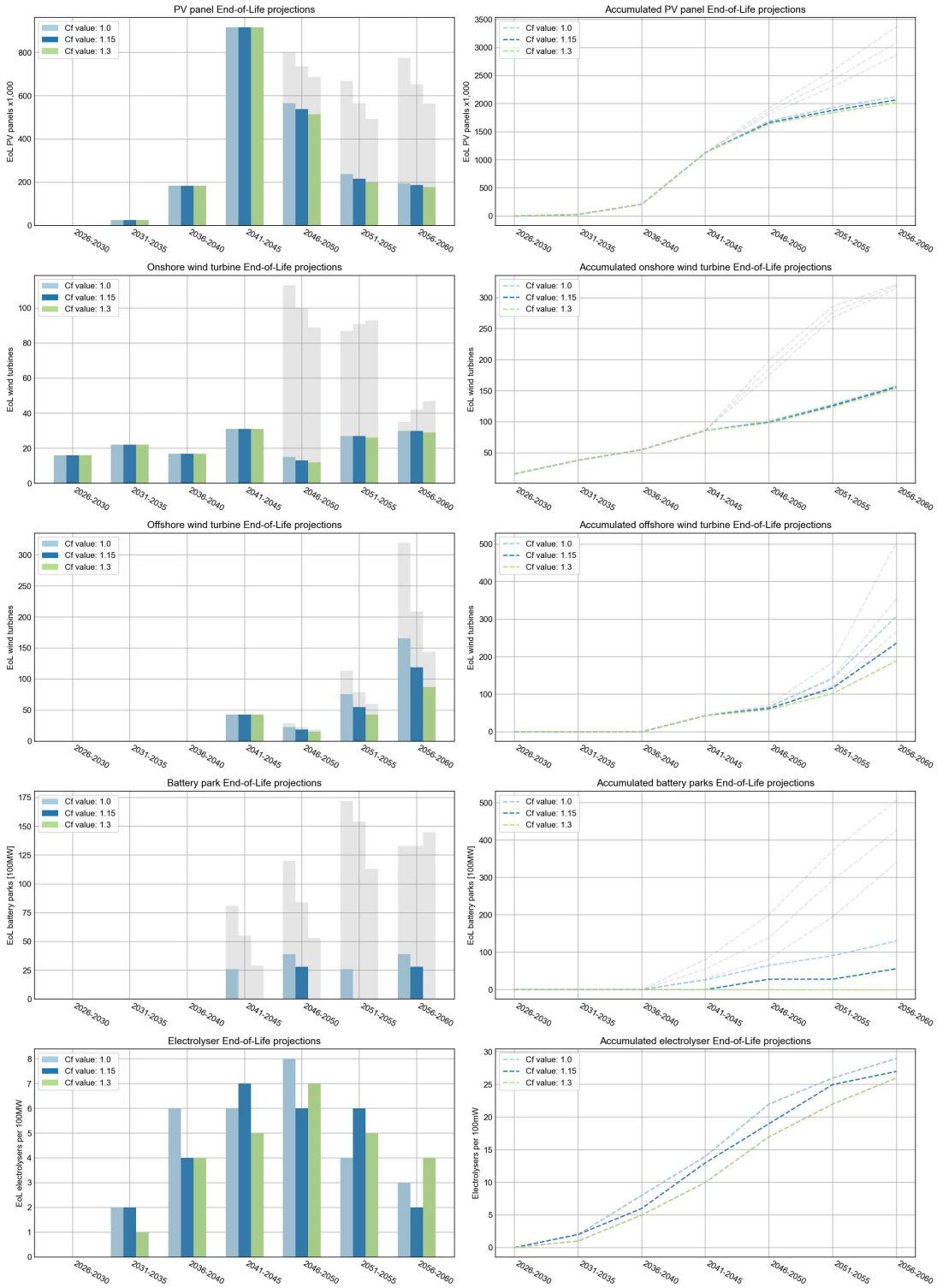

Fig. 5.25 Simulated projections of the End-of-Life renewable technology waste flow. The graphs represent scenario 1 B.

Relative to the reference strategy, no real change in job opportunities are projected post-2050, as both strategies balance around 20,000 additional yearly full-time equivalent workloads. However, due to the required workforce in the newly built reactor, the increase in workload is projected to occur two decades earlier. While the potential for innovation is growing, it still pales in comparison to the additional workload potential of the reference strategy. Between 2020 and 2050, an increase of 90,000 fte's is projected for the current nuclear scenario, while an increase of 220,000 fte's is projected for the reference strategy.

5.3.5 Material requirements

Another potential impediment to the region's proposed energy transition is the anticipated increase in critical raw material demand. The reference scenario featured demand intensifications of up to 600 times current demand (for dysprosium). These intensifications are significantly less for the current strategy. While many of the elements used in PV-panels-panels, wind turbines, and batteries are still in high demand, the increases are not as dramatic. Almost all elements see a decrease in their intensification factor. As a result, the potential material bottleneck discussed in the reference scenario is reduced.

Nonetheless, some nuclear reactor materials are expected to become more scarce. These include nickel, chromium, iron, copper, limestone, and aggregates, in descending order of expected increase.

5.3.6 Natural gas demand projections

Natural gas demand trends are unlikely to change in comparison to the reference scenario because the strategy's power production share is only revised. Nonetheless, natural gas demand is projected to be slightly lower between 2030 and 2045 due to the inactivity of the surplus gas combustion power plants. Reducing the projected 2030 demand peak by 3,000 tonnes.

5.3.7 Sub-scenario

Slight adjustments to scenario 1 are made to better understand the effects of energy buffers on a scenario including nuclear energy. Additionally, the removed hydrogen buffer is replaced by an advanced molten salt reactor thermal plant. The following results represent the sub-scenario (electrification A) with no battery systems, half the hydrogen capacity and one major MSR twin power/thermal plant (2 GW). Other parameters are similar to scenario 2.

Resulting from the simulation some findings were expected. Due to the decrease in hydrogen electrolysers the power consumption in the region drops significantly. Next, similar to the reference sub-scenario, a decrease in buffer support systems lowers the required amount of critical raw materials and reduces the EoL electronic waste flow significantly. Additionally, the construction of new nuclear reactors results in the increase of employment, innovation and direct cost rates. Nevertheless, as these

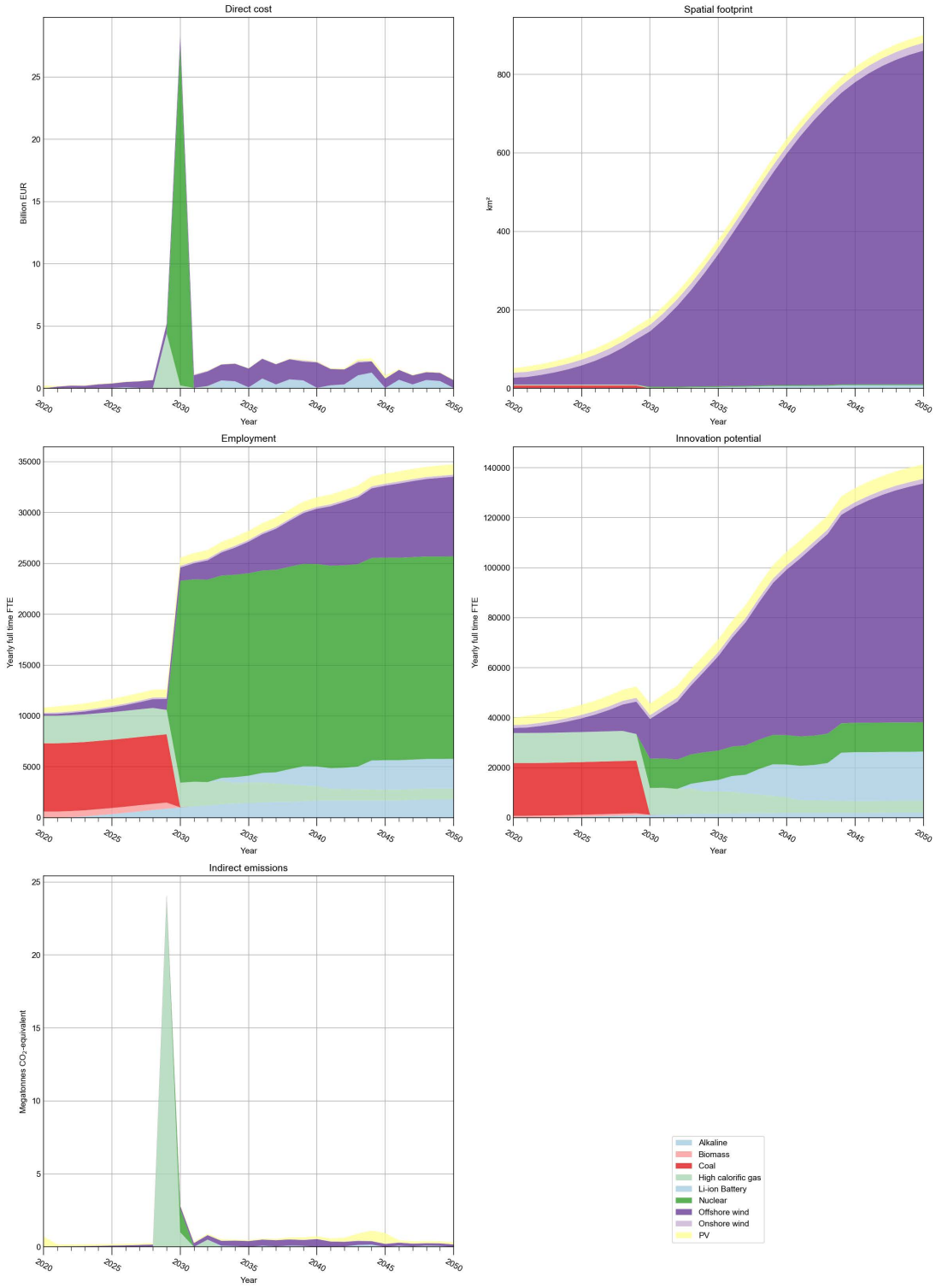

Fig. 5.26 Overview of the projected implications resulting from the energy strategy scenario. The graphs represent scenario 1 A under standard projection conditions.

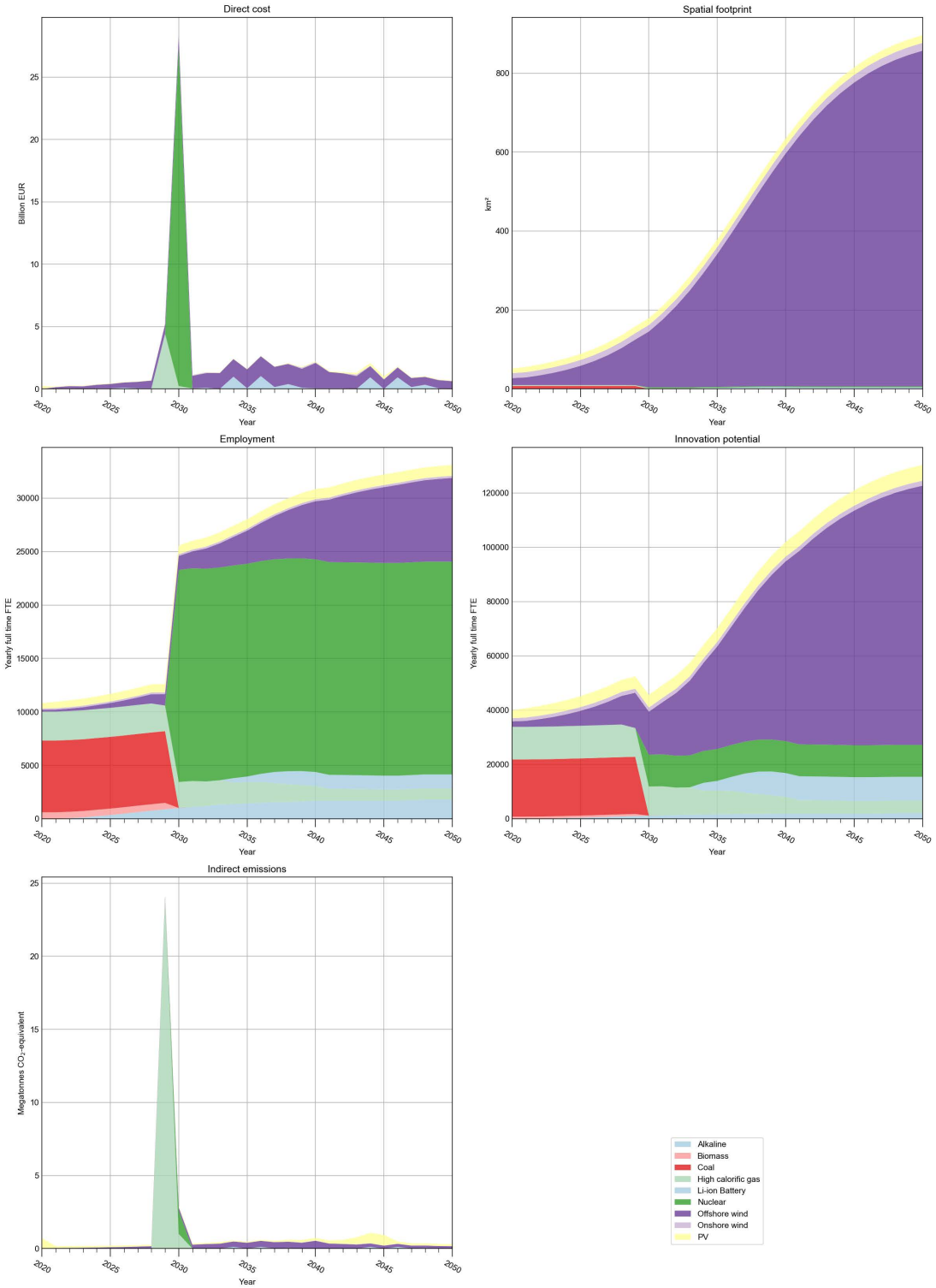

Fig. 5.27 Overview of the projected implications resulting from the energy strategy scenario. The graphs represent scenario 1 B under standard projection conditions.

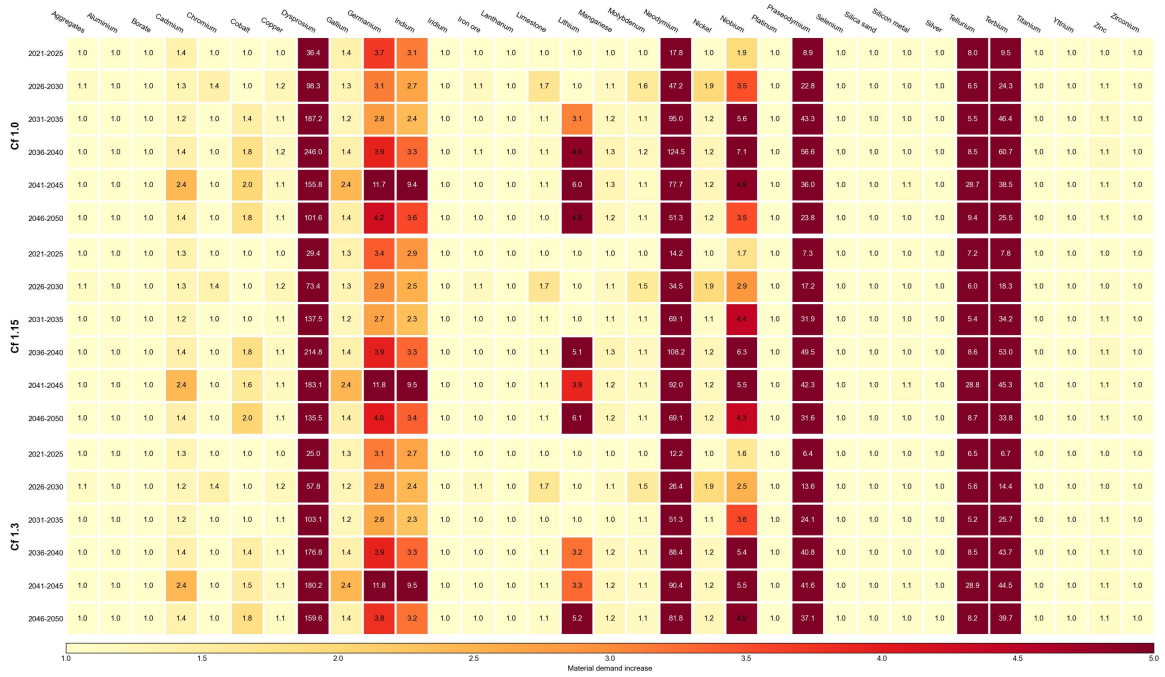

(a)

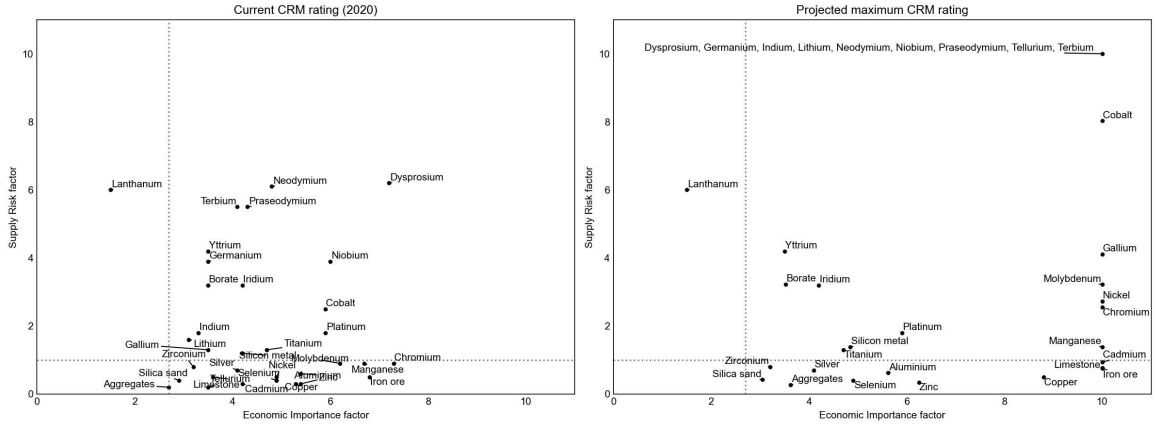

(b)

Fig. 5.28 Overview of the major materials in the European Union and the projected requirement intensification. The graphs represent scenario 1 A. (a) material demand increases, (b) current critical raw material plot (left) and the estimated trend behaviour (right) for standard trend projections (Cf=1.0).

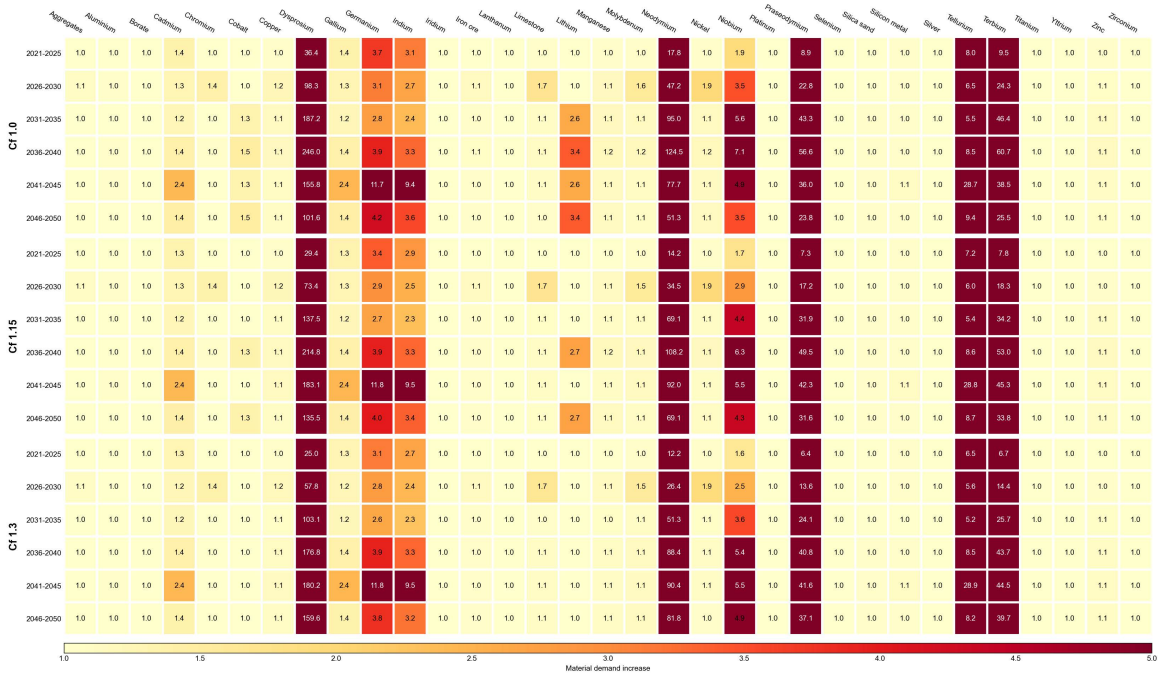

(a)

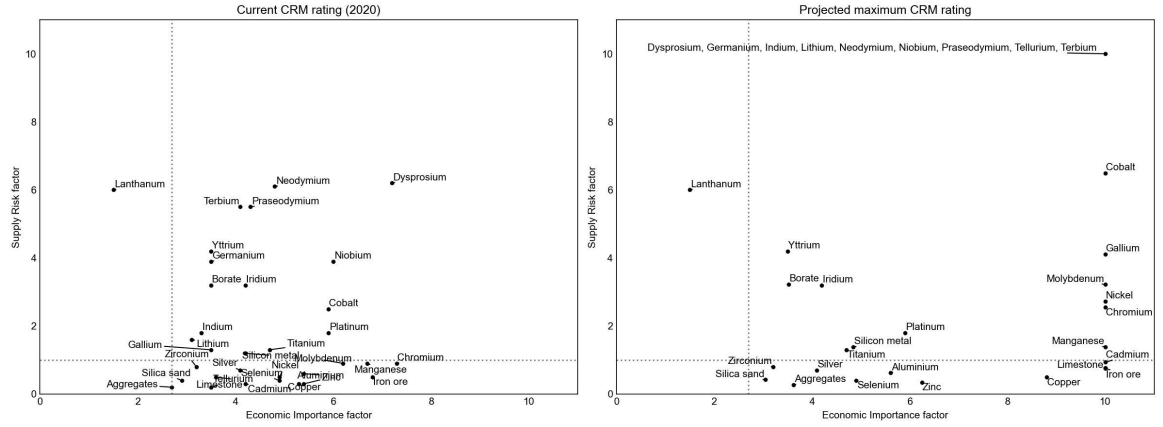

(b)

Fig. 5.29 Overview of the major materials in the European Union and the projected requirement intensification. The graphs represent scenario 1 B. (a) material demand increases, (b) current critical raw material plot (left) and the estimated trend behaviour (right) for standard trend projections (Cf=1.0).

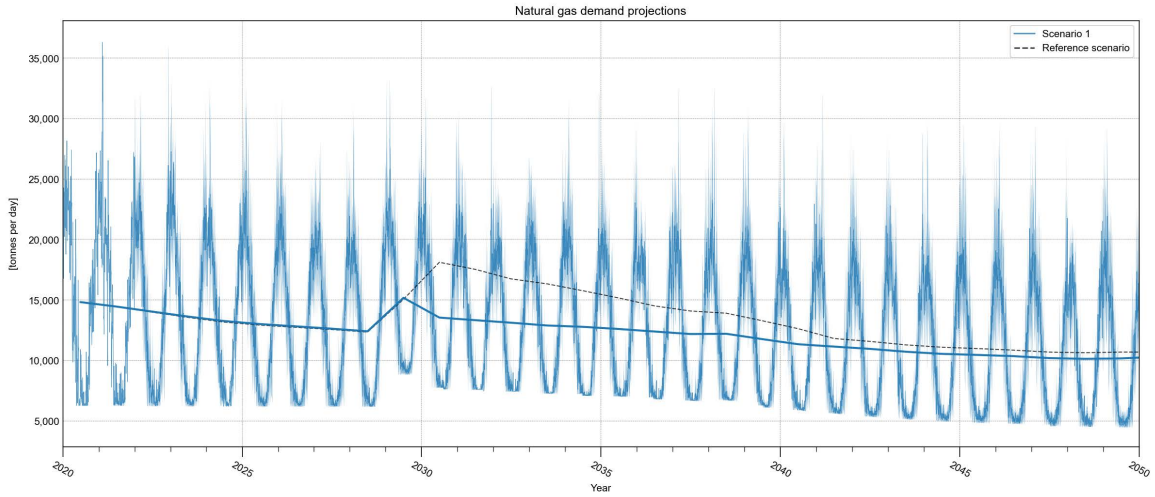

(a)

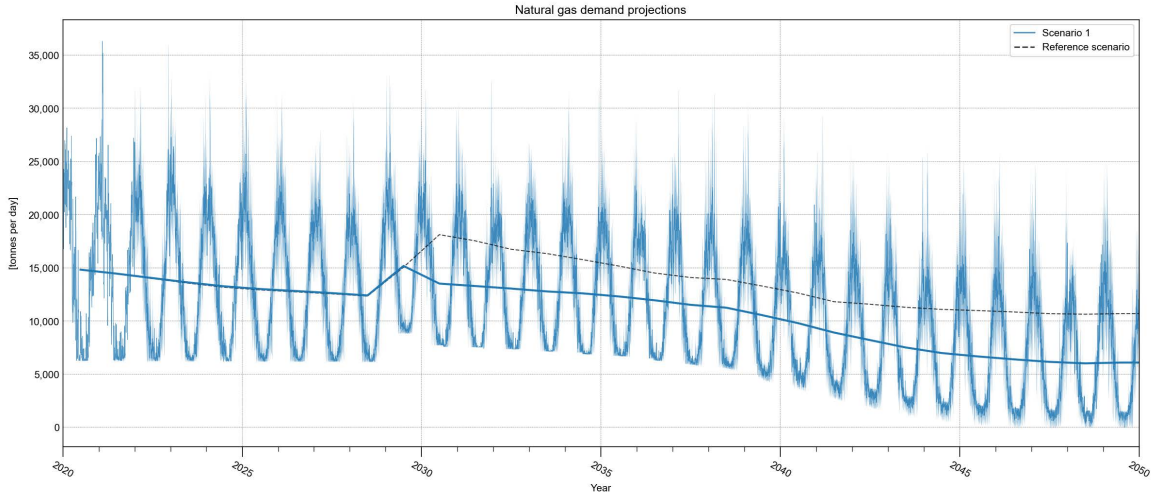

(b)

Fig. 5.30 Projections for daily natural gas demand in the MRDH region for scenario 1 under standard conditions. (a) electrification scenario A, (b) electrification scenario B.

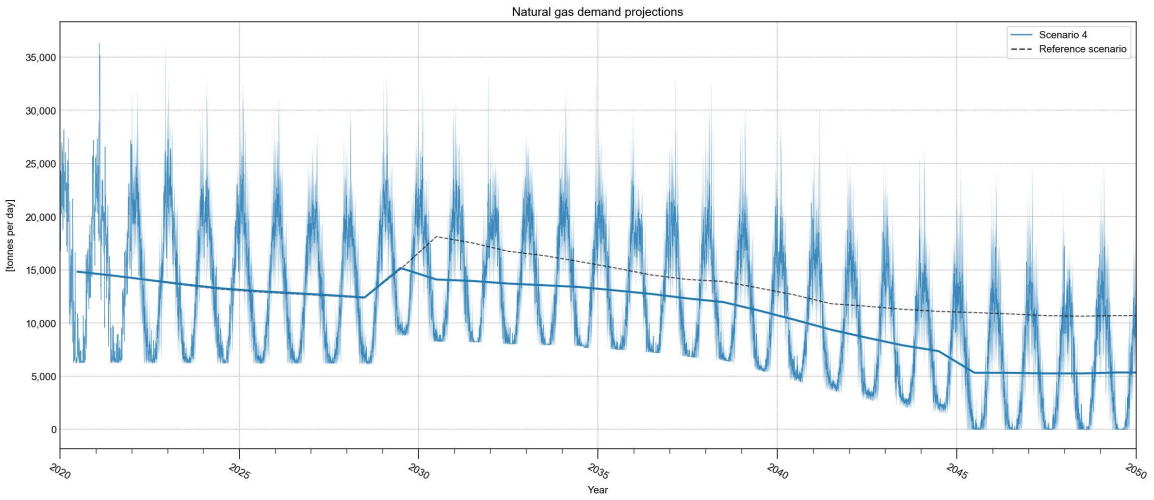

Fig. 5.31 Projections for daily natural gas demand in the MRDH region for the reference sub-scenario under standard conditions, electrification scenario B.

reactors are constructed late in the transition period a large share of the transition is characterised by an increased amount of chemical and GHG pollution relative to scenario 1.

More surprising is the capability of a second nuclear twin reactor to prevent net instability. Implementation of multiple nuclear reactors necessitates fewer support systems, such as batteries and electrolysers. This decrease in support systems is directly translated into significant lower operational costs of roughly 15%. Nevertheless, even while stability is maintained in the late-transition period, during the transition period the negative effects of a low storage support system share do not outweigh the benefits.

5.3.8 Conclusion

Nuclear scenario 1 will be compared to the currently proposed reference strategy in the following conclusion. Benefits, challenges, and bottlenecks discussed previously will be re-evaluated for the nuclear strategy.

General outcome Emissions show little to no improvement when compared to the reference scenario. Some cost savings are anticipated as a result of the drastically reduced transition investment cost. In conjunction with the reduction of indirect cots, this could result in more affordable electricity.

Advantages Many of the advantages discussed are also reflected in the nuclear scenario. Human health risks and biodiversity reductions are significantly improving in comparison to the current situation. In addition, similar to the reference scenario, the transition strategy is expected to create a large new job market. Unlike the previous strategy, which focused on renewable technology

Fig. 5.32 Performance overview of the two strategies of scenario 1 relative to all researched scenarios. Values range from worst (1) to best (5). The grey area represents the reference scenario.

construction and maintenance, the nuclear strategy creates many new jobs around its reactor facility. Therefore, many jobs become available early in the transition period.

Lower innovation potential projections are observed in comparison to the reference scenario. Nonetheless, industry potential will increase when compared to current estimates and is therefore not seen as a potential disadvantage.

In the late transition stage nuclear facilities have the ability to steadily reduce the dependence on support storage systems. Consequently lowering the requirement for additional technologies with their negative implications such as material requirements, additional electronic waste flows and operational costs.

Challenges In terms of transition challenges, the strategy that includes nuclear power significantly reduces potential issues. While the spatial footprint of the reference energy mix was extremely large, the nuclear power plant drastically decreased this value. Such reductions leave more room for other necessary regional developments such as housing and environmental preservation.

Second, the strategy's water degrading potential is nearly halved, lowering the potential long-term consequences on the region's water bodies.

Despite the aforementioned improvements, nuclear implementation will present a new challenge in the form of radioactive waste. Nonetheless, with the current simulated capacity, nuclear waste generation is minimal. If all produced radioactive waste is stored at the national nuclear waste facility Corva, no potential problems are expected.

Bottlenecks By incorporating a nuclear power plant into the regional energy strategy, the most pressing potential bottlenecks are mitigated. The potential problems with EoL waste handling caused by the accumulation of electronic waste, as well as the potential supply risks for required transitional

materials, are greatly reduced. As a result, the unpredictability of future decommissioning costs and material prices is reduced.

Furthermore, as electricity imports and, to a lesser extent, natural gas demand decline, the region's reliance on its energy system decreases over time. Because of its lower vulnerability to a potentially volatile energy market, this decline could protect energy affordability. Nuclear fuel instability is regarded as a minor threat to energy affordability due to its low cost and abundant global supply.

5.4 Scenario 2

The second nuclear-focused strategy investigates the potential benefits and drawbacks of intensive integration of small modular reactors post-2036. Exploring the alternative to the ambitious electrification of intermediate temperature industry.

5.4.1 Transition strategy overview

Figure 5.33 clearly shows that integrating many small modular reactors in the late 2030s dramatically reduces the total constructed capacity of high calorific gas plants, as nuclear energy can provide both low- and intermediate heat. For high temperature industrial processes, some gas combustion capacity is still required. Despite this, hydrogen is expected to meet the majority of the region's high temperature needs due to its significantly reduced reliance on high calorific gas.

Heat production and consumption

The addition of small modular thermal reactors transforms the thermal energy system of the region almost instantly after the construction of the first ASMRs. Because these reactors are only providing heat with temperatures just above 300 °C, some high temperature thermal gas plants are still operating well after 2035, as seen in figure 5.34.

When the heat balances of both electrification scenarios are examined, as shown in figure 5.34 (c-d), it is clear that electrification of the intermediate temperature industry is likely to result in natural gas dependence after 2050. However, if some of the reactors are converted into power plants with hydrogen electrolysers, this natural gas combustion could be avoided. Nevertheless, this would be a very inefficient approach. As a result, for the proposed energy system composition, electrification scenario A would be the most efficient strategy.

Power production and consumption

A high concentration of nuclear power plants is expected to significantly stabilise the region's electricity grid. As a result, this stability will ensure maximum electrolyser performance, delivering a consistent amount of hydrogen for high-temperature applications. As illustrated in Figure 5.36, the energy system's relatively stable maximum power capacity generates a large amount of electricity.

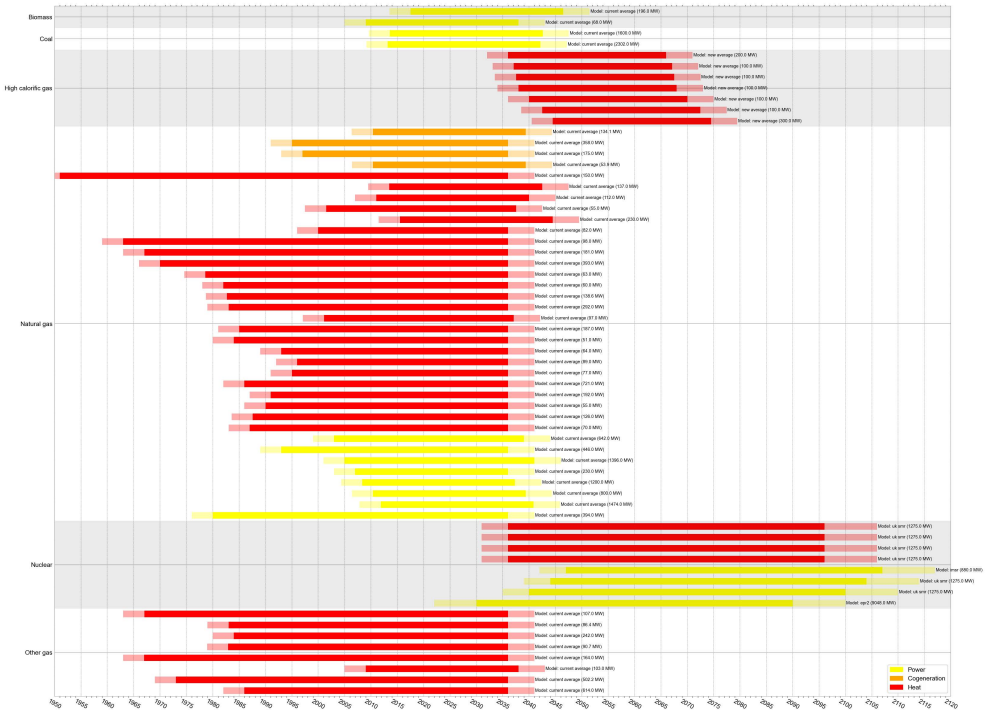

(a)

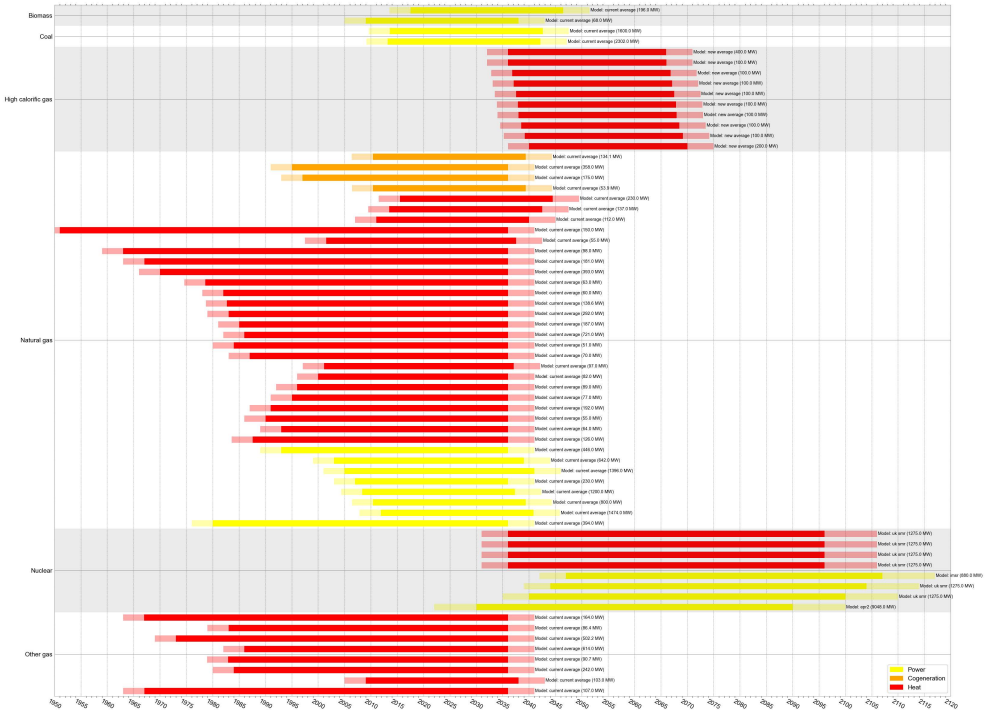

(b)

Fig. 5.33 Overview of the non-renewable energy plants over time in scenario 2. The plants are classified by their output energy- and fuel type. (a) electrification scenario A, (b) electrification scenario B.

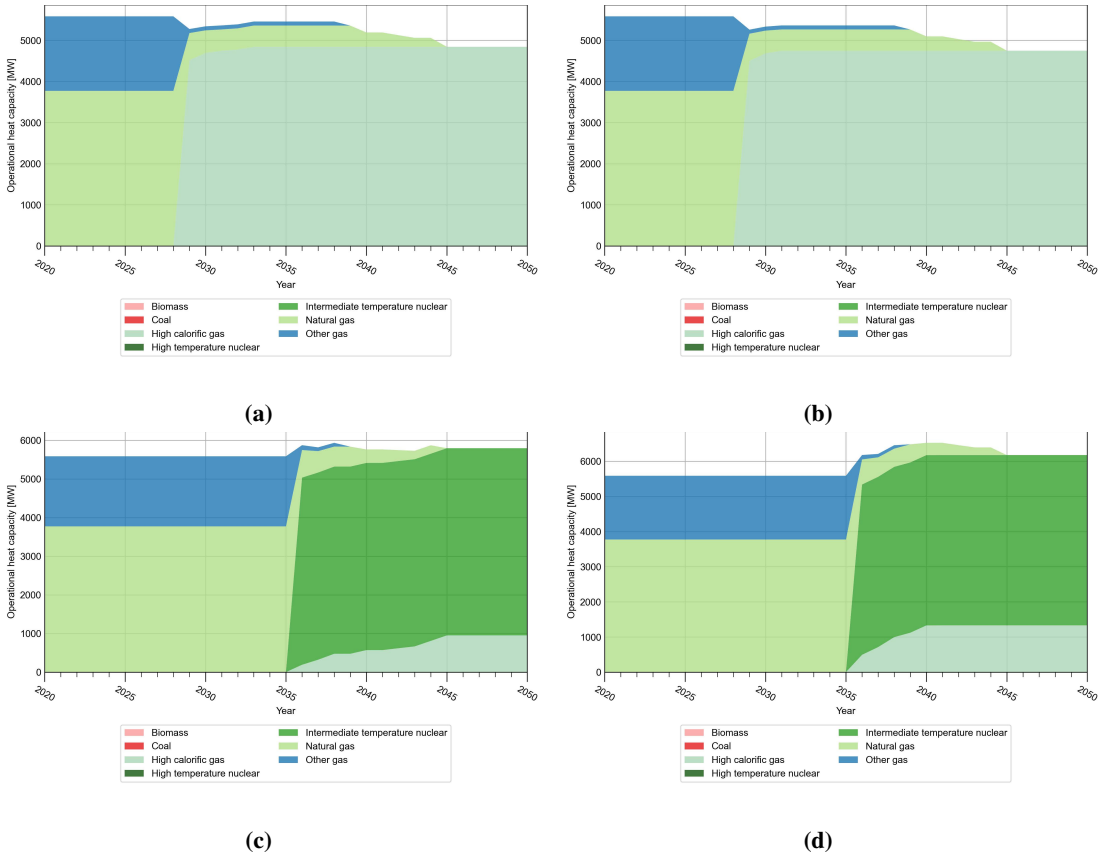

Fig. 5.34 Overview of the heat production capacity per fuel type at low, intermediate, and high temperatures for scenario 2 (c-d). (a) reference scenario A, (b) reference scenario B, (c) electrification scenario A, (d) electrification scenario B.

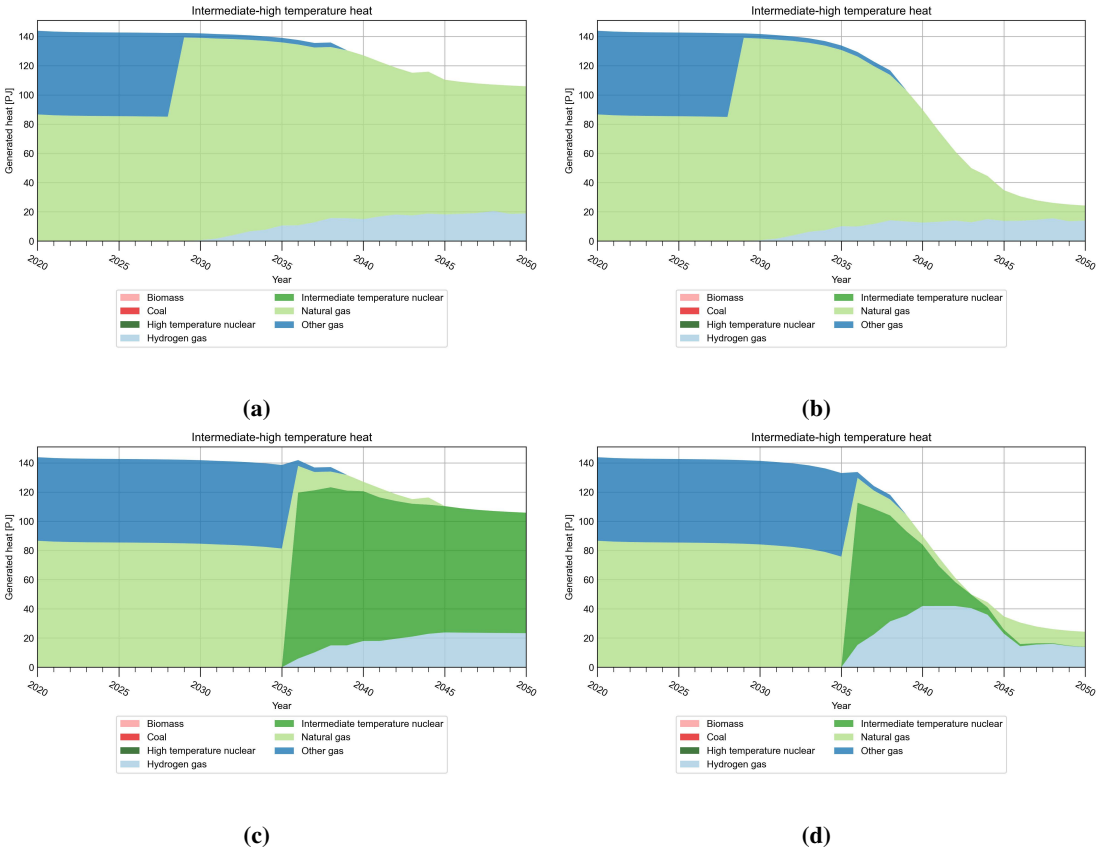

Fig. 5.35 Heat related energy balance including heat production by fuel type at low, intermediate, and high temperatures for scenario 2 (c-d). (a) reference scenario A, (b) reference scenario B, (c) electrification scenario A, (d) electrification scenario B.

A direct result of a high energy density and production efficiency electricity grid. In comparison to scenario 1, the generated power output is significantly higher (around 15 PJ), owing to the peak performance of all the region's electrolysers.

5.4.2 Assessment life cycle results

When the projected operational implications of the currently investigated transition strategy are compared, it is clear that the strategy performs exceptionally well for many of the evaluated elements. Figures 5.37 and 5.38 show that biodiversity, human health risks, chemical waste, water pollution factor, and direct emissions drop to levels not seen in the other evaluated strategies. All of these substantial reductions are projected with relatively narrow uncertainty ranges.

The direct effect of ASMR implementation is clear from these projection graphs. The negative impact of the transition strategy diminishes with each new reactor that comes online. This is especially true for thermally focused reactors.

What becomes clear from these projection graphs is the direct effect of ASMR implementation. Every time a new reactor becomes operational the negative impact of the transition strategy shrinks. This effect is especially strong for thermal focused reactors. The development of more small modular power plants appears to have a limited influence on further reductions.

On the other hand, as more reactors are built, radioactive waste production will rise steadily. Because the majority of the reactors operate at maximum performance rates, the output projections are fairly certain. With annual production peaking at around 630 cubic metres in the late 2040s. This translates into a real radioactive waste volume of 23.3 m^3, or 177.5 cubic metres of low-to-intermediate level waste and 53.6 cubic metres of high level waste per ten years. More high-level waste storage facilities would be required to safely store the produced volume. Nevertheless, construction of a small modular molten salt powere reactor is expected to lower yearly radioactive waste production by 130 cubic metres.

Finally, due to complete electricity independence and lower operational and management costs, the total indirect cost is projected to be slightly lower than in the reference scenario. The early shift away from natural gas is most likely the cause of mid-transition cost savings compared to the other two strategies. The construction of multiple thermal modular reactors resulted in a 500 million euro annual indirect cost savings. Another half a billion in cost savings is expected when the IMSR begins operations, as both fuel and waste disposal costs fall.

5.4.3 End-of-life projections

As seen in figures 5.39 and 5.40, no significant differences from scenario 1 occur for the projected years.

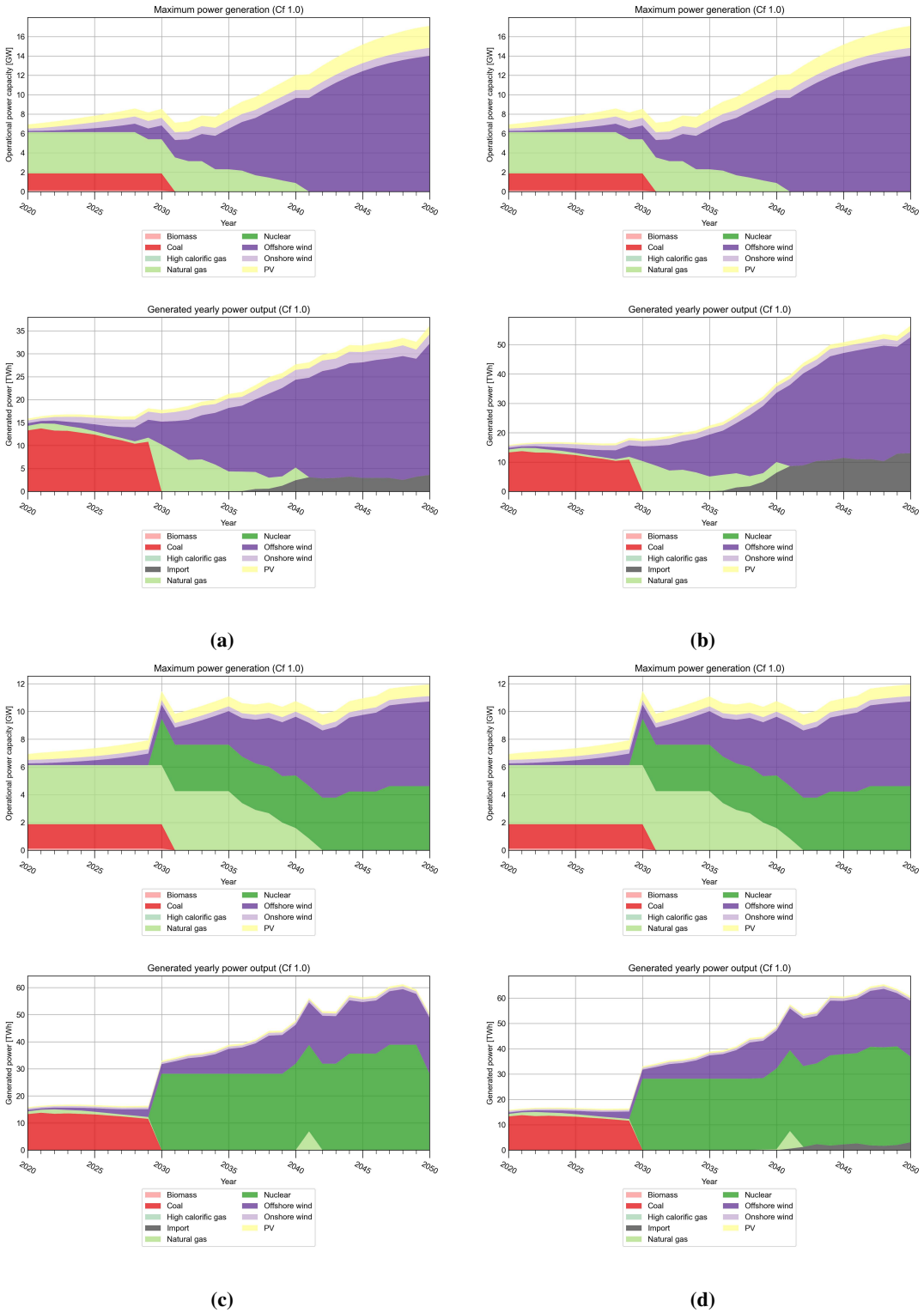

Fig. 5.36 Maximum installed power capacity and simulated electricity balance including power production by fuel and technology type for strategy scenario 2 (c-d). (a) reference scenario A, (b) reference scenario B, (c) electrification scenario A, (d) electrification scenario B.

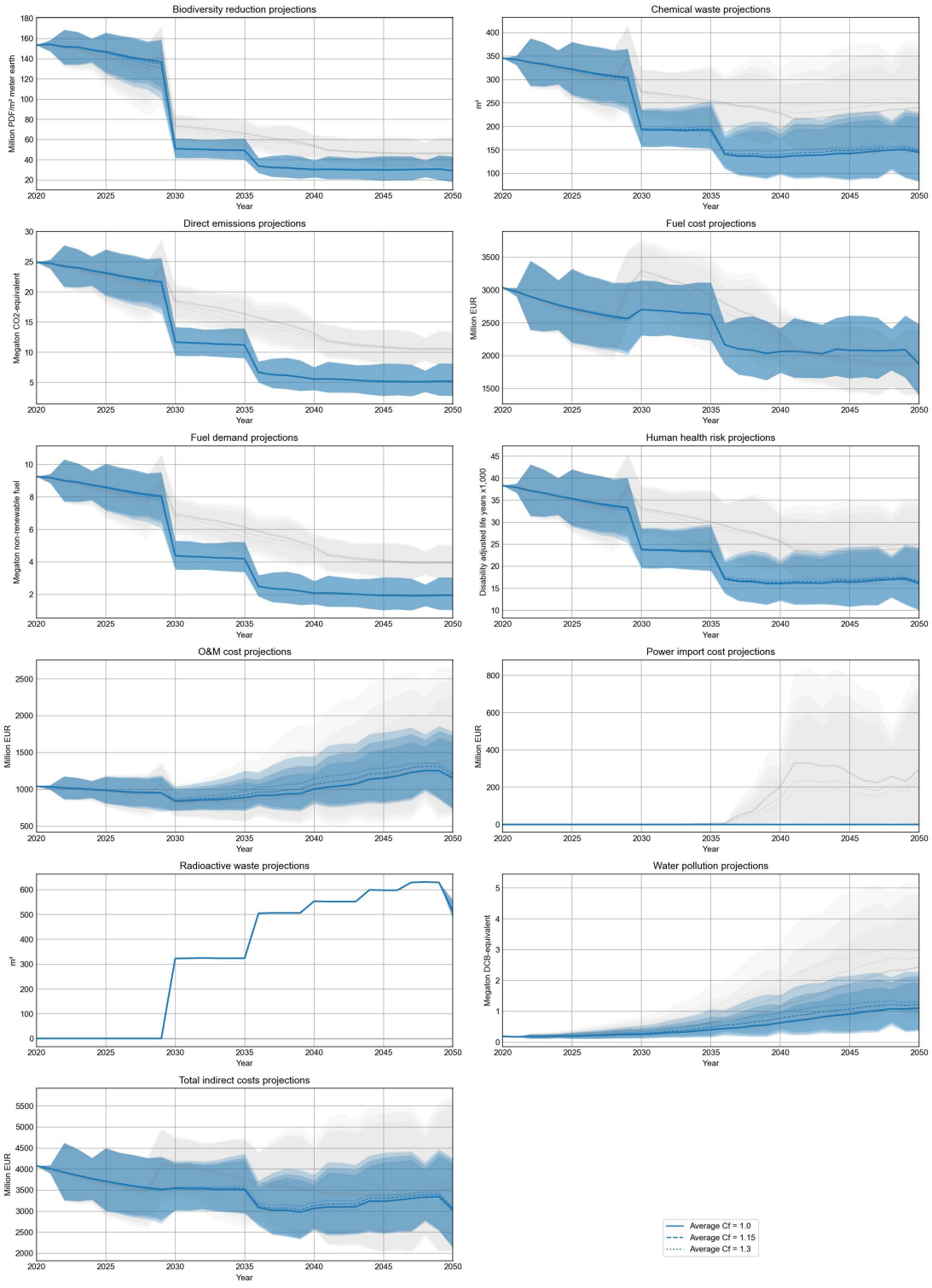

Fig. 5.37 Overview of the yearly projected operational effects following from the assessment framework. The graphs represent scenario 2 A. The plotted area represents the uncertainty range for all included climate scenarios. Transparent areas are classified as unlikely extremes.

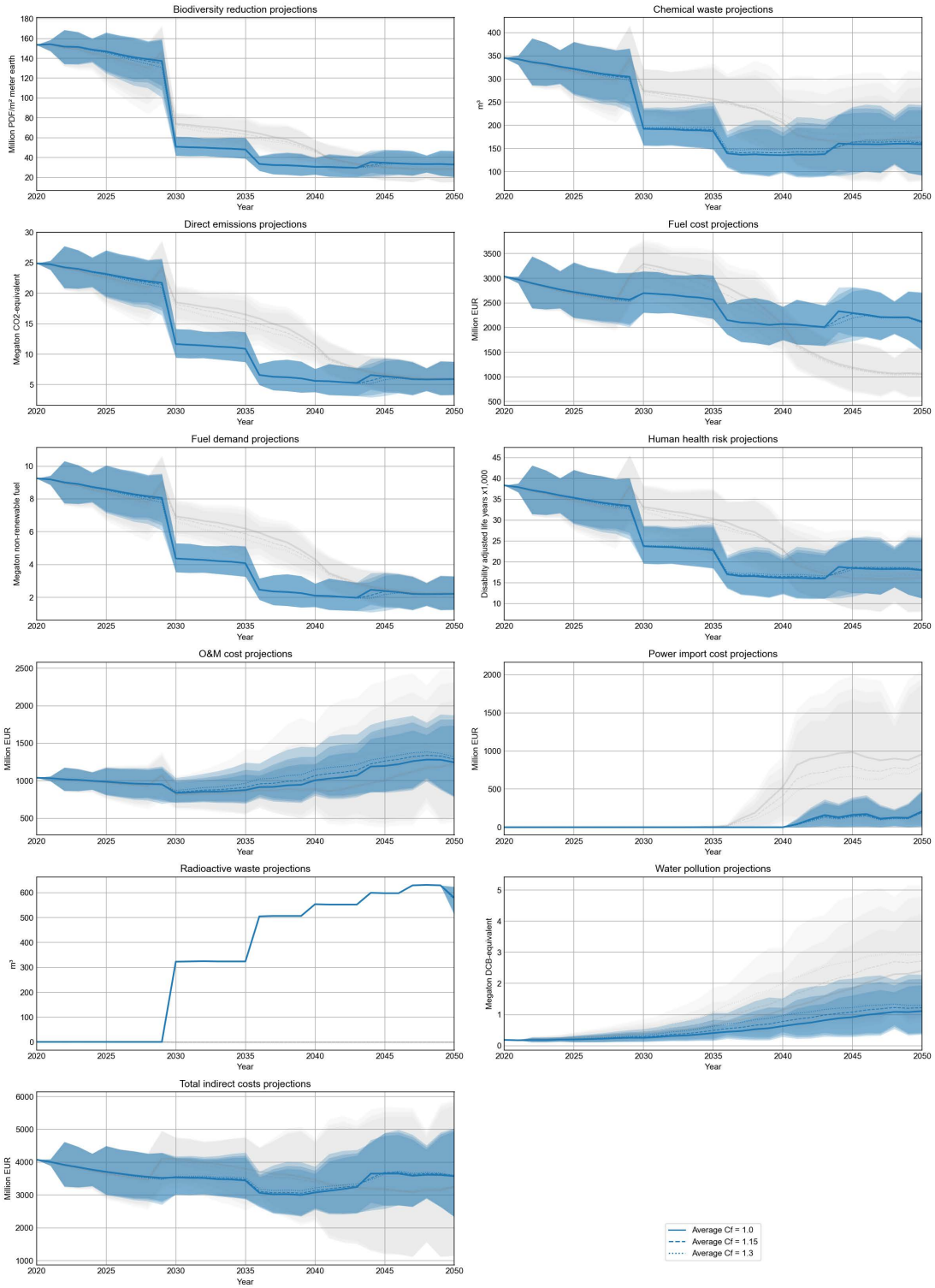

Fig. 5.38 Overview of the yearly projected operational effects following from the assessment framework. The graphs represent scenario 2 B. The plotted area represents the uncertainty range for all included climate scenarios. Transparent areas are classified as unlikely extremes.

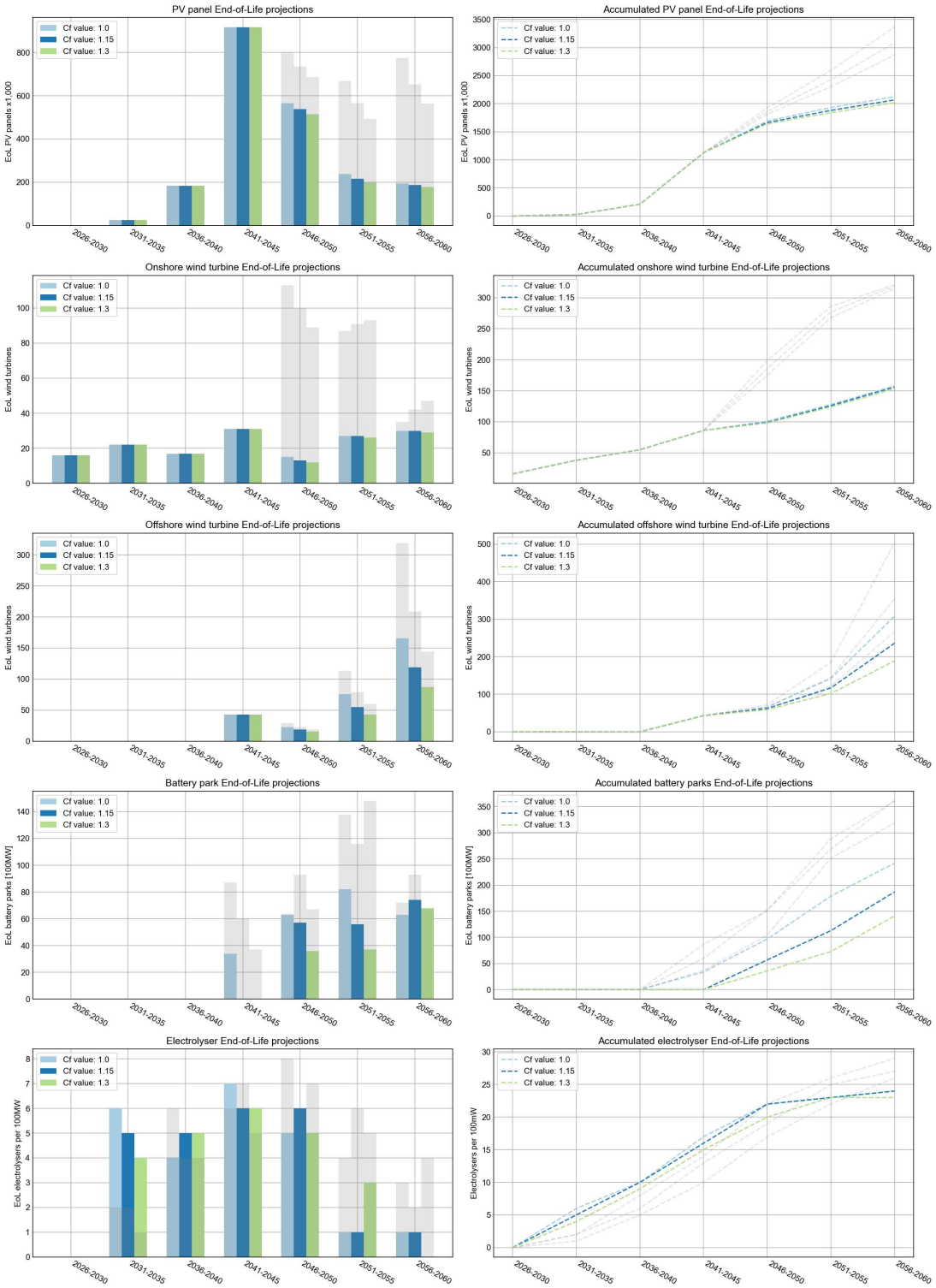

Fig. 5.39 Simulated projections of the End-of-Life renewable technology waste flow. The graphs represent scenario 2 A.

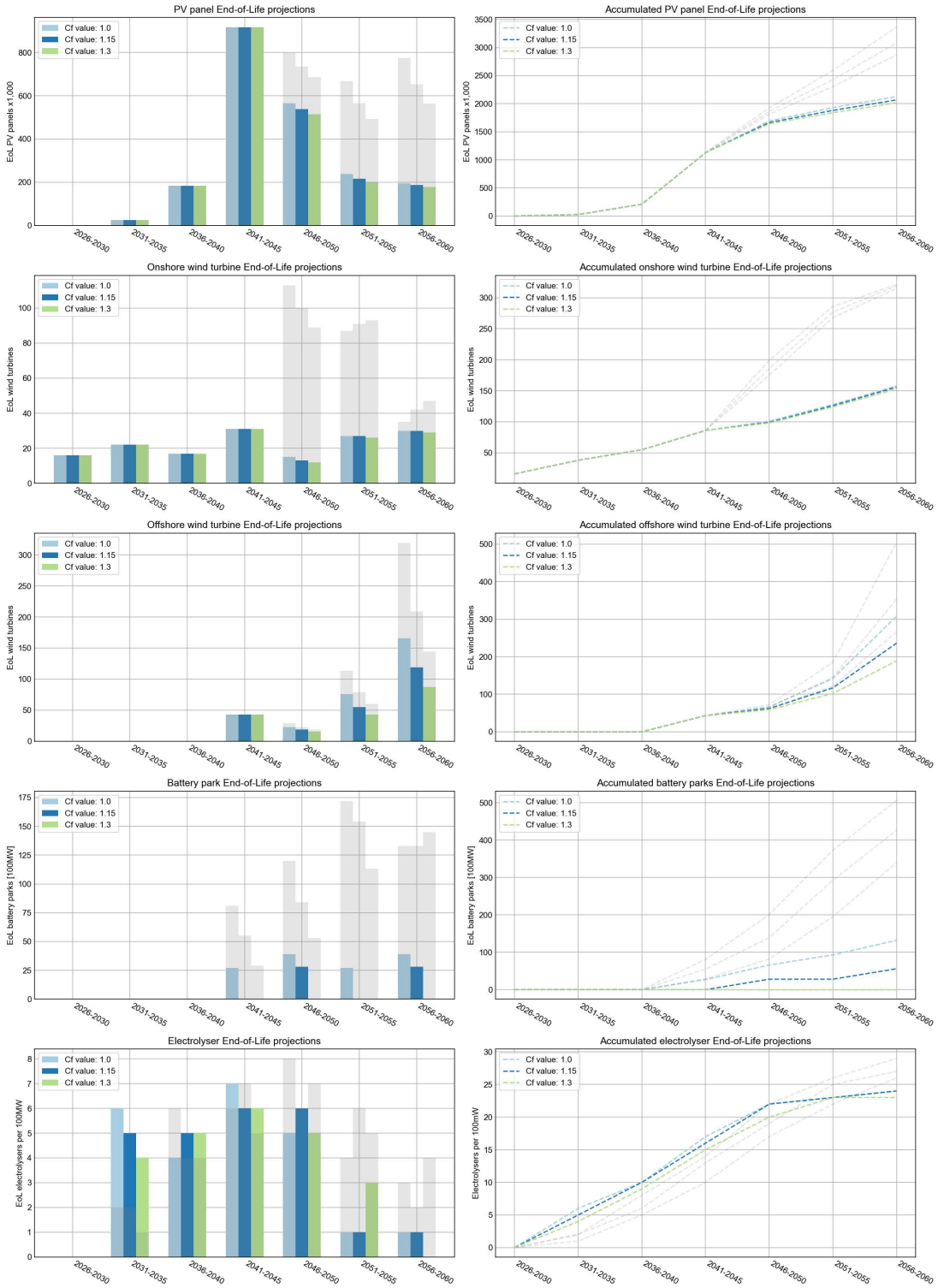

Fig. 5.40 Simulated projections of the End-of-Life renewable technology waste flow. The graphs represent scenario 2 B.

5.4.4 Energy strategy implications

Figure 5.42 shows the implications of the transition strategy regarding employment, innovation potential, direct cost, spatial footprint and indirect emissions. Cost-wise it is eminent that transition costs are projected to be significantly higher than the previous discussed scenario with only one twin reactor. Total transition costs are expected to be roughly 84 billion euros, or 2.8 billion per year, for electrification scenario A. Combined with the estimated indirect costs this could potentially increase the annual yearly cost to 2,423 EUR per citizen. Roughly 140 euros above the previous discussed strategy.

Nonetheless, this minor cost increase may be worthwhile because construction emissions are reduced to 22.6 Mton of GHG-emissions, nearly half of scenario 1. This reduction is achieved by the reduction in constructed gas boilers.

There will be no discernible differences in terms of spatial footprint or innovation potential. Because no reductions in renewable energy producers have occurred.

Employment, on the other hand, increases in comparison to the other scenarios. Employment rates for scenario 1 were estimated at 34,000 fte's at the end of the transition, whereas employment values for the current simulated strategy are expected to exceed 50,000. This increase is due to the operation of multiple nuclear reactors, as slight increases are seen with the construction of each reactor.

5.4.5 Material requirements

Figures 5.43 and 5.44 show that there are no notable shifts in material intensity or critical raw material projections. This could be explained by nuclear facilities' low material requirements.

5.4.6 Natural gas demand projections

The introduction of numerous thermal nuclear reactors has a positive effect on natural gas demand, which is steadily decreasing over time. As shown in figure 5.45, natural gas consumption will fall to its lowest point in the late 2030s. Only natural gas-fueled boilers in the built environment and agricultural sector will consume natural gas at that time. As a result, it is possible to conclude that the use of small modular reactors has a positive impact on the reduction of natural gas consumption. Allowing the region to become nearly self-sufficient in natural gas by 2036.

5.4.7 Conclusion

The following conclusions are drawn from the differences between the previously assessed strategies.

General outcome In comparison to the reference scenario and strategy 1, the evaluated elements perform exceptionally well in this scenario. Emissions, human health risks, biodiversity losses, water

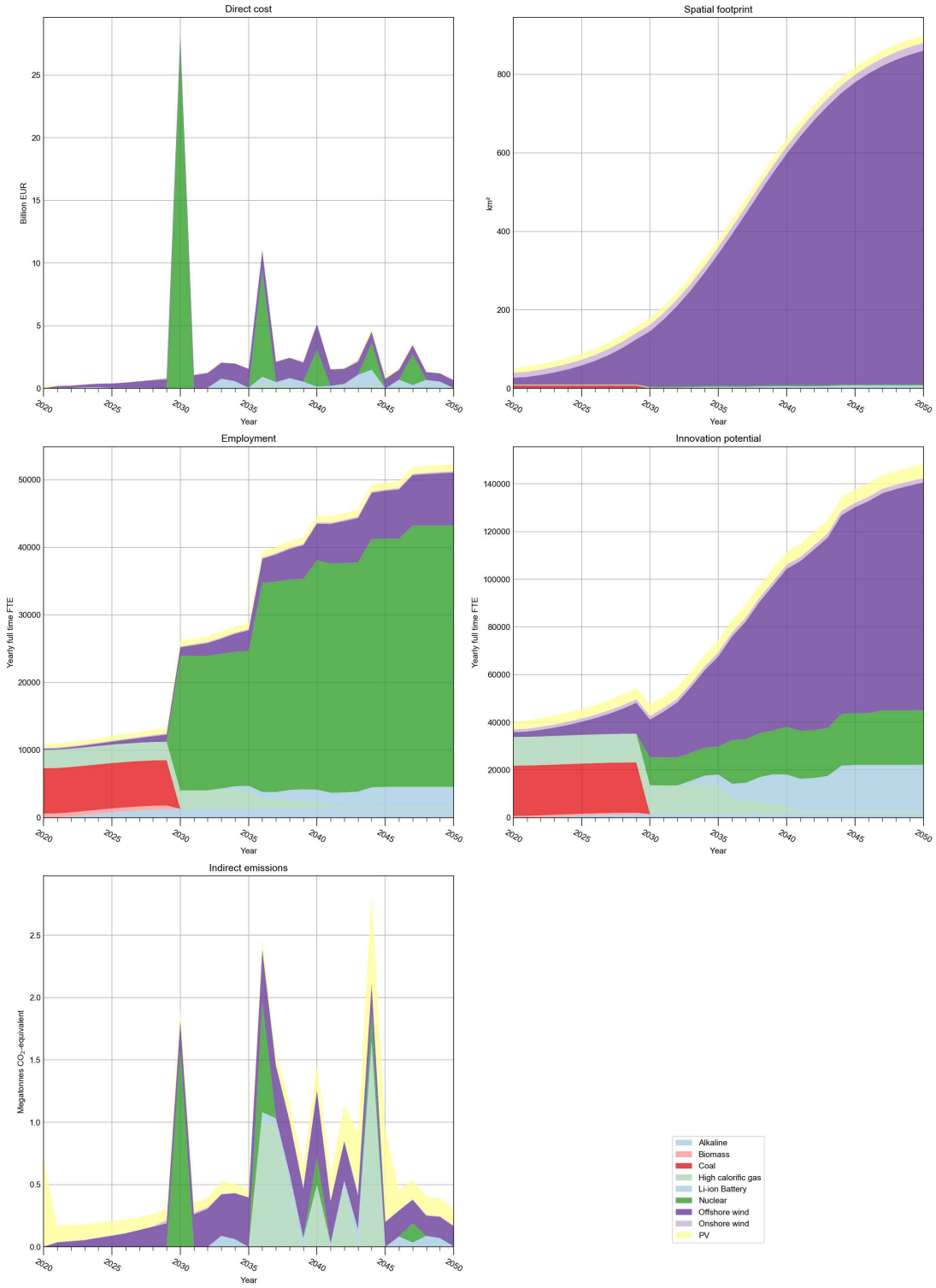

Fig. 5.41 Overview of the projected implications resulting from the energy strategy scenario. The graphs represent scenario 2 A under standard projection conditions.

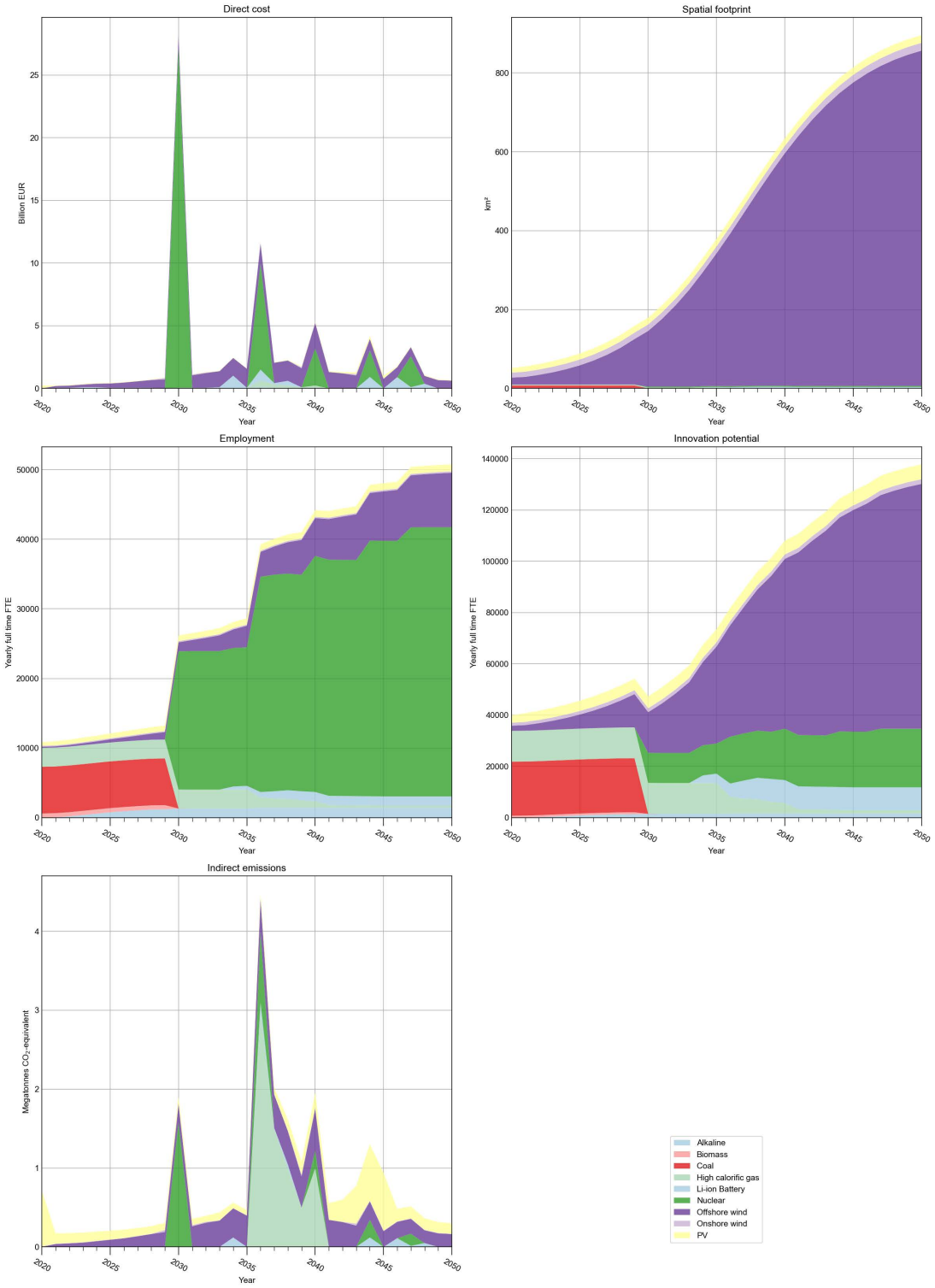

Fig. 5.42 Overview of the projected implications resulting from the energy strategy scenario. The graphs represent scenario 2 B under standard projection conditions.

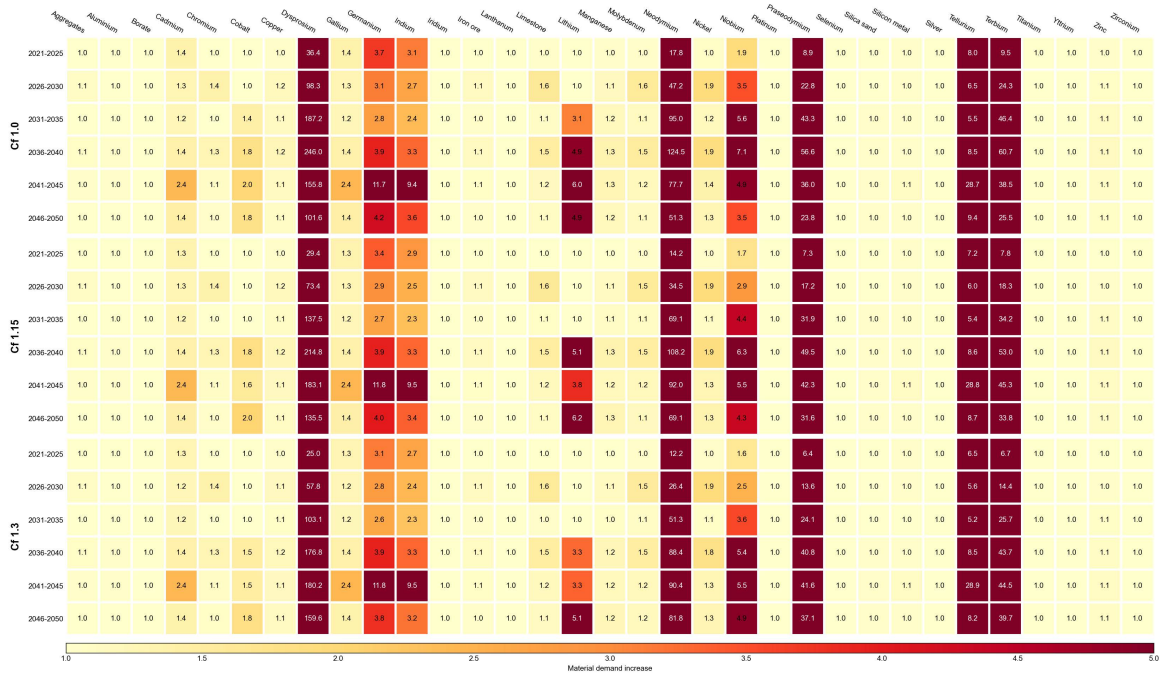

(a)

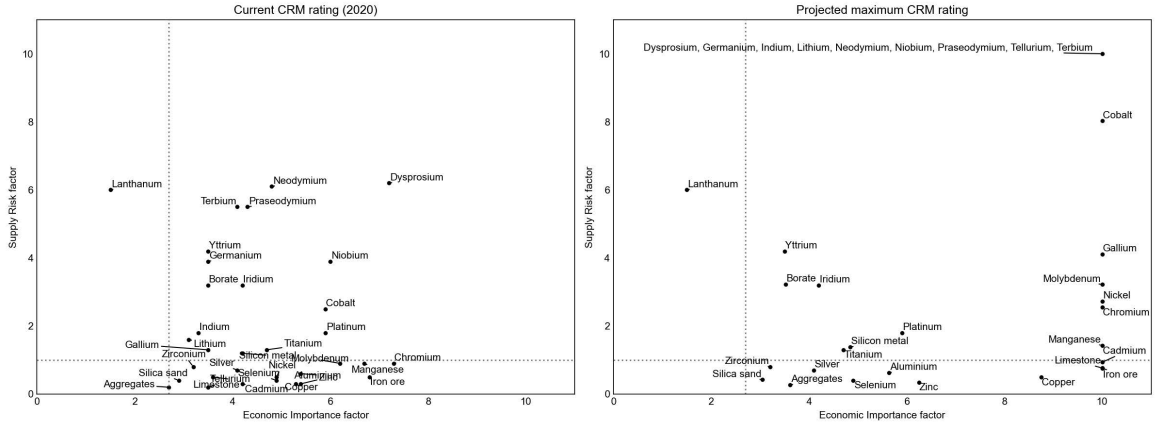

(b)

Fig. 5.43 Overview of the major materials in the European Union and the projected requirement intensification. The graphs represent scenario 2 A. (a) material demand increases, (b) current critical raw material plot (left) and the estimated trend behaviour (right) for standard trend projections (Cf=1.0).

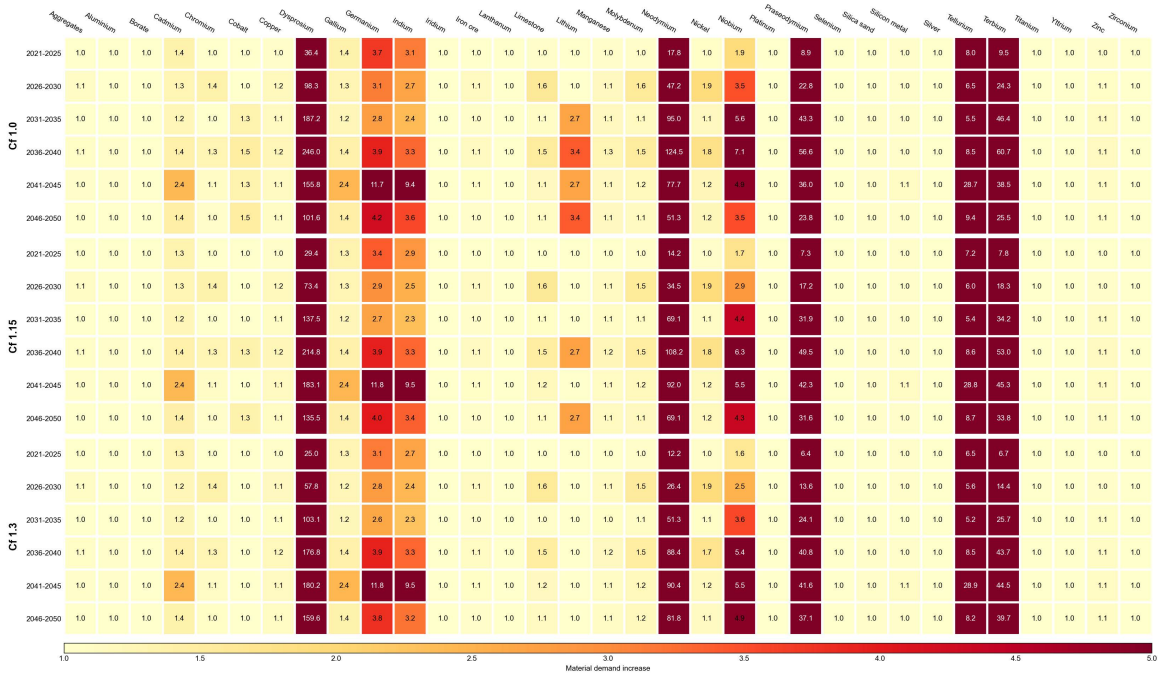

(a)

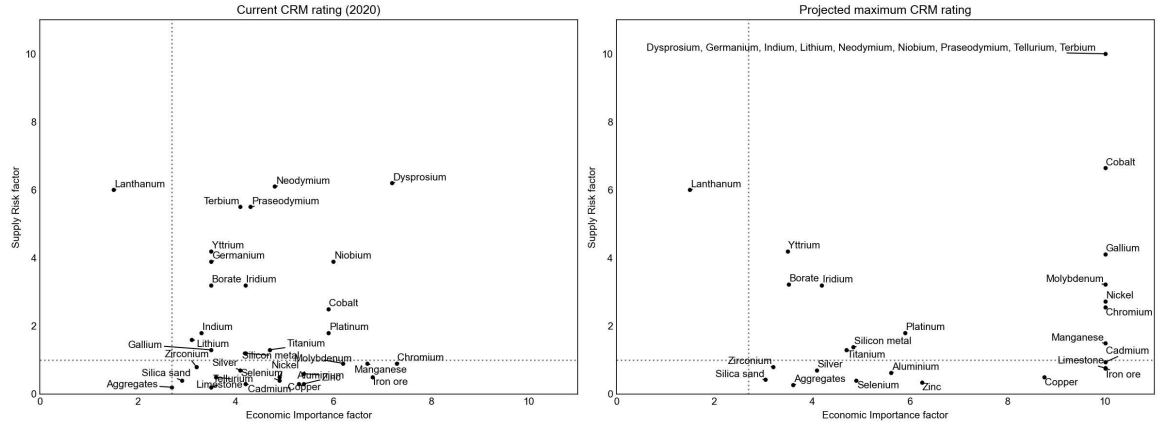

(b)

Fig. 5.44 Overview of the major materials in the European Union and the projected requirement intensification. The graphs represent scenario 2 B. (a) material demand increases, (b) current critical raw material plot (left) and the estimated trend behaviour (right) for standard trend projections (Cf=1.0).

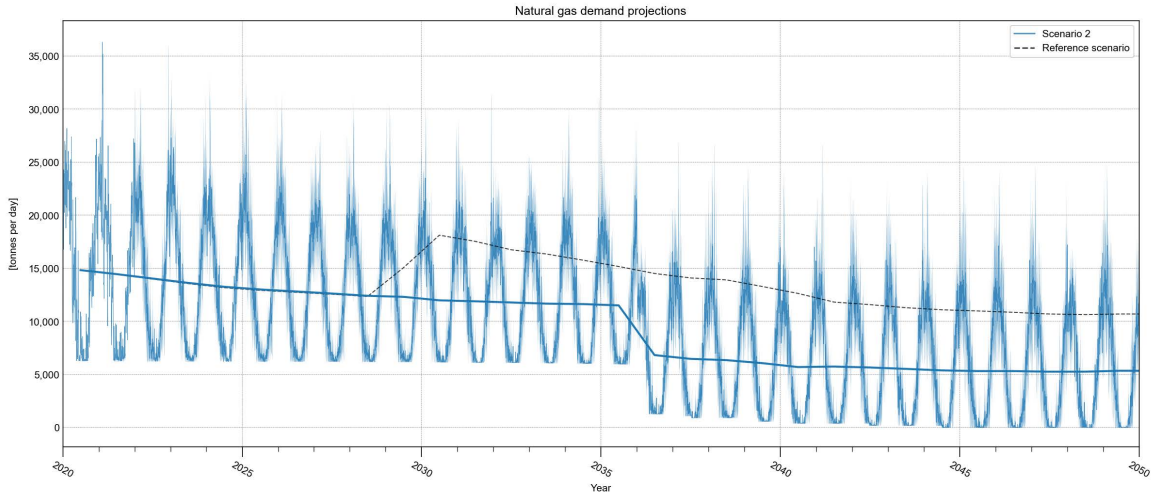

(a)

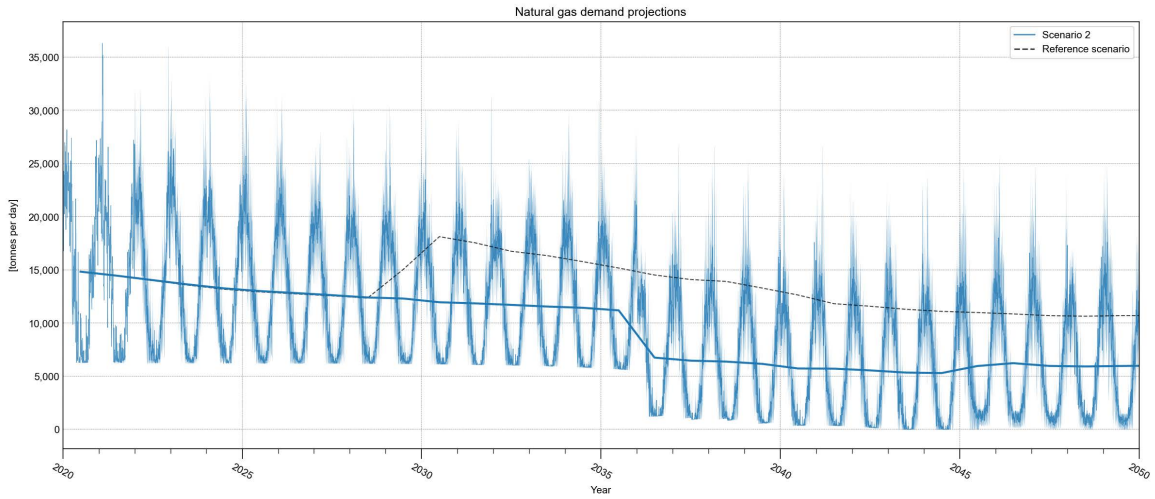

(b)

Fig. 5.45 Projections for daily natural gas demand in the MRDH region for scenario 2 under standard conditions. (a) electrification scenario A, (b) electrification scenario B.

Fig. 5.46 Performance overview of scenario 2 relative to all researched scenarios. Values range from worst (1) to best (5). The grey area represents the reference scenario.

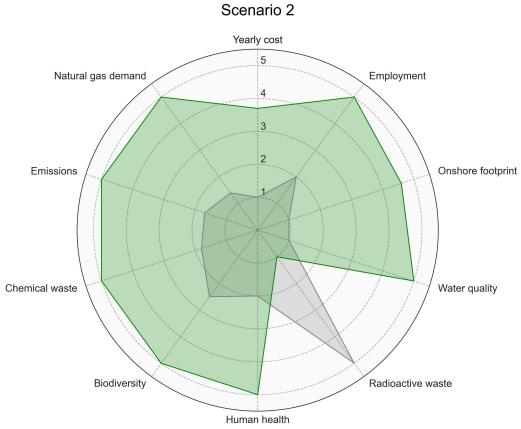

pollution, and chemical waste all fall to unprecedented lows. All of this comes at a slight increase in projected energy costs.

Advantages Because of the many modular reactors operating in the region, there is a significant increase in job opportunities compared to scenario 1. Because of the abundance of job opportunities, the region has the potential to become a nuclear knowledge hub. Other advantageous aspects of the described scenario are similar to those discussed previously.

Challenges and bottlenecks While no new challenges arise, the production of nuclear waste will steadily increase due to the many new nuclear reactors. Because most of these reactors are based on generation-III+ technology the fuel and waste flows are assumed relatively high. To store this amount of waste new storage facilities near or inside the region are most likely required. If no new storage facilities are built, this waste flow could become a bottleneck. Forcing the region to ship its radioactive waste elsewhere, most likely at considerable cost. Nonetheless, replacing reactors in the late 2040s with new generation IV reactors could potentially mitigate this risk, as large reductions in waste generation due to the IMSR reactor are already projected in the current strategy for 2049 and 2050.

Chapter 6

Discussion

For research purposes, simulating complex systems can be a useful tool for evaluating specific system elements. A wide range of uncertainties can be considered because large data sets can be easily computed at high rates using the described methodology for dynamic system analysis. Including those factors that cause uncertainty helps to better understand the system by highlighting potential future bottlenecks and challenges.

However, this prominent advantage of computational system analysis can also be its drawback. The system's accuracy is limited by the number of elements it contains. As a result, in order to accurately describe and discuss the complex system projections, it is essential to consider the simulation's shortfalls.

To achieve acceptable projections, the computational script designed for this experimental research needed to include a high level of system variables. Important conditioning factors such as climate change and societal willingness create a range of uncertainties in the coming decades. Changing weather patterns could potentially result in renewable energy performance differences and even changing consumption patterns. While societal willingness could slowdown or even prevent the implementation of certain elements within the transition strategy. Therefore a set of dynamic variables were used in the simulation.

Nevertheless, because the project was time-limited, the inclusion of these dynamic variables resulted in the simplification of other elements. Components deemed most important to the research goal were included, while others were excluded. The significance of certain system elements, and thus their inclusion, was based on literature. Regardless of the elements chosen, the system analysis tool may be subject to an unknown error margin. Ergo, these elements are discussed briefly.

The selection and approach to fuel and electricity import prices was one of the most notable, and likely most influential, simplifications. Only the stable 2019 prices were considered in the experimental work. However, in the previous two quarters (2021 Q4 and 2022 Q1), these prices were all but stable, as electricity and fuel prices (with an emphasis on natural gas) skyrocketed. When these

extreme price fluctuations are factored in, the projections and eventual evaluation of certain transition strategies change significantly.

The same is true for simplifying climate change projections. While some important factors are considered, such as temperature increases and relative humidity projections, others are excluded due to time and complexity constraints. A shifting weather pattern may result in a significant decrease or increase in average regional wind speeds or solar irradiation. Having a direct impact on renewable energy production. When combined with the likely change in energy consumption behaviour, such as less heating during the winter months and more electric cooling during the hot summer days, these factors could have significantly favoured one transition strategy over the other. If hourly climate change projections become available, these elements could be further integrated into the simulation (currently only available for a three hour interval). The availability of actual hourly heat demand could aid in understanding the relationship between consumption and weather. Hence, providing the model with more accurate projections.

Other aspects are expected to be less important because they only affect a small portion of the assessed elements. Excluding (combustion) plant outage rates, both planned and unplanned, will affect potential shortage peaks but is unlikely to have any other effects on total transition cost or material requirements. Similarly, the generalisation of projected generation and storage technology models may result in higher energy yields or lifespans, but this has no direct effect on the energy transition investment costs. Due to the small regional scale, the weather data grid (generalised as land- and sea climate), the flexibility of combustion- and nuclear plants to change their output capacity and the industrial heat usage efficiency (fixed at 100%) are all classified as a minor influence because they only affect the scale of the transition rather than deviating projections per scenario.

Inclusion of these elements would enhance simulation performance and is therefore implied for future research. Nonetheless, they are labelled as less important to the current research objective.

Overall, the current system analysis model retains a high level of future uncertainty due to numerous simplifications. However, returning to the thesis's research goal, it can be stated that it works sufficiently to provide an acceptable outlook on the potential benefits of nuclear energy in the MRDH region. The model predicts many inherently significant benefits of nuclear implementation, which, despite a large margin of error, can be viewed as a potential addition to the current energy transition strategy.

At its current development stage the energy transition analysis tool can only be used as a supportive system to energy transition research and development. The outcomes are solely estimates of the expected consequences. As a result, energy transition experts who would like to research possible outcomes and evaluate specific implications of these strategies can use the tool. Hence, assisting them in optimising both quantitatively and qualitatively analysis for the development of a long-term, industry-neutral strategy.

Chapter 7

Conclusions and recommendations

7.1 Conclusion

Alternatives must be investigated in order to develop sustainable decision making. Following the structural exclusion of specific routes and technologies in the development of an energy transition strategy, this study concentrated on the potential of nuclear energy in the MRDH region. A region known for its low adaptability to extensive change due to its scarce space and high population density.

Nuclear energy reactors have a very high energy density, making them an appealing alternative to other energy sources. However, to truly investigate the technology's potential, an extensive study on the effects of nuclear implementation on the long-term sustainable progression of given energy strategies must be conducted. As a result, the following research question emerged:

'To what extent can modern nuclear reactors benefit the future of the Rotterdam-The Hague metropolitan area sustainable transition and energy mix compared to other energy sources classified as sustainable?'

Using the discussed assessment framework, various sub-objectives are investigated to answer the research question raised above. These sub-objectives are described below, along with their conclusions. Sub-objective 2 and 3 are combined into one conclusion. Finally, the research question's conclusion is presented.

1. Determine the current proposed energy transition strategy's challenges, bottlenecks, and benefits.

The given conclusions below are seen as likely outcomes for the currently proposed energy strategy.

Benefits

- Transition generates many more jobs relative to the current energy system.

- The region's continued reliance on system technologies results in the potential of many new innovation industries.
- Energy system related impact on human health and biodiversity reductions improves steadily throughout the transition.

Challenges

- Low energy density of transitional energy system results in a high spatial requirement. Changing the region into an energy-focused landscape.
- The ongoing construction of many wind turbines is likely to pollute the region's water bodies.

Bottlenecks

- Accumulating electronic EoL flow has the potential to have an counterproductive effect on the region's sustainability flow. Likely increasing decommissioning costs and consequently energy prices.
- Continuing high demand of critical raw materials is likely to cause material shortages, increasing yearly upkeep costs post-2050.
- Energy net instability as a result of variable energy sources necessitates reliance on both fuel and power imports. Putting energy affordability in jeopardy.

2. Investigate the integration of various nuclear energy scenarios, including the use of the sustainable assessment method and compare the benefits and drawbacks of various energy generation strategies and their associated techniques.

Integration of an EPR2 twin reactor in 2030

- Reduces transition feasibility by lowering yearly investment costs, likely to improve overall energy affordability for the region.
- Because of the power plant's construction and operation staff requirements, many job opportunities emerge early in the transition.
- The construction of a twin reactor is not expected to add significantly to the regional innovation potential.
- The integration of a twin reactor drastically reduces the energy system footprint, alleviating the region's land area scarcity issues.
- Water pollution risks are reduced when the energy system's reliance on wind turbines is reduced.
- The current national facility COVRA can handle the storage of the system-generated radioactive waste for the next several decades.

- Reduced reliance on short-lifetime technologies improves the system's EoL flow, reducing potential decommissioning cost issues post-transition.
- The critical raw material demand for Generation III+ reactors is low. As a result, substituting PV panels and wind turbines reduces reliance on these scarce materials, reducing potential construction cost issues.
- Nuclear power integration in a primarily variable generation source system greatly improves net stability and reduces import dependence. Affecting electricity affordability positively.

ASMR focused energy transition after 2036

- The integration of numerous small modular reactors reduces annual values for emissions, human health risks, biodiversity losses, water pollution, and chemical waste to previously unheard-of lows.
- The transition from a gas-powered thermal system to a nuclear-driven system greatly enhances job opportunities. This could lead to the region becoming a nuclear knowledge hub.
- The substantial rise in radioactive waste could hinder the transition strategy because new storage facilities are required. Nonetheless, the construction of modern generation-IV reactors in the late 2040s could significantly reduce waste flow. The implementation of these reactors is also expected to significantly reduce nuclear fuel demand.
- A thermal energy system dominated by nuclear energy is able to diminish natural gas consumption in less than 15 years.

Main objective

The main objective of this research thesis can be concluded as follows:

Major findings:

- Both light to heavy implementation of nuclear energy sources will benefit the sustainable transition by lowering the negative operational impact of the energy system, both relative to the current situation as well as the proposed RES strategy.
- Integration of nuclear energy systems, both thermal and electric, lower the required total investment of the energy transition relative to a renewable-driven system.
- Nuclear power, like a renewable-powered electricity grid, is expected to reduce electricity costs.

Expected findings:

- Energy net stability from nuclear plants boosts the region's energy self-sufficiency, ensuring energy affordability after 2050. While renewable-focused strategies rely more on costly supporting storage facilities or import to remain stable.
- Nuclear power plants require far fewer critical materials. As a result, future supply risks are reduced, as are potential End-of-Life accumulation issues.
- By incorporating nuclear energy into the system, the energy system's footprint is drastically reduced. The majority of the region's land cover will be retained for non-energy purposes.

7.2 Recommendations

In this master thesis only a few possible transition routes have been investigated in terms of their potentially beneficial integration impact. Ergo, more research into many more strategies including different technology focuses is advised. To facilitate such in-depth research, it is suggested that the current Python script be improved and streamlined into a simulation script that could optimise given input strategies at high calculation speeds. This would imply additional research into the relationships between various system elements. For example, the correlation between low heat demand and weather conditions.

Second, additional research into the pre- and post-operational effects of energy generation and storage technologies would greatly expand the potential scope of life cycle assessments related to specific transitional strategies and their corresponding technologies. Such research could look into the material requirements of technology manufacturing of models that are still in development. Such research allows for early adaptation of potentially beneficial technologies for given future energy systems.

Furthermore, due to the broad scope of the experimental work, many more aspects of the system could be investigated further. Nonetheless, it is critical that various scientific fields, industrial sectors, and governmental bodies begin to collaborate. Linking proven concepts, innovative research, legislation, and integration studies are essential to the formation of sustainable and adaptable long-term strategies. To help facilitate this multi-disciplinary approach , an analysis tool could be a good starting point for future research into underinvested but potentially interesting strategies.

References

1. *The Physical Science Basis Summary for Policymakers Working Group I contribution to the Sixth Assessment Report of the Intergovernmental Panel on Climate Change* AR6 (eds Masson-Delmotte, V. *et al.*) (Cambridge University Press, Cambridge, Aug. 2021).
2. United Nations. *Sustainable development goals* https://www.un.org/sustainabledevelopment/ (2022).
3. Government of the Netherlands. *Klimaatbeleid* https://wetten.overheid.nl/BWBR0042394/2020-01-01 (2021).
4. Ministerie van Economische Zaken en Klimaat. *Klimaatakkoord* tech. rep. (Dutch government, June 2019).
5. Ministry of Economic Affairs and Climate Policy. *Klimaatplan 2021-2030* tech. rep. (Ministry of Economic Affairs and Climate Policy, Apr. 2020).
6. EBN. *Energie in Nederland* https://www.energieinnederland.nl/feiten-en-cijfers/uitgebreid/ (2021).
7. Energie Beheer Nederland. *Energie in Nederland in 2019* https://www.energieinnederland.nl/feiten-en-cijfers/uitgebreid/2019 (2021).
8. Borst, T. *'Nieuwe kerncentrale gespreksonderwerp aan formatietafel'* https://www.nrc.nl/nieuws/2021/11/12/nieuwe-kerncentrale-gespreksonderwerp-aan-formatietafel-a4065234.
9. Hensen, C. *Nu gas zoveel kost, toch maar kernenergie omarmen in Europa?* https://www.nrc.nl/nieuws/2021/10/19/nu-gas-zoveel-kost-toch-maar-kernenergie-omarmen-in-europa-a4062254.
10. Kuijers, T. *et al. Klimaat Energie Ruimte: : Ruimtelijke Verkenning Energie en Klimaat* ISBN: 978-90-828256-0-2. https://www.wegenwiki.nl/Autobezit (Ministry of Economic Affairs and Climate Policy, The Hague, Feb. 2018).
11. PBL. *Netherlands Climate and Energy Outlook 2021* tech. rep. (Netherlands Environmental Assessment Agency (PBL), The Hague, Oct. 2021). www.pbl.nl/kev.
12. CBS. *Gemiddelde energietarieven voor consumenten* https://www.cbs.nl/nl-nl/cijfers/detail/84672NED (2021).

13. CBS. *Electricity and heat; production and input by energy commodity - 2019 [DATASET]* https://opendata.cbs.nl/statline/#/CBS/en/dataset/80030eng/table?ts=1639055827055 (2021).

14. CBS. *Energy balance sheet; supply, transformation and consumption - 2019 [DATASET]* https://opendata.cbs.nl/statline/#/CBS/en/dataset/83140ENG/table?fromstatweb (2021).

15. CBS. *CO2 emissions from biomass burning on the rise* https://www.cbs.nl/en-gb/news/2021/48/co2-emissions-from-biomass-burning-on-the-rise (2021).

16. ENCO. *Possible role of nuclear in the Dutch energy mix in the future* tech. rep. (ENCO, 2020).

17. CBS. *CO2 emissions from biomass burning on the rise* https://opendata.cbs.nl/#/CBS/nl/dataset/82610NED/table (2021).

18. Den Ouden, B. *et al. Klimaatneutrale energiescenario's 2050* tech. rep. (Berenschot, Mar. 2020).

19. Scheepers, M., Faaij, A. & van den Brink, R. *Scenario's voor klimaatneutraal energiesysteem* tech. rep. (TNO, May 2020).

20. Energy Transition Model. *Emission factors* https://docs.energytransitionmodel.com/main/co2-emission-factors/ (2021).

21. Hund, K., La Porta, D., Fabregas, T., Laing, T. & Drexhage, J. *Minerals for Climate Action: The mineral intensity of the clean energy transition* tech. rep. (World Bank Group, 2020). www.worldbank.org.

22. Watari, T. *et al.* Total material requirement for the global energy transition to 2050: A focus on transport and electricity. *Resources, Conservation and Recycling* **148,** 91–103. ISSN: 0921-3449 (Sept. 2019).

23. Offerman, S. E. *Critical Materials* ISBN: 978-981-327-104-3. https://www.worldscientific.com/worldscibooks/10.1142/11007 (World Scientific Publishing Co. Pte. Ltd., Mar. 2019).

24. Van Exter, P., Bosch, S., Schipper, B., Sprecher, B. & Kleijn, R. *Metal demand for renewable electricity generation in the Netherlands: Navigating a complex supply chain* tech. rep. (METABOLIC, 2018). www.metabolic.nl.

25. Carrara, S., Dias, A., Plazzotta, B. & Pavel, C. *Raw materials demand for wind and solar PV technologies in the transition towards a decarbonised energy system* EN 30095 EN. ISBN: 9789276162254. https://publications.jrc.ec.europa.eu/repository/handle/JRC119941 (Publication Office of the European Union, Luxembourg, 2020).

26. Joint Research Centre (JRC). *Raw Materials Information System (RMIS)* https://rmis.jrc.ec.europa.eu/?page=crm-list-2020-e294f6 (2022).

27. World Economic Forum. *Fostering effective energy transition* tech. rep. (World Economic Forum, Apr. 2021).

28. Calvo, G., Mudd, G., Valero, A. & Valero, A. Decreasing Ore Grades in Global Metallic Mining: A Theoretical Issue or a Global Reality? *Resources* **5.** ISSN: 2079-9276. https://www.mdpi.com/2079-9276/5/4/36 (2016).
29. International Energy Agency. *The Netherlands - key energy statistics* https://www.iea.org/countries/the-netherlands (2021).
30. International Energy Agency (IEA. *Projected Costs of Generating Electricity* tech. rep. (International Energy Agency (IEA), Paris, 2020).
31. European Environment Agency. *Emerging waste streams: Opportunities and challenges of the clean-energy transition from a circular economy perspective.* https://www.eea.europa.eu/publications/emerging-waste-streams-opportunities-and/emerging-waste-streams-opportunities-and (2022).
32. Energieopwek. *Energieproductie* https://energieopwek.nl/ (2021).
33. ENTSO-E. *Dataset: Total Load - Day Ahead / Actual (Actual Total Load [6.1.A])* https://transparency.entsoe.eu/ (2021).
34. KPMG. *Marktconsultatie kernenergie* tech. rep. (KPMG Advisory N.V., Amsterdam, July 2021).
35. Stuurgroep Energiestrategie regio Rotterdam Den Haag. *Regionale Energiestrategie Rotterdam Den Haag (RES 1.0)* tech. rep. (Rotterdam-The Hague metropolitan area, 2021).
36. Abousahl, S. *et al. Technical assessment of nuclear energy with respect to the 'do no significant harm' criteria of Regulation (EU) 2020/852 ('Taxonomy Regulation')* tech. rep. (JRC, Luxembourg, 2021), 1–11. https://ec.europa.eu/jrc.
37. *Thorium Energy for the World* (eds Revol, J.-P. *et al.*) ISBN: 978-3-319-26540-7 (Springer International Publishing, Cham, 2016).
38. World Nuclear Association. *The Nuclear Debate* https://world-nuclear.org/information-library/current-and-future-generation/the-nuclear-debate.aspx (2021).
39. Generation IV International Forum (GIF). *Nuclear Power in a Clean Energy System* tech. rep. (Generation IV International Forum, May 2019).
40. Kharecha, P. A. & Hansen, J. E. Prevented mortality and greenhouse gas emissions from historical and projected nuclear power. *Environmental Science and Technology* **47,** 4889–4895. ISSN: 0013936X (May 2013).
41. Ros, J. & Schure, K. *Vormgeving van de energietransitie* tech. rep. (Planbureau voor de Leefomgeving (PBL), The Hague, Feb. 2016).
42. United States Nuclear Regulatory Commission. *General site suitability criteria for nuclear power stations* https://www.nrc.gov/docs/ML1218/ML12188A053.pdf.

43. International Energy Agency. *Energy Technology Perspectives 2017 [data set]* https://www.iea.org/data-and-statistics/data-product/energy-technology-perspectives-2017-2#scenario-data (2021).

44. World Nuclear Association. *Heat Values of Various Fuels* https://world-nuclear.org/information-library/facts-and-figures/heat-values-of-various-fuels.aspx (2021).

45. Hargraves, R. & Moir, R. Liquid Fluoride Thorium Reactors: An old idea in nuclear power gets reexamined. *American Scientist* **98,** 304–313. ISSN: 00030996. https://www.jstor.org/stable/27859537 (2010).

46. Dolan, T. J. *Molten salt reactors and thorium energy* ISBN: 978-0-08-101126-3 (Woodhead Publishing, 2017).

47. World Nuclear Association. *Supply of Uranium* http://www.world-nuclear.org/information-library/nuclear-fuel-cycle/uranium-resources/supply-of-uranium.aspx (2022).

48. World Nuclear Association. *Thorium* http://www.world-nuclear.org/information-library/current-and-future-generation/thorium.aspx (2022).

49. Kabinet 2021-2025. *Coalitieakkoord 2021-2025: Omzien naar elkaar, vooruitkijken naar de toekomst* https://www.kabinetsformatie2021.nl/documenten/publicaties/2021/12/15/coalitieakkoord-omzien-naar-elkaar-vooruitkijken-naar-de-toekomst (2021).

50. Ministry of Economic Affairs. *Vestigingsplaatsen voor kerncentrales* 1986.

51. EPZ. *Visie EPZ op kernenergie in Nederland na 2033* https://www.epz.nl/publicatie/1262/ (2021).

52. World Nuclear Association. *Physics of Uranium and Nuclear Energy* https://world-nuclear.org/information-library/nuclear-fuel-cycle/introduction/physics-of-nuclear-energy.aspx (2021).

53. *Thorium—Energy for the Future* (eds Nayak, A. & Sehgal, B. R.) (Springer Singapore, Singapore, 2019).

54. World Nuclear Association. *Plutonium and weapons* https://world-nuclear.org/information-library/nuclear-fuel-cycle/fuel-recycling/plutonium.aspx (2021).

55. CATF. *Advanced Nuclear Energy* tech. rep. (Clean Air Task Force, Boston, USA, Apr. 2018). http://www.catf.us/publications/files/Advanced_Nuclear_Energy.pdf.

56. Kerlin, T. & Upadhyaya, B. *Dynamics and Control of Nuclear Reactors* (Elsevier, 2019).

57. Breeze, P. *Nuclear Power* ISBN: 978-0-08-101044-0 (Elsevier, 2017).

58. Kadak, A. C. *A COMPARISON OF ADVANCED NUCLEAR TECHNOLOGIES* tech. rep. (Columbia University, New York, USA, Mar. 2017). www.sipa.columbia.edu.

59. Zohuri, B. & McDaniel, P. *Advanced Smaller Modular Reactors* (Springer International Publishing, 2019).

60. International Atomic Energy Agency (IAEA). *Advanced Large Water Cooled Reactors Advanced Reactor Information System* tech. rep. (International Atomic Energy Agency, 2015). http://www.iaea.org/books.

61. Martin, M. & Sharif, A. *Abu Dhabi Said to Revive Debt Plan for First Nuclear Plant* https://www.bloomberg.com/news/articles/2015-09-03/abu-dhabi-said-to-revive-debt-plan-for-first-nuclear-power-plant-ie3wyuib (2021).

62. IAEA. *Advances in Small Modular Reactor Technology Developments* tech. rep. (International Atomic Energy Agency, 2020). http://aris.iaea.org.

63. U.S. Energy Information Administration (EIA). *Construction cost data for electric generators installed in 2019: Generators installed in 2019 by major energy source* https://www.eia.gov/electricity/generatorcosts/ (2021).

64. World Nuclear News. *Rolls-Royce on track for 2030 delivery of UK SMR* https://world-nuclear-news.org/Articles/Rolls-Royce-on-track-for-2030-delivery-of-UK-SMR (2021).

65. NuScale Power. *page 1: Small Emergency Planning Zone, page 2: The Benefits of NuScale's Technology* https://www.nuscalepower.com/ (2021).

66. SMART Power Co. *SMART Key Data and Attractions* http://smart-nuclear.com/tech/key_data.php (2021).

67. Terrestrial Energy. *Versatile* https://www.terrestrialenergy.com/technology/versatile/ (2021).

68. *Handbook of Generation IV Nuclear Reactors* (ed Pioro, I.) ii. ISBN: 978-0-08-100162-2 (Elsevier, 2016).

69. Generation IV International Forum (GIF). *Generation IV Roadmap: Description of Candidate Gas-cooled Reactor Systems Report* tech. rep. (Generation IV International Forum, 2002).

70. Generation IV International Forum (GIF). *Technology Roadmap Update for Generation IV Nuclear Energy Systems* tech. rep. (Generation IV International Forum, 2014).

71. Institut de radioprotection et de sûreté nucléaire (IRSN). *Review of Generation IV Nuclear Energy Systems* tech. rep. (Institut de radioprotection et de sûreté nucléaire, Apr. 2015).

72. World Nuclear Association. *Fast Neutron Reactors* https://world-nuclear.org/information-library/current-and-future-generation/fast-neutron-reactors.aspx (2021).

73. European Commission. *Horizon 2020: A Paradigm Shift in Reactor Safety with the Molten Salt Fast Reactor* https://cordis.europa.eu/project/id/661891 (2021).

74. SAMOFAR. *Concept: Molten Salt Fast Reactor* http://samofar.eu/concept/ (2021).

75. Merle, E. *Concept of Molten Salt Fast Reactor* https://www.gen-4.org/gif/upload/docs/application/pdf/2017-05/07_elsa_merle_france.pdf.

76. European Atomic Energy Community (Euratom). *Final Report EVOL project* tech. rep. (European Atomic Energy Community, 2015). http://www.gen-.

77. Ministry of Infrastructure and Water Management. *Klimaatmonitor database* https : / / klimaatmonitor.databank.nl (2021).

78. Provincial Council of South Holland. *Ontwerp Notitie Reikwijdte en Detailniveau Module Energietransitie* tech. rep. (Provincial Council of South Holland, 2021).

79. Stichting Warmtenetwerk. *Warmtenetwerk voor de energietransitie* https://warmtenetwerk.nl/map/ (2021).

80. Gasunie. *Integraal Ontwerp Warmtetransport Zuid-Holland* tech. rep. (Gasunie, 2021).

81. PBL Netherlands Environmental Assessment Agency. *Verkenning energietransitie industriecluster Rotterdam* tech. rep. (PBL Netherlands Environmental Assessment Agency, 2021).

82. CES Rotterdam-Moerdijk. *Cluster energie strategie: industriecluster Rotterdam-Moerdijk* tech. rep. (Cluster Energie Strategie (CES) Rotterdam-Moerdijk, 2021).

83. Rotterdam-Moerdijk industry cluster work group. *THREE STEPS TOWARDS A SUSTAINABLE INDUSTRY CLUSTER ROTTERDAM-MOERDIJK IN 2050* tech. rep. (Port of Rotterdam, 2018).

84. KNMI. *Graaddagen in gasjaar 2021* https://www.knmi.nl/over-het-knmi/nieuws/graaddagen-in-gasjaar-2021 (2022).

85. Netherlands Enterprise Agency (RVO). *Database WarmteAtlas: GroteStookInstallaties* https://rvo.b3p.nl/geoserver/WarmteAtlas/wfs? (2021).

86. Joint Research Centre. *PHOTOVOLTAIC GEOGRAPHICAL INFORMATION SYSTEM TOOL* https://re.jrc.ec.europa.eu/pvg_tools/en/ (2022).

87. IEA. *Projected Costs of Generating Electricity* tech. rep. (International Energy Agency, Paris, 2020).

88. Trading Economics. *Coal* https://tradingeconomics.com/commodity/eu-natural-gas (2022).

89. Trading Economics. *Coal* https://tradingeconomics.com/commodity/coal (2022).

90. Enevoldsen, P. & Jacobson, M. Z. Data investigation of installed and output power densities of onshore and offshore wind turbines worldwide. *Energy for Sustainable Development* **60,** 40–51. ISSN: 23524669 (Feb. 2021).

91. UNECE. *Life Cycle Assessment of Electricity Generation Options* tech. rep. (United Nations, Geneva, 2021).

92. P.J. Zijlema. *The Netherlands: list of fuels and standard CO2 emission factors* tech. rep. (Netherlands Enterprise Agency, Jan. 2020).

93. Engineering ToolBox. *Fuels - Higher and Lower Calorific Values* https : / / www . engineeringtoolbox.com/fuels-higher-calorific-values-d_169.html (2022).

94. World Nuclear. *Nuclear Fuel Cycle Overview* https://world-nuclear.org/information-library/nuclear-fuel-cycle/introduction/nuclear-fuel-cycle-overview.aspx (2022).

95. Carrara, S., Alves Dias, P., Plazzotta, B. & Pavel, C. *Raw materials demand for wind and solar PV technologies in the transition towards a decarbonised energy system* tech. rep. (European Commission. Joint Research Centre., Luxembourg, 2020).

96. Eynard, U. *et al. Study on the EU's list of Critical Raw Materials: Critical Raw Materials Factsheets (Final)* 2020. http://www.europa.eu.

97. Eynard, U. *et al. Study on the EU's list of Critical Raw Materials: Non-Critical Raw Materials Factsheets (Final)* tech. rep. (European Commission, Luxembourg, 2020). http://www.europa.eu.

98. Spath, P. L. & Mann, M. K. *Life Cycle Assessment of a Natural Gas Combined Cycle Power Generation System* tech. rep. (National Renewable Energy Laboratory, Golden, Colorado, 2000). http://www.doe.gov/bridge.

99. Bright New World. *Materials use in a Clean Energy future* https://www.brightnewworld.org/media/2021/1/27/materials-use-project (2022).

100. IEA. *Minerals used in clean energy technologies compared to other power generation sources* https://www.iea.org/data-and-statistics/charts/minerals-used-in-clean-energy-technologies-compared-to-other-power-generation-sources (2022).

101. Czako, V. *Employment in the Energy Sector* tech. rep. (European Commission, Joint Research Centre, Petten, 2020).

102. Hersbach, H. *et al. ERA5 hourly data on single levels from 1979 to present.* Copernicus Climate Change Service (C3S) Climate Data Store (CDS). (Accessed on < 04-03-2022 >), 10.24381/cds.adbb2d47. 2022. https://cds.climate.copernicus.eu/cdsapp#!/dataset/reanalysis-era5-single-levels?tab=overview (2022).

103. Zouine, M. *et al. Mathematical models calculating PV module temperature using weather data: Experimental study* in *Lecture Notes in Electrical Engineering* **519** (Springer Verlag, 2019), 630–639. ISBN: 9789811314049.

104. Hemming, S. *et al. Optimaal gebruik van natuurlijk licht in de glastuinbouw* tech. rep. (2004). www.agrotechnologyandfood.wur.nl.

105. Vej, N. J. *Modelling of the Variation of Air Density with Altitude through Pressure, Humidity and Temperature* tech. rep. (2005). www.emd.dkorwww.windpro.com.

106. Lucas Bauer, S. M. *Windturbines database* https://en.wind-turbine-models.com/turbines (2022).

107. Center for Sustainable Systems, University of Michigan. *Wind Energy Factsheet* https://css.umich.edu/factsheets/wind-energy-factsheet (2022).

108. Chem Europe. *Lapse rate* https://www.chemeurope.com/en/encyclopedia/Lapse_rate.html (2022).

109. GraphPad. *Regression curves* https://www.graphpad.com/guides/prism/latest/curve-fitting/index.htm (2022).

110. CBS. *Regionale prognose 2020-2050; bevolking* https://opendata.cbs.nl/#/CBS/nl/dataset/84525NED/table?searchKeywords=inwoners%5C%20rotterdam (2021).

111. CBS. *Regionale kerncijfers Nederland* https://opendata.cbs.nl/statline/#/CBS/nl/dataset/70072NED/table?fromstatweb (2022).

112. Sovacool, B. K. How long will it take? Conceptualizing the temporal dynamics of energy transitions. *Energy Research & Social Science* **13,** 202–215. ISSN: 22146296 (Mar. 2016).

113. Van der Velden, N. & Smit, P. *Energiemonitor van de Nederlandse glastuinbouw 2017* tech. rep. (Wageningen Economic Research, Wageningen, Nov. 2018).

114. Segers, R., Niessink, R., van den Oever, R. & Menkveld, M. *Warmtenetten monitor 2019* tech. rep. (TNO, the Hague, Aug. 2020).

115. Sungrow. *Energy Storage System Products Catalogue* tech. rep. (Sungrow Power Supply Co., Ltd., 2021).

116. Ghezel-Ayagh, H. *Modular SOEC System for Efficient H2 Production at High Current Density* https://www.hydrogen.energy.gov/pdfs/review20/ta019_ghezel-ayagh_2020_p.pdf (2022).

117. Nel. *Water electrolysers / hydrogen generators* https://nelhydrogen.com/water-electrolysers-hydrogen-generators/ (2022).

118. World Bank Group. *Climate Projections - The Netherlands* https://climateknowledgeportal.worldbank.org/country/netherlands/climate-data-projections (2022).

119. Fedkin, M. & Dutton, A. *Efficiency of Inverters* https://www.e-education.psu.edu/eme812/node/738 (2022).

120. Delft university of technology. *Verliezen bij stroomtransport* http://eduweb.eeni.tbm.tudelft.nl/TB141E/?elektriciteitstransport-verliezen (2022).

121. Ardelean, M. & Minnebo, P. *HVDC submarine power cables in the world* tech. rep. (European Commission. Joint Research Centre. Institute for Energy and Transport., 2015).

122. Ministry of Infrastructure and Water Management. *Windparken Noordzee (Nederlands Continentaal Plat)* https://data.overheid.nl/en/dataset/12520-windparken-noordzee--nederlands-continentaal-plat- (2022).

123. Ministry of Infrastructure and Water Management. *Kabels en leidingen - pijpleidingen op de Noordzee* https://data.overheid.nl/en/dataset/9378-pijpleidingen-op-de-noordzee (2022).

124. Eurostat. *Material flow accounts in raw material equivalents - modelling estimates* https://ec.europa.eu/eurostat/databrowser/view/env_ac_rme/default/table?lang=en (2022).

125. NAM. *Gas- en olie productiecijfers* https://www.nam.nl/gas-en-olie/gaswinning.html#iframe=L2VtYmVkL2NvbXBvbmVudC8_aWQ9Z2Fzd2lubmluZyN0YWItZ3JvbmluZ2Vu (2022).

126. COVRA. *Jaarrrapport 2020* tech. rep. (Nieuwdorp, 2021). www.covra.nl.

Part II

Materials Science and Engineering:
Microstructural evolution of heat-treated MONICR

Chapter 8

Background

8.1 Materials for nuclear (molten salt) applications

In a Molten Salt Reactor (MSR) a three layered concrete structure encloses the reactor processing systems, storage tanks, heat systems and the fission core, as earlier discussed in the nuclear reactor technology section of part I. The outer layer of the containment accommodates the less radioactive systems that produce little to no radiation and heat, while the reactor vessel, the second containment structure, accommodates the systems that produce some radiation and thus require more radiation shielding. Finally, the core of the reactor and its supporting systems are contained by the core vessel, also named the fuel casing, a highly radioactive zone which produces high intensity of radiation and heat. This area shelters many critical components that operate under extreme conditions, such as the piping system, heat exchangers and the core reflector, which is the component receiving the highest radiation dose. These materials are constantly exposed to high doses of radiation such as damaging neutrons and helium nuclei (α-particles) and to high temperatures of around 725°C with fluctuations of roughly 100°C [1, p. 17; 2, p. 4], which in combination with the molten salt coolant and fuel result in corrosion and erosion, as well as radiation damage and microstructural changes [3, p. 199]. By combining these environmental factors with the criticality of the components a list of required material properties can be set [3, p. 199]:

- **Embrittlement resistance**
- **Microstructural stability**
- Resistance to radiation damage
- Creep resistance
- Corrosion resistance
- Fatigue resistance
- Sufficient strength and toughness at operating temperature
- Low activation for End-of-Life (EoL) management
- Weldability and formability
- Volume deformation resistance

Due to the complexity of this engineering challenge only *embrittlement* and *microstructural stability* of the material, with their underlying processes, are extensively discussed in this thesis.

To conclude, the material requires appropriate and inherent high temperature properties. Nevertheless, two external factors, enhanced by high temperatures, can degrade the material and thus reduce these properties, namely the corrosive molten salt fluid and radiation. Currently, material degradation is the primary reason for the short operational lifetimes of molten salt reactors. Ergo, multiple materials, all with specific beneficial properties in one of the required engineering properties, are researched on their behaviour in MSR-like environments in the *ENICKMA* project.

The ENICKMA project

Nuclear material research is a very complex and time consuming process as it requires many special facilities and expertise. For that reason most researched materials for nuclear applications focused on in-use reactor designs, thus low-to-intermediate temperatures (around 300°C) and low neutron flux intensities of thermal reactors such as the *pressurised water reactor* and *boiling water reactors*. Yet, in the Netherlands the Nuclear Research and Consultancy Group (NRG) conducts research on a more experimental nuclear technology, namely the Molten Salt Reactor. The irradiation studies are conducted in the High Flux Reactor (HFR) reactor located in Petten, the Netherlands, that is able to simulate fast reactor environments, allowing the research of potential fast reactor materials.

Their material research focuses on the corrosion rates of materials exposed to molten fuels under irradiation (*Salient-03* program) and irradiation studies of candidate alloys for MSR applications (*ENICKMA* program) [4], with the latter being fully in the scope of this master research thesis.

The ENICKMA project focuses on five potential alloys for MSR: four Ni-based alloys and the stainless steel 316 L(N). Stainless steel is widely researched for nuclear applications due to its resistance to irradiation at low-to-intermediate temperatures, while the Ni-based alloys are known for their excellent resistance to molten salt corrosion.

Nevertheless, these promising alloys still require further research, particularly in relation to their behaviour under MSR operation conditions. The ENICKMA project focuses on the effect of neutron irradiation and high temperature on the microstructure and mechanical properties of the candidate alloys, in order to gain information about performance of materials and embrittlement mechanisms. The investigated alloys (for chemical compositions see table 8.1) are listed below:

- 316L(N): Low carbon, nitrogen strengthened 316 stainless steel
- HN80MTY (Ni-based alloy)
- Hastelloy N
- Hastelloy 242
- MONICR: Czech variant of Hastelloy N

Table 8.1 The chemical composition of reference Hastelloy alloys with exceptionally low carbon content (<0.02 wt%). The carbon content used in the isothermal calculations by [5] are 0.02 and 0.015 for C-276 and C-4 respectively. These used numbers are higher than the official limit for both alloys. Note, accuracy data is missing due to limited information received from the MONICR alloy producer.

	Chemical composition [wt%]													
	C	**Mn**	**Si**	**Cr**	**Mo**	**Ni**	**Fe**	**Al**	**Co**	**W**	**Cu**	**Ti**	**Nb**	**B**
MONICR [6]	0.006	0.042	0.031	5.9	15.0	bal.	1.52	0.010	0.048	0.032	0.030	-	-	<0.002
HN80MTY [7]	0.025	0.013	0.04	6.81	13.2	bal.	0.15	1.12	0.003	0.072	0.02	0.93	0.01	
Hastelloy N [7]	0.06	0.55	0.57	7.1	16-17	bal.	4-5	0.03	0.14	-	<0.01	-	-	
Hastelloy 242 [8]	0.03	0.80	0.80	7-9	24-26	bal.	2.0	0.5	1.0	-	0.5	-	-	-
C-276 [5; 8]	0.01	1.0	0.08	14.5-16.5	15-17	bal.	4-7	-	2.5	3-4.5	0.5	-	-	-
C-4 [5; 8]	0.01	1.0	0.08	14-18	14-17	bal.	3	-	2.0	-	0.5	-	-	-

NRG is currently performing an extensive 9 cycle (1 month per cycle) high-temperature (650°C) and high-flux irradiation study on the described alloys. This experiment will give an extensive insight into the behaviour of the materials under both high temperature and irradiation.

In parallel to irradiation, NRG is conducting a series of mechanical testing and microstructural analyses on the materials in the as-received condition and after annealing at 800°C for 1 month and at 650°C for 4 and 9 months. Mechanical testing includes: tensile testing, low-cycle fatigue, stress relaxation and small punch testing. Microstructural analyses comprehend optical microscopy, Scanning Electron Microscopy and Transmission Electron Microscopy, analysing radiation-induced defects and any possible nano-sized constituents of the microstructure. Preliminary tensile tests conducted on the alloys in the as-received condition, at room temperature and at 650°C, showed that the MONICR has the weakest performance, with both ductility and strength being drastically reduced at this temperature [6].

Despite its poor mechanical response at 650°C, the MONICR alloy is further investigated in this master thesis. It is of great interest, both scientifically and in terms of application, to understand the underlying microstructural causes of the mechanical performance. Such knowledge will allow the determination of processing routes and understanding of the compositional changes under certain operational conditions that can improve the mechanical behaviour of the MONICR alloy in MSR operating conditions. The MONICR alloy is produced by Škoda and Centrum výzkumu Řež (CVŘ) and was specifically engineered for an excellent molten salt corrosion resistance.

The research focuses on the microstructural evolution of the alloy under different heat-treatment time spans, and the consequences on the mechanical properties causing the drop in strength and ductility. An investigation on this behaviour eventually supports the ENICKMA project irradiation experiments by describing microstructural behaviour as a function of temperature and time rather than a combination of temperature and irradiation. Additionally, more characterisation information under different circumstances will be made available for further research, as little is currently known about the microstructure of the MONICR alloy.

This chapter provides background information on the thermodynamic processes determined by heat treatment and irradiation of the material, which are discussed separately. Finally, these microstruc-

tural changes will be linked to the effects on mechanical properties that have been documented in the literature, creating a theoretical framework for the interaction of microstructure and macro-mechanical behavior.

8.2 Molten Salt Reactor (MSR) alloy research

Historically investigated materials for MSR applications mainly focus on alloys that have acceptable stability and corrosion resistance at elevated temperatures. The first molten salt reactor in operation (MSR Experiment at Oak Ridge National Laboratory, 1960s) used the Hastelloy N alloy for its reactor core vessel materialisation. Hastelloy N is a nickel-based alloy containing roughly 6wt% chromium (Cr) for oxidation resistance and around 16 wt% molybdenum (Mo) to strengthen the material. The experimental reactor operated at roughly 650°C and operated the equivalent of 1.5 years over a period of 4 years. After this period the reactor core materials were studied, and they found significant cracking in its surface. After analysis researchers from the Oak Ridge National Laboratory concluded that the cracking was linked to grain boundary embrittlement by helium bubble formation and the fission product tellurium (Te). The helium bubbles were able to form by a two-step transmutation of nickel (Ni), as seen in reaction 8.1 [9].

$$\begin{aligned} {}^{58}\mathrm{Ni} + n &\rightarrow {}^{59}\mathrm{Ni} \\ {}^{59}\mathrm{Ni} + n &\rightarrow {}^{4}\mathrm{He} + {}^{56}\mathrm{Fe} \end{aligned} \tag{8.1}$$

Because of these problems with material embrittlement, addition of some alloying elements was proposed. First was the addition of *carbide* forming elements, as *incoherent precipitates*, to trap helium, hence reducing helium migration to the grain boundaries. Chosen elements for carbide formation were titanium (Ti) and niobium (Nb) as they do not reduce weldability as much as other possible elements such as zirconium (Zr) and hafnium (Hf). For high temperature applications the niobium performed significantly better as the titanium formed coarse carbides, hence reducing the helium trapping efficiency. Second, to reduce irradiation creep and strengthen the material at high temperatures, the addition of *refractory* elements[1] was proposed, as these elements with their high melting point are able to enhance hardness and the creep resistance of the material, making it possible to increase operational lifetime of these materials. All these changes are of great importance to obtain an alloy that can operate for roughly 50 to 60 years at temperatures in the range of 750 to 800°C and radiation levels far exceeding those of currently used nuclear reactors. These additions resulted in several alloys of interest, with most of them being modifications on the original Hastelloy N alloy. Other investigated alloys for MSR applications are 316 stainless steel and Oxide Dispersion Strengthened (ODS) alloys [9].

[1] Niobium (Nb), molybdenum (Mo), tantalum (Ta), tungsten (W) and rhenium (Re) are all classified as refractory elements with melting temperatures above 2000°C.

Currently, most nuclear reactor research focuses their reactor core material research on 316 stainless steels. The reasoning behind this focus is the worldwide standardization of this steel alloy group. Yet, the suitability of this alloy in the MSR environment is not substantiated, as the steel only performs adequately at temperatures below 700°C because of the loss in corrosion resistance and creep resistance at elevated temperatures [9, ch. 7].

Consequently, it is of importance to research the other potential alloys that possibly better withstand the extreme MSR environment. This leaves the Hastelloy group and ODS alloys due to their excellent corrosion resistance and microstructural stability, respectively. The latter have not yet been researched, therefore little evidence exists about its behaviour in the reactor core environment. Ergo, most ongoing research focuses on the corrosion resistant Hastelloy alloys [9].

Nickel-based superalloy microstructure

The MONICR alloy is part of the nickel-based superalloy group, a material family that is known for its excellent behaviour at high temperatures, primarily due to the properties of the matrix phase of these alloys, namely the FCC gamma, γ, phase. The γ-phase is known to have a high elastic modulus and many slip systems. The matrix phase has a low diffusivity for alloying elements, consequently making it a suitable phase for high-temperature environments. Together with its high solubility for many alloying elements extensive use of hardening by the solid solution strengthening is possible. Additionally, refractory elements such as molybdenum can further improve the high temperature behaviour as they increase the melting point of the alloy [10, p. 28; 11, p. 2027].

Additionally, two different close-packed intermetallic phases can form in nickel-based superalloys, both affecting the mechanical properties related to of the material. Important precipitates in these alloys that are known to have beneficial effects on the mechanical properties of the material are categorised as Geometrically Close-Packed (GCP). The characteristic of this type of intermetallic is its close-packed crystal structure, resulting in a very dense material. These phases have the A_3B formula [10, p. 29; 12]. Second are the Topologically Close-Packed (TCP) intermetallics, phases that are, in many cases, seen as unfavourable in engineering materials. The TCP-phase is characterised by its close-packed atomic layering that is regularly interrupted by layers of relatively larger atoms. Many of the TCP precipitates are reported to be brittle and act as crack initiation and/or propagation sites due to the plate/needle -like precipitate geometry that tends to form [13; 14; 15]. Yet, some studies reviewed by Geddes *et al.* [10, pp. 41-42] and Belan [12] report that very low concentrations of some TCP-phases may have a beneficial effect on the material its creep-rupture strength.

Ni-Cr-Mo based superalloys

Because the MONICR alloy is part a Ni-Cr-Mo-based alloy (such as many of the Hastelloys), the general behaviour of the Ni-Cr-Mo group will be discussed, followed by a more detailed comparison

and microstructural behaviour study of two alloys that are most related to MONICR, namely *Hastelloy C-276* and *Hastelloy C-4*. These alloys are chosen because of their similar carbon content (< 0.01 wt% C) that is, related to other Hastelloys ($0.02 - 0.10$ wt% C), low. As a consequence, low carbide concentrations are assumed as fractions of approximately 0.02 to 0.2 wt% C are required for carbide formation [12, p. 941]. Both reference alloys and MONICR have carbon concentrations lower than the solubility, with MONICR presenting a C content one order of magnitude below this lower limit. The presence of carbides is of importance as these precipitates are known to alter the mechanical properties and microstructural behaviour significantly [10, pp. 34-39; 12, p. 941]. Although the concentration of carbon is somewhat similar in these reference alloys, the other alloying elements deviate more significantly from MONICR, such as the chromium and iron content.

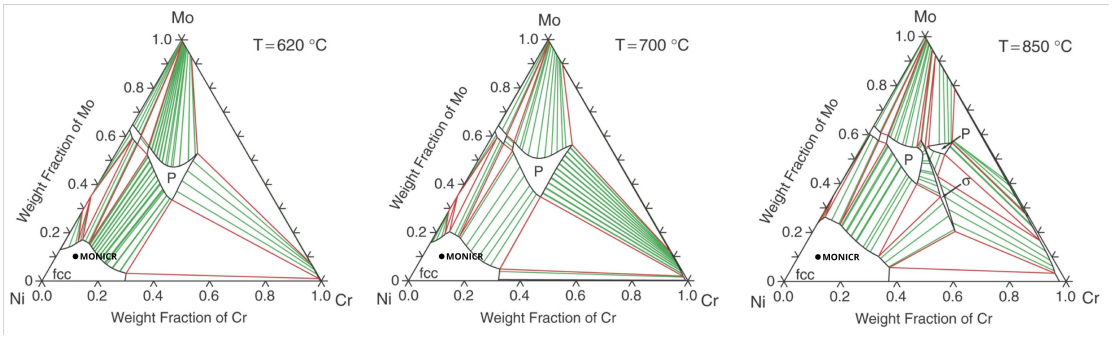

Fig. 8.1 The calculated isothermal ternary phase diagrams of Ni-Cr-Mo based alloys at 620, 700 and 850°C. Reprinted and modified from Turchi *et al.* [5, pp. 76-77].

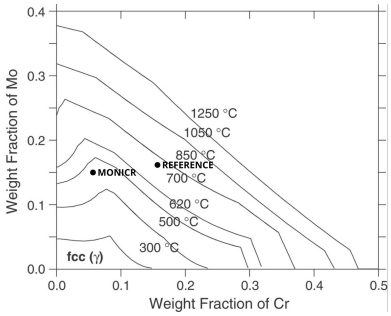

Fig. 8.2 The calculated FCC stability domain for the Ni-Cr-Mo phase diagram. The lines represent the isopleths for the matrix phase. The annotation 'REFERENCE' refers to the discussed Hastelloy alloys C-4 and C-276. Reprinted and modified from Turchi *et al.* [5, p. 77].

While the superalloy group exhibits excellent corrosion resistance in both corrosive and radioactive environments, little experimental research is conducted on the microstructure and its mechanical properties, as their engineering use is very specific and limited. Nevertheless, some computational microstructural stability simulations were carried out. Turchi *et al.* [5] presented a study about the phase stability of this unique alloy group, combining both computational modelling and relevant experimental studies.

Figure 8.1 shows the calculated ternary phase diagram for a selection of temperatures relevant to this research thesis. The compositions of the calculated alloys exclude other alloying elements. It can be seen that for all temperatures within the researched range (650-800°C) the MONICR alloy, when ignoring other compositional elements, is stable in the γ-phase. Further calculations conducted in the study from Turchi *et al.* [5] concluded that the stability of γ-phase diminishes as temperature decreases. This relation between γ-phase stability, temperature and composition is illustrated in figure 8.2. From this computational study it can be

assumed that the MONICR alloy will behave somewhat similar to the reference alloys Hastelloy C-4 and C-276, yet being more stable at lower temperatures. However, the complex phases (γ, P and μ) might form as a result of local microstructural discrepancies sch as alloying fraction deviations from the bulk.

To summarise, for the given MSR operational temperature range, this computational model estimates a single-phase (γ-matrix) microstructure with alloying elements Mo and Cr dissolved in the matrix. Yet, this calculation excludes the effect of other alloying elements on the microstructural stability.

Nevertheless, as the MONICR alloy alloying element fractions differ, the microconstituents of the alloy are likely to be different from these computational Ni-Cr-Mo alloy results. For that reason, it is important to compare the more elaborate computational and experimental data of researched reference alloys. As discussed, only the somewhat similar Hastelloy alloys with very low carbon content will be used as reference alloys; Hastelloy C-276 and C-4. The chemical composition of these alloys and of MONICR is given in table 8.1.

While figure 8.2 states that the γ-phase of both these alloys must be stable above 800°C, further data from the discussed study [5] predicts differently as these calculations include the other alloying elements. As illustrated in figure 8.3, both alloys seem to have multi-phase microstructures below 900°C. This is, however, not unexpected as several precipitates are known to form in the 600 to 900°C range in Ni-Cr-Mo based superalloys.

After long-term heat treatment, weeks to months range due to the relatively low Mo interdiffusion rate in the γ-matrix, these precipitates were found in the researched microstructures. The most reported phases were the complex phases μ and the P-phase, but also M_6C carbides, oP6-phase [$Ni_2(Cr,Mo)$] and the NiMo-phase [$NiMo$]. Additionally, a low stacking fault energy for the nickel matrix was found for both alloys. This results in a high density of annealing twins formed during (re-)crystallisation [11] and grain growth [16].

Precipitates Several different second-phases are known to form in Ni-Cr-Mo alloys, an overview of the most common phases is given in table 8.2. Of all the different phases the μ-phase [Ni_7Mo_6] forms in many Hastelloy alloys with a high molybdenum or tungsten content (above 6 wt%), while present in most Hastelloys they are not observed in the thermodynamic models of the reference alloys discussed in figure 8.3. The phase forms around grain boundaries and the grain interior. It is known to be very brittle and hard, hence increasing the hardness while decreasing the ductility. This behaviour was reported for heat-treated Hastelloy C-276 at 850°C. The phase is also referred to as a *Frank-Kasper* phase that is part of the TCP group [11; 17].

Related to the μ-phase is the P-phase that also has a very complex intermetallic Frank-Kasper crystallographic structure that is known to embrittle the material. This phase forms at high molybdenum concentrations [5].

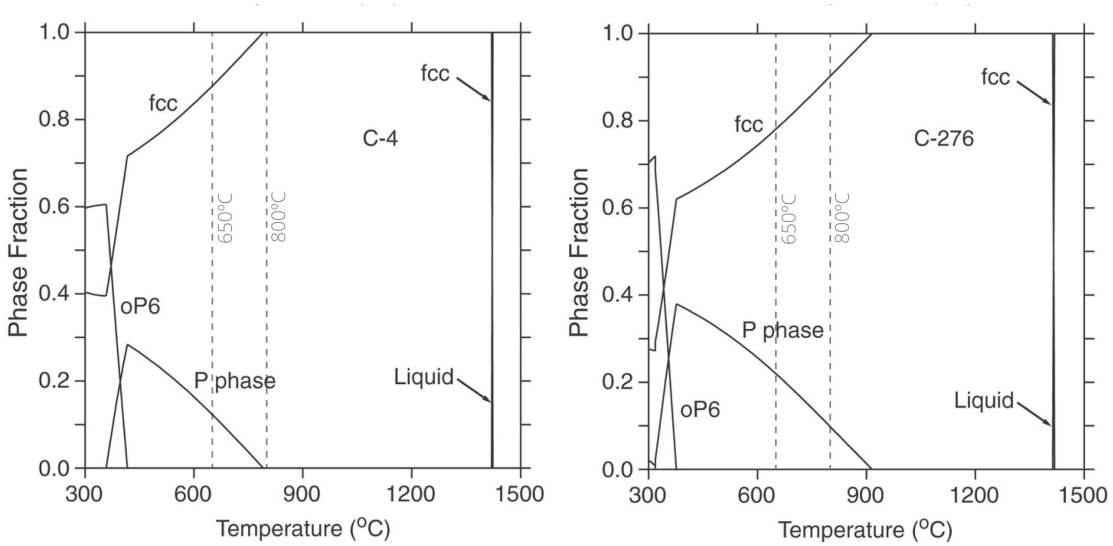

Fig. 8.3 Phase fraction versus temperature (property) diagrams of Hastelloy C-4 and Hastelloy C-276. Phases with fractions smaller than 0.01 are not included in this diagram (mainly carbides). The *oP6*-phase describes Ni_2Cr and to a lesser extent Ni_2Mo. Reprinted and modified from Turchi *et al.* [5, p. 81].

Carbides are likely to form in alloys with a high Mo and W content and are commonly formed in Ni-superalloys. In heat treated C-276, for example, carbides formed at grain boundaries at roughly 800°C, due to the low carbon content only M_6C $[(Ni/Mo)_6C]$ carbides were found in C-276. At elevated temperatures these carbides can embrittle the grain boundaries, hence making the material susceptible to brittle intergranular fracture [11; 17; 18].

To conclude, the formation of molybdenum-and chromium-containing precipitates are expected for the MONICR alloy at these temperatures, consequently making it important to characterise the present phases and morphology of the microstructure under different *long-term* heat treatments in the above mentioned temperature range.

Table 8.2 Observed phases in Ni-Mo-Cr-based reference superalloys and other possible phases for the MONICR alloy. Data is summarised from Geddes *et al.* [10] and Turchi *et al.* [5].

Phase	Crystal structure	Generic formula
γ	cF (fcc)	*nickel-rich solid solution*
δ (GCP)	oP20	A_3B
μ (TCP)	hR13	$A_xB_yC_z$ (commonly: A_6B_7)
carbide M_6C	cF (fcc)	M_6C
η (GCP)	hcp	A_3B
σ (*TCP*)	tP30	$A_xB_yC_z$
Laves (TCP)	hP12	A_2B
P (TCP)	tP56/oP56	$A_xB_yC_z$
NiMo (TCP)	oP56	AB
oP6	oP6	A_2B

8.3 Microstructural evolution at high temperatures

8.3.1 Diffusion[2]

In a crystal system atoms are constantly moving around because of thermal vibrations, allowing movement throughout the bulk material. This means that even when a material is in equilibrium the atoms still move around. This type of diffusion is referred to as *self-diffusion* [20, ch. 3.1]. In a real crystal most atomic structures are not directly in chemical equilibrium due to the presence of external influences on the chemical potential[3]. These potentials can be a result of gravity, elastic fields, electrostatic interactions and many more potential force fields. Therefore, when these external effects are added to the internal chemical potential (due to microstructure, temperature, etc) the total driving force for change is obtained. In many cases this results in atomic movement referred to as flux (J [#atoms/m^{2}s]), in its turn changing the microstructure [21, ch. 5.1].

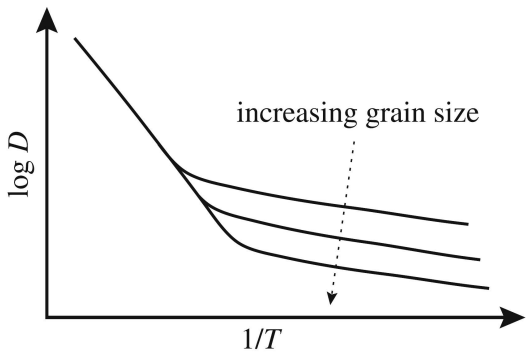

Fig. 8.4 The effect of polycrystallinity (high-diffusivity paths) and temperature on the diffusion coefficient. Reprinted from Was [19, p. 202].

Grain boundaries and phase boundaries affect the diffusion character of the material at primarily low temperatures, because of the preferred atomic movement along *high-diffusivity paths*. Diffusion along these imperfections is faster compared to diffusion in the bulk, because the activation energy

[2] A more elaborate explanation on diffusion can be found in appendix A.1.1.

[3] The chemical potential (μ [J/atom]) is a quantity used in diffusivity and transformations to describe the tendency of matter to change its configuration [20, pp. 40-41].

for movement is reduced as binding energy between atoms is reduced due to the presence of defects. Therefore, a low concentration of defects results in lower diffusivity at low temperatures. At higher temperatures, however, the thermal vibrations increase drastically, allowing for more energy-intensive jumps, hence making high-diffusivity paths nearly obsolete, see figure 8.4. This increase in available energy enables diffusion through many different paths, resulting in a higher diffusivity [19, ch. 4.6; 21, ch. 5]

This increased diffusivity can aid important microstructural processes, like grain growth and coarsening of precipitates, which, in turn, directly affect mechanical properties.

Kirkendall-effect

In an alloy many elements can be present, and when an alloying element or impurity has a preferential association with the atom flux, referred to as *coupling*, it can generate a net flux towards (interstitials) or away (vacancies) from a defect sink such as grain boundaries (GBs), see figure 8.5. This preferential association to a specific defect flux, referred to as the *Kirkendall effect*, is a result from a difference in diffusivity of alloying elements forcing the diffusion by the vacancy mechanism, hence forming a non-zero atom flux [22, ch. 7.2.3; 19, ch. 6].

In figure 8.5 the net atomic flux results in a segregation of elements around the GB, as atoms A are replaced by atoms B. Though, when no other elements are involved (e.g. element extraction as a result of corrosion) the depletion can result in void nucleation named *Kirkendall-porosity*. This formation of voids is a direct consequence of unbalanced diffusion rates of alloying elements [20, p. 117].

Because diffusivity increases with temperature, the Kirkendall-effect accelerates. To reduce these effects, diffusivity must be reduced.

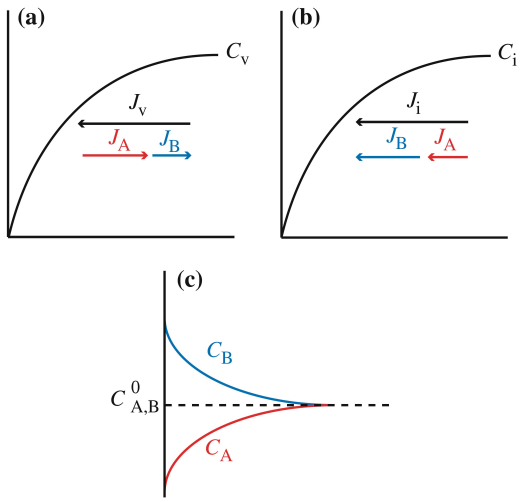

Fig. 8.5 Kirkendall-effect in a binary (50% A-50% B) alloy. (a) showing the vacancy concentration towards the GB and the net atom flux by vacancies, (b) the interstitial flow towards the GB and the net atom flux by interstitials, and (c) the resulting concentration profile. For image (a) and (b) the x-axis describes flux and the y-axis concentration. For image (c) the x-axis describes distance and the y-axis concentration. Reprinted from Was [19, ch. 256].

8.3.2 Phase transformations and precipitation[4]

For any given temperature and pressure the microstructure of an alloy configures itself in a specific way. When one of these variables change the configuration or phase of a given element can transform to lower its free energy at these conditions. For many alloys the added elements are soluble to some extent, spreading the solutes homogeneously over the crystal sites as substitationals, or when smaller as interstitials. When conditions change the solute can create supersaturation of that element in the matrix. This supersaturation results in the nucleation of precipitates that, when created, lower the free energy of the system by creating a new phase compared to the supersaturated crystal. The formation of such a phase results in new interfaces between the matrix and the precipitate that generate new strains in the system [21, ch. 4]. When these precipitates increase in size their, at first, coherent interface change to an incoherent interface to lower the free energy of the boundary. This transformation greatly affects the dislocation mobility mechanisms of the alloy, and consequently altering the mechanical behaviour of the material [21, ch. 9.2.1].

When these precipitates nucleate they are able to grow, if energetically favourable. This growth can be quantified because of the included energies; the formation of the new phase configuration lowers the free energy, while the interface area with the matrix results in an increase. If we now think of the precipitate as a sphere it is possible to calculate the decrease in energy related to the phase transformation in the spherical volume. The increase in energy by the interface can be calculated with the interface area of the sphere. The volume of the sphere increases by a factor radius to the power 3 (r^3), while the surface only increases by r^2. Combining these two it is clear that at some radius the decrease in energy dominates over the increase, meaning that at some radius the precipitate can lower the free energy by growing in size, this effect is named the *Gibbs-Thomson effect* [20, ch. 2.3.4].

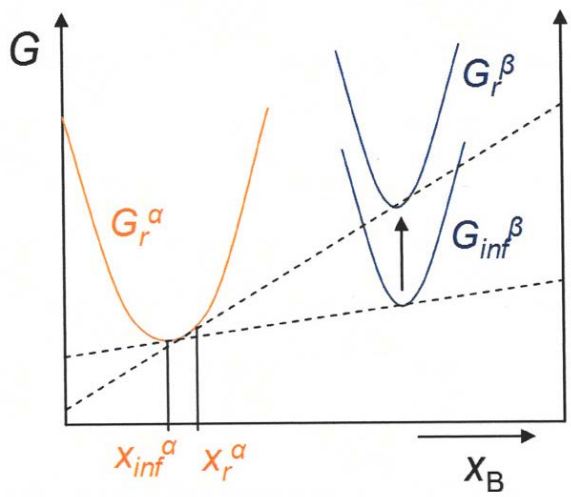

Fig. 8.6 Free energy differences related to different precipitate sizes. Reprinted from Santofimia & Sietsma [20, p. 163].

As discussed the growth of these precipitates, referred to as *precipitate coarsening*, can be energetically favourable as small precipitates cause a high free energy of the system. At higher

[4] A more elaborate explanation on phase transformations can be found in appendix A.1.2.

temperatures such as in the reactor environment, diffusion between these precipitates becomes common. As earlier discussed, smaller precipitates have a higher free energy (Gibbs-Thomson effect), this results in a higher concentration of the alloying element (x_r^α) at the interface between matrix and precipitate compared to that of a larger precipitate (x_{inf}^α), as seen in figure 8.6. Between these two precipitate interfaces a concentration gradient exists, allowing diffusion of alloying elements from the high concentration at the small precipitate interface to the low concentration interface of the big precipitate, resulting in the growth of the already larger precipitate and shrinking of the small precipitate. The aforementioned diffusion mechanism is called *Ostwald ripening*. Precipitate coarsening rates are dependent on; (i) the diffusivity of alloying elements through the matrix, (ii) the interface concentration gradient and (iii) the solubility of the alloying element [20, ch. 4.5.2]. The interface concentration gradient ($\frac{x_r}{x_\infty}$) is described by:

$$\frac{x_r}{x_\infty} = \exp\left(\frac{2\gamma V_m}{rRT}\right) \tag{8.2}$$

The equation is reprinted from Santofimia & Sietsma [20, eq. 2.73]. It shows the relation between the interface energy per area γ [J/m^2], temperature T [K], precipitate radius r [m], the molar volume of the precipitate element V_m [m^3] and the gas constant R [J/mol-K]. As a result, at higher temperatures, the precipitates tend to coarsen even faster.

8.3.3 Recovery, recrystallisation and grain growth [21, ch. 7]

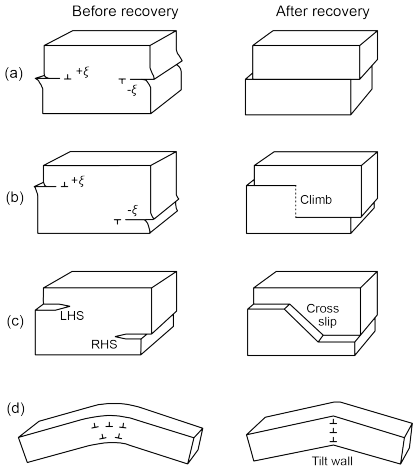

Fig. 8.7 Recovery processes of interacting dislocations in a strained lattice crystal. Reprinted and modified from Royce [23].

When dislocations are present in a high density, the system is out of its thermodynamic equilibrium and rather in a quasi-mechanical equilibrium. At lower temperatures and stresses this means that dislocations cannot leave their glide planes by climb or cross-slip, hence leaving the system in its meta-stable state. When the temperature increases the mobility of the dislocations is enhanced, making interactions between the dislocations possible. Edge dislocations can leave their slip plane by climb, while screw dislocations can change the slip plane this by cross-slip. This mobility can result in important microstructural altering mechanisms, namely; *recovery*, *recrystallisation* and *grain growth*.

Recovery Because dislocations have a long-range stress field they can attract or repel other dislocations, this interaction can result in a process

named *recovery*. Figure 8.7 shows possible recovery processes due to dislocation interaction in a strained lattice system. (a) Interaction between two edge dislocations at the same slip plane and of opposite sign (ξ), annihilating each other, hence reducing the dislocation density of the system and therefore lowering the internal energy. (b) Same sort of edge dislocation annihilation but now the dislocations are on different planes, therefore requiring *climb* or creation of a vacancy. (c) Interaction of two screw dislocations of opposite directions (LHS, left hand screw and RHS, right hand screw) that annihilate each other as a result of cross slip over their common cross-slip plane. (d) *Polygonisation*, or formation of sub-grains, a favourable configuration that requires dislocations glide of similar sign (ξ) towards a more favourable aligned position, creating a low-angle tilt boundary in return (see appendix B.2 figure B.11). At last (not given in the diagram), the movement of a dislocation towards the crystal surface can annihilate the dislocation too. All these recovery mechanisms reduce the dislocation energy and consequently reduce the present back stress from dislocations in the microstructure.

Recrystallisation During annealing of the material, a time-dependent process that happens at intermediate-to-high temperatures, the grains can recrystallise when they are deformed as a result of cold working[5] or *creep*. Deformed grains store strain energy that increases the free energy of the system, therefore at a certain value the nucleation of a new strain-free grain around a GB becomes favourable. Nevertheless, recrystallisation of cold worked materials only happens once after the component manufacturing, creep has the ability to deform the grains over a specific stress and time span. At a certain creep-induced grain elongation the polycrystalline matrix starts to nucleate new strain-free grains. The difference between the strained grain and the unstrained equivalent represents the driving force of this process. This mechanism is referred to as *dynamic recrystallisation* and also happens during deformation.

Recrystallisation happens at temperatures above roughly 0.4-0.5T_m, and develops quickly at very high temperatures but can take long at lower temperatures. Nevertheless, other processes play an important role, as recovery of the material greatly reduces the nucleation of new grains, because the related processes lower the free energy in the system and thus driving force for recrystallisation. The process can significantly change the microstructure after short-term heat treatment. However, when controlled this process is of little importance to long-term heat treatment.

Grain growth Another important mechanism that alters the microstructure and its properties at high temperatures is the growth of grains. This process starts when recrystallisation and recovery are finished and the system wants to further lower its internal energy by reducing the total grain boundary area.

[5]Cold working is a manufacturing process that is not commonly used for nuclear components because it results in post-processing strains that require additional heat treatments to reverse the hardening effects. This annealing treatment can be difficult to control during industrial processing.

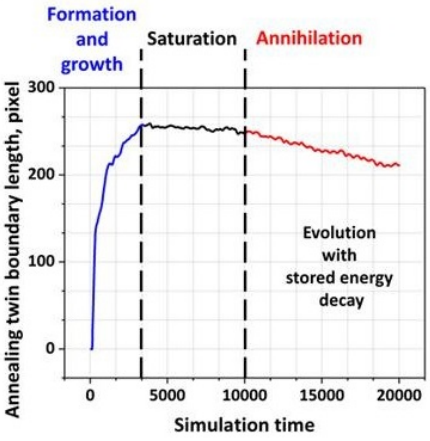

Fig. 8.8 Balance between formation of annealing twins and annihilation by boundary movement. Reprinted and modified from Jeyaraam *et al.* [24].

Under this driving force certain GBs become mobile (especially high-angle GBs), driven by thermally activated atom jumps from high energy grains to low energy grains, consequently lowering the GB interface surface. This mobility is the result of a net number of diffusional jumps from the shrinking grain to the growing grain, at last eliminating the small grain, increasing the average grain size and reducing the overall internal energy, consequently altering important mechanical properties while under long-term heat treatments.

Additionally, the migrating grain boundaries due to the grain growth mechanism can result in so-called *growth fault annealing twins*. These twins form at grain boundaries and triple junctions. Most of the annealing twins are formed during recrystallisation [24; 25]. Both simultaneous mechanisms of annihilation and annealing twin formation create a relation between annealing, thermal treatment time and total twin length, as visualised in figure 8.8. Twin boundaries also have the ability to annihilate by grain boundary and twin boundary migration [24; 25]. These twins strengthen the material by refining the grains, therefore annihilation leads to softening [26].

8.4 Microstructural evolution of irradiated materials

8.4.1 Activation

During irradiation elements in the alloy can form unstable isotopes that decay over time, this process is referred to as *activation*. For example, cobalt-59 forms the very unstable cobalt-60 isotope that releases a β^- particle and γ-radiation. This unstable element makes the structural material radioactive, making many processes such as maintenance, waste storage or even recycling of the metal more difficult due to potential health hazards related to the constant radiation emission. Another possible effect is the transmutation of an element into (eventually) a stable isotope, altering the mechanical properties during the process. One example is the transmutation of tungsten (W) into rhenium and stable osmium. The effects of these transmutations are mostly unknown and further research is required to understand the resulting behavioural changes. Due to the scope of this research thesis the effect of activation on the material its microstructure and properties is not analyzed. The effects on the microstructure are seen as minimal due to the usage of low activation alloying elements in the researched alloys. These alloys are selected by use of empirical data.

8.4.2 Displacement cascade

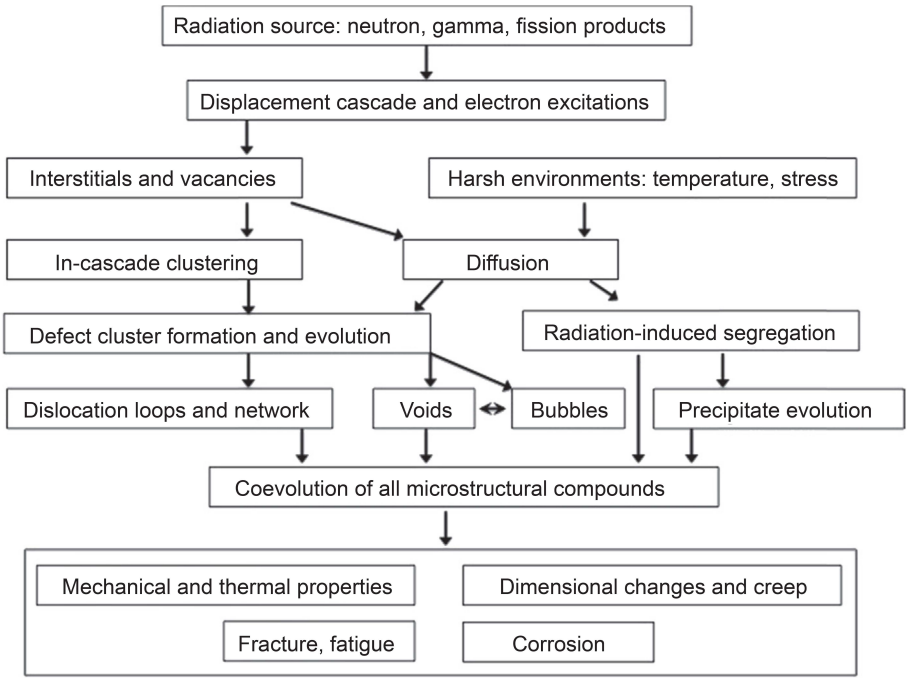

Fig. 8.9 Schematic diagram of material irradiation mechanisms and the resulting defect formation. Reprinted from Yvon [22, p. 255].

Irradiated materials can form a meta-stable state with a high density of defects because of displacements and excitations of bombarded atoms [21, p. 71]. Figure 8.9 shows the defect formation mechanisms of an irradiated metal.

As seen in figure 8.10 the Molten Salt Reactor, relative to other reactor technologies, is exposed to high operating temperatures and levels of radiation that result in a high density of displaced atoms. In the figure the term displacements per atom (dpa)[6] is used, which is directly related to the amount of high energy radiation interacting with the material. The many transmutations in the core of the reactor result in a variety of energy carrying particles and electromagnetic waves released from the fissile reaction, named radiation. Radiation affects local areas that come in contact with the particles or waves, resulting in atom-scale energy absorption that on its turn induces structural and electronic changes [27, p. 3].

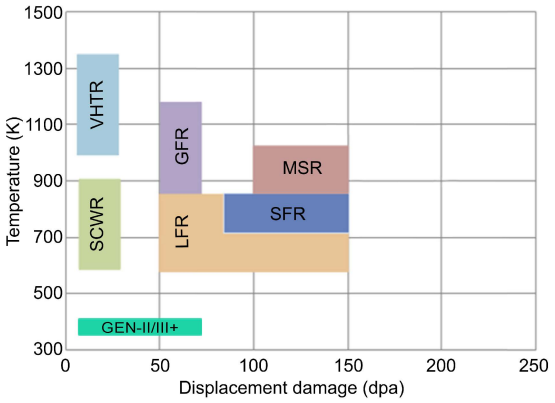

Fig. 8.10 Operation temperature and dose range of reactor core technologies. Reprinted from Yvon [22, p. 254].

[6]The value of dpa is a calculated average number of displacements an atom has made because of irradiation.

Such changes can drastically alter the microstructure of the material, hence inherently changing the material properties. Below a list of the main reactor material damaging radiation is given, including energy ranges:

- X-rays, electromagnetic waves [0.1-10 keV]
- γ-rays, electromagnetic waves [$>$10 keV]
- β-radiation, high-energy electron [$>$1 keV]
- Neutrons, thermal [0.5 Ev] to fast [$>$0.1 MeV]
- α-particle, helium nuclei [^{4}He, 5 MeV]

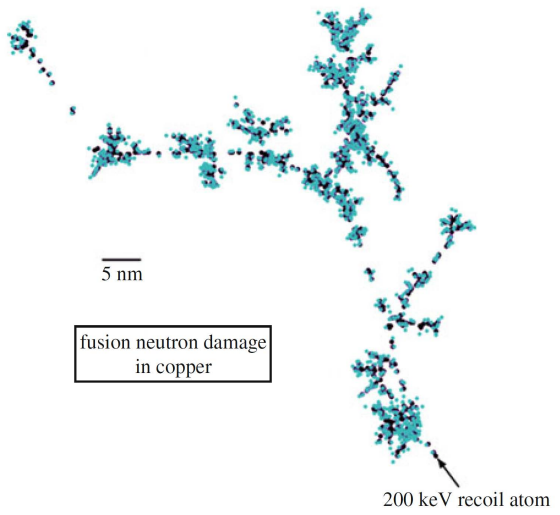

Fig. 8.11 Computational model of the Frenkel pair formation of a neutron radiation induced collision cascade in copper. The blue areas represent enriched interstitial zones, with the dots characterizing clusters. The black spots illustrate the low density vacancy clusters. Reprinted from Was [19, ch. 141].

In general, X-rays, γ-rays, α-radiation and β-radiation are seen as *ionizing radiation*, radiation that can ionize atoms and heat up the affected area. Generally this ionization is able to disrupt interatomic bonds and break them, except for α-radiation. Next to ionization of an atom, β-radiation is also able to displace an atom from its initial lattice position, by deposition of kinetic energy. The electromagnetic waves mainly excite atoms and deposit heat[7], but rarely displace an atom, however, when a γ-photon interacts with an electron it can cause *Compton scattering*, a mechanism that forces an electron out of its initial position, thereby creating a β-particle and a photon. The scattered electron is able to displace an atom [28, pp. 71-75].

Heavy charged particles[8] and neutrons generated in the reactor core are very energetic, allowing them to transfer a substantial amount of kinetic energy to the impacted atom, the so called 'knock-on' atom, causing displacement of atoms out of their original lattice position, while also possibly ionizing the affected atoms[9]. These ionized atoms are now able to cause a *cascade* of secondary 'knock-on' atoms, in turn, possibly ionizing them and thus facilitate further displacements. Depending on the impact energy of the neutron or heavy particle, it can cause a *collision/displacement cascade*, leaving many atoms displaced from their initial position [28, pp. 74-75; 22, p. 255]. The collision cascade generally happens around a certain area close to the Primary Knock-on Atom (PKA), generating a dense zone of secondary, tertiary, etc displaced atoms. This area is also referred to as the heat spike because the average energy

[7] γ-rays are able to deposit heat over a fairly considerable distance [28, p. 74].

[8] Fission fragments are generally seen as high energy particles, but because of their high mass and charge they travel only short distances relative to the other discussed particles [28, p. 70].

[9] Energy that was not used for displacement can ionize the atom.

of these atoms right after the collision cascade on to the order of 10,000 K. This thermal spike roughly lasts 30 lattice vibrations and hence can be seen as a short-lived thermodynamic system [29, p. 455].

The type of interaction a particle has with the impacted matter is greatly dependent on its mass, charge and energy. Greater charge and mass imply stronger interactions, while an increase in kinetic energy results in a reduction of particle interaction efficiency, resulting in different interactions [27, p. 3]. Low energy *thermal* neutrons react directly with the impacted atom's nuclei as they are absorbed, possibly causing fission (activation), γ-emissions[10] or charged-particle emissions. Fast neutrons and even highly energetic γ-rays and particles, however, are more likely to cause a substantial collision cascades, resulting in many defects[11] throughout the lattice [28, p. 75].

According to a study by Kirk & Blewitt [30] an atom receiving 20 keV results in the displacement of roughly 8800 atoms in a cascade. Atoms that are displaced from their lattice position form a Frenkel pair, as the displaced atom leaves a vacancy, while moving to an interstitial site. Many of these Frenkel defects will eventually recombine during the cascade process as interstitial atoms move to an available vacancy site [22, p. 256]. The remaining defect pairs are concentrated around the cascade impacted knock-on atoms, as seen in figure 8.11 [19, p. 167]. After the cascade several processes occur [19, p. 221]: (i) a portion of the interstitials will diffuse into a vacancy-rich zone and recombine, hence reducing the defect concentration. (ii) Another fraction of the interstitials will interact and agglomerate, forming so called interstitial dislocation loops and precipitates. (iii) The other interstitials are able to escape the cascade zone and migrate away. (iv) Vacancies that do not recombine can form clusters, such as voids and dislocation loops.

Clustering [29, ch. 2.2] The heat spike, earlier referred to as the cascade collision zone, contains two main regions, namely the low density (depleted/vacancy-rich) zone in its core and a high density (enriched/interstitial-rich) zone around its border. The thermodynamic system, despite being short-lived, turns the solid zone temporally into a hot liquid for around 10 ps that quickly cools down (several ps). During the solidification the material re-crystallizes and tends to form a perfect thermodynamic crystal, therefore recombining many formed Frenkel pairs. Yet, some isolated interstitials remain at the border of the heat spike zone as they are ballistically moved away from the vacancies because of high kinetic energies present during the cascade. The formation of interstitial clusters in this zone are less understood but observed. Additionally, a vacancy cluster forms at the center of the heat spike, because vacancies are pushed towards the core as a result of the re-crystallization process. In figure 8.11 these zones are illustrated in connection with the cascade path. The blue areas represent enriched interstitial zones, with the dots characterizing clusters. The black spots illustrate the depleted vacancy clustering.

In many cases the most stable configuration for defects is a cluster of two similar defects. This could be a dumbbell interstitial or di-vacancies configuration. Nevertheless, when point defect density

[10] When a γ-photon results in an excitement state that leads to particle emitting decay, it is called *photodisintegration*.

[11] In the case of high energy particle collision the high density of Frenkel pairs can result in a phenomena referred to as *clustering*.

increases and larger clusters form a more stable compound, the preferred configurations differ. Other important factors that influence the preferred configuration are temperature, alloying elements, crystal structure and many other factors dependent on internal and external forces. For example, when clusters are small to intermediate they can form in many cases stable dislocation loop configurations, while bigger clusters tend to be more stable as volumetric defects such as voids. As an example, the formation energies of various vacancy clusters as a function of cluster size in stainless steel at a certain temperature are given in figure 8.12. In this example the stainless steel can form very stable large voids, while loops are less favourable.

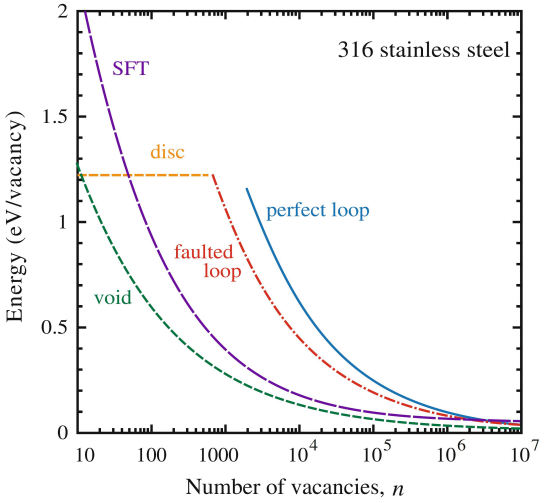

Fig. 8.12 Formation energy for a variety of vacancy clusters at a fixed temperature for 316 stainless steel. Reprinted and modified from Was [19, p. 348].

The general stability of vacancy clusters is relatively low compared to that of Self-Insterstitial Atom (SIAs) because diffusion of vacancies have fewer available movement 'paths' compared to interstitial diffusion. For that reason many of the vacancy clusters are thermally unstable, making them highly dependent on temperature, resulting in a decrease of vacancy clustering by dissolution (vacancy emission) as temperature rises. In the case of interstitial clusters the opposite is true, higher temperatures indicate more time for diffusion and possible interaction, thus increasing cluster growth and nucleation [19, pp. 335-337].

8.4.3 Irradiation induced diffusivity

[19, ch. 5] Irradiation of the material produces a high concentration of local defects in affected areas, creating a defect flux in the system driven by the cascade-formed chemical potential gradient of the defects. In combination with high temperature, and thus a high thermal diffusion coefficient (see section 8.3.1), the atomic flux in the crystals can drastically increase. The diffusivity (D) of the system is now given as a combination of both thermal diffusivity and radiation diffusivity as diffusion is possible with both mechanisms, as seen in equation:

$$D_{total} = D_{thermal} + D_{radiation} \tag{8.3}$$

Normally at very high temperatures, like the operating temperature of a MSR (see figure 8.10), diffusivity is mainly dependent on the thermal diffusion coefficient due to the significant presence of thermal vacancies. Yet, the Molten Salt Fast Reactor does not only endure very high temperature it also generates an large amount of irradiation-induced displacements (see figure 8.10), increasing the share of radiation induced diffusion greatly. This enhanced diffusion, also referred to as Radiation-

Enhanced Diffusion (RED), can result in more clustering of defects, defect migration driven solute segregation, creep and accelerated recovery.

8.4.4 Defect formation

As discussed in section 8.3.2 supersaturation leads to the formation of volume defects (precipitates) by agglomeration of alloying elements. Combining this formation mechanism with high-temperature irradiation a system with very high diffusivity is obtained that contains many formed defects. The high diffusivity and (local) defect concentrations form a hotbed for volume defect formation and growth. Three types of defects are induced or enhanced by radiation at high temperatures, namely; dislocations loops, voids (and indirectly bubbles), alloy segregation and precipitation.

Dislocation loops

As discussed, irradiation-induced collision cascades can result in vacancy-rich and interstitial-rich zones. In these areas the point defects tend to reorganise into a more stable configuration to lower the overall energy of the system. The configuration and size of these (quasi-)stable structures are dependent on the number of defects in the cluster, alloy composition, temperature and overall crystal lattice structure.

Nucleation and growth [19, ch. 7] Right after the heat spike the unstable agglomerates collapse onto the close-packed plane and create faulted[12] dislocation loops referred to as *Frank loop*, also known as prismatic dislocation loops. Seen in figure 8.13, condensed vacancies form a intrinsic stacking fault, while interstitials create an extrinsic stacking fault. The dislocations attached to the intrinsic fault are named single fault Frank dislocations (S-Frank loop), while for the extrinsic fault they are named double fault Frank dislocations (D-Frank loop). Both these loops are *sessile* (immobile), but the loop can transform into both *glissile* (mobile) dislocation networks and glissile perfect dislocation loops, by interacting with a dislocation line or autocatalytically[13]. At the operating temperatures of the Molten Salt Fast Reactor most of the formed clusters will be annihilated or unfaulted into dislocation lines adding

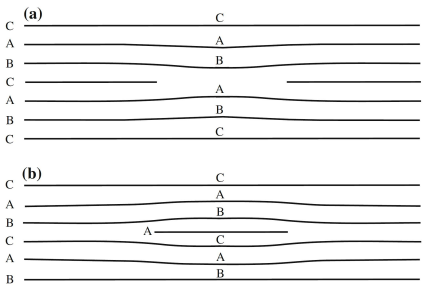

Fig. 8.13 Stacking fault configuration of a Frank loop. Letters a, b and c represent the stacking planes in a crystal. (a) intrinsic stacking fault due to vacancies, (b) extrinsic stacking fault due to interstitials. Reprinted from Was [19, p. 331].

[12] Faulted refers to a high energy state in which a stacking defect (e.g. ABCAB|ABC) is present.

[13] The autocatalytical transformation is a thermally activated process that is dependent on cluster size, it mainly happens at high temperatures [22, p. 258].

them to the dislocation network. As a result of loop unfaulting the dislocation density increases, thus affecting the plasticity of the material.

In FCC crystals with a low stacking fault energy, like the Ni-Mo-Cr alloy group, a third stable configuration is possible, named the Stacking Fault Tetrahedra (SFT). When a perfect intrinsic loop grows by consuming more vacancies it can reach a critical point in which the configuration is not in thermodynamic equilibrium anymore. To lower its internal energy by unfaulting the loop, it can split into three *Shockley partials*, leaving low energy stair-rod dislocations behind. When these faulted Shockley partials meet each other they form a pyramid shaped SFT structure.

Both sessile Frank loops and vacancy SFT clusters are able to grow steadily when there is a net positive flux of point defects (supersaturation). Nevertheless, interaction with dislocations can imbalance the configuration and eventually lead to dissolution, emitting many of the point defects in the process.

Cluster mobility The glissile dislocation loops formed during a cascade event can interact with other impurities as they move around the crystal by thermally assisted glide. At higher temperatures the dislocation loops can overcome more energy barriers they encounter, making them more mobile. These, in many cases interstitial, glissile dislocation loops move along their crowdion axis. Movement of these clusters increases the probability of interactions that can lead to recombination, or coupling and clustering with impurity atoms, hence changing the microstructure of the crystals, and mechanical properties [19, ch. 7.3.3].

Void- and bubble formation/growth[14]

During a displacement cascade a high concentration of vacancies can form and possibly form a vacancy cluster in the cascade core. When these vacancies are not all recombined the concentration of vacancies far exceeds the equilibrium vacancy concentration given. This supersaturation of vacancies can be the driving force to forming void embryos in the metallic structure. These embryos are mainly small vacancy clusters ($N_v \geq 4$) that 'occupy' lattice sites, hence following the crystal structure. N_v describes the amount of clustered vacancy sites. This process is referred to as void nucleation [19, p. 381]. The formation of these voids is an important reactor material problem as it causes volumetric swelling [22, p. 253; 19, ch. 8] and enhances chances of intergranular fracture when voids concentrate around GBs [31, p. 231], greatly reducing the lifetime of the material, and are thus unwanted.

Normally these voids, or empty vacuum cavities, are found in the material following the crystal structure and orientation, as seen in figure 8.14. This similar structure is clearly visible as the cavities are visible as distinctive geometrical shapes. But because of the constant irradiation of the material some of the metals transmute and emit α-particles that are insoluble but mobile as individual atoms in the alloy. These particles generate a driving force for void formation, by decreasing the free energy of formation G_n^0 (see appendix B.2, figure B.10). The small gas atoms diffuse through the lattice,

[14] A more elaborate explanation on void formation and growth can be found in appendix A.1.3.

similar to hydrogen, and move towards a void, where they are able to recombine and fill the void with helium gas. After a certain time the void will fill, pressuring and transforming the void into a spherical bubble that stabilises the structure by increasing the energy barrier for vacancy absorption, permanently swelling the material [19, ch. 8.1 & 8.8].

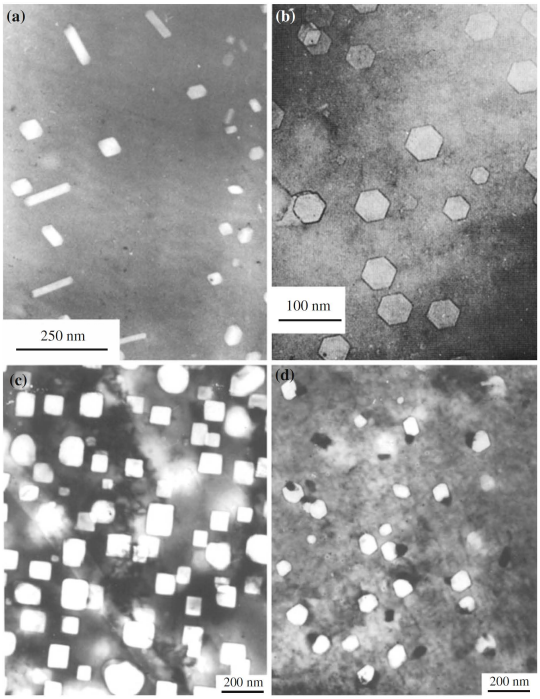

Fig. 8.14 Irradiation induced voids in (a) stainless steel; (b) aluminium; and (c-d) magnesium. Reprinted from Was [19, ch. 380].

When a vacancy is stable, it can absorb new vacancies that move through the system. When a smaller void becomes unstable, it emits vacancies, increasing the vacancy flux in the system. This allows the stable void to expand until it is in balance with the system. When temperature rises, this growth is accelerated. The critical void dimensions increase at higher temperatures, making the formation of new voids more difficult. Diffusion, on the other hand, is significantly increased, resulting in a preferable flux towards the existing voids and bubbles [19, p. 416].

Interaction with precipitates and grain boundaries When a void forms next to a precipitate it can directly be affected by the precipitate that behaves as a point defect sink. Incoherent precipitates in particular can accept a flux of any point defect and accumulate these defects. If the precipitate is neighbouring a void this flux can interact with the void. If the accumulation is that of interstitial defects the void can shrink, while a vacancy flux to the void will grow the void significantly [19, pp. 453-455]. For bubbles the shrink mechanism works to a lesser extent because the pressure increase by the helium results in a higher energy requirement for recombination of vacancies in the void (compressive strains).

The formation of voids at the grain boundaries has a somewhat similar constraint. In many materials the void concentration directly around the GBs is deluded because the vacancies close to this

area are attracted to the interface because it acts as a defect sink. This flux towards the GB reduces the supersaturation of the sink, thus decreasing void nucleation. In the case of a cascade event next to the GB the area adjacent to the denuded zone will contain many diffusing interstitials, removing SIAs from the matrix. As a result this increases the vacancy concentration, thus enhancing void nucleation and growth, it forms a nearly void-free zone next to the GB and a void peak zone adjacent to this area [19, pp. 455-460].

When a material is susceptible to precipitate formation, the void-related swelling and embrittlement can become problematic for the reasons stated above. As a result, it is important to first understand the precipitation, but also grain growth, behaviour of the material in a high temperature environment.

Induced segregation

Segregation of an alloy element can change the material properties dramatically, because the diffusional mechanism can deplete or enrich specific areas in the polycrystalline material (mostly around defect sinks) of their alloying elements. This produces a concentration profile over the system that has the ability to change local material properties and make these areas susceptible to embrittlement, radiation damage, local corrosion, etc [22, p. 262; 19, p. 255].

The heterogeneously distributed point defects generated by irradiation will form a defect flux in the system that has the possibility to increase segregation in alloys when solutes interact with the defect diffusion by the Kirkendall effect (see section 8.3.1). This enhanced variant of segregation is referred to as Radiation-Induced Segregation (RIS).

For alloys RIS mainly happens at intermediate temperatures (0.3-0.5T_m), as for lower temperatures the diffusivity is not sufficient and for higher temperatures the large concentration of thermal defects leads to defect annihilation and back-diffusion[15] of segregated elements [22, ch. 7.2.3; 19, p. 255].

Induced precipitation and recoil dissolution

The defect flux generated by irradiation greatly affects the stability of precipitates that exert strains on the matrix. Coherent precipitates have a minor stress field around them as a result of the strain between the matrix and the precipitate, resulting in the attraction of defects, trapping them at the interface. This increase of point defects around the interface finally results in the nucleation of an incoherent precipitate. These newly formed incoherent precipitates now behave as defect sinks that are able to absorb and emit point defects, consequently affecting the stability of the incoherent phases. Incoherent precipitates with a high fractional difference in volume of the precipitate than that of the matrix ($\delta > 0$)[16] results in a compressive strain, while those with a smaller fractional difference generates a tensile strain. As a consequence of vacancy generation by irradiation, the precipitates

[15] Back-diffusion refers to segregated elements diffusing away from their current position around defect sinks because of strong concentration gradients.

[16] The fractional difference in volume with the matrix is calculated by $\delta = \frac{\Omega - \Omega_m}{\Omega_m}$, with Ω being the atomic volume of the precipitate and Ω_m the atomic volume of the matrix.

mainly have a positive vacancy flux towards their surface. This flux can greatly impact the stability of precipitates due to strain relief of the interface between precipitate and matrix. The arrival of vacancies can lower the compressive strains around an interface, while it increases the tensile strains if present. This means that some thermally stable incoherent precipitates start to dissolve under irradiation as they become unstable, while other typically thermally unstable phases can suddenly become stable and nucleate incoherent precipitates by growing, as illustrated in figure 8.15. This type of irradiation-induced stability is referred to as irradiation-induced incoherent precipitation nucleation [19, ch. 9.4-5].

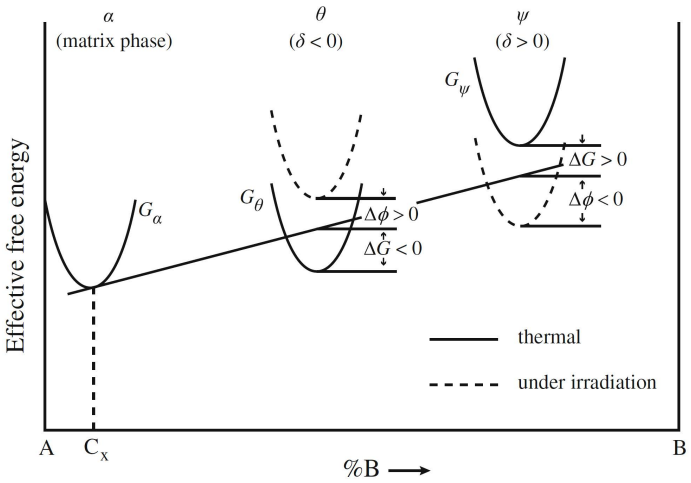

Fig. 8.15 Example of incoherent precipitate stability under non-radiated and irradiated circumstances. θ ($\delta < 0$) is the thermally stable phase, ψ ($\delta > 0$) is thermally unstable. The atomic volume difference relative to that of the matrix is given by δ. Reprinted from Was [19, ch. 507].

Recoil dissolution Nonetheless, irradiation can also result in the dissolution of precipitates in the collision cascade zone. During these collisions precipitates can ballistically be forced into the matrix around the precipitate, consequently shrinking and increasing the solute concentration around the affected area. This reduction process is named *recoil dissolution* and can be seen as the inverse of precipitate coarsening (precipitation re-solution). To understand the effect of recoil dissolution the relation described by Was [19, eq. 9.6] is given:

$$\frac{\partial r_p}{\partial t} = -\zeta K_0 \Omega + \frac{3DC}{4\pi r_p C_p} - r_p^2 D\rho \tag{8.4}$$

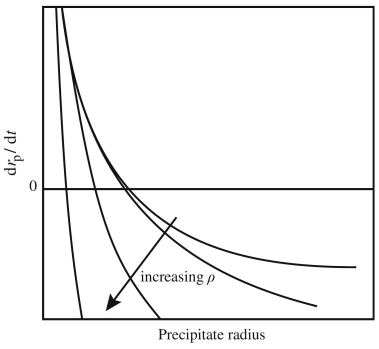

Fig. 8.16 Precipitate growth rate of irradiated material with recoil dissolution as described by equation 8.4. Reprinted from Was [19, ch. 489].

It gives the radial growth rate $\frac{\partial r_p}{\partial t}$ [m/s] of the precipitate affected by irradiation. Note that the equation does not include precipitate *coarsening* by Ostwald ripening. The rate is a combination of RED (see 8.4.3) and recoil dissolution. Variables in the equation are; the atom movement from the precipitate surface per dpa ζ [#/m^2-dpa],

displacement rate in the system K_0 [dpa/s][17], atomic volume related to the vacancy Ω [m^3], total solute diffusion coefficient D [m^2/s], total concentration of the solute C [#/m^3], radius of the spherical precipitate r_p [m], concentration of the solute in the precipitate C_p [#/m^3] and the precipitate density ρ [#/m^3].

Figure 8.16 schematically illustrates the effect of precipitate density and size (radius) on the growth rate of the precipitate, based on equation 8.4. It shows that when a precipitate is small the growth rate is positive, and when the precipitate radius increases to a certain size the precipitate starts to shrink. The same goes for an increase in the displacement rate as this lowers the growing rate of the affected area. All in all, the microstructural phase stability as a function of the precipitate stability of the alloy is highly dependent on both precipitate coarsening[18], by cause of irradiation-enhanced interdiffusion and Ostwald ripening, and dissolution by ballistic mixing. At last, ballistic mixing can contribute to segregation of the material. Resolution of precipitates lowers the precipitate concentration and newly formed precipitates are likely to form around displaced zones, altering the initial distribution of precipitates (*precipitate disordering*), subsequently changing *local* mechanical properties [19, ch. 9.2].

8.5 Mechanical properties and microstructure

8.5.1 Material properties

The mechanical properties of a material are extremely important as they tell us something about the behaviour of the structural element at certain conditions. For a structural component some of the most important properties are its yield strength, ductility and creep behaviour. In combination with other material constants they give a better understanding of the behaviour of materials, as it enables us to calculate elastic responses, brittleness, fracture toughness and many other important mechanical parameters. Figure 8.17 is a generic stress-strain curve that tells many of these properties already as it illustrates behaviour at certain elongations. Mechanical properties are directly linked to defects present in the microstructure as they can affect mobility of dislocations. At operational temperatures of the MSR ($\approx 0.5T_m$) these defects mainly consist of solutes, precipitates, dislocation networks and voids/bubbles (with molten salt corrosion or irradiation).

[17] Together ζK_0 represent the flux of alloying elements from the precipitate surface.

[18] For recoil dissolution precipitates coarsening the term re-precipitation is also commonly used.

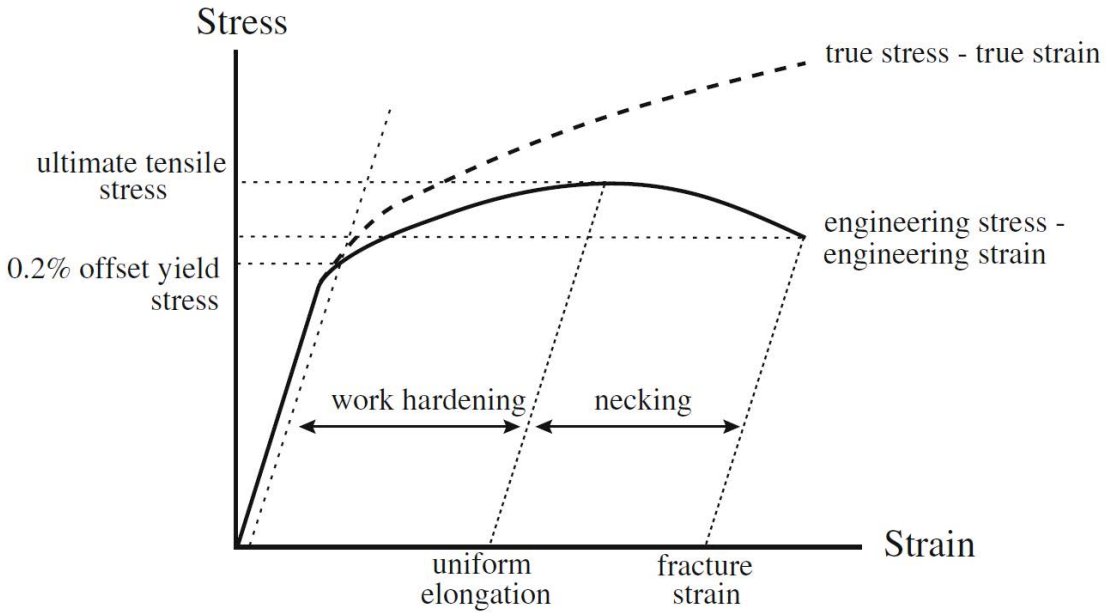

Fig. 8.17 Key parameters of the engineering stress-strain curve for metals. Reprinted from Was [19, ch. 678].

Plasticity is one of the key factors to structural stability and is therefore important for operational control; as deformation of metals will result in permanent damage or even fracture. In the case of external tensile stresses due to gravity or pressure the material will start to elongate elastically by stretching the bonds between atoms gradually. But at a certain stress, the yield stress (σ_y), this elastic behaviour is not sufficient anymore and the material starts to plastically deform. This deformation requires the formation of dislocations in order for slip to occur. These dislocations are generated by a *Frank-Read source* that unpins under a certain shear stress. This mechanism supports further elongation of the material. At first this will happen in a uniform manner because *strain/work hardening* processes ($\frac{\partial \sigma}{\partial \varepsilon} > 0$)[19] dominate over local softening mechanisms. This is recognizable by the increase in engineering stress as the material can tolerate higher stresses due to increased dislocation resistance. the most stress that a material can endure while being stretched before fracturing. When stresses further increase localised softening of the material starts to dominate ($\frac{\partial q}{\partial \varepsilon} < 0$)[20], diminishing the effect of work hardening and eventually result in accelerated mobility at certain regions, following a localised reduction of the cross section, referred to as *necking*. This localised plastic deformation becomes less predictable compared to the work hardening plasticity region as macro-mechanical processes do not happen uniformly anymore. This creates many different stresses in the system as the cross section becomes irregular, increasing localised strains to such an extent that fracture becomes inevitable, as illustrated in figure 8.17 [21, ch. 6.2].

[19] σ represents the external engineering stress and ε the engineering strain.
[20] q represents the cross section.

Yield strength [19, ch. 12]

When the material is mechanically loaded an external stress field is applied over the crystals. This stress can elastically elongate the material by stretching the bonds between metallic atoms and when the stress exceeds the yield strength (σ_y) the material will plastically deform, permanently changing its shape. This plastic deformation is supported by mobility of dislocations that allow slip of the atomic lattice. The yield strength refers to the stress, and thus energy, required to allow dislocation glide through the system. In a polycrystalline metal the yield strength is a function of; (i) initial lattice resistance (σ_i), also known as friction stress, required for glide, (ii) stress required to overcome the repulsive forces between dislocation lines (σ_{LR}), known as long-range stresses, and at last (iii) stress required to overcome obstacles such as incoherent precipitates, voids/bubbles, dislocation loops and in some cases grain boundaries (σ_{SR}), known as short-range stresses. The relation is by:

$$\sigma_y = \sigma_i + \sigma_{LR} + \sigma_{SR} \tag{8.5}$$

Long-range stresses (LR) For dislocations to start moving they first need to overcome the repulsive forces between the dislocations in the system. This increment in resistance, and thus yield strength $\Delta\sigma_y$, is given by the the Bailey-Hirsch relation as:

$$\Delta\sigma_y = \alpha G b \sqrt{\rho_p} \tag{8.6}$$

As the resistance is a result of repulsive forces between the dislocations the increment is dependent on the dislocation density ρ_p [m^{-2}], the magnitude of the Burgers vector b [m], a material-specific dislocation strengthening coefficient α and the shear modulus G [Pa] (elastic shear stiffness). From this equation it is clear that the increment in yield strength is proportional to the root of the dislocation density.

Likewise, the presence of grain boundaries and *sub-boundaries* (twins and sub-grains) can increase the yield strength by acting as a hard barrier that most of the dislocations cannot pass. Creating a pile-up of dislocations at GBs, increasing repulsive stresses (back-stresses) and thus ceasing plastic deformation at that given stress. In many cases this pile-up is a result of dislocation generation at a specific source such as a Frank-Read loop source that are activated at a certain shear stress. This effect is highly dependent on the density of grain boundaries and thus the grain size. The resulting increment in yield strength is described by the *Hall-Petch* relation:

$$\Delta\sigma_y = \frac{k_y}{\sqrt{d_{grain}}} \tag{8.7}$$

Variables in the equation are the crystal grain diameter d_{grain} [m] and the material-specific Hall-Petch constant k_y [MPa-$\sqrt{\text{m}}$]. The effectiveness of the grain boundaries in preventing dislocation slip is expressed by the Hall-Petch constant. As seen, the increment is proportional by the inverse of the

grain size, meaning finer grains result in a higher yield strength, this process is referred to as *source hardening*.

Another effect of the high stresses at the tip of the pile-up next to the GB is the possibility of source activation, a mechanism that results in *friction hardening*. These stress fields are felt not only in the grain of the pile-up but also at neighbouring grains, hence possibly increasing the shear stresses at that a given source in the neighbouring grain that can become activated, therefore releasing more newly formed dislocations. This process increases the dislocation density, as a consequence increasing the back-stresses and thus the yield strength, as described by equation 8.6.

Short-range stresses (SR) The dislocation mobility resistance forced by obstacles can be (by)passed by several mechanisms as illustrated in figure 8.18. These mechanisms can be categorised into athermal and thermal stress interactions. Athermal passage, being independent of temperature, is possible when a dislocation receives enough elastic energy by shear stress to be able to bow around an obstacle (also known as *Orowan bowing*) and eventually 'pinch-off', creating a dislocation loop (except for voids/bubbles) around the obstacle and releases the dislocation to continue glide. Nevertheless, the formed dislocation loop around the obstacle results in a stronger obstacle, hence increasing the resistance of these obstacles and consequently hardening the material. To quantify the athermal resistance of these obstacles the increment of the yield strength is calculated with use of the obstacle strength β, obstacle density N [m^{-3}], obstacle size d [m], shear modulus G [Pa], magnitude of the dislocation Burgers vector b [m] and the correctional Taylor factor M to accommodate the local strains between grains in polycrystalline metals. The relation between resistance and the increment in yield strength, referred to as the *Orowan hardening model*, is described by:

$$\Delta\sigma_y = \beta MGb\sqrt{Nd} \tag{8.8}$$

The obstacle strength β for voids and precipitates is close to 1 (very hard barrier), while that of other defects such as loops and clusters is way lower.

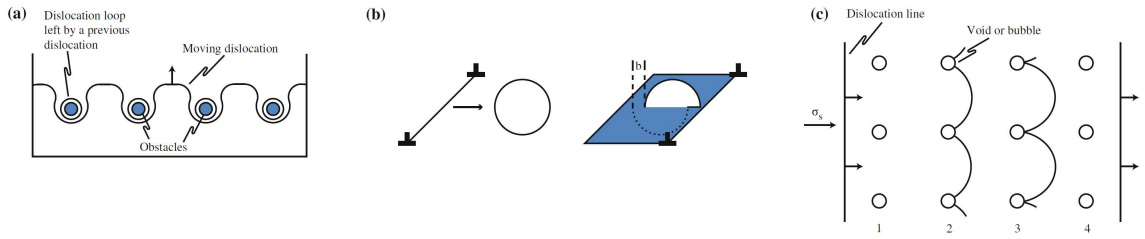

Fig. 8.18 Short-range stresses: dislocation-obstacle interactions resulting in friction hardening. (a) Dislocation bowing around incoherent precipitate, (b) Dislocation cutting mechanism through obstacle, (c) Dislocation bowing around void/bubble. Reprinted from Was [19, p. 689].

Thermal dislocation passage is also possible at higher temperatures. Thermal energy can activate certain processes that make it possible for a dislocation line to overcome these obstacles by bypassing or cutting through the volume defect. In many cases cutting through an obstacle requires less energy, thus being achievable at lower shear stresses. In a system without any external stresses the free energy required to overcome the obstacle is quantified as ΔF [eV] and can be lowered when an external shear stress is present σ_s [Pa]. The activation energy reduction factor is calculated by obtaining the fraction between the present external shear stress and the athermal required shear stress σ_s^0 [Pa]. The reduced required thermal free energy is now given as $\Delta G(\sigma_s)$ [eV]:

$$\Delta G(\sigma_s) = \Delta F \left(1 - \frac{\sigma_s}{\sigma_s^0}\right) \tag{8.9}$$

Whether the dislocation line wants to climb over or cut through the obstacle is highly depending on the size and composition of the particle. When the dislocation climbs over the obstacle it continues to glide without shearing the particle. Yet, when it cuts through the obstacle it can deform the volume defect. By continued shearing the void, bubble or precipitate can become elongated and even split into two smaller obstacles.

To summarise, thermal interaction reduces the resistance of obstacles by allowing more mobility mechanisms to happen, therefore an increase in temperature lowers the friction hardening ability of obstacles, resulting in a somewhat lower yield strength at higher temperatures.

Softening As discussed in section 8.3.3 at a certain very high temperature and/or stress the dislocations can start to annihilate each other, consequently reducing the dislocation density and the resistance to plastic deformation, hence softening the material by *recovery*. When this process is driven by stress it is referred to as non-thermal recovery. Three mechanisms are seen as non-thermal recovery processes, namely *cross-slip*, *Orowan bowing* and *cutting*. All these processes result in a friction, drastically enhancing dislocation movement, consequently supporting plastic deformation. In FCC crystals, such as the MONICR matrix, the cross-slip mechanism is allowed as the dislocations have the ability to bypass obstacles by simply switching to another slip plane.

In a high temperature environment the hardening ability of an obstacle can decrease by a mechanism named *Ostwald ripening*. This mechanism coarsens large precipitates at the cost of smaller precipitates to reduce the total interface energy of the obstacles, consequently lowering the planar density of obstacles. This reduction is possible because the required shear stresses for both bypassing and cutting through the obstacle are related differently to precipitate size and their coherency to the matrix. While smaller precipitates tend to have (semi-)coherent interface with the matrix, bigger precipitates, formed at higher temperatures, mainly have an incoherent interface. In general it is easier for a dislocation to shear a coherent small precipitate, as Orowan bowing requires a substantial amount of energy. Yet, when the precipitates become incoherent their interface can act as hard barrier similar to that of grain boundaries, meaning the stress to cut through the precipitate drastically increases. Therefore, Orowan bowing becomes the preferred bypass mechanism for the dislocation.

This relation between shear stress and particle size, consequently interface coherency (see 8.5.1), is given in figure 8.19. Bypassing these obstacles by Orowan bowing requires a shear stress τ_{orowan} proportional to the inverse of the obstacle size r ($\tau_{orowan} \propto \frac{1}{r}$), while the required shear stress for cutting τ_c is proportional to square root of the obstacle size r ($\tau_c \propto \sqrt{r}$) [21, ch. 6.7]. When plotting these relations it becomes clear that the obstacle has a maximum strength at an optimum size [21, ch. 6.7]. When these obstacles grow even further bowing around them becomes the preferred bypass method, resulting in a lower required passage strength. Additionally, because of *Ostwald ripening* (see section 8.3.1) the concentration of precipitates decreases at higher temperatures. Combining these two phenomena, also referred to as *overaging*, results in a reducing strength, consequently softening the material [21, ch. 9.2.1.5].

While the first two discussed mobility mechanisms act mainly uniformly on the material, cutting can result in local softening. When a certain obstacle is sheared by multiple dislocations the volume defect can dissolve and form a *dislocation channel*. This mechanism clears the path of obstacles and forms a channel in which dislocation can glide with little resistance, consequently softening the material locally. Nevertheless, in a FCC matrix with a low stacking fault energy twinning is expected to cause localised deformations [19, ch. 12.3.1].

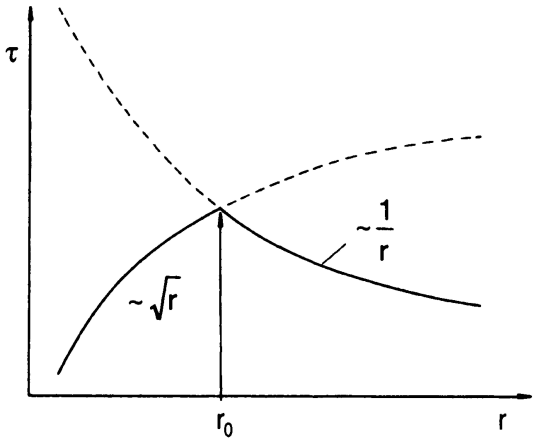

Fig. 8.19 Schematic representation of the strengthening dependence on the particle size of a precipitate, or in other words its interface coherency. Reprinted from Gottstein [21, ch. 279].

It is important to note that the material will continue to strengthen but because of the softening the material cannot support uniform plastic deformation anymore. This means that at a certain point in the material the mobility increases so drastically that the increase in stress becomes greater than its load carrying ability. This process starts at the point of maximum stress and enhanced local deformation starts to occur, consequently reducing the cross section, increasing stresses and accelerating further local plastic deformation. This plastic instability is referred to as necking and is the starting point of fracture as true stresses at this point drastically increase and are able to break bonds and initiate and propagate crack growth.

Ductility, brittleness and fracture [19, ch. 14]

Ductility is the ability to plastically deform under a tensile load before fracture. When a material is loaded with a certain stress it stores the energy in an elastic manner. This energy is at certain values able to unpin dislocations in the lattice to continue glide, or be able to break bonds between atoms,

creating a new surface. This crack initiation and propagation requires a substantial amount of energy that can only be achieved by localised buildup of energy. Two mechanisms play a key role in this buildup, namely the strength of the material and the stress increases around imperfections.

Materials with a high yield strength (resistance to dislocation glide) have the ability to store a large amount of elastic energy. This buildup in energy eventually unpins the dislocations, once again allowing glide and offsets plastic deformation. As earlier discussed in section 8.5.1, the plastic deformation can strengthen the alloy at first, hence increasing the stored elastic energy within the material when stresses increase.

Second is local intensification of stress around imperfections such as the surface (roughness) and voids/bubbles. Normally stress is distributed homogeneously over the cross section of the material. Yet, when a micro-crack is present, resulting from component manufacturing, stress intensifies around the inner crack tip because the crack surface does not have the ability to store energy by straining. This increase in stress is represented by the *stress intensity factor* K_1 [MPa-m$^{1/2}$].

When the energy at the crack tip equals the plastic work required to increase the crack wall area the (micro-)crack propagates. This resistance to crack wall formation is referred to as *fracture toughness* K_c [MPa-m$^{1/2}$], this material property is highly dependent on the microstructure of the material.

Materials with a high fracture toughness and low hardening abilities allow for extensive plastic deformation before fracture. These materials are referred to as ductile ($\sigma_{yielding} < \sigma_{fracture}$). In contrast, materials with a high strength and low fracture toughness display crack propagation over plastic deformation in many cases allowing for little plastic deformation before fracture. These materials are known as brittle ($\sigma_{yielding} \approx \sigma_{fracture}$).

Note, the toughness of a material is dependent on the yield strength and the ductility. The reason for this dependence follows from the ability to plastically deform the crack tip area to compensate for the enhanced stresses. Larger plastically deformed areas therefore mean more stored energy by plastic deformation. As described by Janssen *et al.* [32, p. 61] the ability to compensate for this stress is proportional to the inverse of the yield strength, meaning a high yield strength results in a less tough material when ductility does not change. Consequently, materials that harden lose their ability to plastically deform around the crack tip, resulting in a lower toughness and hence being more brittle.

8.5.2 Lasting effects of long-term heat treatment

Hardening and softening

The discussed microstructural kinetic processes permanently alter the microstructure during long-term exposure to high temperatures. Mechanisms such as recovery relax the material by decreasing dislocation density and internal strains, softening the material and increasing dislocation mobility. As a result, the yield strength is reduced while the ductility is increased. Processes such as *precipitation hardening* (the formation of precipitates, both TCP and GCP) and *dispersion hardening* (carbide

formation), on the other hand, reduce dislocation mobility. As a result, the yield strength increases while the ductility decreases, following potential embrittlement of the metal.

The diagram in figure 8.20 summarises the various microstructural mechanisms and their relationships to some important mechanical parameters. The diagram is split into softening and hardening. The increase or decrease of mechanical properties that are directly related to these changes are also given.

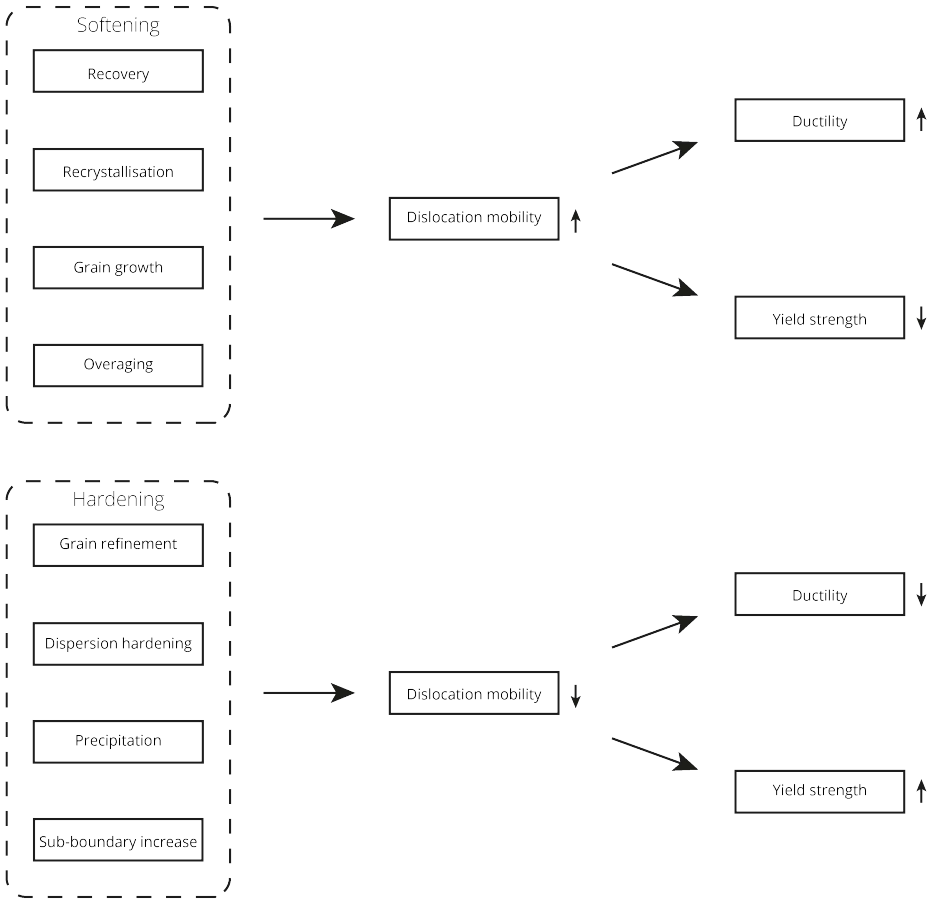

Fig. 8.20 Summary illustration of the various microstructural mechanisms and the related alterations in mechanical parameters. The figure is based on the discussed literature.

Embrittlement and fracture

Embrittlement of the material is caused by changes in the microstructure. A decrease in both ductility and yield strength can significantly reduce the material's toughness. As a result, the material is uniformly embrittled. Furthermore, the formation of certain obstacles can exacerbate this embrittlement. TCP precipitation facilitates crack nucleation and propagation due to its distinct geometry.

Overview

Figure 8.21 illustrates the various temperature-driven microstructural kinetics and their lasting effects on the material. These changes in the microstructure have a significant impact on the mechanical behaviour of the material and potentially degrading important mechanical properties to values below its operational limit. Ergo, it is important to analyse the above mentioned microstructural changes during long-term heat treatment experiments.

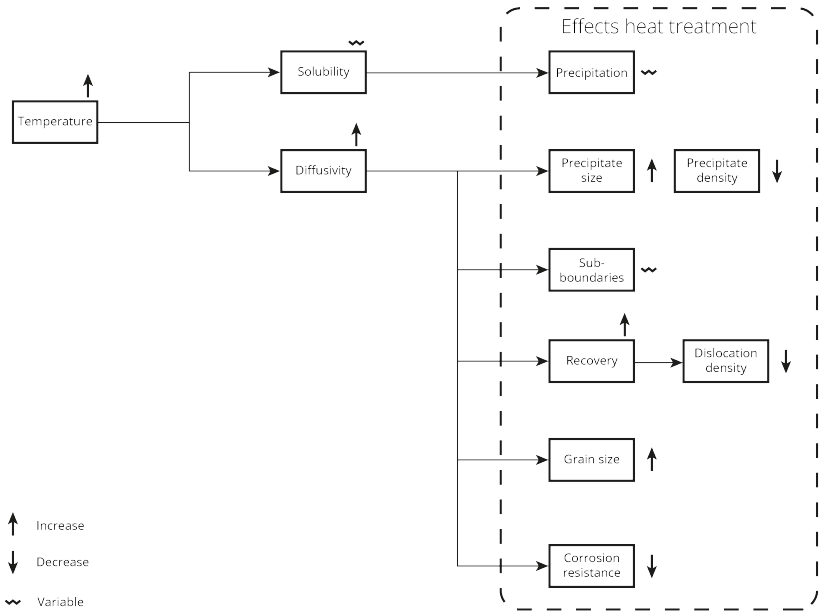

Fig. 8.21 Effect of high temperature (increase) on the evolution of the microstructure.

8.5.3 Lasting effects of irradiation

Irradiated material at intermediate-to-high temperatures ($\approx 0.5T_{\mathrm{m}}$) contains a high density of voids, bubbles, irradiation-induced precipitates, but also many mobile dislocations [19, ch. 12.2.3]. These obstacles and dislocations interact, resulting in dislocation channeling, twinning (FCC only), friction and work hardening, softening, creep, embrittlement and eventually fracture of the metal. While some of these mechanisms improve the fracture stress limit, others decrease it significantly, resulting in a balance between temperature and irradiation induced processes. For this reason this section will elaborate further on the main effects of high-temperature irradiation on material properties and fracture.

Irradiation hardening and softening

As earlier discussed in section 8.5.1 the presence of defects greatly affects the yield strength. In a molten salt fast reactor environment these defects will mainly be voids, dislocation networks and precipitates due to the high temperatures and radiation. Additionally, the size and phase of these

precipitates can greatly differ from that of unirradiated materials (see section 8.4.4).

The increased density of volume defects results in a higher obstacle density thus improving the friction hardening mechanisms in the system, resulting in a higher yield strength. Additionally, the presence of these irradiation-induced defects such as dislocation loops and networks also enables the material to form more dislocation sources thus further enhancing source hardening, while processes such as *recoil dissolution* (see section 8.4.4) are able to soften the material locally. Contrarily, at higher temperatures ($\frac{T}{T_m} > 0.5$) irradiation-enhanced *overaging* can occur, softening the material.

In the end, the material's hardening or softening is heavily influenced by two primary factors: temperature and irradiation intensity. These two factors constantly change the microstructure, resulting in a variety of mechanical properties. As a result, a delicate balance between these two factors is required. This balance can be discovered by conducting heat and irradiation experiments on potential materials.

Irradiation induced embrittlement and fracture [19, ch. 14]

During irradiation many things evolve in the microstructure. Precipitates form and grow, new phases are created and the dislocation density increases. As earlier discussed, these changes sometimes harden the material, increasing dislocation glide resistance. In combination with new phases the toughness of the material can decrease and the formed voids/bubbles increase stresses locally., all in all forming hot spots for crack initiation and propagation, hence embrittling the material and reducing the required fracture stress. The high temperature conditions do anneal out some of the defects (softening), resulting in a decrease of the embrittling effect. Yet, with the high neutron flux of the fast reactor embrittlement is expected. Additionally, the presence of voids/bubbles in a chain can form a high risk crack zone, as crack propagation is fairly easy because of the stress intensity around the voids/bubbles. By serving as a defect sink, incoherent precipitates can speed up this mechanism.

Next to embrittling, irradiation hardening will increase the yield strength. In combination with the decreased fracture stress the ductile-to-brittle transition temperature will increase, making the material more susceptible to unexpected brittle failure when cooled down to room temperature.

Overview

Figure 8.22 illustrates the various irradiation-driven microstructural kinetics and their lasting effect on the microstructure. These changes have a significant impact on the mechanical behaviour of the material and are thus important during long-term irradiation (combined with high temperature) experiments.

The results of the irradiation-affected microstructural evolution literature study show that it is critical to balance a material's diffusivity properties under extreme temperature and irradiation conditions so that they cancel each other out. Hence, balancing hardening and softening of the material during long-term exposure. Furthermore, the microstructural kinetics of a material must

be determined before conducting irradiation experimentation studies to correctly characterise these processes induced by high temperatures and irradiation.

Additionally, irradiating the material can result in the formation of many new obstacles, potentially TCP precipitates and voids/bubbles, a so called cracking chain can develop, hence further embrittling the material and resulting in early failure. To reduce the risks of this embrittlement mechanism the formation of TCP phases must be limited.

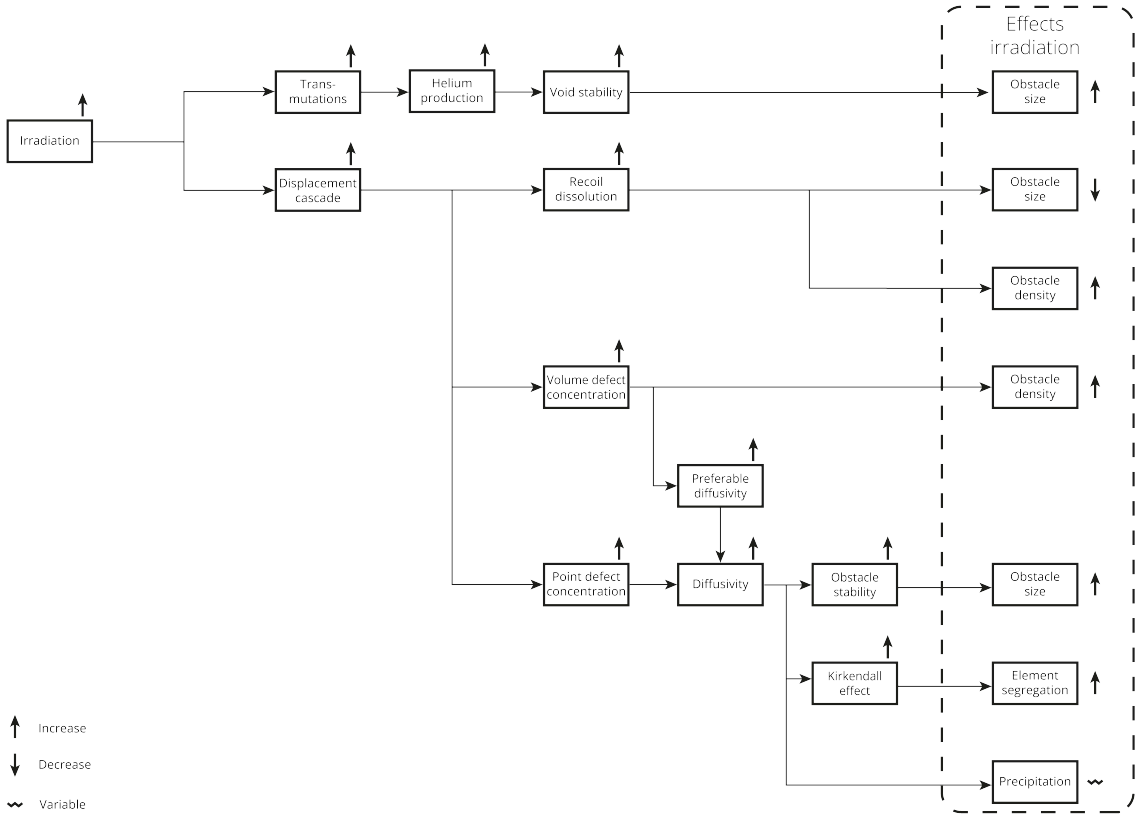

Fig. 8.22 Effect of irradiation on the evolution of the microstructure.

8.5.4 Microstructural requirements

Overall, a microstructure that uniformly softens is required to counteract the hardening (in many cases localised) effects of irradiation in a high neutron flux environment. Next, the formation of undesirable phases must be limited, consequently reducing the risk of embrittlement and extend the operational lifetime of the MSR reactor core components over time. Furthermore, irradiation significantly increases the creep range for both stress and heat. Additionally, due to the numerous changes in the microstructure, the material's expected non-irradiation induced creep behaviour may change. Grain growth reduces diffusional creep rates, increasing the minimum conditions for low-stress creep, while material softening facilitates high stress dislocation creep. As a result, to meet the

high operational lifetime requirements, excellent creep resistance at elevated temperatures seen in the reactor core environment is required.

The parameters mentioned in figure 8.20, yield strength and ductility, cover the two important factors that affect the operational lifetime of reactor core components, namely *embrittlement*.

8.6 Conclusion

The various topics discussed in this background chapter give an overview of the microstructural evolution and the resulting mechanical property changes. Combining these theories with the requirements of the MSR reactor core component material, the most important parameters and kinetic mechanisms can be listed, allowing for the set-up of a specified long-term evolution study of materials. The conducted literature review can be summarised as follows:

- Ni-Mo-Cr alloys are known to form embrittling TCP precipitates when exposed to reactor temperatures. Under irradiation void and bubble formation may lead to further embrittlement along grain boundaries, hence making TCP precipitates even more undesirable.
- Irradiation enhances and induces hardening mechanisms, consequently embrittling the material. Long-term thermal softening could be beneficial for operational lifetime.
- Formation of sub-boundaries (LAGB and twin boundaries) during grain growth embrittles the material. Annihilation of boundaries makes the material more ductile by increasing the material's work hardening ability.
- The material may become more brittle under irradiation as a result of recoil dissolution, which can change the size and density of precipitates in the material.

8.7 Research objectives

The literature review reveals that the extreme environment of an Molten Salt Reactor core poses significant challenges for the material's operational lifetime. Furthermore, due to limited research capacity and high costs, only a small number of materials have been thoroughly investigated for nuclear applications.

This thesis contributes to NRG's ENICKMA project by investigating the long-term effects of high temperature on the MONICR alloy, with a particular focus on the known embrittlement problem that was revealed during earlier tensile tests. The main research focus of this thesis is to *"Investigate embrittlement of the MONICR alloy under short-to-long-term heat treatments"*. This research objective is a result of the literature review conclusion. A set of sub-objectives based on the above-mentioned objective are investigated in order to properly research the research focus. These sub-objectives are listed below:

1. Determine the present phases in the microstructure as a function of heat-treatment time and temperature.
2. Characterise the phases' composition, geometry and crystallographic structure to determine embrittling potential.
3. Investigate the relation between mechanical property degradation and microstructural changes resulting from heat-treatment.

Chapter 9

Material and methods

9.1 Research material: MONICR

As earlier discussed (section 8.1), the *MONICR* alloy is one of the many researched alloys of the ENICKMA project. However, due to its interesting mechanical behaviour at high temperatures, the corrosion and heat resistant alloy was chosen for further research. As mentioned before, the research specifically covers the microstructural evolution of heat treated specimen as currently little is known about the microstructure and its mechanical behaviour. The research includes extensive Charpy and Vickers hardness testing combined with microscopy.

A collection of specimens with mostly unique thermal treatment times was analysed using a variety of mechanical tests and microstructural characterization tools. Table 9.1 lists the specimen names, total thermal treatment time, and all tests and analyses performed on them.

Table 9.1 Overview of all specimens and the tests that were run on them. X: test conducted on sample, $\simeq$: only *non-instrumented* test, -: no test conducted.

Name	HT time [hours]	Number of specimens	Hardness	Charpy	SFA	OM	SEI/BEI	EBSD	XRD
Reference	0	1	X	$\simeq$	X	X	X	X	X
	0	2	X	X	X	X	-	-	-
T800-6h	6	1	X	-	-	-	-	-	-
T800-11h	11	1	X	X	X	X	X	-	-
T800-17h	17	1	X	-	-	X	X	-	-
T800-1D	24	1	X	X	X	X	X	X	-
T800-2D	48	1	X	X	X	X	X	X	-
T800-5D	120	1	X	X	X	X	X	X	-
T800-1W	168	1	X	X	X	X	X	-	-
T800-2W	336	1	X	X	X	X	X	-	-
T800-1M	744	1	X	X	X	X	X	-	-
	744	2	X	X	X	X	-	-	-
T800-2M	1,536	1	X	X	X	X	X	-	X
	1,536	2	X	X	X	X	-	-	-
T800-3M	2,232	1	X	X	X	X	X	-	-
	2,232	2	X	X	X	X	-	-	-

9.1.1 Bulk chemical composition

The chemical composition of the MONICR alloy is presented in table 9.2. Noteworthy are its very low carbon (0.006 C/T 0.01 wt%), iron (1.52 C/T 3-7 wt%) and chromium (5.9 C/T 14-18 wt%) content, compared to (C/T) similar Hastelloy alloys (see table 8.1).

Table 9.2 The chemical composition of the MONICR alloy. The alloying elements are given in weight percentage. Values presented in this table is reprinted from the chemical composition data of the ENICKMA project [6].

Chemical composition [wt%]											
C	**Mn**	**Si**	**Cr**	**Mo**	**Ni**	**Fe**	**Al**	**Co**	**W**	**Cu**	**B**
0.006	0.042	0.031	5.9	15.0	77.41	1.52	0.010	0.048	0.032	0.030	<0.002

9.1.2 As-received conditions

Unfortunately, only little information on the fabrication route of the MONICR plate was available. For that reason it was assumed that the plate was traditionally casted, hot rolled and thermal treated before being cut to its final dimensions. This fabrication procedure would result in randomly orientated crystals. The plate dimensions were measured to be 84 mm by 196 mm with a thickness of 8 mm.

Resulting from the plate dimensions *Charpy* samples were chosen to maximise the amount of samples out of the plate. With the given plate dimensions 24 pieces can be cut out of the plate, all following the same directions, as illustrated in figure 9.1. To ensure only the non-machined plane is analysed the side of the test pieces will be prepared for further characterisation. This side is clearly visible in the top view of the plate cutting pattern illustrated in figure 9.1.

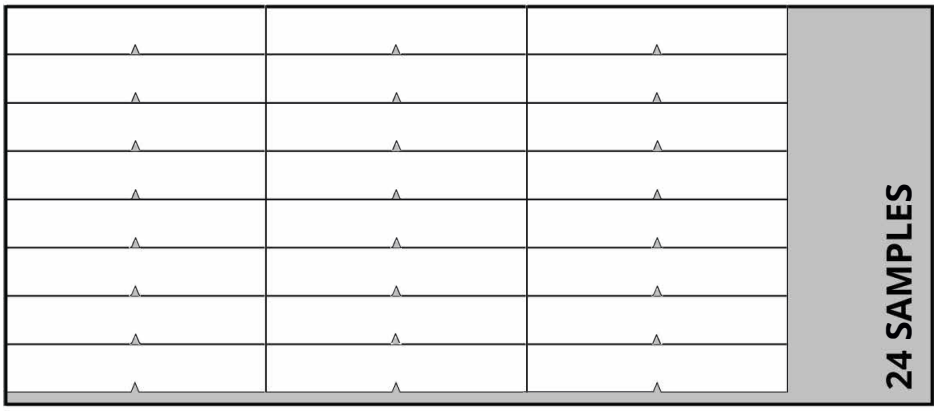

Fig. 9.1 Cutting pattern of the Charpy test pieces out of the given MONICR plate.

9.2 Methodology

9.2.1 Computational characterisation: Thermo-Calc

Information on the formation of thermally stable phases can be found by a the use of thermodynamic equilibrium computational software *Thermo-Calc* (CALPHAD phase equilibrium computing methodology). Thermo-Calc gives an estimation of present phases following thermodynamic stability of the composition at given temperatures. It is important to note that the real material is also influenced by many kinetic processes discussed in chapter 8. The resulting diagram is a combination of phase equilibrium calculations and a database containing phase information of comparable alloys.

For the simulation the TTNI6 database was used. The chemical composition used in the calculations are similar to the MONICR composition given in table 9.2.

9.2.2 Heat treatment

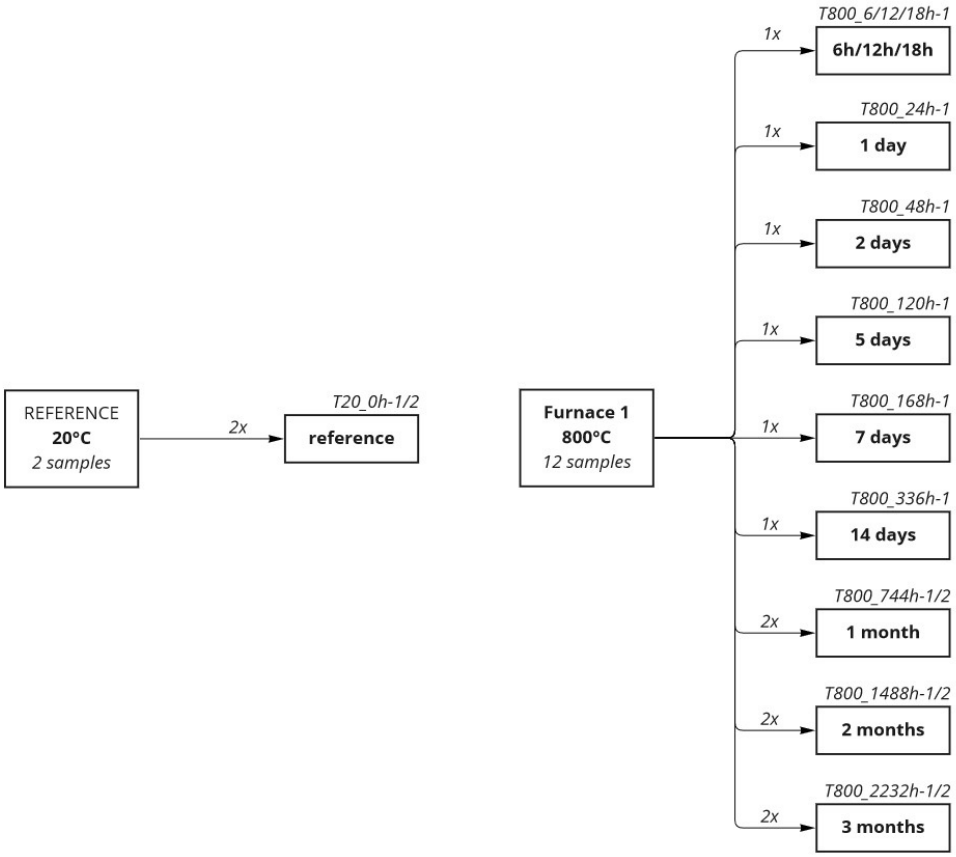

Fig. 9.2 Overview of the sample heat treatments, including sample naming.

To study the evolution of the material under different heat treatment (HT) scenarios, the samples need to be heat treated under a constant environment. This uniformity was achieved by using a thermal treatment furnace, the Nabertherm L5/S27, that was set at the studied temperature, 800°C. This temperatures was chosen to mimic the upper-temperature limit of the molten salt reactor, as discussed in chapter 8. As these temperatures are rarely reached the thermal treatment mostly describes the accelerated microstructural processes during long-term exposure to a MSR temperature relative to normal reactor temperature conditions (650°C). The temperatures also correspond with the *ENICKMA* irradiation experiment performed at NRG.

The samples in the oven were air cooled after heat treatment and did not experience any major fluctuations during heat treatment. The internal oven temperature variations were found to be roughly $\pm$2°C. The only major temperature variations were a result of removal of other samples. These fluctuations were between -25°C and -35°C during sample removal. After the removal procedure the

oven heats up to between 5-8°C above the set temperature.

Figure 9.2 gives an overview of the entire heat treatment arrangement. The diagram also includes the sample naming, which consists of; HT temperature - HT time - series number.

9.2.3 Mechanical characterisation

Just as with the characterisation of the microstructure, the measurement of mechanical properties can reinforce the understanding on the effects of heat treatments on the given material. As discussed in chapter 8, a variety of excellent engineering properties are necessary for the use in molten salt nuclear reactors. Of these properties the most important, with regard to heat and irradiation degradation, are the mechanical properties related to *embrittlement*. Ergo, these properties related to these important evolution properties are measured by a set of characterisation techniques. An overview of the mechanical characterisation flow is given in figure 9.3.

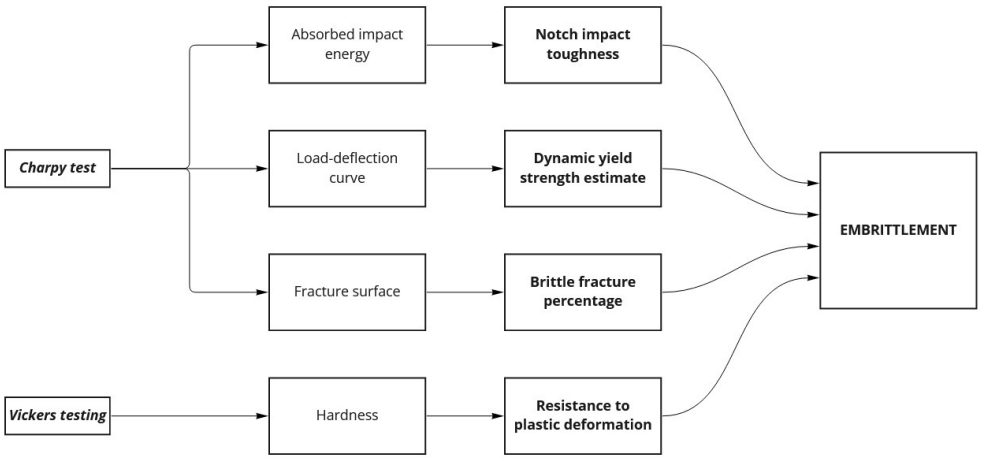

Fig. 9.3 Overview of mechanical related characterisation route and techniques. The techniques in italics and bold represent the main characterisation techniques. The final big boxes represent the required mechanical properties.

9.2.4 Instrumented Charpy test

Sample preparation

To research the microstructural evolution during long-term heat exposure, a set of samples were prepared that all undergo different heat treatments. Charpy samples were used to observe changes in mechanical properties, measuring the impact toughness, strength, fracture appearance and hardness.

The dimensions of the specimen, as illustrated in figure 9.4, were chosen to measure the impact properties using Charpy testing.

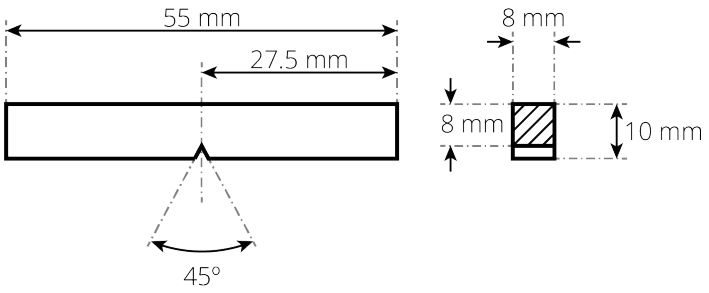

Fig. 9.4 Charpy V-notch test piece dimensions based on the European standard Charpy pendulum impact test norm. The thickness of the piece (8 mm) differs from the norm which is normally set at 2.5, 5, 7.5 or 10 mm [33].

The cutting was done by wire-cut machining (electrical discharge machining) to allow for high quality samples with little surface damage due to minor excess pressure of the machining tool. This procedure only leaves a very thin *white layer* that does not affect the impact testing measurements.

Charpy impact test

The instrumented Charpy pendulum test is a characterisation technique used to determine the energy absorption behaviour of a material, therefore exposing the ductility of the sample. The test works with a weighted pendulum that hits a v-notched Charpy specimen, consequently measuring the absorbed energy resulting from the potential energy of the pendulum. Additionally a fracture surface is created through the pendulum impact. This surface can be analysed for further information on the types of occurring fracture.

The main goal of the test is to characterise the fracture mode and ductility of the sample, when done over a range of specimen with different conditions or treatments important transition points for fracture behaviour can be derived. Values such as the *absorbed impact energy*, *lateral expansion*[1], *notch toughness* and the *shear fracture appearance* percentage, obtained by the pendulum impact test, help to understand the materials behaviour to high-strain scenarios more coherently [33].

This thesis focuses on three aspects that can be derived from the instrumented Charpy test, namely the notch impact toughness, load-deflection curve and the fracture surface topography (shear fracture appearance). All of these measurements can be used to calculate or estimate certain mechanical properties that can be seen as a function of heat treatment time and temperature.

The pendulum impact test system used for the experiments is the MTS EXCEED Model E22. It has an impact speed of 5.24 m/s and an impact energy of 450 J [34].

Shear fracture appearance SFA

To analyse the fracture of the post-impact Charpy samples the Shear Fracture Appearance (SFA) is measured by the use of a caliper.

[1]The lateral expansion is the amount of deformation in millimeters of the test piece due to the impact, it is a measure of ductility.

The SFA, a value measured as percentage of shear, is an useful, yet subjective, method for determining the amount of ductile fracture after a Charpy test. The fraction of brittle fracture versus annealing time relates to the embrittlement of the material as a function of thermal treatment.

Shear fracture areas, that are assumed to be entirely ductile, are recognisable due to their dull appearance, while shiny areas are categorised as cleavage (brittle) fracture [33]. A percentage table based on the dimensions of the cleavage area are seen as most accurate of all methods for determining the SFA, because these tables are based on measurements rather than rough estimates. For the distinctive dimensions of the used Charpy specimen the SFA indications are given in table 9.5.

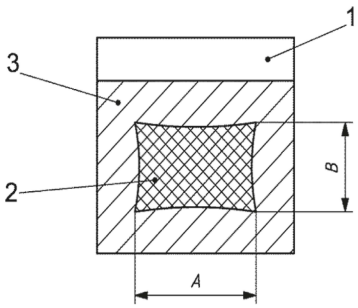

Key

1 notch
2 cleavage area (brittle)
3 shear area (dull)
A dimension measured to estimate the cleavage area
B dimension measured to estimate the cleavage area

B [mm]	A [mm]														
	1.0	1.5	2.0	2.5	3.0	3.5	4.0	4.5	5.0	5.5	6.0	6.5	7.0	7.5	8.0
	SFA [%]														
1.0	98	98	97	96	95	95	94	93	92	91	91	90	89	88	88
1.5	98	96	95	94	93	92	91	89	88	87	86	85	84	82	81
2.0	97	95	94	92	91	89	88	86	84	83	81	80	78	77	75
2.5	96	94	92	90	88	86	84	82	80	79	77	75	73	71	69
3.0	95	93	91	88	86	84	81	79	77	74	72	70	67	65	63
3.5	95	92	89	86	84	81	78	75	73	70	67	64	62	59	56
4.0	94	91	88	84	81	78	75	72	69	66	63	59	56	53	50
4.5	93	89	86	82	79	75	72	68	65	61	58	54	51	47	44
5.0	92	88	84	80	77	73	69	65	61	57	53	49	45	41	38
5.5	91	87	83	79	74	70	66	61	57	53	48	44	40	36	31
6.0	91	86	81	77	72	67	63	58	53	48	44	39	34	30	25
6.5	90	85	80	75	70	64	59	54	49	44	39	34	29	24	19
7.0	89	84	78	73	67	62	56	51	45	40	34	29	23	18	13
7.5	88	82	77	71	65	59	53	47	41	36	30	24	18	12	6
8.0	88	81	75	69	63	56	50	44	38	31	25	19	13	6	0

Fig. 9.5 (left) Shear fracture appearance dimension fraction table with corresponding SFA values. Note that when A and B are both zero the fracture surface is fully shear. (right) Measurement determination illustration. (left) Method reused and (right) reprinted from Royal Netherlands Standardization Institute [33, p. 17].

9.2.5 Hardness testing

Sample preparation

After performing the Charpy test the post-test specimen can be used for further analysis. However, first a series of preparation steps are needed to ensure a very smooth surface that is required for the other techniques. The preparation route is described in the overview given in figure 9.6.

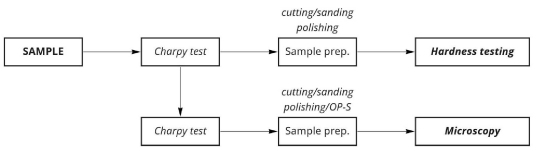

Fig. 9.6 Overview of the sample preparation route, including intermediate Charpy test.

Cutting Due to the modest dimensions of the sample pieces after the Charpy test, roughly half of the test piece length if fully fractured, only little cutting is needed. The size of a post-Charpy test piece are roughly 27.5 mm by 10 mm with a thickness of 8 mm. Nevertheless, to efficiently analyse the sample the non-fractured side of the specimens were cut into 10x10x8mm pieces. These pieces were then embedded into a non-conductive resin.

The cutting of the sample was performed with a regular circular metal cutting machine, namely the Stuers Discotom-6 with a 66A25 cut-off wheel. This step is expected to damage the surface of the sample closest to the cutting plane, for that reason only the interior of the sample will be analysed.

Grinding and polishing For characterisation techniques that require a highly reflective surface, such as microstructural microscopy and hardness testing, further preparation steps are needed. The first of which is grinding.

As very high surface smoothness is required for the SEM, the samples will be smoothed to a very fine grinding grain size (grit) in successively manner. The grinding steps are, from coarse to fine, P180, P320, P800, P1200, P2000 and P4000 grit respectively. All these successive steps remove material from the sample surface, consequently reducing the amount of damage such as scratches and thus planarising the sample characterisation plane. Each grinding step is done on a rotating disk with an ample flow of water on the given grinding paper. A water flow is required to reduce friction and, as a result, heating problems such as melting resin. Additionally, with the coarsest grit the sharp sides around the research plane are sharpened away to ensure as little damage to the polishing cloths used in the following step.

Polishing of the samples will be done in two consecutive steps, once again from coarse to fine. The process removes deformations formed during grinding, such as relatively thick scratches. Before every polishing step the samples are cleaned ultrasonically for 2 minutes in a bath of isopropyl alcohol, or also known as isopropanol. This process removes all the debris from the previous grinding steps, including the used polishing grains. Next, the sample will be placed on a rotating polishing cloth of a certain fabric that goes along with the diamond paste used that cloth. These two steps are repeated 2 times with Struers MD-Mol cloth and 3 μm diamond paste and at last with MD-Nap cloth and 1 μm diamond paste.

Vickers hardness testing

To determine the hardness of the sample a indentation test can be conducted. The test measures the hardness of a material locally by applying a certain force for a given period of time on the sample with a known geometrical indenter. This indenter leaves a indentation on the sample which area can be measured. Dividing the applied force of the indenter with the area of indentation gives the hardness value. In the case of the Vickers hardness test this results in a Vickers Hardness [HV] value. For the Vickers test the indentation procedure is illustrated in figure 9.7. Equation 9.1 gives the compliant

Vickers calculation method following European standards. Variables used in the equation are the gravity, g_n [m/s^2]; the applied force, F [N]; pyramidal indenter angle α [°]; and the arithmetic mean of the two diagonal lengths of the indent d [mm]. [35].

$$\mathrm{HV} = \frac{1}{g_n} \cdot \frac{2F \cdot sin(\frac{\alpha}{2})}{(d)^2} \tag{9.1}$$

As this value only complies to the tested local microstructure, multiple tests need to be performed at random locations on the sample to obtain the mean hardness over a given specimen or microstructure feature.

Two different Vickers indenters can be used, both operating at different scales and forces. The most commonly used Vickers technique is the macro-hardness test, which indents with higher forces. This test is mostly used to determine the mean hardness of the sample as a whole. Nevertheless, when more specific features of a microstructure need to be analysed the micro-hardness test can be performed. This test applies forces magnitudes lower compared to the macro test, meaning even small precipitates can be researched [35].

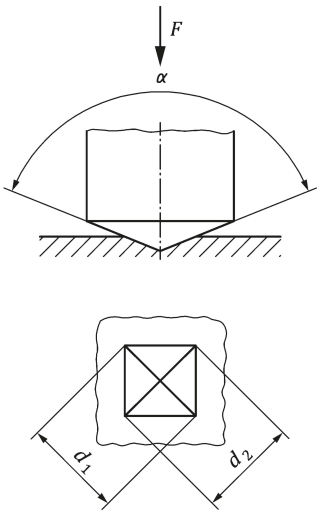

Fig. 9.7 Principle and geometry of the Vickers indentation test. Reprinted from Royal Netherlands Standardization Institute [35, p. 2].

The hardness testing equipment used for the experiments discussed in this thesis are for macro- and micro-hardness testing. A Zwick/Roell DuraScan G5 machine was used with a Vickers conform pyramid diamond indenter with an angle of 136°. The force applied on the sample is limited to HV 0.5 (micro) and measured with a 60x magnification microscope lens. To measure the micro–hardness values a series of 20 indentations per sample was made. The spacing between indentations is set at 0.25 mm.

9.2.6 Microstructural characterisation

As discussed earlier, the microstructural features of the MONICR alloy are not discussed in literature. For this reason extensive microstructural characterisation is required to analyse the microstructural evolution processes. Figure 9.8 gives an overview of the characterisation techniques, their sub-techniques, characterisation possibilities and, at last, the required information per feature.

These features are of importance to further analyse the behaviour towards heat treatment and the resulting microstructural evolution. Yet, due to time limitations this research thesis will focus on the most notable transitions happening in the microstructure after long-term heat treatment. With the use

of a selection of different microscopes and techniques, some interesting patterns can be selected for further research.

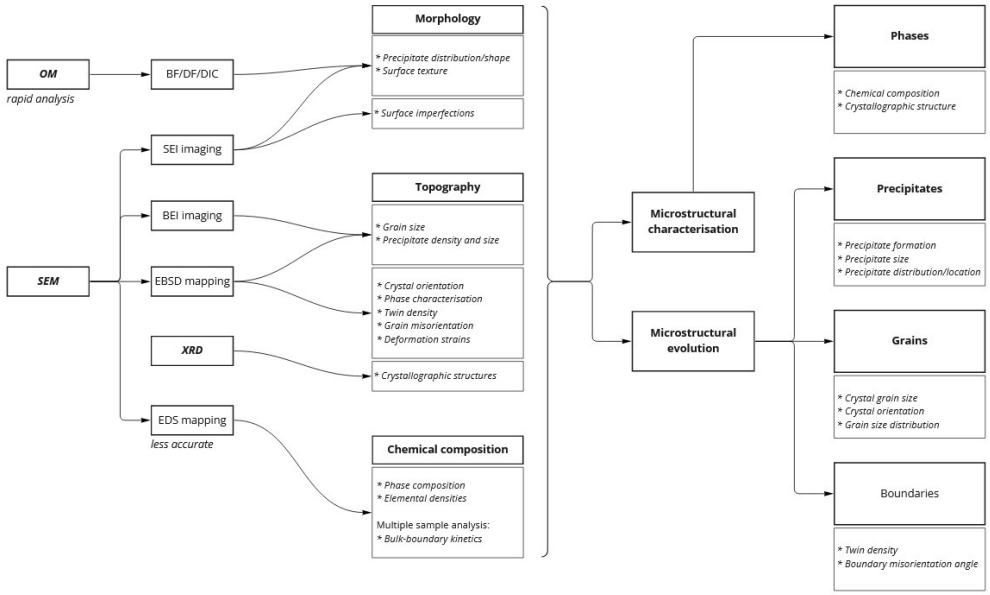

Fig. 9.8 Overview of microstructure related characterisation route and techniques. The techniques in italics and bold represent the main characterisation techniques.

Optical microscopy (OM)

After the Charpy pendulum test the sample can be prepared for further characterisation. Optical microscopy will be used for early pattern characterisation, meaning it will be used as a tool to evaluate the amount and distribution of precipitates (if visible), grain boundaries and annealing twin density for the different microstructures as a function of heat treatment time. The OM will therefore be used as the first characterisation tool.

Two optical microscopes are used for early characterisation. The most used microscope is the LEICA DMLM, used for Bright Field (BF) imaging and Differential Interference Contrast (DIC) imaging. While the Olympus BX60M Trinocular Inspection microscope with a ZEISS Axiocam 705 was used for Dark Field (DF) imaging. The latter is also able to take DF images.

In most cases BF (standard OM) imaging is enough to produce clear images, nevertheless DIC imaging can be chosen if contrast between the visible features is limited. Contrast is enhanced by polarising the light and creating two parallel rays via a prism, these rays refract differently when hitting the sample, hence after recombination of the rays enhancing contrast. In some cases DF imaging can be beneficial to enhance visibility of imperfections as only scattered light, due to a special lens, produces an image.

Scanning electron microscope (SEM)

Because not all microstructural features can be characterised by the optical microscope it is necessary to use more complex techniques to characterise the composition and structure of the present phases in the samples. The SEM, with respect to normal optical microscopy, is able to magnify the sample to a nanometer-scale due to the interaction of an electron beam with the surface atoms of the specimen at different depths, with very high accuracy. These atom-electron interactions consequently generating radiation. Several types of radiation are produced, namely Auger electrons, secondary electrons, back-scattered electrons, characteristic X-rays, continuum x-rays and fluorescent x-rays, as visualised in figure 9.9. Nevertheless, only a couple of these radiation types are primarily used for SEM characterisation, namely *secondary electrons*, *back-scattered electrons* and *characteristic x-rays*.

Secondary electrons are produced by an inelastic interaction between electrons, as a result replacing the initial electron in the atom shell by the primary electron and ejecting a secondary electron. These electrons are characterised by their low energy. Back-scattered electrons on the other hand, are electrons from the primary electron beam that are elastically deflected. A stronger electron deflection around the atom nuclei signifies a heavier atom (higher atomic number). These strong deflections formed by heavier atoms result in brighter spots on the processed image. The last type of radiation used in characterisation are the emitted characteristic X-rays. These x-rays are produced when the primary electron ejects an electron from the atoms' inner shell and a high-energy electron, from another shell, replaces the removed electron while emitting the remaining energy as x-rays. The wavelengths of these x-rays can be measured with Energy-Dispersive X-ray Spectroscopy (EDS), allowing for identification of the elements, their abundance and distribution in the analysed surface [37].

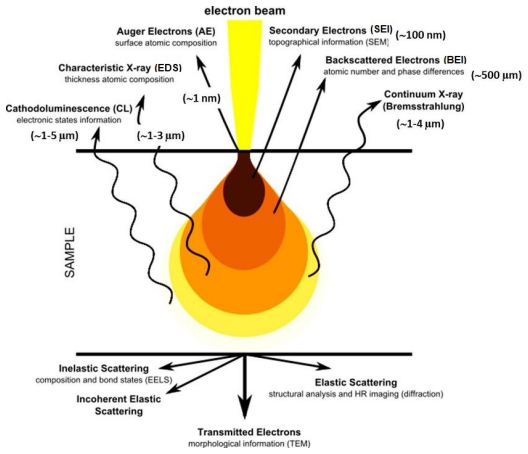

Fig. 9.9 The electron-matter interaction signals emitted in a Scanning Electron Microscope (SEM). Reprinted from [36].

For SEI, BEI, EDS and EBSD characterisation, a SEM *JEOL JSM-6500F* was used.

Secondary Electron Image (SEI) mapping SEI mapping can be a potent tool to characterise and analyse the morphology and topography of the sample its surface. As secondary electrons are generated all over the sample by the primary beam, the locations with a higher roughness emit more electrons directed towards the detector as it is easier to leave the sample, while at flat surfaces this concentration is lower as the secondary electrons are trapped within the sample. This contrast in

secondary electron count on the detector translates into a specific brightness, low count equaling darker patches and a high count bright patches.

This technique is convenient for analysing atypical structures in the microstructure, such as cavities and cracks. For this research thesis SEI will mainly be used for high magnitude imaging when interesting abnormalities are seen.

Backscatter Electron Image (BEI) mapping BEI mapping is used to characterise the different densities present in the sample surface. As this technique makes use of the backscattered electrons created by the primary beam and atom interaction the heavier atoms create more scattering. This scattering is detected and is translated into a signal mapped with a specific brightness. Heavier atoms produce brighter spots, while light atoms result in darker patches.

In the experiments conducted in this thesis the BEI images are used to analyse the surface microstructure its topography. These images can give a clear image of present precipitates, which are used for phase size, distribution and density studies.

For the measurements an electron beam of 15 kV was used, resulting in a scatter sphere diameter of approximately 0.5 μm.

Energy-Dispersive X-ray Spectroscopy (EDS) SEM characterisation methods that focus on the detection of characteristic x-rays released from the sample during electron beam interaction, make it possible to distinguish different elements in the sample. For that reason differences such as composition and concentration can be clearly mapped out. Very light elements do not have electrons in an outer shell, consequently characteristic X-rays cannot be emitted and thus are not detectable. Using the EDS technique it is possible to analyse specific features in the microstructure (area specific, such as precipitates) and obtain their chemical composition. For a more accurate result the SEM requires more operation time per analysing location. Additionally, rapid scanning is also possible with EDS, creating a spectral image of the sample its surface. Generally, EDS is used for rapid analysing, while more accurate characterisation requires the implementation of Wavelength-Dispersive Spectroscopy (WDS), a more accurate detection technique used in EPMA [38].

In this experiment EDS was used for chemical composition mapping of both the matrix and the found precipitates.

Electron Backscatter Diffraction (EBSD) Due to the metallurgical focus of this master thesis the characterisation of the crystal structure is of importance, as this allows for quantification of the microstructural features present in the microstructure. Consequently allowing for researching evolution processes with the use of quantified data.

While scanning the sample with EBSD many features can be measured such as the phase distribution, grain size, boundary characteristics (misorientation), crystal orientation, preferred texture and even strains. All of these features can be computed as backscattered electrons, generated by the electron beam, are transformed into a signal by use of a phosphor screen. The signal forms unique

patterns that are specific to a crystal structure, thus enabling for clear distinction between different phases [39].

For this thesis EBSD is used to measure grain sizes, grain boundary misorientation angles and annealing twin density. Additionally, the reference samples without heat-treatment were analysed to research the deformation texture of the as-received material. To generate these maps the *HKL Flamenco* software was used. Furthermore, the sample was placed in the SEM with a 70° tilt with the EBSD detector set at 182.0 mm and a step size of 1 μm.

X-Ray diffraction (XRD)

X-Ray Diffraction is a characterisation technique that characterises crystal structures of the microstructure by measuring the spatial arrangement of atoms. This data is obtained by measuring the diffracted X-ray beams (elastic scattering) from a X-ray source that interacted with the sample under different angles. This interaction results in a so called diffractogram that shows the constructive interference intensities per measured angle, or in other words the diffraction pattern. From this pattern, when compared to a pattern database, the composition, unit cell and its dimensions and material density can be measured. Due to background noise only phases with a fraction above 5% are observed through XRD [40]. X-ray energies used for XRD are copper K-α (1.54 Å) and cobalt K-α (1.79 Å).

For the thesis experiments XRD was used to obtain main phases present in the material as a function of thermal treatment time.

9.2.7 Sample preparation

Due to size limitations of the SEM (25x25x10mm^3 maximum), the post-Charpy specimen needs to be cut somewhat to reduce its length. The sample will be cut parallel to the fracture surface of the Charpy sample, so that the unaffected surface on the outer wings of the specimen can be analysed and the fracture surface can be preserved for further analysis. The earlier prepared hardness samples are not used as they are embedded in resin.

The cutting procedure follows the same steps as the hardness samples, but without embedding the samples. Initially, the sample follows the same path as previously described (grinding and polishing). However, the sample requires two additional polishing steps due to the reflectivity requirements for both optical and electron microscopy. First, the sample is polished with OP-Nat cloth and 0.25 μm diamond paste, following a similar procedure as the previous polishing steps. The MONICR alloy is then polished with an OP-S (oxide polishing suspension) grain size of 40 nm. The suspension is used on a MD-Chem cloth. Because the alloy is a soft material, this final polishing step is sufficient to reveal some important microstructural features such as grain boundaries and twins.

After some testing this final polishing method was seen as more beneficial for SEM characterisation than etching.

9.3 Calculations

9.3.1 Instrumented Charpy test data

Notch impact toughness

The impact toughness of the sample can be derived from the absorbed energy measured during the test. This impact toughness is nothing more that the absorbed energy divided by the impact surface. In other words, the fracture surface plane. Due to the deviating dimensions, relative to the standards, this notch impact toughness value can be calculated following relation:

$$K_{ni} = \frac{\Omega}{A_f} \tag{9.2}$$

Symbols used in the equation stand for; notch impact toughness, K_{ni} [kJ/m^2]; absorbed energy, Ω [kJ]; fracture surface plane area, A_f [m^2]. The used specimen have a fracture surface plane area of; $(8 \cdot 10^{-3}\text{m})^2 = 6.4 \cdot 10^{-5}$ m^2.

Dynamic yield- and tensile strength estimates

Because instrumented Charpy pendulum tests are performed, the load-deflection data is measured. This allows for the estimation of both the dynamic yield strength, as well as the dynamic tensile strength. The latter of which is only used for comparing tensile strength estimates from the hardness tests, because the load-deflection estimation is not proven for Hastelloy-group alloys. In general the dynamic strength is more conservative than the static strength, meaning the values are most likely below the values determined by a tensile test [41].

The dynamic yield strength can be determined by using the general yield force which is relating to the dynamic yield strength as proven by Server. This relation was translated into an equation by Server, given as:

$$\sigma_{YS,d} = \sigma_{GY} = \frac{2.793 \cdot F_{GY} \cdot W}{B(W-a)^2} \tag{9.3}$$

Note that this equation is only valid for a V-notched sample with a 8mm striking radius. The symbols in the equation symbolize; dynamic yield strength, $\sigma_{YS,d}$ [MPa]; general yield strength, σ_{GY} [MPa]; general yield force, F_{GY} [kN]; sample width (10mm), W [mm]; sample thickness (8mm), B [mm]; notch depth (2mm), a [mm]. Note that this estimate is only valid at the experienced strain rate on the pre-cracked surface during the test [42].

With the given Charpy sample dimensions this gives us the relation between general yield force and dynamic yield strength, as given in:

$$\sigma_{YS,d}\ [\text{MPa}] = 54.55 \left[\frac{\text{MPa}}{\text{kN}}\right] \cdot F_{GY}\ [\text{kN}] \tag{9.4}$$

Lucon [42] modified Server's relation to also obtain the dynamic ultimate tensile strength derived from the maximum general force, F_m [kN]. A new relation parameter was derived from experimental data on different *steels*, allowing for a conservative estimate of the dynamic tensile strength, $\sigma_{TS,d}$ [MPa], given by:

$$\sigma_{TS,d} = \frac{2.385 \cdot F_m \cdot W}{B(W-a)^2} \tag{9.5}$$

With the given Charpy sample dimensions this gives us the relation between general yield force and dynamic yield strength, as given in:

$$\sigma_{TS,d}\ [\text{MPa}] = 46.58 \left[\frac{\text{MPa}}{\text{kN}}\right] \cdot F_{GY}\ [\text{kN}] \tag{9.6}$$

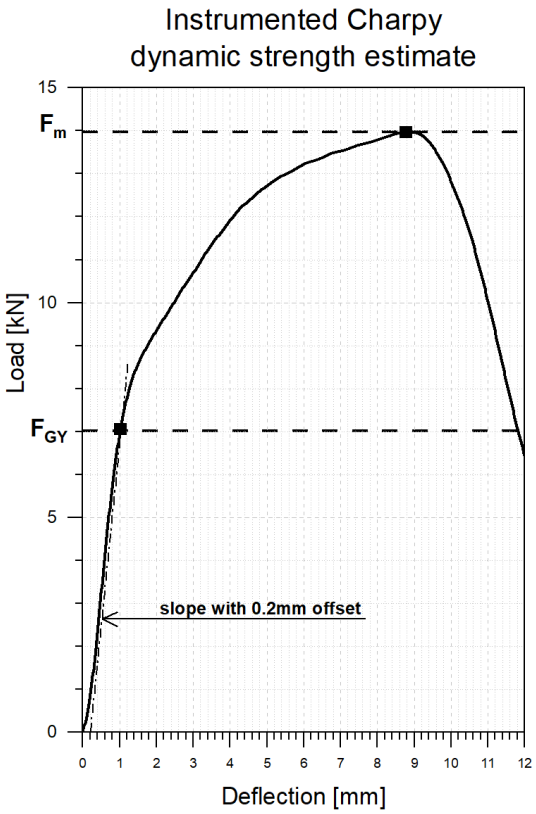

Fig. 9.10 Determination of the dynamic yield force and maximum force based on the instrumented Charpy specimen loading and deflection curve.

9.3.2 Vickers hardness data

Changes in average micro-hardness values in a heat-treated material correspond to changes in mechanical strength. Therefore, in many cases the hardness value is converted into an estimate for the yield strength [19; 21].

Yield strength estimate The relation between Vickers hardness value (H_v [kgf/mm^2] or approximately [10^1 MPa]) and the yield strength (σ_y [MPa]) found by Tabor is given as (reprinted from [19]):

$$H_v\ [\text{kgf/mm}^2] = 3.55 \cdot \sigma_y\ [\text{MPa}] \tag{9.7}$$

Because no empirical hardness-yield strength studies on Ni-Mo-Cr alloys have been conducted, the calculated yield strength is only an approximation. As a result, the hardness values will be the primary focus of the analysis.

Chapter 10

Results

10.1 Reference microstructure

A sample was analysed to characterise the texture, morphology and present phases of the as-received material, i.e., the reference microstructure. Secondary Electron Image (SEI) and Backscatter Electron Image (BEI) were used to analyse the morphology of the microstructure. Electron Backscatter Diffraction (EBSD) mapping was used to further analyse topographical features including texture, grain size and twin boundaries. Finally a combination of X-Ray Diffraction (XRD), BEI and Energy-Dispersive X-ray Spectroscopy (EDS) was used to characterise the phases and inclusions present. The present section discusses qualitative observations first, followed by a quantitative study covered in the microstructural evolution section.

10.1.1 Morphology, texture and twin boundaries

First the morphology of the microstructure was analysed. Figure 10.1 illustrates how the sample's microstructure could be readily seen with Backscatter Electron Image (BEI) imaging[1]. A variety of grain sizes are observed, ranging from approximately 5 µm to 30 µm in diameter, with many of them including twin boundaries. The presence of dark patches is also visible in the BEI image, indicating the presence of lighter atom clusters relative to the matrix. These volumes within the matrix can be identified as precipitates (alloy-based) or inclusions (processing-based). To further investigate these irregularities characterisation with EDS is required.

Topographical characterisation

To analyse the twin boundaries and texture of the microstructure further characterisation with EBSD was performed. Figure 10.2 shows the result of this analysis.

[1] SEI images at a magnification of 50 are less detailed due to the high number of OP-S particles that reduce image quality at this magnification.

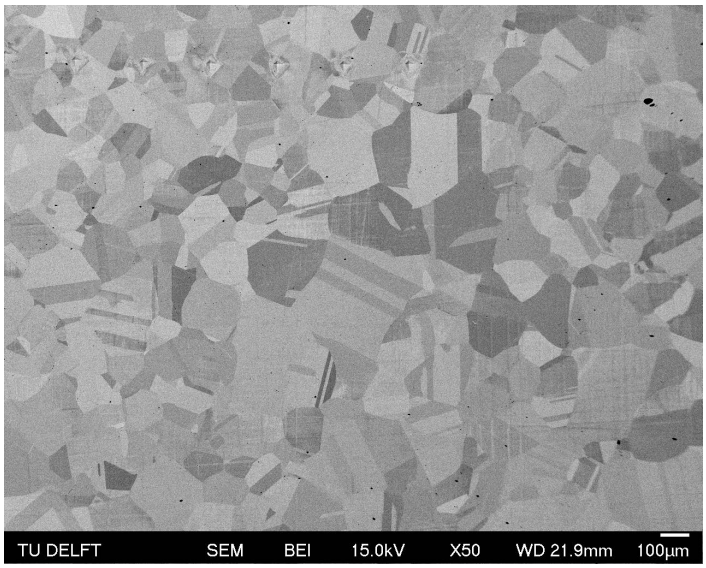

Fig. 10.1 BEI image of reference sample at 50x magnification. The Vickers hardness indentations are visible as a series of pyramid-shaped geometries on the top left of the image. Black pixel clusters indicate the presence of inclusions.

The high twin boundary prevalence in both smaller and larger grains is noteworthy as most of the grains house at least one twin, as shown in figure 10.2-A. The image indicates a homogeneous distribution of these twin boundaries. To analyse the type of twin boundaries present, their morphology was compared to the general twin types given in figure 10.3. Most of the twin boundaries appear as straight lines (type I and II), indicating the presence of annealing twins. Although some deformation twins were discovered in the studied microstructure, their density was relatively low.

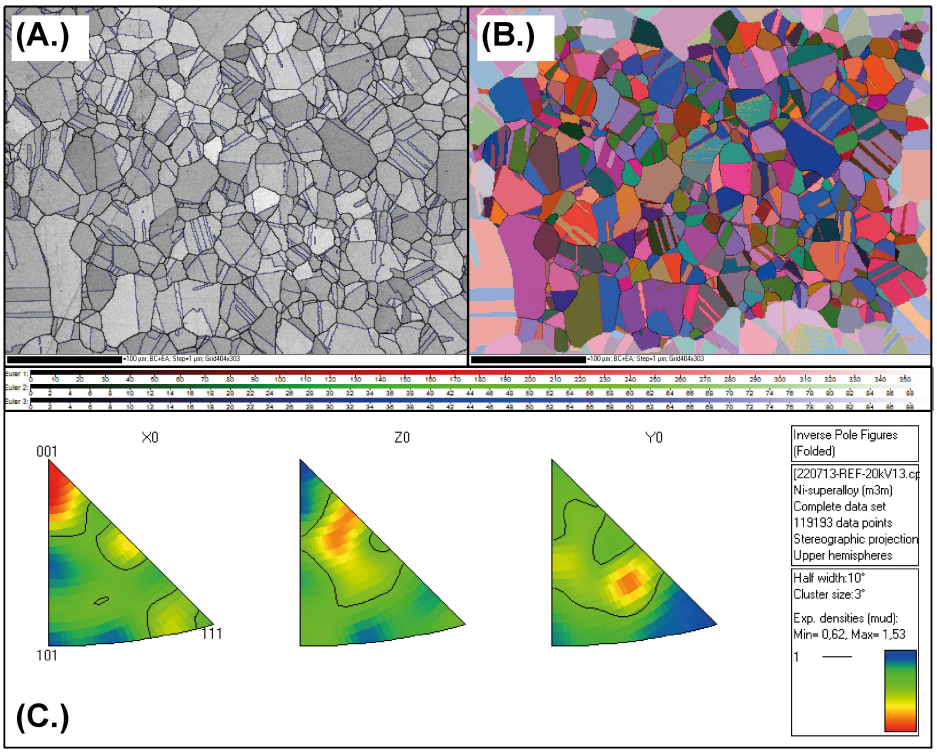

Fig. 10.2 EBSD images of reference sample. The scale bar of image (A.) and (B.) equals 100 µm (Not visible due to resolution limitations).(A.) Band contrast image with grain boundaries and twins processed from EBSD data. Grain boundaries are represented by black lines, and the twins are represented by blue lines. (B.) Euler angle contrast map. (C.) Inverse Pole Figure (IPF) multiple of uniform density (MUD) maps with blue representing the lower limit of 0.62 MUD and red the upper limit of 1.53 MUD.

The EBSD map was analysed to reveal the crystal orientation of the grains. Using Euler angle contrast and Inverse Pole Figure (IPF), it was discovered that the crystallographic texture of the investigated plane was oriented randomly, with no preferred direction as seen in figure 10.2-B/C. Figure C summarises the statistical texture intensities in the pole figures by Multiple of Uniform Density (MUD) value maps. Note, blue represents the lower measured limit of 0.62 MUD, and red the upper limit of 1.53 MUD. A MUD-value of 1 indicates random oriented grains while values significantly larger represent a preferred orientation. The MUD values found in the reference sample are below 2 MUD and therefore substantiate the indifference to preferred orientations.

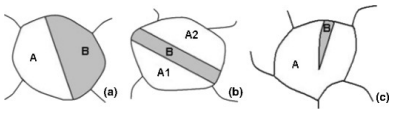

Fig. 10.3 Twin boundary morphology of annealing and deformation twins. (a) Type I annealing twin, (b) Type II annealing twin, (c) deformation twin. Reprinted from Cronjé *et al.* [43].

This uniform crystallographic texture implies that the as-received MONICR plate was indeed thermally treated following the hot rolling process as no preferred crystal orientations were found. This arbitrary orientation indicates a non-deformed crystallographic state, suggesting that recrystallisation occurred earlier than the thermal treatment used in this study. Following this discovery, all samples'

analysed planes are suitable for appropriate microstructural characterisation and analysis.

Next, the samples were carefully examined for signs of deformation associated with sample preparation in order to confirm the validity of the microscopy data. The material was soft, which made the preparing procedure efficient. Nevertheless, as is seen in figure 10.2-A certain scratches were present on the various specimens. These scuffs are the result of earlier grinding steps, or even from surface-embedded inclusions being detached from the surface. Abnormalities arising from these scratches are taken into account, these scratches typically do not cause a reduction in data quality. For EBSD data analysis the scratches would result in incorrect measurements, therefore the faulty data points around scratches are excluded from the analysis. In general these erroneous data points present themselves as short Low-Angle Grain Boundaries (LAGBs). This exclusion is done manually with the image processing tool *ImageJ*.

10.1.2 Phases present

Table 10.1 Average composition of matrix γ-phase and oxide inclusions in the analysed reference sample. Data obtained from multiple EDS measurements, see appendix figure B.3.

Phase	**O**	**Al**	**Cr**	**Fe**	**Ni**	**Mo**
			[wt%]			
Matrix	-	-	7.0 $\pm$0.2	1.22 $\pm$0.16	76.9 $\pm$0.7	14.9 $\pm$0.2
Oxide inclusion	35.1 $\pm$0.5	22.15 $\pm$0.12	38.0 $\pm$0.3	-	4.4 $\pm$0.3	0.42 $\pm$0.07

The composition of the matrix and possible phases were analysed using EDS. 16 points within the matrix were characterised, with an additional 20 measurements for the observed dark clusters. The measurements revealed the expected Ni matrix and the presence of oxide particles. Table 10.1 displays the average composition of the two phases. The matrix phase is found to be very similar to the theoretical MONICR composition given in table 8.1. The various types of dark volumes identified with BEI were all measured to be of similar chemical composition.

X-Ray Diffraction measurements were conducted on the sample to reveal potential phases. Diffraction did not reveal any impurities; only the cubic FCC Ni-matrix phase was visible, as seen in the diffraction pattern (figure 10.4). Due to the low detection limit of XRD phases with a volume fraction of less than 5% are not observed. The scale of the intensity values of the resulting diffraction pattern in figure 10.4 is presented with a square-root scale to reveal smaller peaks. The peaks were compared to the ICDD pdf4 database to find known phases with similar chemical composition. Note, smaller peaks visible in the diffraction pattern correspond to K-β X-rays.

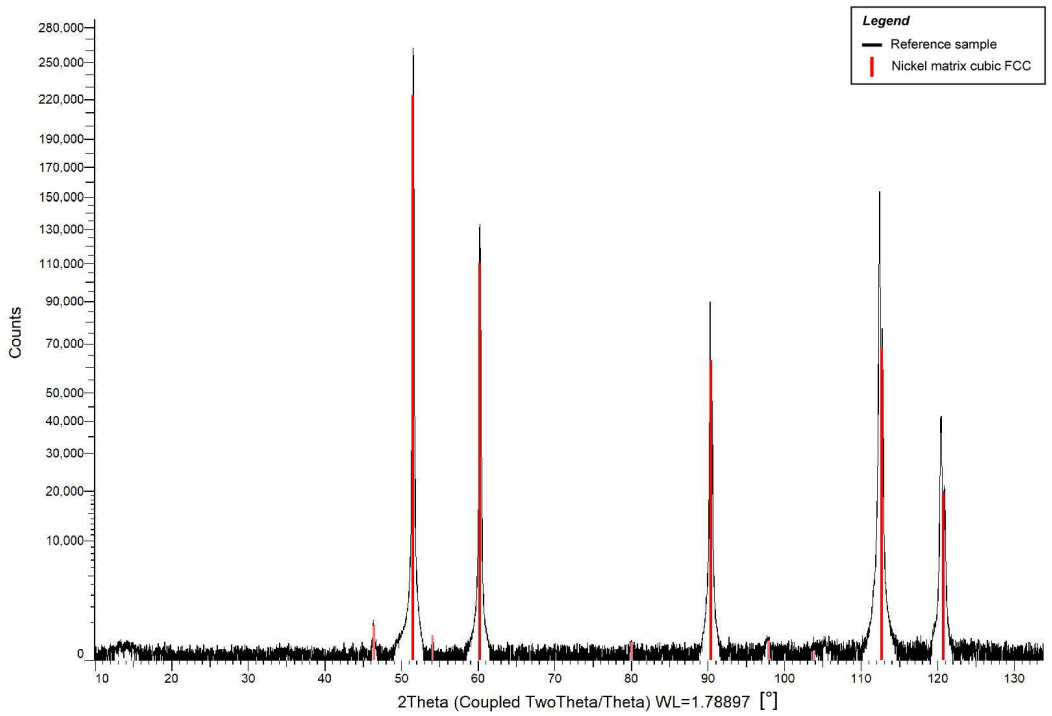

Fig. 10.4 X-ray diffraction patterns of the reference sample. A Bruker D8 Advance diffractometer Bragg-Brentano geometry and Lynxeye position sensitive detector with Co Kα was used. For visibility reasons the intensity scale is square rooted and the background subtracted. The diffraction pattern was compared with the ICDD pdf4 database.

Oxide inclusions

The diameters of the inclusions present in the material range between 0.1 µm and 30 µm and are observed in the grain interior and grain boundaries. As seen in figure 10.5 the smaller inclusions tend to cluster around the grain boundaries, while the larger particles are found in the interior. This inclusion configuration is observed on the entire analysed surface.

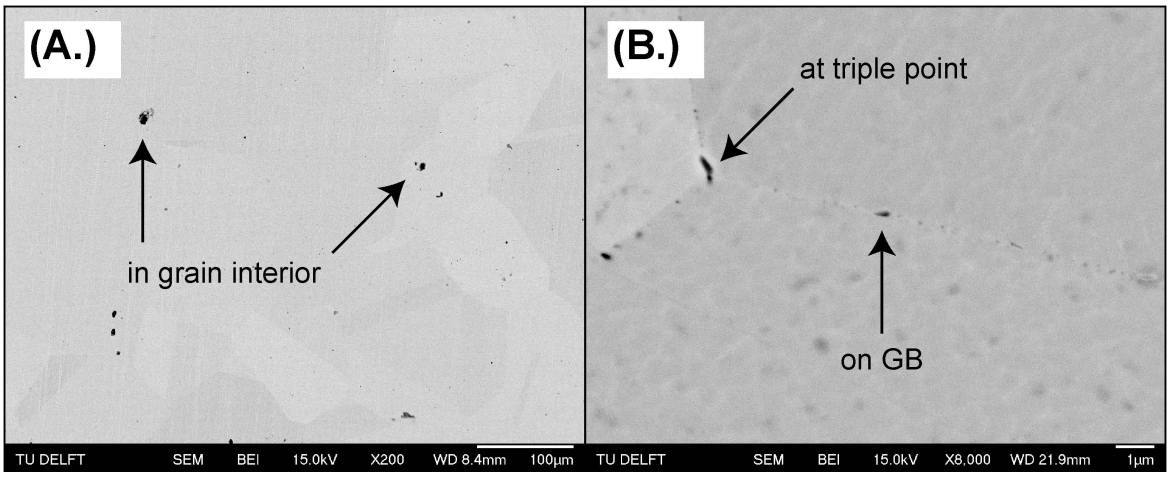

Fig. 10.5 Small oxide inclusions (0.1-5 µm) as observed in BEI images. (A.) inclusions in grain interior, (B.) inclusions in grain boundary and triple points. The grey spots are the leftovers from the OP-S polishing, and the black patches are inclusions.

The as-received alloy contains a variety of inclusion configurations, including: (1) sole inclusions, (2) series of fragmented inclusion particles, and (3) clustered inclusions. The different configurations in the analysed microstructure are presented in figure 10.6. Larger solitary inclusions are mostly found in the grain interior, whereas clustered inclusions are mostly found along grain boundaries (see figure 10.5-B), although clusters of larger inclusions are sometimes observed in the grain interior. Series of fragmented inclusions, like sole inclusions, are located inside the material rather than along the grain boundaries. The existence of these fragmented inclusions points to a manufacturing deformation procedure like hot rolling. This finding shows that the oxide inclusions are most likely a by-product of the production process.

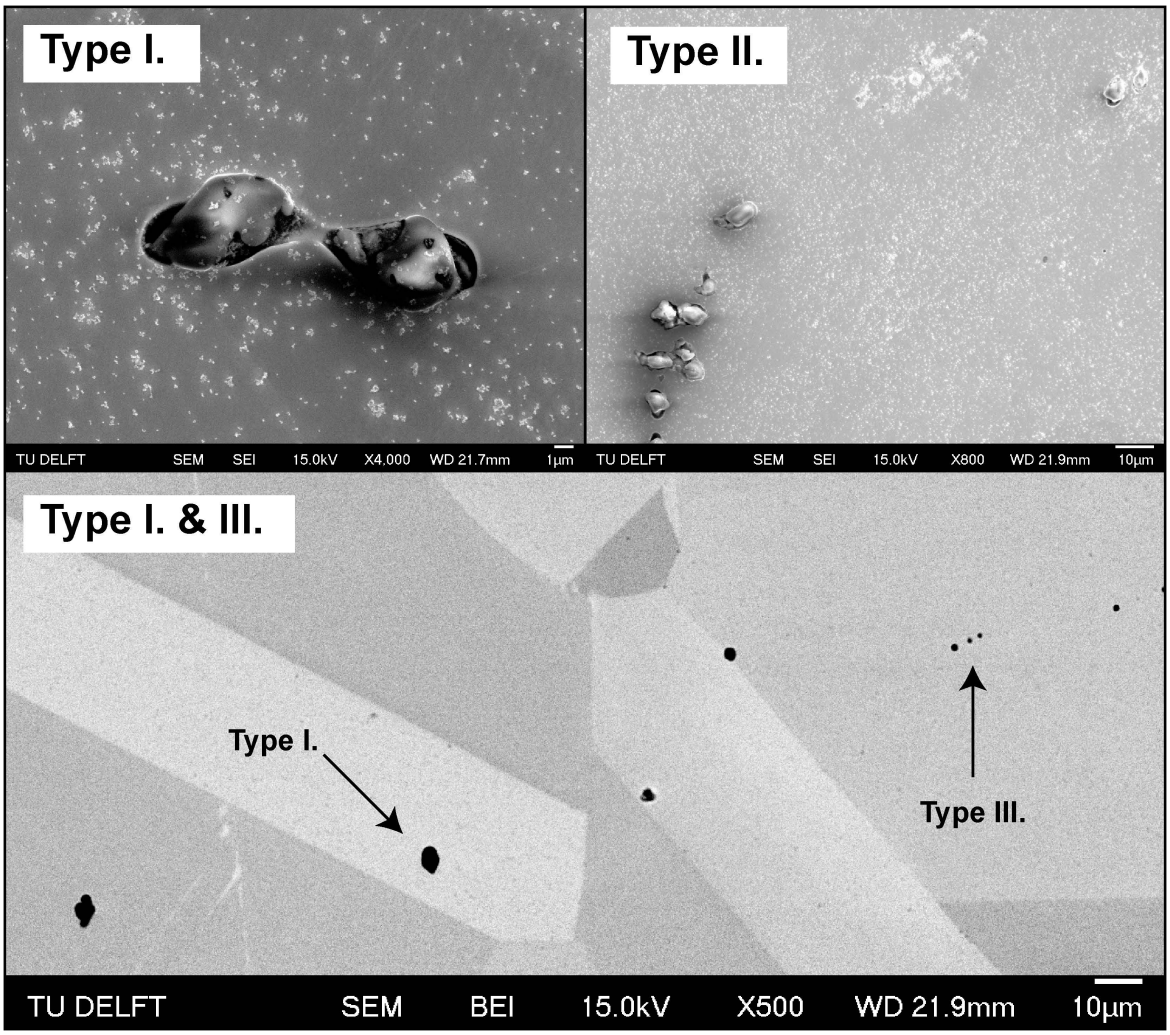

Fig. 10.6 Oxide inclusions as observed in the reference's microstructure. The top two images are detailed SEI images of type I and II inclusions. The bright spots in those images are OP-S particles. The bottom BEI image shows inclusion type I and III.

The ratio of metal to oxide atoms is approximately 2:3, as evidenced by the measured composition of the oxide inclusions (matrix subtracted): 60.3±0.8 O, 24.42±0.12 Al and 15.24±0.13 Cr at% (calculated from average wt% presented in table 10.1). This ratio is consistent with the formation of both common oxide components of Al and Cr: *alumina* (Al_2O_3) and *chromia* (Cr_2O_3). It is estimated that the inclusions are approximately 60% alumina and 40% chromia. All inclusion configurations are producing similar results.

Oxide inclusion evolution The evolution of inclusions during thermal processing is analysed to learn more about the origin of these inclusions. The average inclusion fraction on the examined specimen is shown in figure 10.7 . Both optical and scanning electron microscopy can identify the inclusions and are therefore both used to estimate the volume fraction of inclusions. The graph

displays data that was obtained using an optical microscope. The results are validated using samples that underwent SEM (BEI) analysis. There were no significant differences between BEI and optical microscopy results. Using a brightness threshold, the inclusions were extracted from the microscopy images using the image processing software *ImageJ*. The inclusions in Optical Microscopy (OM) and BEI can be distinguished by their distinctive dark colour.

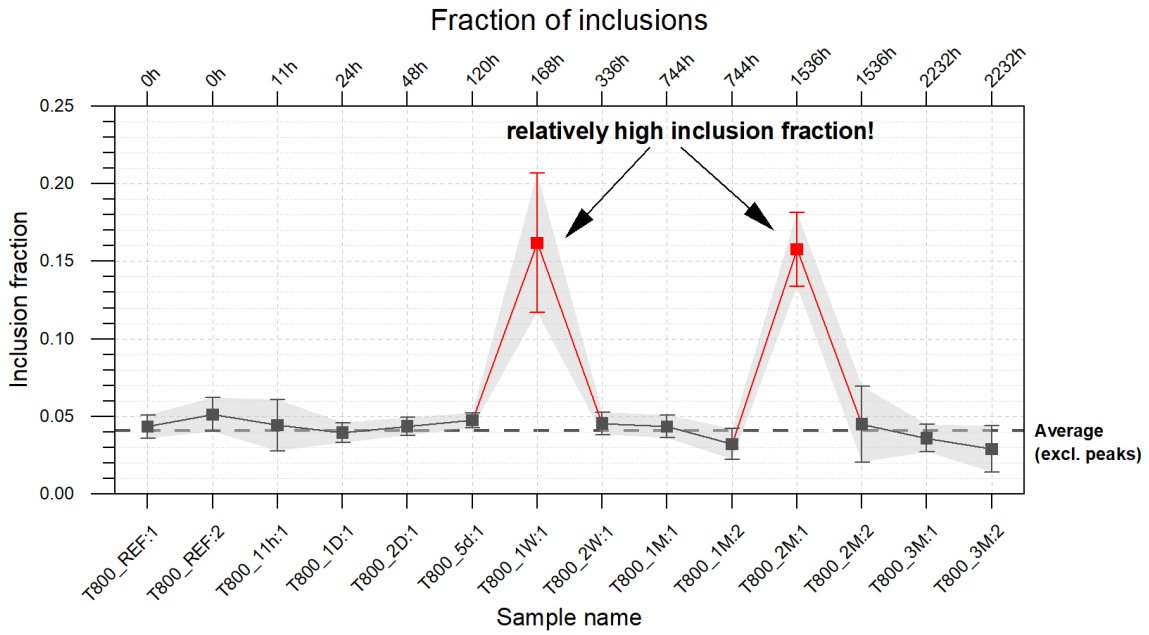

Fig. 10.7 Fraction of inclusions present in the specimen as a function of thermal treatment time.

The inclusion fraction in the T800-1W:1 (168h) and T800-2M:1 (1,536h) samples is roughly three times higher than the average of all specimens. The fraction of inclusions in the other samples is roughly the same and is unaffected by the thermal treatment time of the specimen. As a result, thermal treatment at 800°C is thought to have no effect on the inclusions. Therefore, it is assumed that the inclusions in the deviating specimens are a result of unevenly distributed inclusions throughout the as-received plate, leading to their arbitrary results.

A significant cut (30 mm by 30 mm) of the plate was examined in order to look into the potentially uneven distribution of inclusions in the as-received material. To examine the distribution of inclusions, a stitched optical microscopy image of the polished plate was created. The density of inclusions found over the plate is presented in figure 10.8. Note, the diagram next to the fraction distribution shows the analysed surface relative to the Charpy sample extraction pattern. This image clearly shows that the inclusions on the plate are distributed unevenly, with a very high inclusion proportion on the plate's left side. This unequal distribution is likely a by-product of the manufacturing techniques.

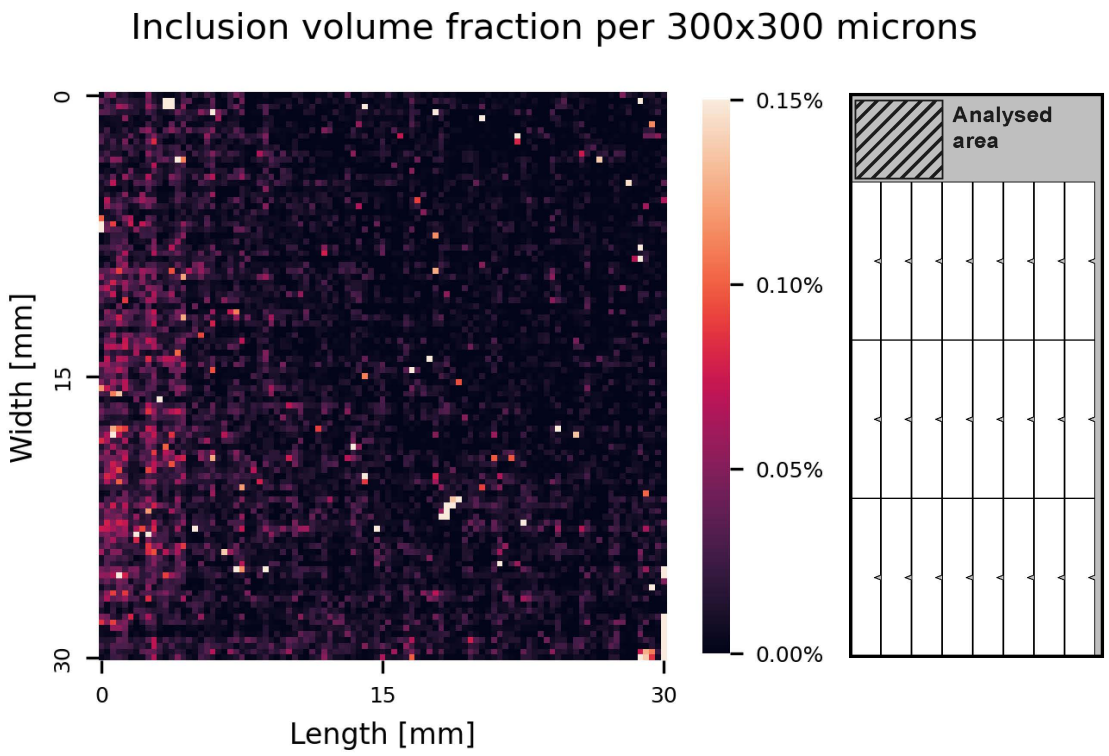

Fig. 10.8 Analysed inclusion distribution of as-received plate with dimensions 30 mm by 30 mm. Inclusions are extruded from microscopy image with ImageJ and processed per 300 µm by 300 µm raster. Lighter pixels describe raster tiles with inclusion fractions above 0.10%. The diagram illustrates the analysed surface in reference with the Charpy sample cutting pattern discussed in chapter 9.

Inclusion related uncertainty Following the relatively large deviation of inclusion fraction per specimen an additional uncertainty margin is added to the mechanical testing results. As seen in figure 10.9 the samples with a high inclusion fraction of over 0.15% exhibit, relative to the other samples, poor mechanical performance. No significant trend is observed for the specimens with an inclusion around 0.04%.

To calculate the added uncertainty range first the normalised mechanical property (Q_{nom}) value needs to be calculated with the measured mechanical property value (q), the given average inclusion fraction per specimen (φ_i [%]) as presented in figure 10.7 and the average inclusion fraction of the plate ($\bar{\varphi}$ [%]). Normalisation is calculated as follows:

$$Q_{nom} = q \cdot \left(\frac{\varphi_i}{\bar{\varphi}} \right) \tag{10.1}$$

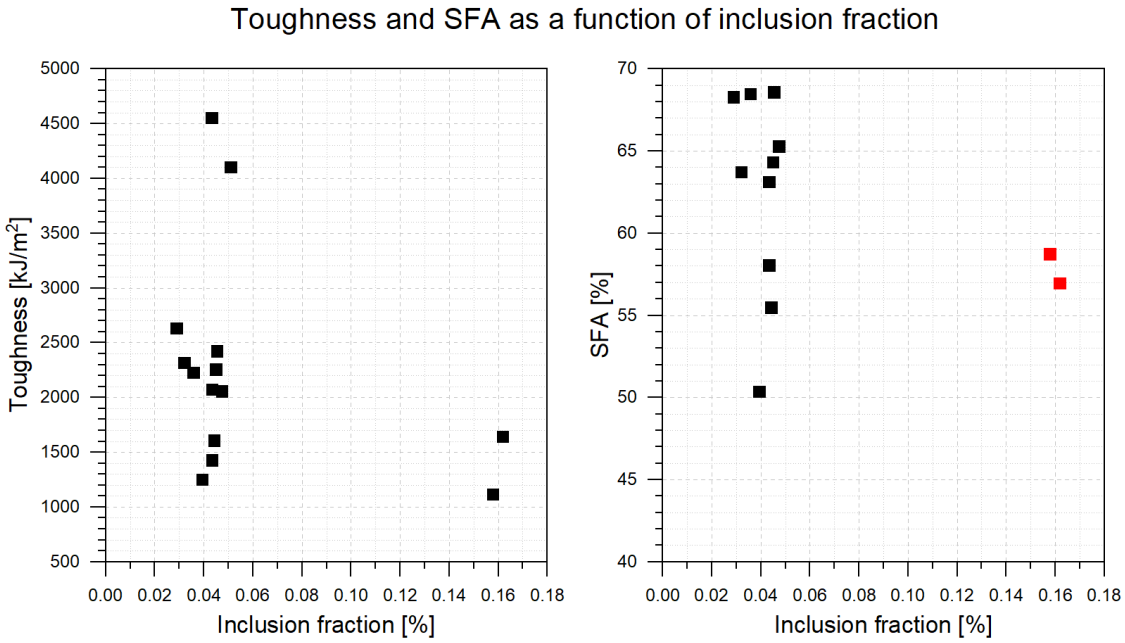

Fig. 10.9 Notch impact toughness and SFA as a function of inclusion fraction.

To find the inclusion fraction related uncertainty range the sample standard deviation (s_x) between the measured and normalised values (x_i) is computed following normal procedure:

$$s_x = \sqrt{\frac{\Sigma(x_i - \bar{x})^2}{n-1}} \tag{10.2}$$

Note, $\bar{x}$ describes the average of the measured and normalised value. n describes the number of measurements, in this case $n = 2$.

The resulting uncertainty range is added to the other uncertainty factors that are taken into account, namely (if applicable); measurement error and standard deviation of tests ($\pm 1\sigma$). The sum of these uncertainties is presented in the mechanical testing results as an error bar and error area.

10.2 Microstructural evolution

10.2.1 Computational results: Thermo-Calc

With the use of *Thermo-Calc* a list of thermodynamically stable phases at 800°C was calculated. Chemical composition estimates for all potential phases were also calculated. For these calculations the chemical composition of MONICR (table 9.2) was used. Additional, calculations were made with MONICR excluding alloying elements with chemical fractions of less than 0.01wt%. The second major-constituent simulation is referred to as major-MONICR. These additional calculations can be

useful because of the limiting size of the used TTNI6 thermodynamic database, which sometimes results in the simulated stability of unlikely phases.

Ternary phase diagram Ni-Mo-Cr

Figure 10.10 gives the quasi-ternary phase diagrams of Ni-Mo-Cr at 800°C simulated for MONICR (A.) and major-MONICR (B.). Compared to the ternary phase diagrams (Ni-Cr-Mo) given in figure 8.1 it is clear that the literature on Ni-Mo-Cr thermodynamic equilibria does not correspond to the presented Thermo-Calc results. This difference is likely a result of the included databases for the thermodynamic simulations and the difference between a ternary and quasi-ternary diagram. The given diagrams make use of the TTNI6 nickel database, while the study by Turchi *et al.* [5] uses a modified version of the thermo-chemical database SSOL. The most significant difference is absence of the P-phase in the present results, and the presence of the M6C carbide and delta-, mu- and NiMo-phase.

As seen in the quasi-ternary diagrams only the FCC matrix, with potentially the M6C carbide, is stable at the given thermal treatment temperature and chemical composition (see cross in diagrams). With the phases σ $[(Cr,Mo,Ni)_1(Cr,Mo,Ni)_2]$ (Topologically Close-Packed (TCP)), δ $[(Cr,Ni)_3(Mo,Ni)_1]$ (Geometrically Close-Packed (GCP)), NiMo $[(Ni)_1(Mo)_1]$ (TCP) and μ $[(Ni,Cr)_7(Ni,Mo)_6]$ (TCP) being stable at a chemical composition relatively close to MONICR.

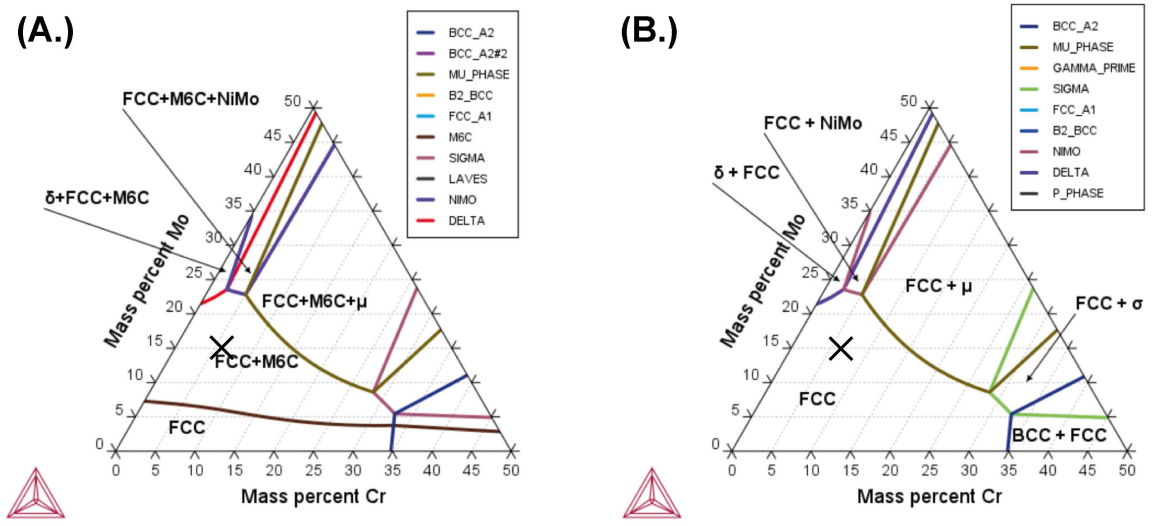

Fig. 10.10 Quasi-ternary phase diagram of Ni-Mo-Cr at 800°C. The cross represents the chemical composition of MONICR. Diagram (A.) presents the quasi-ternary thermodynamic equilibrium with all alloying elements, while diagram (B.) excludes elements with fractions below 0.01wt%. Calculated with Thermo-Calc.

According to the quasi-binary phase diagrams of major-MONICR, see figure 10.11, the alloy should continue to exist in a stable single FCC γ-phase at 800°C. For both Ni-Mo (A.) and Ni-Cr (B.) diagrams second phases are predicted to form at temperatures below 600°C. The addition of minor alloying elements Si, B and C only results in the addition of stable M_6C carbides.

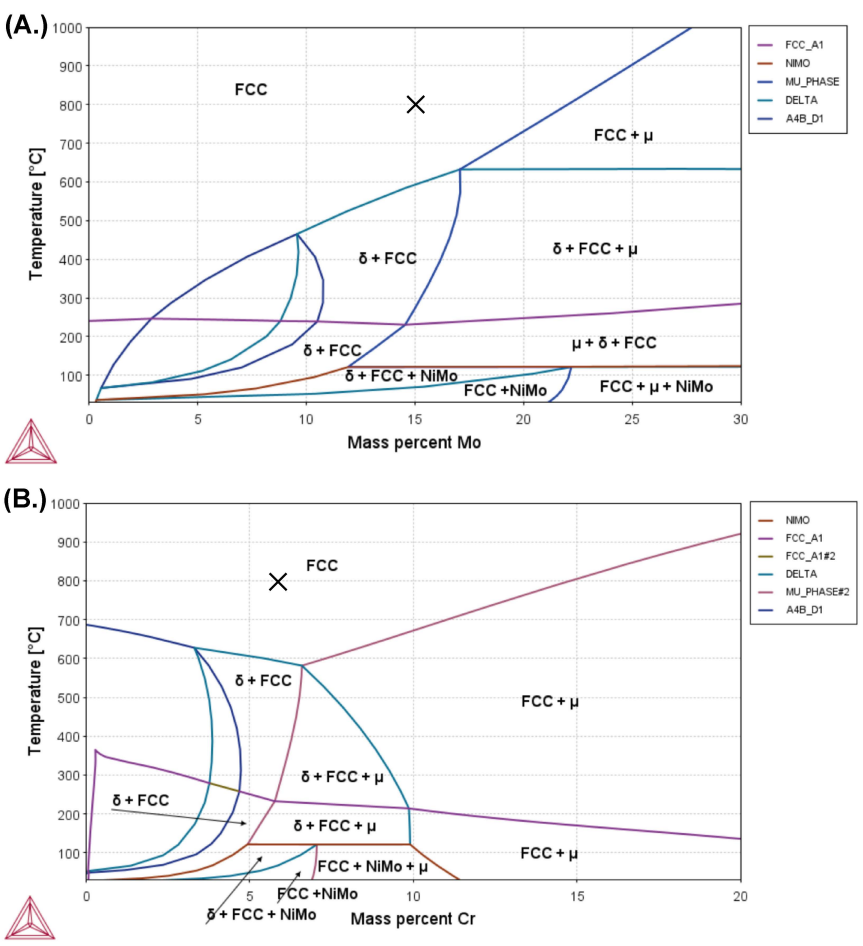

Fig. 10.11 Quasi-phase diagrams of Ni-Mo (A.) and Ni-Cr (B.) including all alloying elements at 800°C. The cross represents the chemical composition of MONICR. Calculated with Thermo-Calc, alloying elements with a fraction below 0.01wt% are excluded from the simulation.

Various chemical composition equilibria of potential phases are calculated to investigate the concentration of elements in the phase as a function of temperature. The composition diagrams are calculated with the chemical composition of MONICR. A number of phases were chosen based on typical precipitates present in related alloys (section 8.2) and the calculated ternary phase diagram. The resulting chemical composition of the second phases, as given in appendix figure B.12, are estimated to be rich in molybdenum with fractions ranging from 35 wt% to 70 wt% at 800°C, which is at least more than twice the matrix concentration of 15.0 wt%. Contrasted to the matrix concentration of 5.9 wt% Cr, chromium variation is projected to be minimal. The concentration is essentially the same in matrix and second phases for the other alloying components.

Diffusion of molybdenum

In comparison to the matrix phase, the precipitates mentioned above have a relatively high Mo concentration. Therefore, it is crucial to study molybdenum's diffusion through the γ-phase as this process dominates the formation of these Mo-rich precipitates. The expected precipitate diameter size can be estimated by calculating the growth of a volume with a specific elevated molybdenum

concentration as a function of thermal treatment time. This calculation is made for diffusion through the grain interior and along grain boundaries.

To calculate the diffusional movement in the alloy the diffusion coefficient of Mo in the Ni FCC matrix at 800°C is required. To calculate the interdiffusion coefficient ($\tilde{D}_{Mo}$) at a given temperature the equation by Divya *et al.* [44] was used:

$$\tilde{D}_{Mo} = 1.15 \cdot 10^{-4} \left[\frac{\mathrm{m}^2}{\mathrm{s}}\right] \cdot \exp\left[-281.3 \cdot 10^3 [\mathrm{J/mol}]/RT\right] \tag{10.3}$$

R represents the gas constant [J/mol·K] and T the thermal treatment temperature [K].

Next, the diffusion depletion zone was calculated with the use of a double sphere model, with the inner sphere representing the precipitate and the outer sphere the depletion zone. The mean-square displacement ($\bar{x}$) of the diffusional element as a function of time (t [s]) was calculated following equation: $\bar{x} = \sqrt{6 \cdot \tilde{D}_{Mo} \cdot t}$. Finally, the required Mo depletion volume was calculated relative to volume of the precipitate. Combining these values results in the approximation of the Mo-rich precipitates size (diameter) as a function of time. Second the diffusion rate of molybdenum along grain boundaries was calculated. This value was used to estimate the accelerated rate of precipitate growth when diffusion over grain boundaries is preferred. The growth rate is estimated by calculating the depletion zone and Mo diffusion rate around grain boundaries (sphere in tube model) combined with the Mo migration rate to the precipitate along GBs. The activation energy for diffusion through the grain boundaries is assumed to be half of that through the Ni lattice. This assumption is based on the higher atomic jump frequency at these boundaries as migration of vacancies within the GB requires less energy. The growth curves per molybdenum concentration for interior diffusion ($\mathrm{D_{interior}}$) and through grain boundaries ($\mathrm{D_{GB}}$) are given in figure 10.12.

The calculated trends indicate the possibility of Mo-rich precipitate formation at 800°C with small precipitates already reaching a potential diameter of 1 μm after 10 hours. Following thermal treatment time a steady decrease in precipitate growth rate is expected for long-term thermal treatments. Precipitate growth by grain boundary diffusion is estimated to be significantly faster compared to interdiffusion through the nickel lattice, consequently increasing the expected precipitate size. Note, the experimental growth rate of Mo-rich precipitates through grain boundary diffusion is expected to be significantly lower due to the formation of multiple precipitates along the GB.

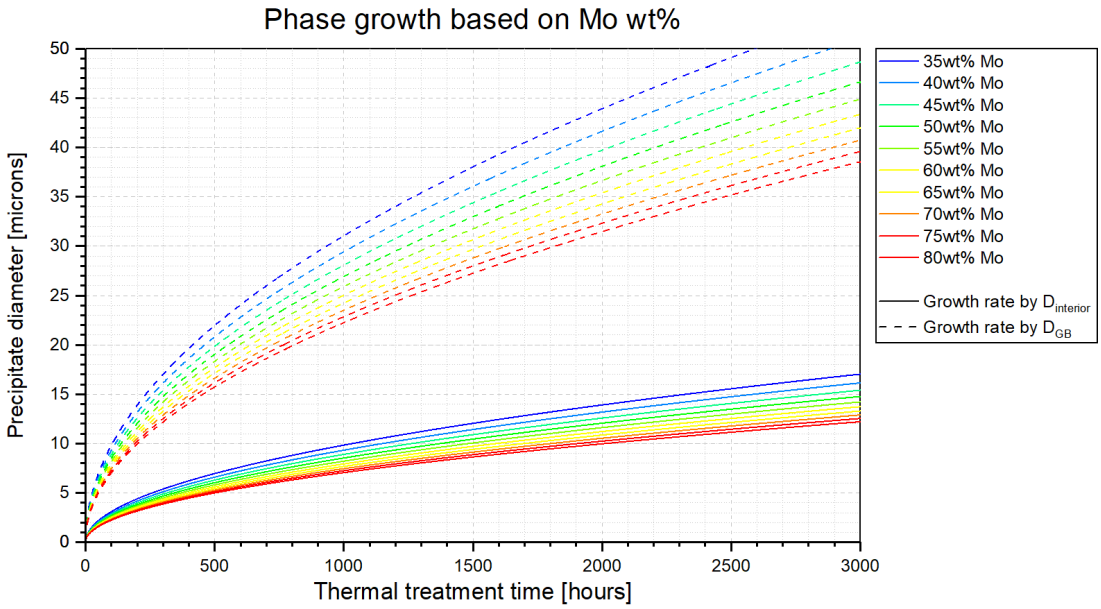

Fig. 10.12 Estimated Mo-rich volume growth as a function of thermal treatment time and the molybdenum concentration of the precipitates.

10.2.2 Precipitation

XRD identification

To investigate any potential new phases in the microstructure of the long-term heat-treated sample (1,536 hours or 2 months), XRD was performed. No new phases were visible in the diffraction pattern, meaning no second-phases with a volume fraction of more than 5% were found. Similar to the reference sample only the cubic FCC matrix phase was visible. The XRD diffraction patterns are shown in figure 10.13. Due to the use of X-ray energy Cu Kα rather than Co Kα, the diffraction pattern differs from the reference sample diffraction pattern that was previously described. For that reason the 2θ-scale of the different X-ray energies were converted to follow copper energy values with the use of the Bragg law:

$$\lambda = 2d \cdot \sin\theta \tag{10.4}$$

Variables in the equation represent the wavelength, λ [m]; spacing of diffracting planes, d [m]; and the reflection angle, θ [°].

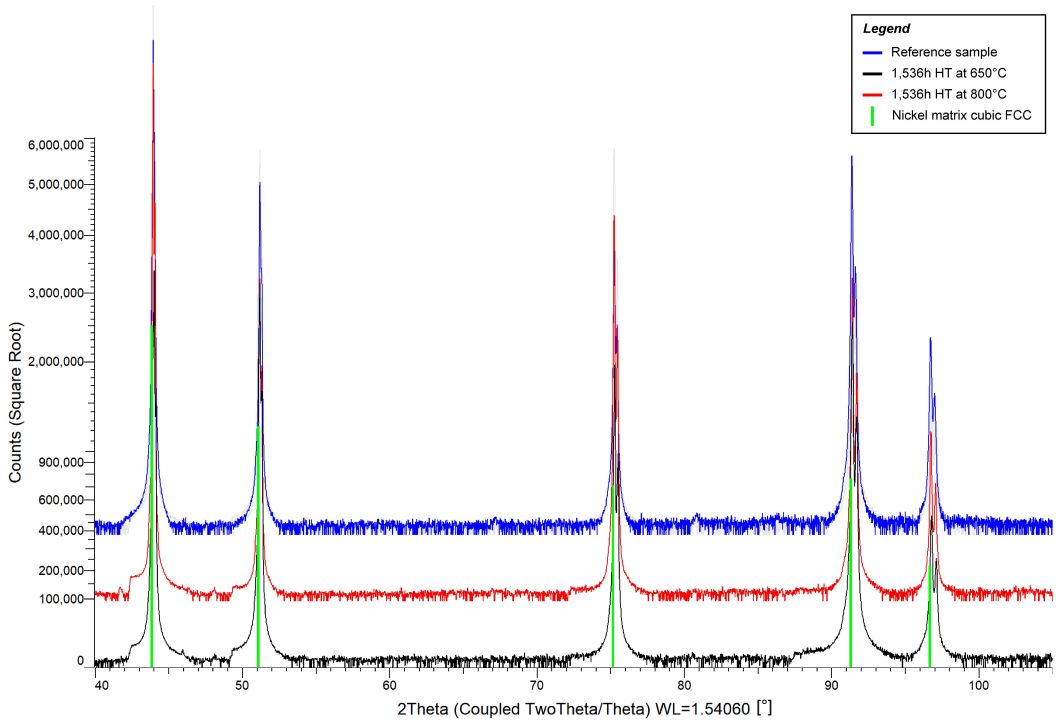

Fig. 10.13 X-ray diffraction patterns of the reference sample and 2 month HT samples (at 650°C and 800°C). A Bruker D8 Advance diffractometer Bragg-Brentano geometry and Lynxeye position sensitive detector with Co Kα and Cu Kα were used and results were corrected. For visibility reasons the intensity scale is square rooted and the background subtracted. The diffraction pattern was compared with the ICDD pdf4 database.

SEM identification

Figure 10.14 shows that tiny precipitates are observed along the grain boundaries and triple points after thermal treatment for several hours (11 hours at 800°C). Following additional heat treatment, these precipitates grow in size and their planar density increases. Figure 10.15 illustrates the presence of a considerable density of precipitates in samples that have been heat treated for longer than a month. The several BEI images under analysis, see figure 10.14 and 10.15, suggest that precipitates only develop along grain borders and never inside the grain. The formation of these precipitates is accompanied with depletion of alloying elements (primarily Mo and Cr), consequently reducing the solid solution strengtheners in the matrix.

Following its distinct elongated shape, which is present in most of the precipitates located along grain boundaries(GBs), the precipitates' geometry is assumed to be plate-like. The star-shaped precipitates found at triple points are presumed to have formed as a result of the coalescence of several plate-shaped precipitates or from growth along three grain boundaries after nucleation at the triple edge.

The images further suggest that certain grain boundaries are preferred by the precipitates over others. Figure 10.15's bottom right image makes this very evident. Such behaviour would suggest that second-phase nucleation occurs most frequently at high-energy grain boundaries where defect energy

is greatest. Furthermore, precipitation coarsening may be facilitated by higher diffusion rates along these GBs. Further characterisation of the observed precipitates with EBSD identified the precipitates as NiMo (oP56, TCP) resulting from its crystallographic structure. The other potential phases, σ, δ, μ and M_6C, were not identified, while the P-phase was not present in the EBSD diffraction pattern database.

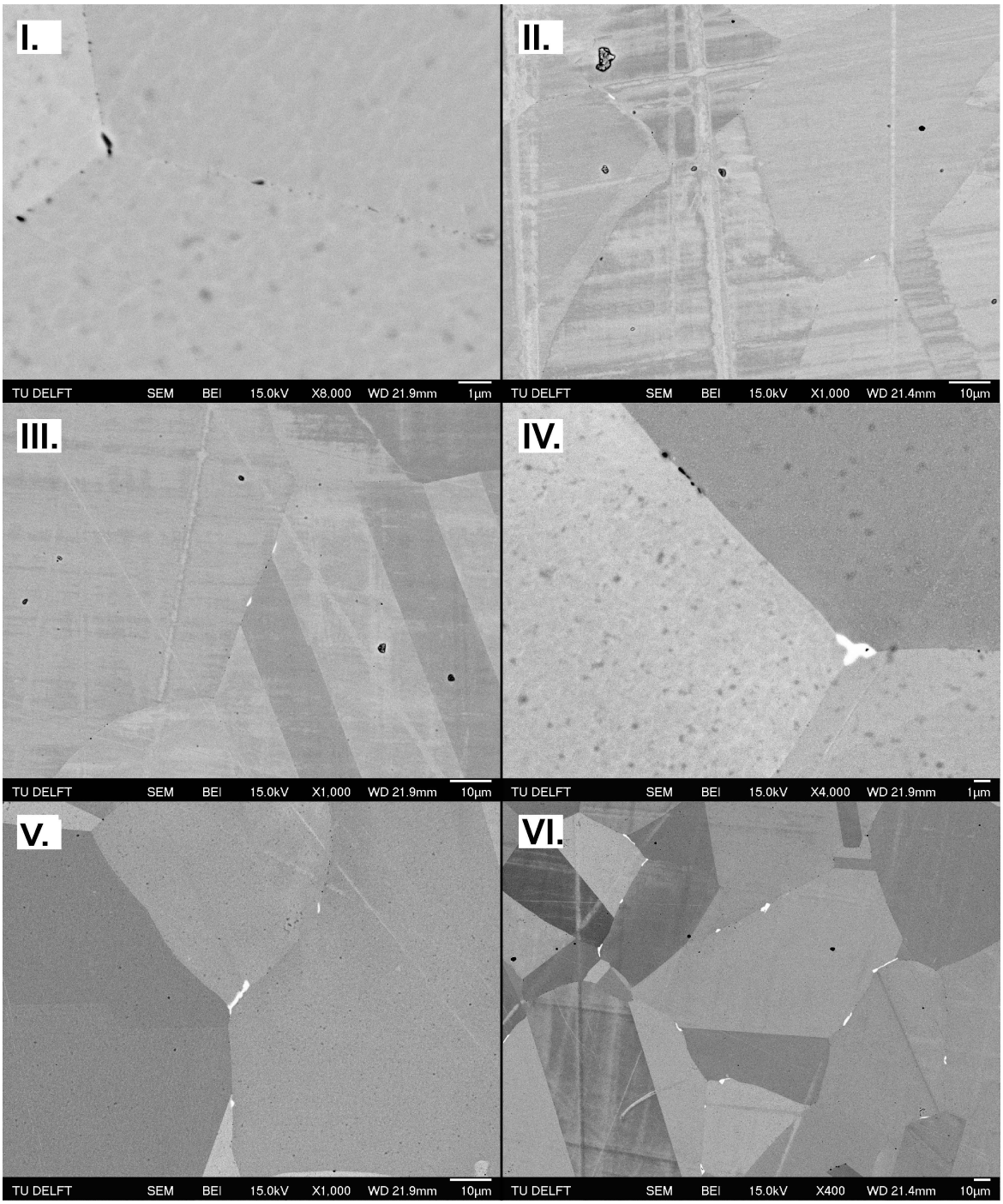

Fig. 10.14 Precipitates in the short-term HT samples as shown in a BEI picture. The oxide inclusions are black, the matrix is grey, and the TCP-phase is observable as bright white patches. The photos depict samples thermally treated for: (I), as-received, (II), 11 hours, (III), 17 hours, (IV) 24 hours, (V.) 48 hours, and (VI.) 120 hours.

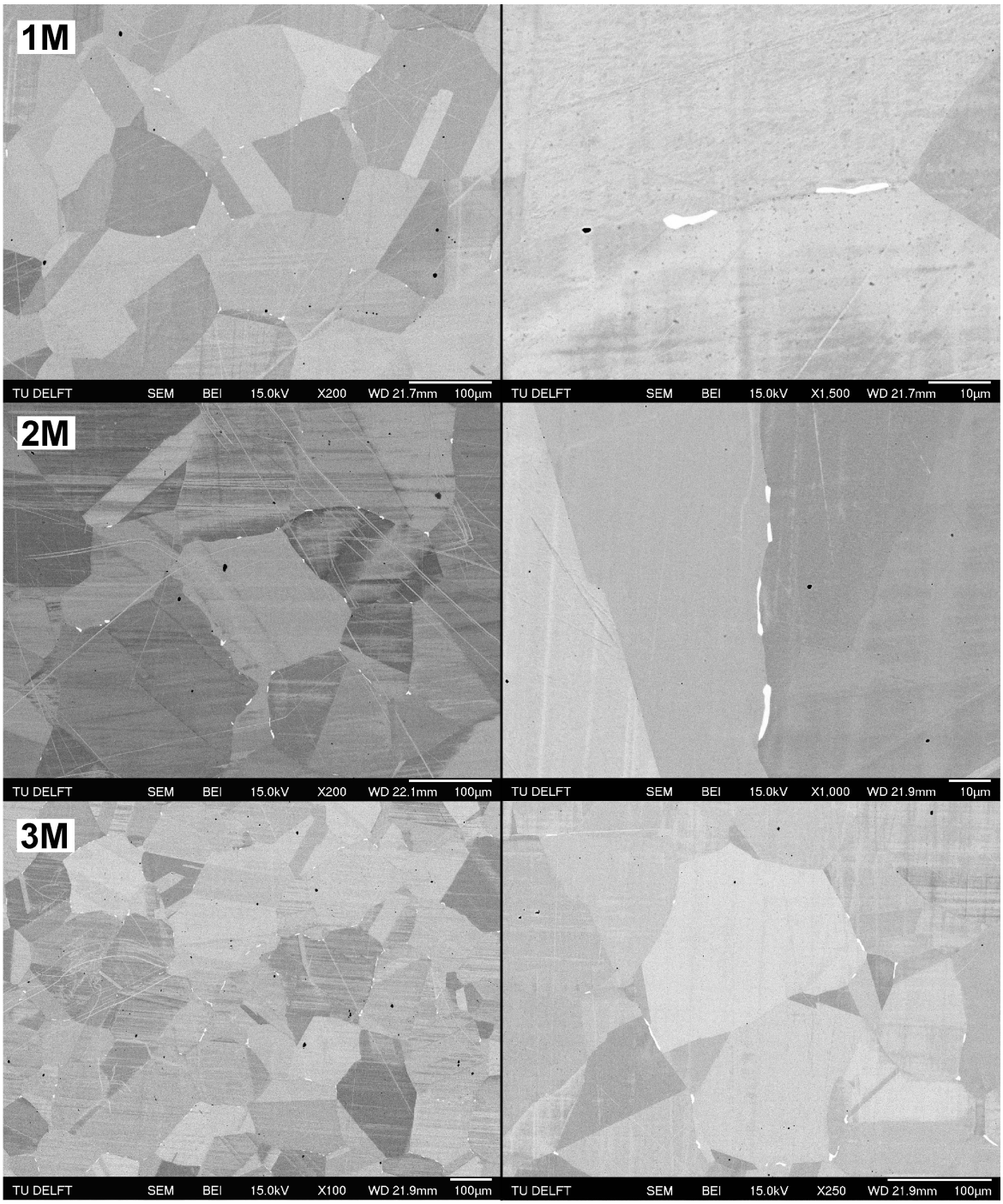

Fig. 10.15 Precipitates in the long-term HT samples as shown in a BEI picture. The oxide inclusions are black, the matrix is grey, and the TCP-phase is observable as bright white patches. The images are ordered vertically by thermal treatment time. From top to bottom the images show 1 month (1M), 2 months (2M) and 3 months (3M) of thermally treatment at 800°C respectively.

Chemical composition Several EDS tests were carried out to analyse the precipitates that had formed, and they all returned comparable compositional results. Table 10.2 provides the theoretical and measured composition of the NiMo-phase and compares it to the matrix. The NiMo precipitates had a substantially greater chromium concentration than the theoretical values extracted from Thermo-Calc. Such a large concentration (19.65 wt% Cr) would not be soluble in the NiMo-phase as it is known that the phase strictly accepts Ni and Mo atoms on its specific sites. Therefore, it is likely that next to the NiMo-phase, the chromium-enriched P-phase (oP56, TCP) formed as this phase does accept chromium atoms on its specific sites. According to a study by Nagashima *et al.* [45], the P-phase in the given Ni-Mo-Cr ternary system is energetically favourable at high Cr concentrations. Therefore, it is possible that the P-phase formed together with the NiMo-phase but was not detected due to their crystallographic similarities. Unfortunately, the used EBSD database did not include the P-phase and therefore identification was not possible. Nevertheless, both phases are identified as TCP phases, for that reason the precipitates will be named TCP-phase from now on. Further identification is required to support this theory.

Table 10.2 Average composition of the NiMo-phase, P-phase and matrix γ-phase in the analysed thermally treated samples. Data obtained from multiple EDS measurements (example measurement see appendix figure B.3). Theoretical data from Thermo-Calc.

Phase	**Cr**	**Fe**	**Ni**	**Mo**
		[wt%]		
TCP-phase (measured)	19.9 ±0.2	-	39.6 ±0.6	40.4 ±0.3
NiMo-phase (theoretical)	2.8	0.6	54.4	42.2
P-phase (theoretical)	8.8	0.4	40.3	50.5
Matrix	7.03 ±0.17	1.22 ±0.16	76.9 ±0.7	14.8 ±0.2

Geometrical evolution As seen in figures 10.16 the geometry of the observed TCP precipitates changes as a function of thermal treatment time. In the first hours of HT the precipitates primarily form as plate-like volumes with jagged tips. When thermal treatment continues the precipitates grow along the grain boundary but also in width. During this growth the geometry of the volume seems to change from its initial jagged plate-like structure to a more globular form. When analysing the bottom images of figure 10.16 the rounded precipitate tips can be observed, yet some tips remain sharp. Due to the brittle nature of the TCP precipitates this evolution in shape is likely of influence on the fracture behaviour of the material, as sharper precipitate tips can lead to crack initiation due to high stress concentrations around the particle, consequently resulting in more brittle fracture. This mechanism is illustrated in figure 10.17. This behaviour has been reported in multiple studies by Wilson [13], Sun & Zhang [14] and Liu *et al.* [15], with the last study finding similar TCP phase geometry transformations in a Ni-Cr-Mo alloy during long-term aging.

The transformation from jagged to more globular (spherical) is already observed at samples that have been heat treated for 2 to 5 days, indicating a minor relief from stress concentrations around

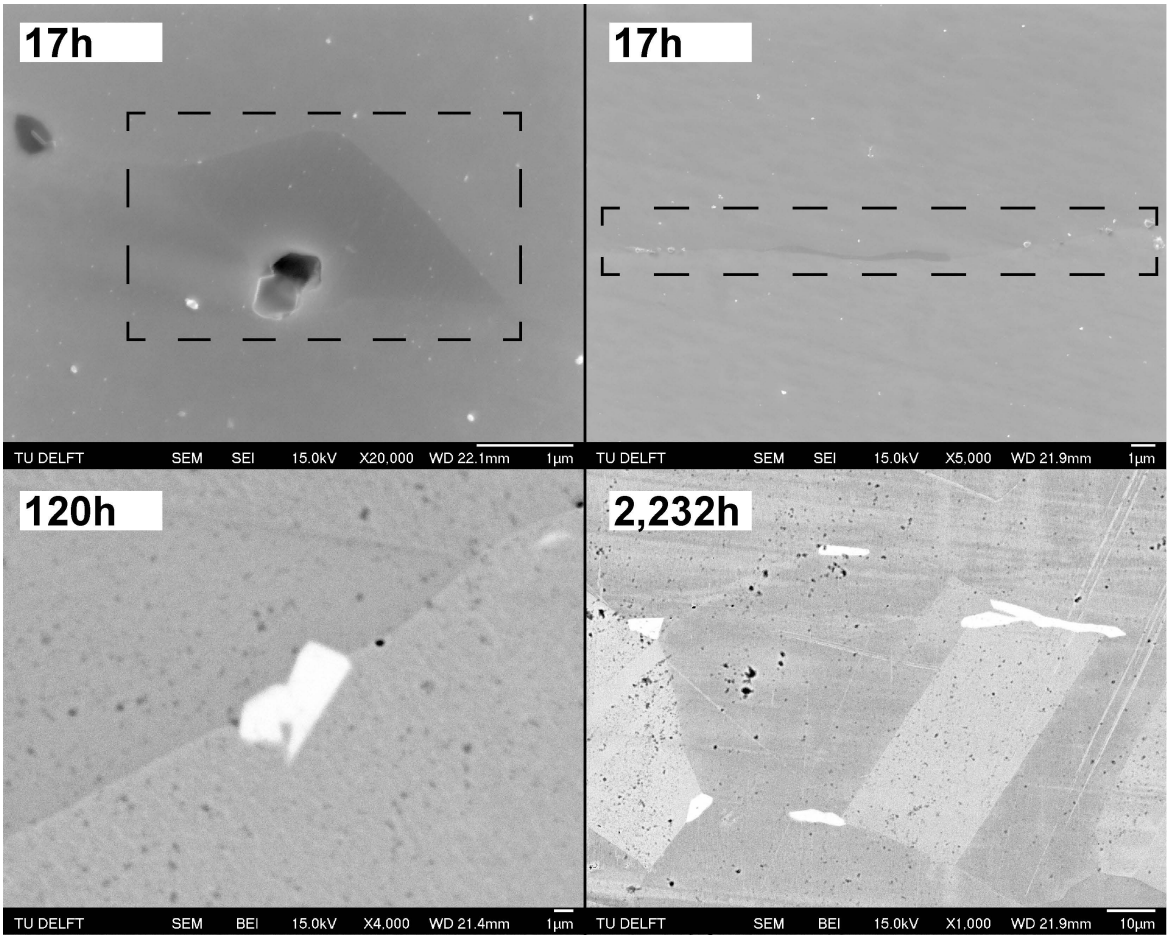

Fig. 10.16 Evolution of precipitate geometry observed during specific thermal treatment times. The top images show SEI images of small precipitates at 17h of HT. The somewhat darker shade shows the precipitate, additional indicated with a dashed box. The bottom images show BEI image of the precipitates at 120h (5 days) and 2,232h (3 months) of thermal treatment at 800°C.

precipitates after 24 hours of thermal treatment. Nevertheless, long-term HT samples are observed to have a higher ratio of globular precipitate tips.

The discussed geometrical evolution of the TCP phase is based on qualitative observations made with SEM images, for that reason further investigation is required to quantitatively identify these transformations. Nevertheless, the change is seen as likely due to similar behaviour of TCP precipitates in other Ni-Cr-Mo alloys.

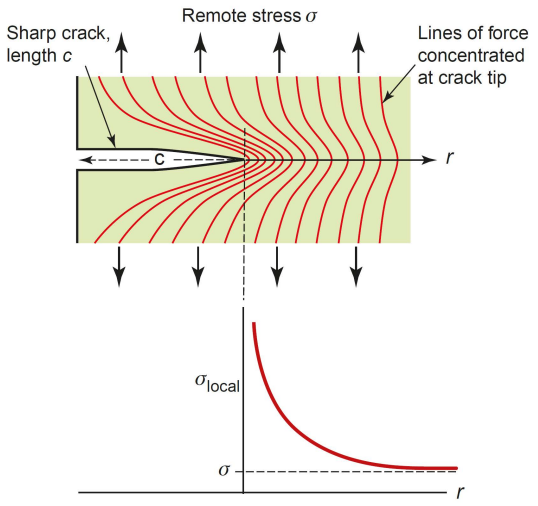

Fig. 10.17 Lines of force in a cracked body under load; the local stress is proportional to the number of lines per unit length, increasing steeply as the crack tip is approached. Reprinted from Ashby *et al.* [46].

Grain boundary activity A series of EDS measurements were used to analyse the Mo activity in the vicinity of the TCP precipitates. The activity describes a preferential diffusion trend within the microstructure. Two measurements were made: one over a grain boundary near the precipitate tip and the other between the matrix and the precipitate. Both methods of measurement look for a decrease and a rise in molybdenum concentration to signify accumulation and consequently precipitation growth/coarsening. The results are given in figure 10.18. The measurements were conducted three times and resulted in similar diagrams.

The findings point to slight molybdenum activity near the grain boundary and precipitate tip since there is a small decrease in Mo followed by an increase in the GB. The matrix around the precipitate contained no molybdenum activity, according to the measurements, hence, suggesting preferred molybdenum diffusion and precipitate growth along GBs. Additional Electron Probe Microanalysis (EPMA) mapping is recommended to investigate the elemental kinetics related to the nucleation and growth of the observed precipitates.

Planar precipitate density The evolution of the precipitate planar density during the course of the thermal treatment process was analysed. For each HT sample, *ImageJ* was used to process and analyse several BEI images with a magnification of 50. By carefully counting the number of precipitates per area, the planar density of the precipitates was determined. Figure 10.19 presents the outcomes. The uncertainty range related to the measurements is presented by the standard deviation ($\pm 1\sigma$) of the four conducted measurements per sample. Specimens with less that four usable BEI images were excluded from the analysis.

Following the first month of thermal treatment, the data show a continuous increase in precipitate density. After this period, the precipitate density appears to stabilise around 120 precipitates per 1 mm^2. For long-term HT no significant trend is observed. Nevertheless, a minor decrease in precipitate density is expected as a result of *Ostwald ripening*, as the total volume fraction of the phase appears

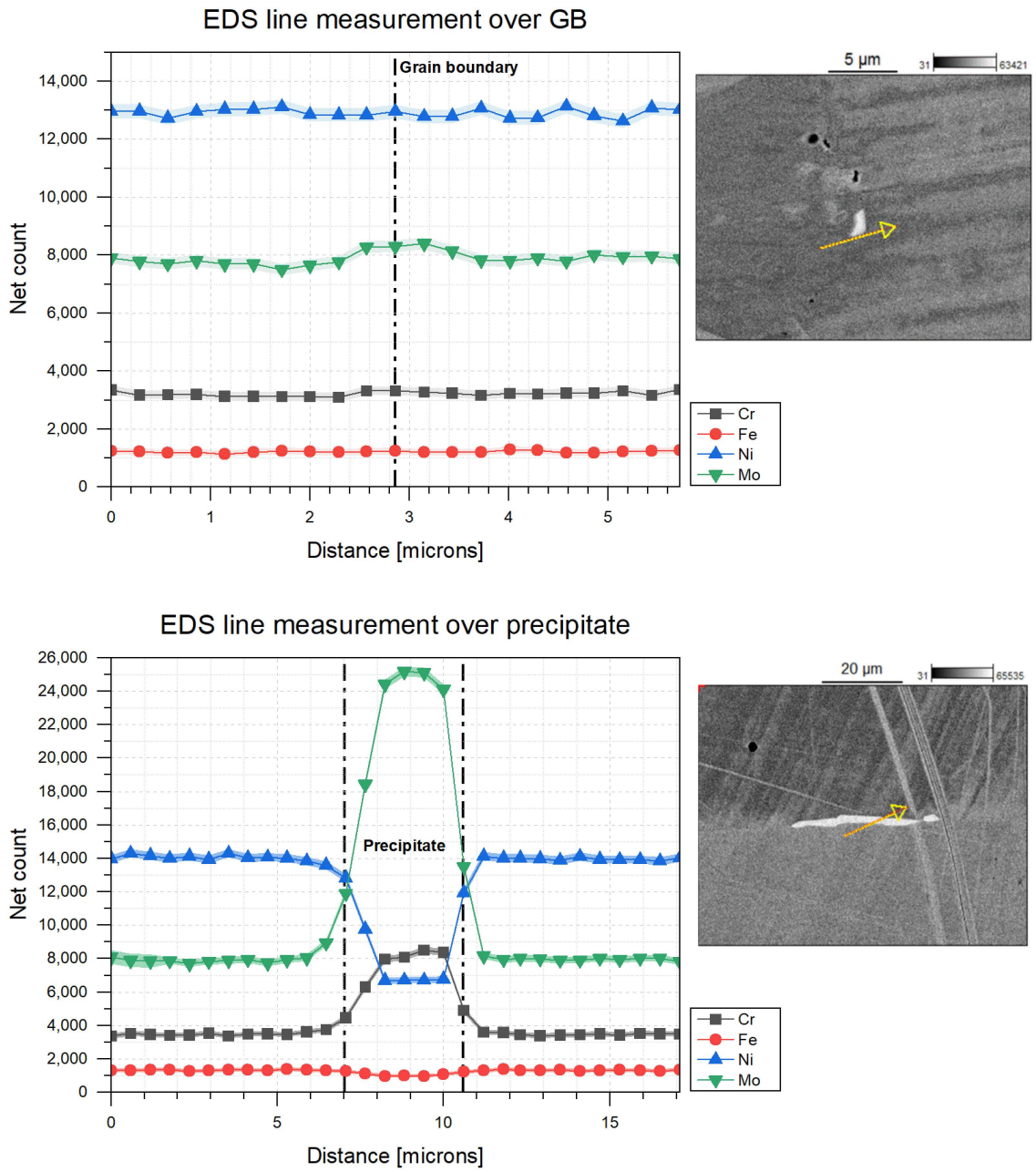

Fig. 10.18 Series EDS measurement around TCP precipitate. (a) measurement over GB next to precipitate tip. (b) measurement over matrix and precipitate.

to be increasing in the long-term samples as observed in the qualitative SEM data. In the last month of thermal treatment (1,536-2,232 h) the size of the precipitates is still increasing but not at a high rate as seen before. Therefore, further long-term HT is needed in order to determine the extent and long-term rate of precipitate coarsening in the material.

The measured TCP precipitate size appears to be consistent when compared to the precipitate diameter approximations in figure 10.12. This suggests that the precipitate growth rate is decreasing significantly for even longer heat-treatments. This behaviour was expected as the qualitative observations indicate an approximately similar growth relative to the estimated growth rate given in figure 10.12.

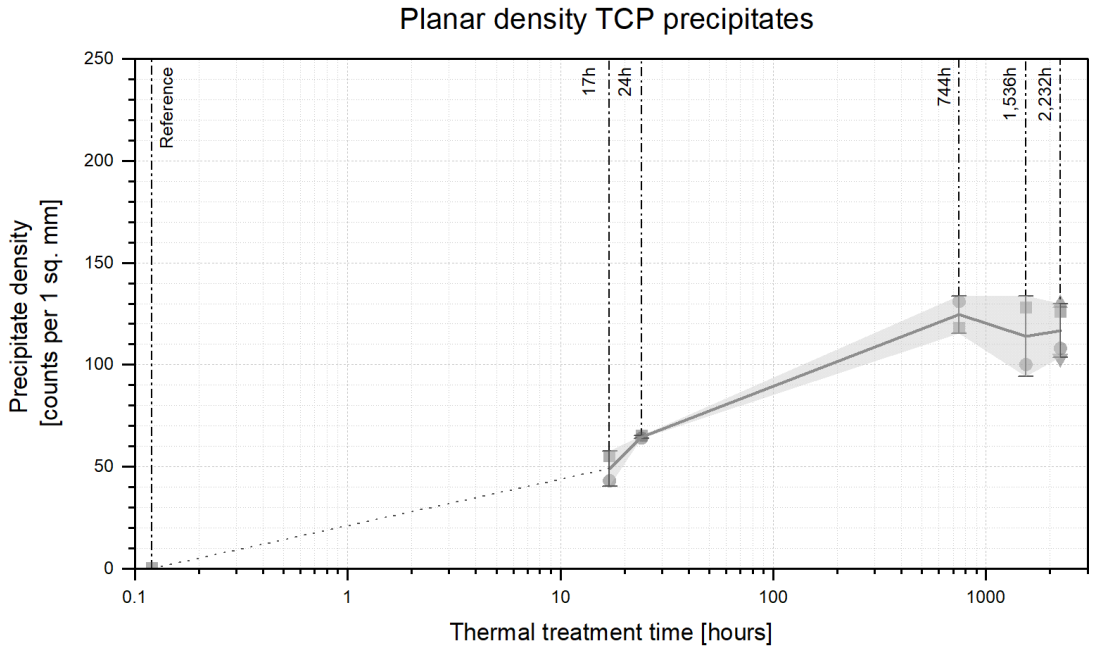

Fig. 10.19 Density fraction of TCP-phase precipitates as a function of thermal treatment time at 800°C. Calculated from BEI images with *ImageJ* counting tool.

Precipitate nucleation location A collection of EBSD and BEI images were analysed to characterise the preferred grain boundaries for precipitate nucleation and growth. Due to its comparatively large precipitate size and high density compared to the other short-term samples, images from the 120h HT sample were selected. Figure 10.20 presents the study's findings and displays the positions of TCP precipitates found in the same studied area as those seen in a BEI image.

The resulting image suggests a correlation between the quantity of precipitates and grain size, with little to no precipitation occurring between bigger grains (see figure 10.20a annotation A) and a higher density in small-grain clusters (see figure 10.20a annotation B). Second a relation between High-Angle Grain Boundaries and precipitates is observed in figure 10.20b, supporting the theory on preferred nucleation at high defect energy locations. Nevertheless, data supporting this relation is limited to only one image. Further EBSD characterisation is recommended to investigate preferred precipitate locations.

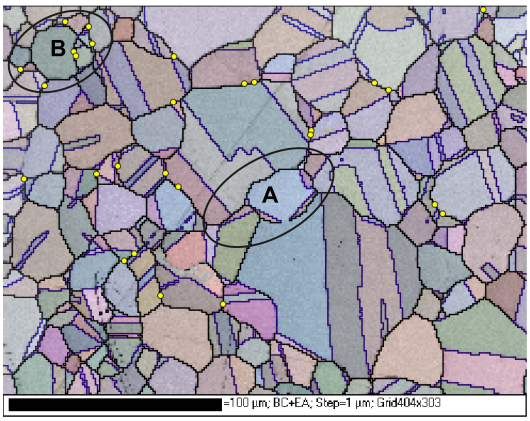

(a) Band contrast EBSD with Euler overlay. Black lines represent grain boundaries and blue lines twin boundaries.

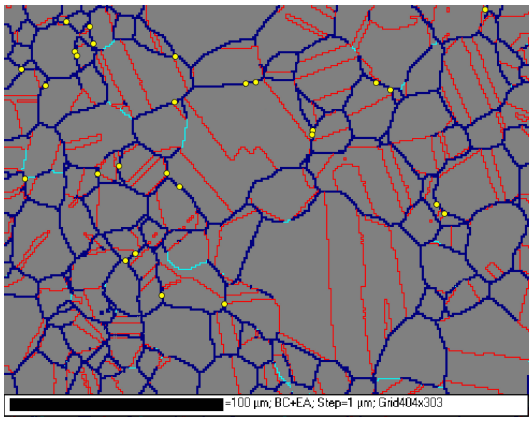

(b) EBSD map only including LAGB boundaries (light blue), HAGB boundaries (navy blue) and twin boundaries (red).

Fig. 10.20 EBSD grain boundary misorientation angle map with annotated (yellow circles) precipitate locations. The figures present the 120h HT sample EBSD map combined with BEI image including precipitate location, see appendix figure B.16.

10.2.3 Grain size distribution

EBSD mapping was employed to analyse the distribution of the alloy's grain sizes. The grain size area and diameter were calculated from this data. Four different specimens—the reference, after 24 hours, 48 hours, and 120 hours of thermal treatment at 800°C—were examined to determine the grain size change over time. The resulting grain size distribution is given in figure 10.21.

The uncertainty range related to the grain size distribution is calculated following the *geometric* standard deviation method ($\pm 1\sigma$) because of its focus on grain size range rather than the arithmetic mean and its distribution width.

It is evident from the image that the fraction of the medium-sized grains (10–30 µm in diameter) decreases. This pattern is expected in the occurrence of grain growth because moving grain boundaries cause small and medium-sized grains to shrink in size, eventually to the point of annihilation, while larger grains expand. The average increase in grain size is clearly visualised in figure 10.22. Additionally, grain growth appears to be slowing down over time as shown in figure 10.23, suggesting grain size stabilisation after 120 h of HT. Additional EBSD measurements of long-term HT samples are required to substantiate this claim.

Given that an area of more than 120,000 μm^2 was examined by EBSD, it is expected that the retrieved grain sizes represent the microstructural average of the samples. Between 190 and 300 grains were counted for each sample.

The increase in grain size can have a direct effect on the deformation behaviour of the material. One of the effects is described by the Hall-Petch relation which describes the decrease in yield strength during grain growth. Second, it is found that in polycrystalline nickel-based materials with a coarse

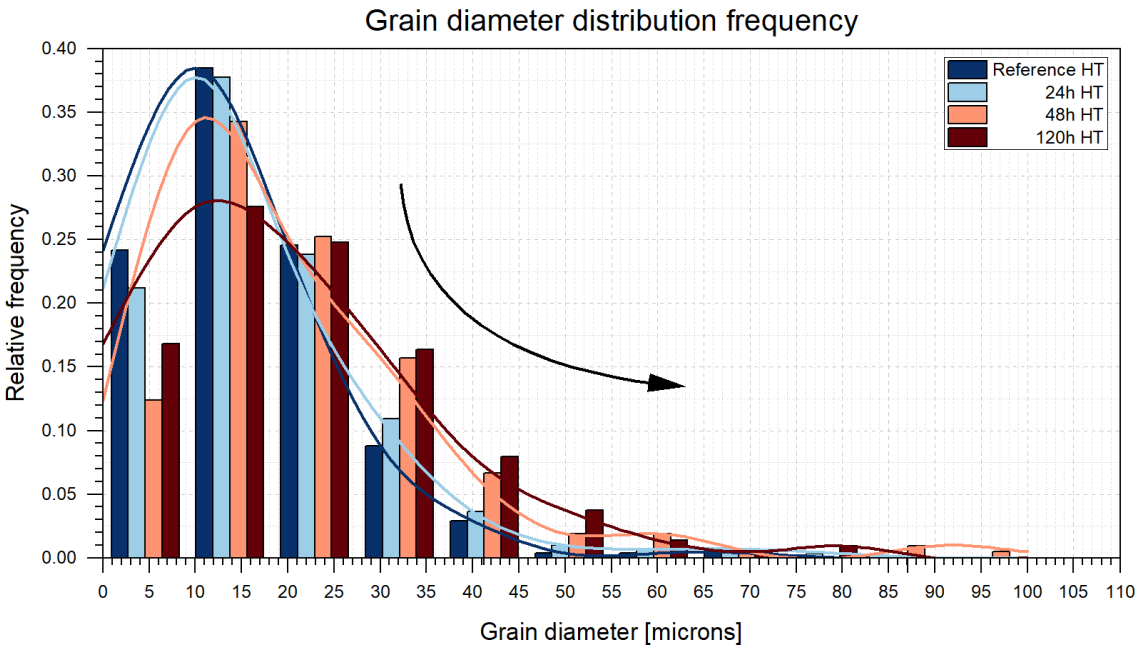

Fig. 10.21 Grain size distribution as function of thermal treatment time at 800°C. The distribution curve clusters the grain diameter per 10 µm. Processed from EBSD data.

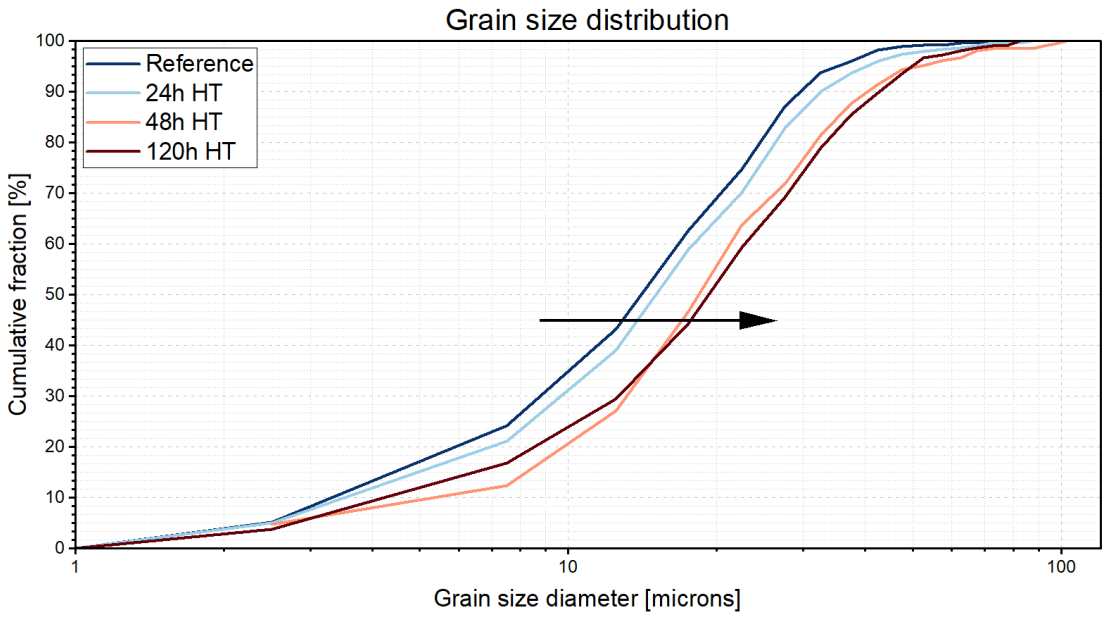

Fig. 10.22 Grain growth as a function of thermal treatment time in the MONICR alloy visualised in a cumulative grain size diagram. Processed from EBSD data.

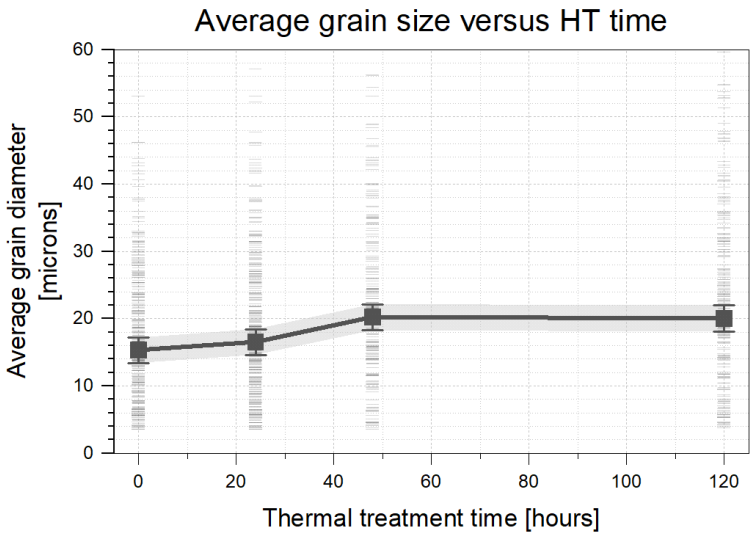

Fig. 10.23 Average grain size as function of thermal treatment time at 800°C. Processed from EBSD data. The presented uncertainty range is based on the geometric mean and standard deviation. The short lines visible in the graph represent the measured grain sizes per EBSD measurement.

grained microstructure ($d_{grain} > 5$ µm) grain growth plays only a marginal role in dynamic recovery [47]. As a result, changes in grain size are less likely to influence the work hardening ability of the material.

10.2.4 Grain boundary misorientation angle

For samples that have been measured by EBSD, the misorientation of grain boundaries was identified. The data is normalised to reflect values per 1 mm^2 because each measurement has a different valid analysis area. Grain boundary length is normalised by multiplying the boundary length with the ratio between measured area and 1 mm^2. As discussed in section 10.1.1, due to the presence of several scratches and one indentation, faulty data points present in the EBSD map were excluded from the analysis. As seen in the EBSD band contrast with LAGB overlay images, figure 10.24, another abnormality is present, namely red dots. These dots, visible as checkerboard-like boundaries, are a result of wrongly indexed EBSD measurements, and for that reason are also excluded in the analysis. The normalised and corrected EBSD data presented as boundary length per misorientation angle for the reference, 24h, 48h, and 120h samples is given in figure 10.25.

Because the grain boundary length measurements are strongly affected by EBSD misindex errors the related uncertainty range takes these false identifications into account. The uncertainty range of the length values ($s_{L,\omega}$) [µm] per EBSD map are calculated as a function of GB misorientation angle fraction, $\chi_{\omega,i}$ [-]; EBSD misindexing percentage, γ_{EBSD} [-]; and the total normalised pixel boundary length (10^6 pixels equaling 1 µm per pixel), P_{EBSD} [µm], resulting in the given uncertainty margin:

$$s_{L,\omega} = \gamma_{EBSD} \cdot \chi_{\omega,i} \cdot P_{EBSD} \tag{10.5}$$

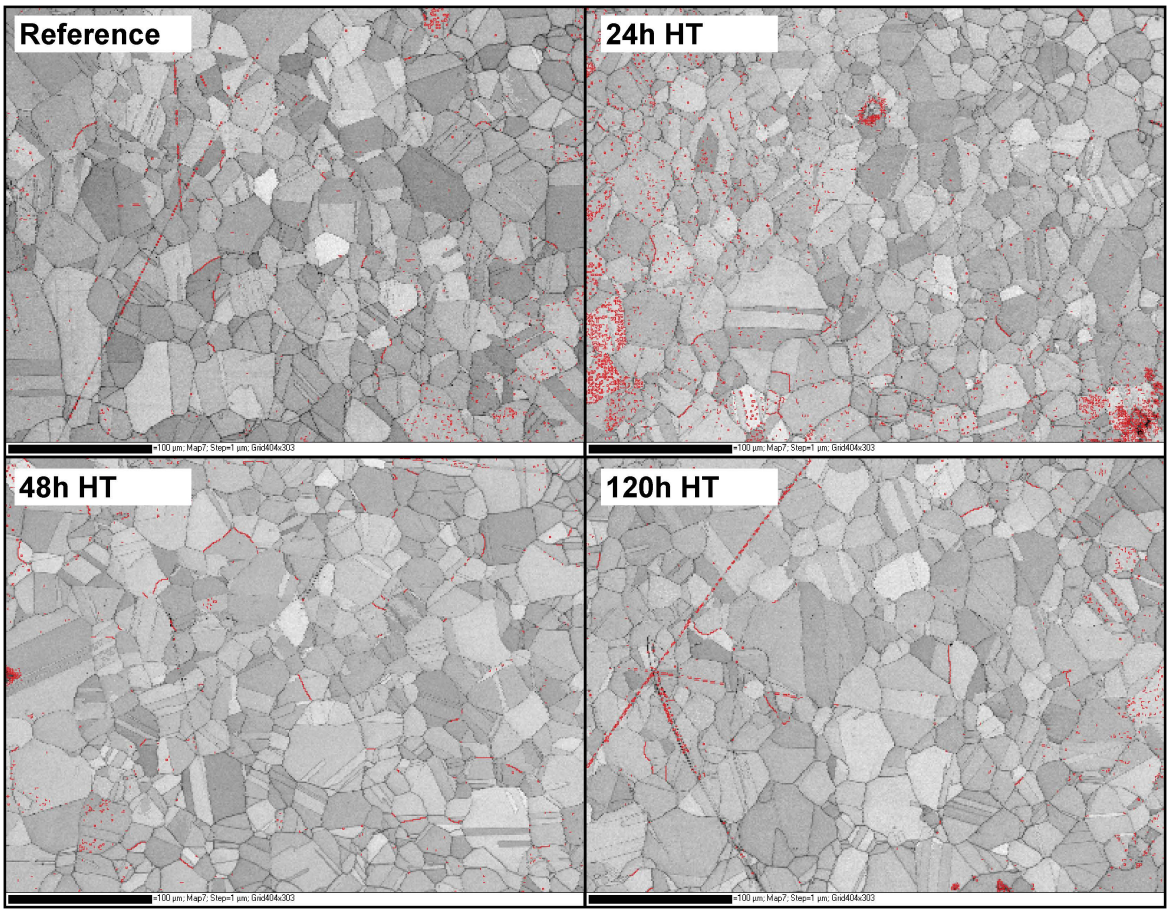

Fig. 10.24 Band contrast EBSD image with Low-Angle Grain Boundary overlay of reference, 24h, 48h and 120h HT samples. Image processed from EBSD data.

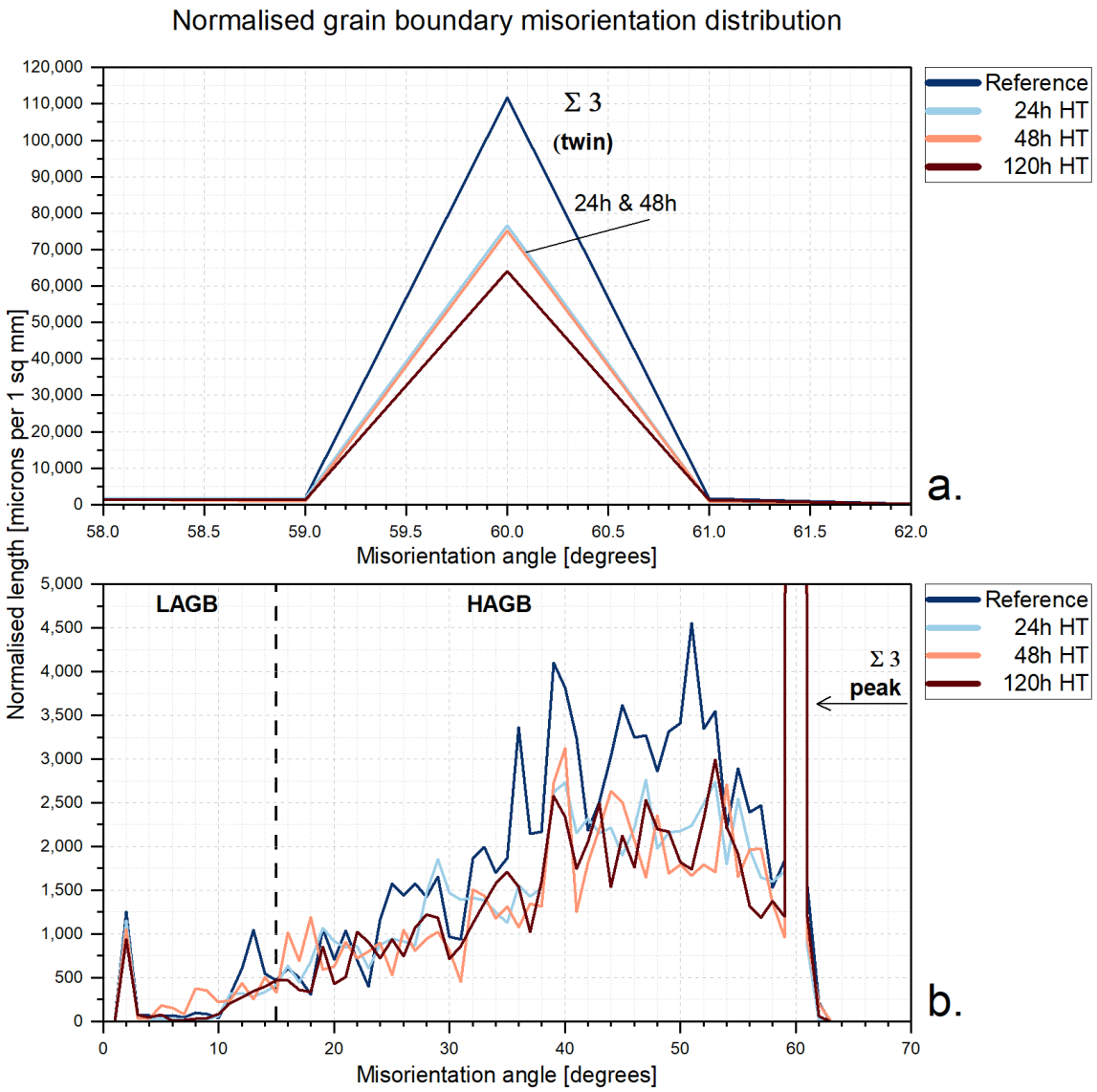

Fig. 10.25 Grain boundary misorientation angle of different thermal treatment times. Sub-figure (a) shows the twin misorientation peak (Σ3) and (b) shows the full angle range excluding the twin peak. All data is normalised to boundary length per 1 mm^2. Processed from EBSD data.

To analyse the effect of thermal treatment on the development of grain boundary density, the given results are presented as a function of HT time, as seen in figures 10.26 and 10.27. Both graphs suggest a decrease in total normalised boundary length for high-angle grain boundaries (HAGB) and twin boundaries. Both these trends indicate strong annihilation of boundaries during the first 24 hours of thermal treatment. After 48 hours of thermal treatment the grain boundary density seems to stabilise. To a certain extent this trend is reflected in the development of the average grain size, suggesting a potential relation between HAGB and twin boundary annihilation with grain growth.

The decrease in twin boundary density has a direct effect on the deformation mechanism of the material during deformation because it decreases the density of dislocation slip barriers. As a consequence dislocation hardening is increased, resulting in an increased work hardening ability of the material. This increase in work hardening will be reflected in the toughness of the material.

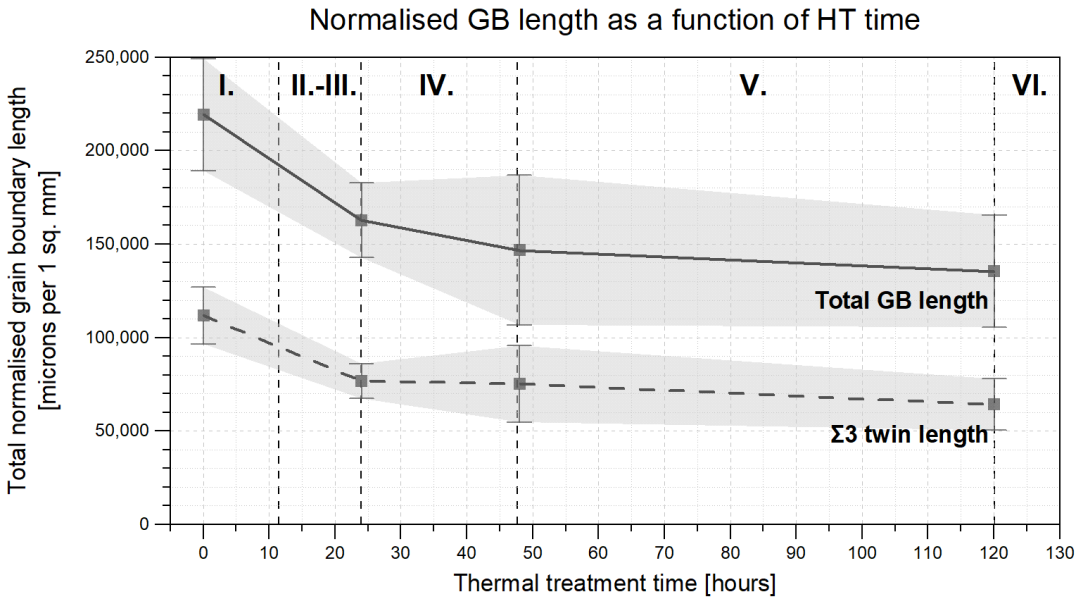

Fig. 10.26 Total GB and twin length as a function of thermal treatment time at 800°C. All data is normalised to boundary length per 1 mm^2. Processed from EBSD data. Roman numbers refer to the general microstructure images given in section 10.2.2.

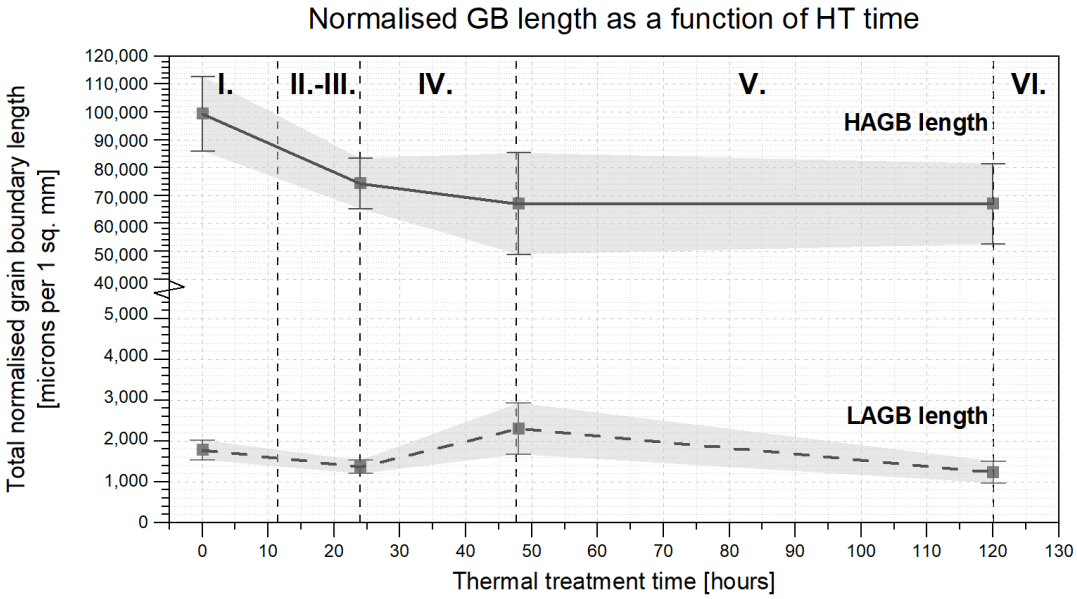

Fig. 10.27 Total normalised length of LAGBs and HAGBs as a function of thermal treatment time at 800°C. All data is normalised to boundary length per 1 mm^2. Processed from EBSD data. Roman numbers refer to the general microstructure images given in section 10.2.2.

10.3 Instrumented Charpy test

10.3.1 Absorbed impact energy

The majority of the samples were submitted to an instrumented Charpy test. The test measures the loading and deflection of the specimen, which allows the area under the curve to be used to calculate the total absorbed energy of the impact. Figure 10.28 shows the load-deflection curve for each of the various tests. Note, only the second reference specimen was submitted to an instrumented test, therefore no reference specimen number 1 data is presented.

The related uncertainty margin of the toughness measurements is based on the inclusion fraction per specimen. The uncertainty margin of the dynamic strength estimates is a combination of this inclusion fraction deviation and the instrumented sensor error. The error related to the instrumented equipment is calculated from the difference between the computed toughness (area under curve) and toughness measured from the pendulum height. A standard deviation ($\pm 1\sigma$) of these results is taken and combined (summation in quadrature) with the inclusion factor error to result in the given uncertainty range.

Unfortunately, external vibrations disrupted measurements for specimen T800-1M:1, causing deflection-load measurements to be inconsistent in the first data points (up to 2 mm deflection) of the experiment. Sadly, the dynamic yield strength is determined using these values. As a result, this yield

strength estimate is disregarded as a valid result in the following section. The deviating curve can be seen in appendix figure B.14.

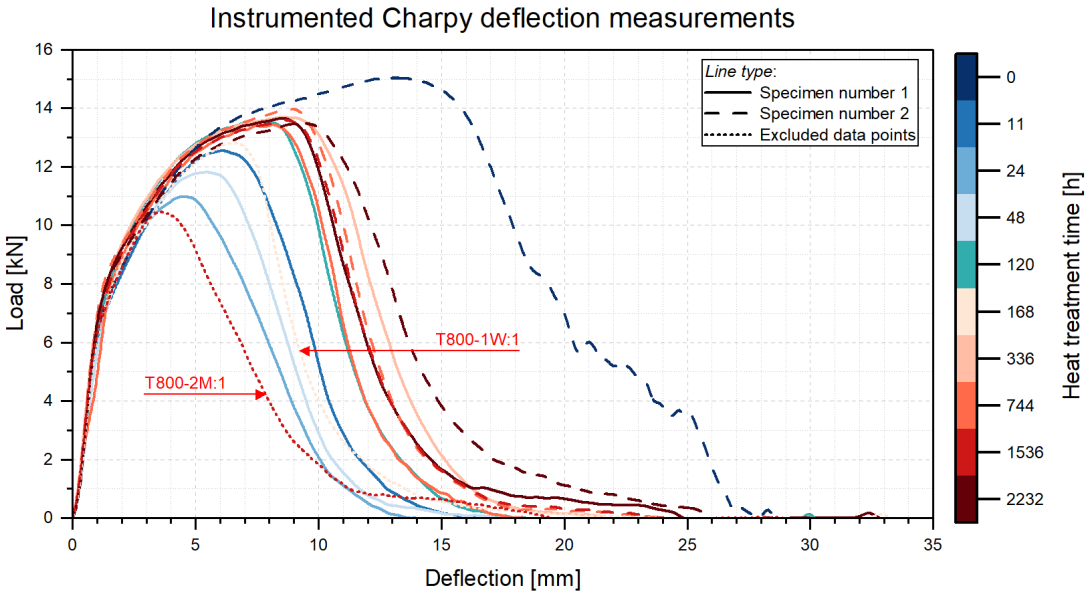

Fig. 10.28 Instrumented Charpy test measurements presented as specimen loading versus deflection. The colours describe the thermal treatment time.

Notch impact toughness The absorbed energy and the specimen's fracture plane's dimensions are used to calculate the specimen's notch impact toughness. This quantity, which is determined by the strength and ductility of the material, is used to investigate how thermal treatment affects the evolution of material embrittlement. Figure 10.30 displays the outcomes for the examined specimens.

T800-1W:1 and T800-2M:1 appear to deviate from the general trend, with significantly lower impact toughness. As discussed in section 10.1.2,samples are observed to have a considerable higher volume fraction of inclusions, suggesting a relation between inclusion volume fraction and impact toughness. These results are ignored in the trend analysis.

The initial reference specimen is able to absorb significantly more impact energy, leading to a relatively high impact toughness. This was anticipated because during the impact test, both reference samples suffered significant *plastic deformation* as opposed to breaking, as seen in figure 10.29. Less than 24 hours of thermal treatment caused samples to gradually lose their ability to absorb the impact energy without fracture, leading to a decrease in impact toughness, with a notable minimum at 24 hours. Additional heat treatment restored the impact toughness to a certain extent. To investigate the cause of this behavioural change in toughness the strength and ductile fracture surface of the material are analysed.

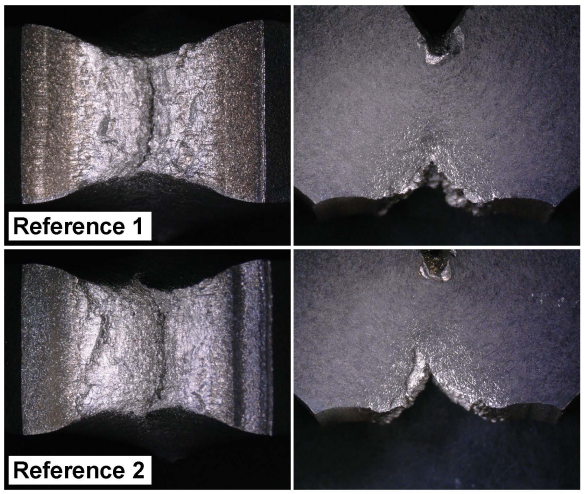

Fig. 10.29 Picture of post-Charpy deformation of reference samples. The picture on the left looks at the notch plane, while the right image looks at the side of the sample.

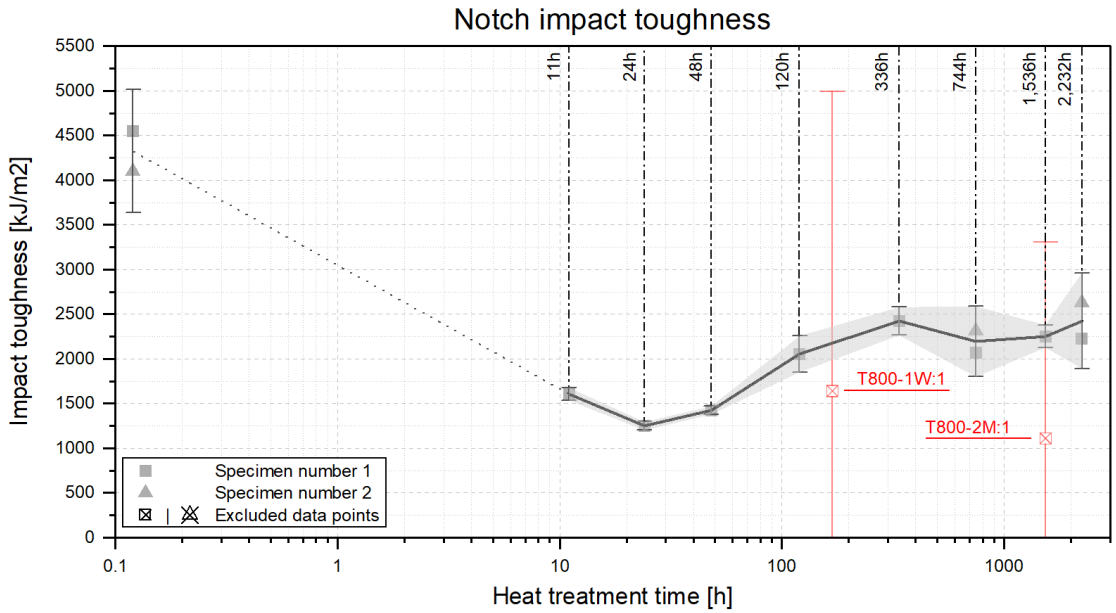

Fig. 10.30 Notch impact toughness as a function of thermal treatment time at 800°C.

Dynamic yield and tensile strength Figure 10.31 displays the results of the calculation (see section 9.3.1) of the dynamic yield and tensile strength using the instrumented Charpy test data. The used equations are:

$$\sigma_{YS,d}\ [\text{MPa}] = 54.55 \left[\frac{\text{MPa}}{\text{kN}}\right] \cdot F_{GY}\ [\text{kN}] \qquad \text{(9.4 revisited)}$$

$$\sigma_{TS,d}\ [\text{MPa}] = 46.58 \left[\frac{\text{MPa}}{\text{kN}}\right] \cdot F_{GY}\ [\text{kN}] \qquad \text{(9.6 revisited)}$$

The graph shows that the estimates of yield strength vary less than the estimates of tensile strength. This behaviour is expected as the yield strength describes the transition between elastic deformation to plastic deformation, while tensile strength is related to the plastic behaviour of the material, thus including the materials ability to work hardening. Due to microstructural evolution the materials ability to deform also changes.

The yield strength results indicate no noteworthy trends following thermal treatment, as the values stay within the standard deviation of the reference value. When analysing the dynamic tensile strength, the results do suggest a certain trend even while the standard deviation of the reference sample is relatively large due to the sample's high inclusion fraction. Nevertheless, even with this high uncertainty a decline, to some extent, in tensile strength is observed during the first 24h of thermal treatment. In the subsequent 96h of thermal treatment a recovery in tensile strength is observed, this recovery is followed by a stable period. Due to the assumed stability of the yield strength a similar trend for work-hardening ($\sigma_{ts} - \sigma_y$) during deformation is evident.

The work-hardening dip observed in the first 24 hours of thermal treatment is a result of microstructural evolution processes at elevated temperatures. A variety of microstructural processes were observed with the SEM. Additional thermal treatment also resulted in further evolution of the microstructure, again suggesting a relation with the recovery in these properties for long-term HT samples.

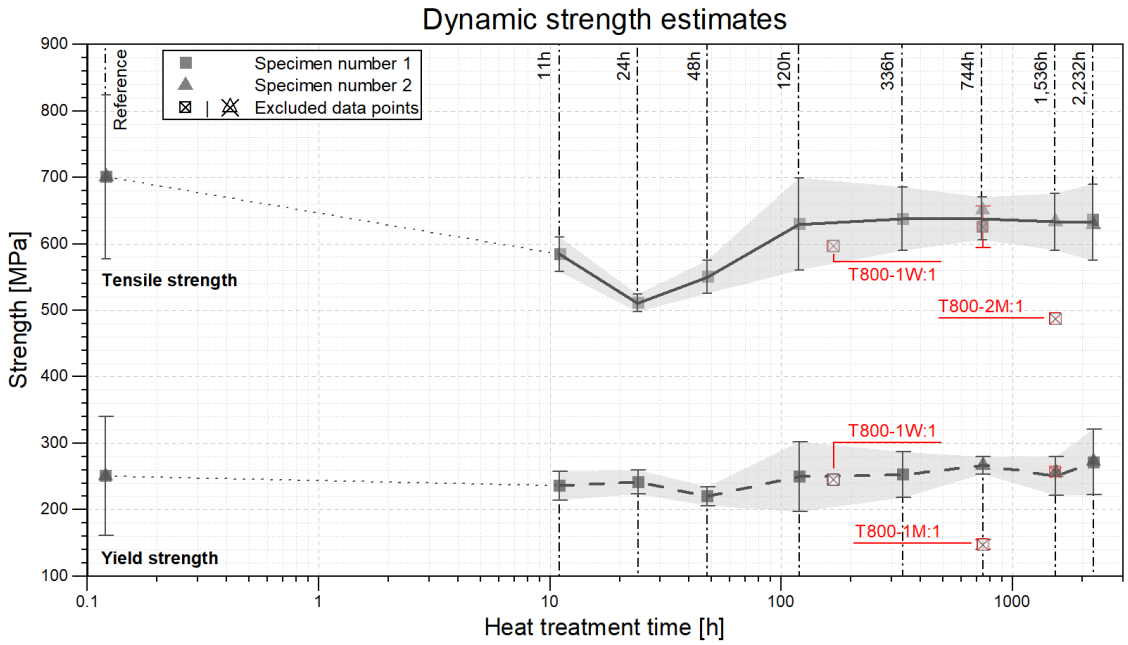

Fig. 10.31 Dynamic yield- and tensile strength estimates as a function of thermal treatment time at 800°C. The values are calculated from the instrumented Charpy test data.

10.3.2 Shear fracture appearance

To investigate the fracture behaviour as a function of thermal treatment time Shear Fracture Appearance (SFA) measurements were taken. Because these measurements are done manually the related uncertainty is relatively large. The presented uncertainty range is a combination of the discussed inclusion fraction error and measurement error. Because the fracture surface is not completely flat a certain error range is expected when measuring the dimensions of the SFA. Given that the length and width of the SFA surface were measured with the use of a caliper a measurement error of ± 0.2 mm was assumed.

As seen in figure 10.32, the fractured Charpy specimen SFA value follows a similar thermal treatment evolution trend as the Charpy dynamic tensile strength estimates, shear fracture appearance and notch impact toughness, making the observed trends more likely to be correct. The most brittle specimen is the 24 hour sample, T800-24h:1, which exhibits a significant dip in the ductile fracture fraction. Longer thermally treated samples gradually become more ductile again, and stabilise at an SFA of 60 to 70 percent. Thermal treatment at 800°C does permanently embrittle the material in comparison to the ductile reference state.

Two data points, sample T800-1W:1 and T800-2M:1, stand out when the behaviour of the trend is examined in more detail due to their deviation from the overall trend. The impact toughness graph and the tensile strength estimate graph show that both exhibit a similar departure from the general pattern. Since the load-deflection data contained no inconsistencies for these samples, the differences are likely related to the inclusion volume fraction in these alloys as this behaviour is also observed for the Charpy results.

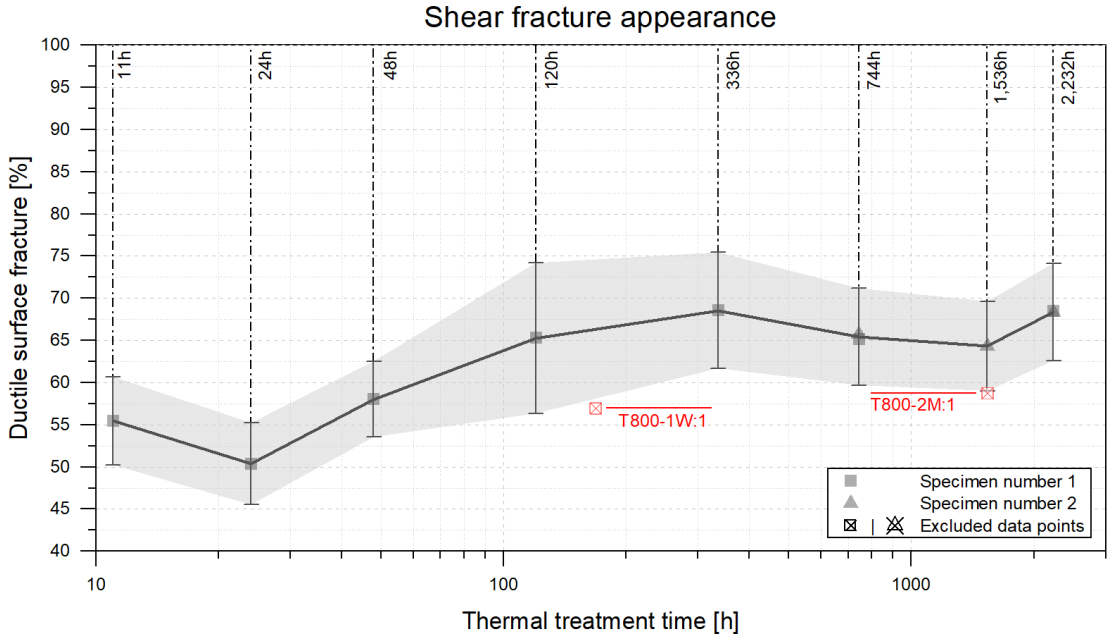

Fig. 10.32 Shear fracture appearance as a function of thermal treatment time at 800°C.

10.4 Hardness testing

Each sample underwent a Vickers hardness test. To investigate the microstructure's hardness range for each sample, 20 micro-indentation measurements were taken, and the average was calculated. The related uncertainty range is a combination of the sample standard deviation ($\pm 1\sigma$) of the indentation measurements and the inclusion fraction found in the samples. Figure 10.33 depicts all the measured values for hardness as a function of thermal treatment time.

There were no discernible differences between the averages of the various measured micro-hardness values. Nevertheless, the found measurements all come with a relatively large uncertainty range resulting from the standard deviation of the indentation series, therefore further testing is required.

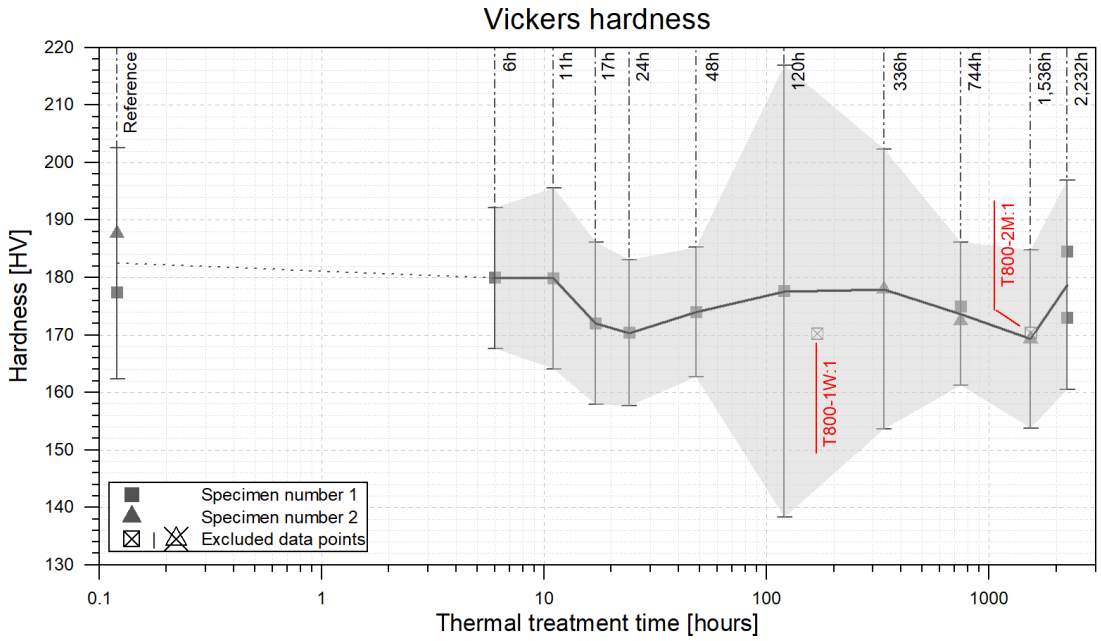

Fig. 10.33 Vickers hardness results as a function of thermal treatment time at 800°C. The average micro-hardness values are calculated from a set of 20 micro-indentations.

10.4.1 Hardness deviations

Further hardness tests are performed to investigate the relatively large error margin in long-term heat-treated specimens. First, the hardness-grain size relationship is investigated by measuring the micro-hardness values of three grain size clusters: small, medium, and large. The corresponding grain diameters are derived from figure 10.21's grain size distribution. The results are shown in Figure 10.34. The plot suggests that hardness and grain size have an inverse relationship. This pattern is comparable to the *Hall-Petch* relationship, combined with the hardness (HV) - yield strength (σ_y) and

yield strength increment from grain refinement ($\Delta\sigma_y$) estimate:

$$\Delta\sigma_y = \frac{k_y}{\sqrt{d_{grain}}} \qquad \text{(8.7 revisited)}$$

$$H_v\ [\text{kgf/mm}^2] = 3.55 \cdot \sigma_y\ [\text{MPa}] \qquad \text{(9.7 revisited)}$$

The standard deviation of the Vickers hardness results is likely (partly) related to the relationship between grain size and hardness value, because the indentation series measures the local hardness values of the microstructure. The indentation measures a line of 5 mm, meaning a variety of local differences influencing the hardness, such as grain size, are measured. Additional observations related to potential grain size clustering in the material could further support these deviations.

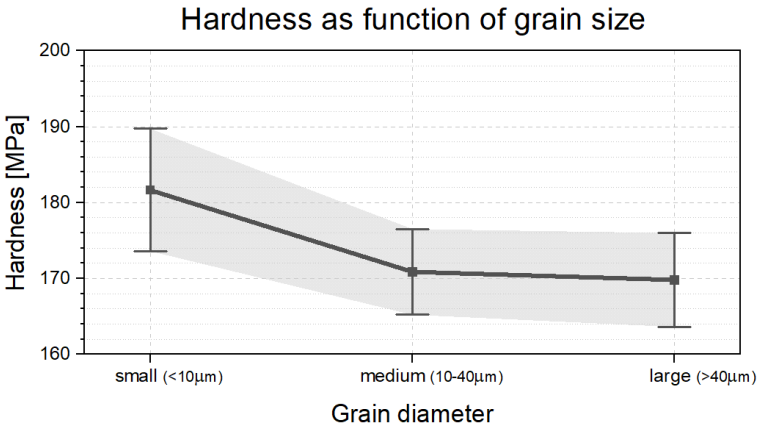

Fig. 10.34 Vickers hardness as a function of grain size. Grain sizes are clustered by average diameter size. Grains with a diameter of <10µm are classified as *small*, between 10-40µm as *medium*, and over 40µm as *large*. Vickers indentation force HV0.5 was used.

Second, the relationship between hardness and twin boundaries was investigated. Grains of approximately the same size were used. Clusters of similar sized grains were classified as having no twin boundaries (no-TB grains) or having twin boundaries (TB grains). Figure 10.35 depicts the results. According to the results, grain clusters with twin boundaries have a more stable hardness value compared to clusters with no twin boundaries. This relation between the presence of twins and resulting hardness value is likely, in combination with grain size, a significant contributor to the relatively large hardness standard deviation present in the material.

The noticeable stability of micro-hardness values in twinned grains relative to non-twinned grains suggests a relation between twin boundaries and the deformation mechanism of the material. As discussed in section 8.5.1 the presence of twin boundaries can harden material by forming additional dislocation barriers. The loss in twin boundary density following thermal treatment could therefore reduce the work hardening ability and consequently hardness of the material.

According to the geometry of the indentation tip and the used Vickers test load of 0.5HV (4.9 N), the maximum found indentation diagonal was 77.7 µm, which corresponds to a maximum indentation depth of 15.7 µm. At this depth the plastic deformation zone formed around the indentation can affect the measurements because of underlying strengthening features that are not visible with the

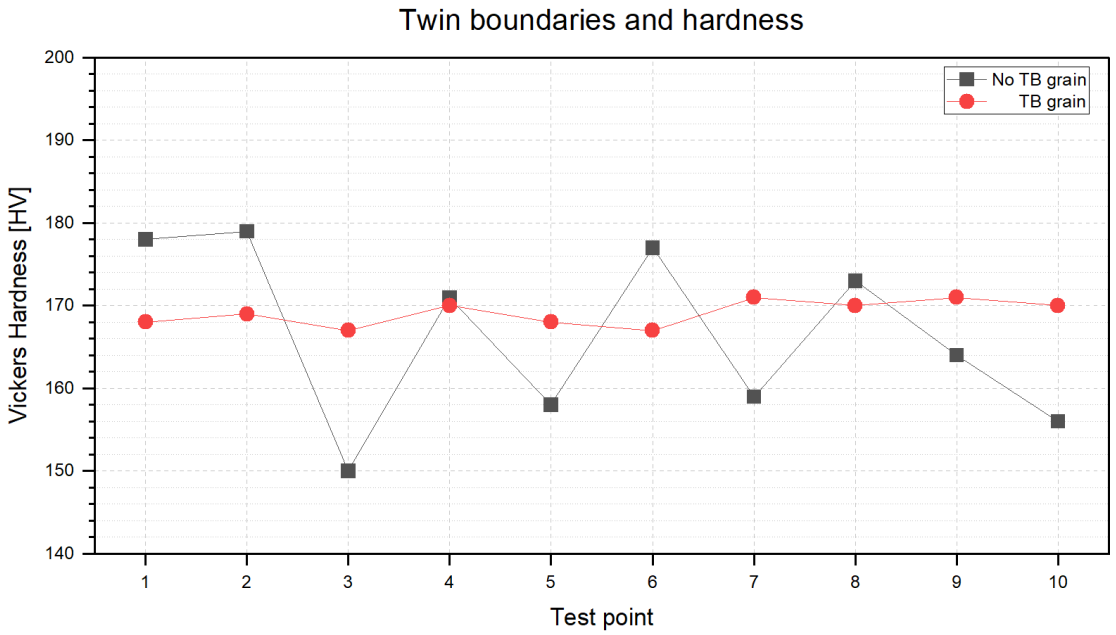

Fig. 10.35 Vickers hardness results for grains with- and without twin boundaries. Vickers indentation force HV0.5 was used.

microscope. When analysing specific microstructural features such as the relation between grain size and hardness values this can result in data scatter. Despite this potential result, scatter of the overall impact of the indentation depth is regarded as insignificant on the presented results due to the quantity of indentations made.

To sum up, the plots do indicate that grain growth contributes to the average reduction in micro-hardness values as grains become coarser over the course of thermal treatment. The relation between twin boundary density and hardness value deviations suggests an additional decrease in hardness as the density is observed to decrease significantly over thermal treatment time.

Nevertheless, a clear trend between thermal treatment time and micro-hardness values, and indirectly the yield strength, was not found. This is largely a result of the strong uncertainty related to the measurements, indicating many local deviations in hardness. Due to the limited size of precipitates in the microstructure no relation between hardness and precipitation was found in this study.

10.5 Mechanical performance of long-term HT samples at 650°C

Six samples have been conducted to long-term thermal treatment at 650°C for 744 h, 1,536 h and 2,232 h (1, 2 and 3 months respectively). The mechanical performance of these specimen was measured by instrumented Charpy including SFA and Vickers micro-hardness testing. Due to time limitations the microstructural evolution of these samples is not investigated, therefore only the mechanical performance graphs are presented in this section.

Because the microstructure was not studied for these specimens the inclusion fraction of the samples is unknown, therefore the presented uncertainty range only includes measurement errors and the standard deviation ($\pm 1\sigma$) of the measurements. In all the given graphs the orange line represents the 650°C thermal treatment samples. Figure 10.36 shows the Charpy impact results followed by the Shear Fracture Appearance measurements from the post-Charpy samples shown in figure 10.37. The instrumented Charpy measurements are used to calculate the dynamic yield and tensile strength, these results are given in figure 10.38. At last the Vickers hardness results are presented in figure 10.39. As seen in these figures somewhat similar behaviour is observed relative to the 800°C HT samples, with especially the instrumented Charpy results suggesting a similar embrittlement recovery. Due to the limited number of samples, both short-and long-term, further investigation is strongly recommended.

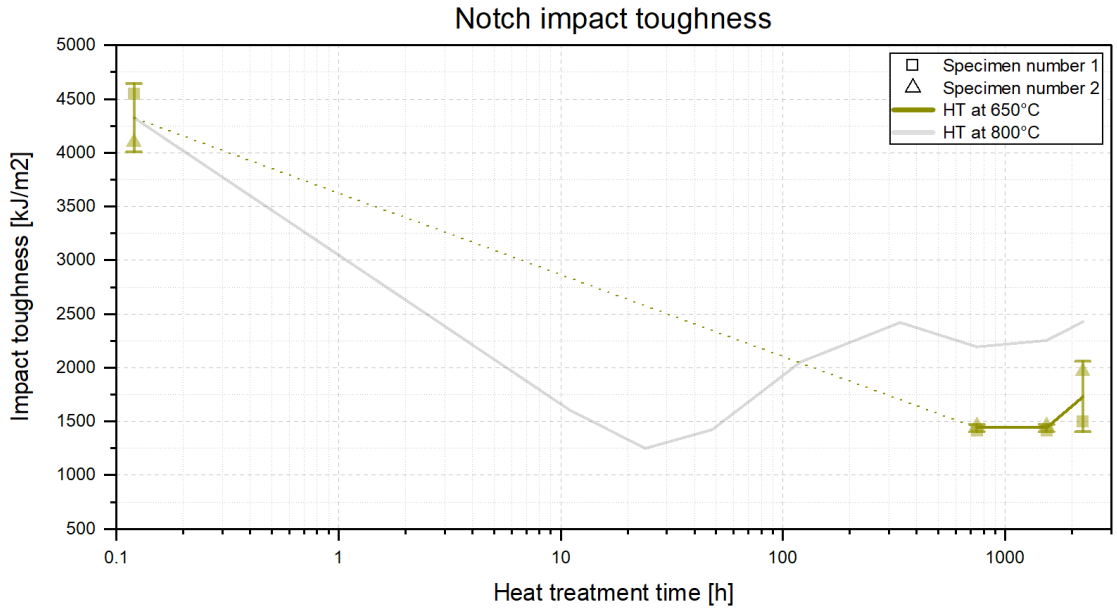

Fig. 10.36 Notch impact toughness as a function of thermal treatment time at 650°C.

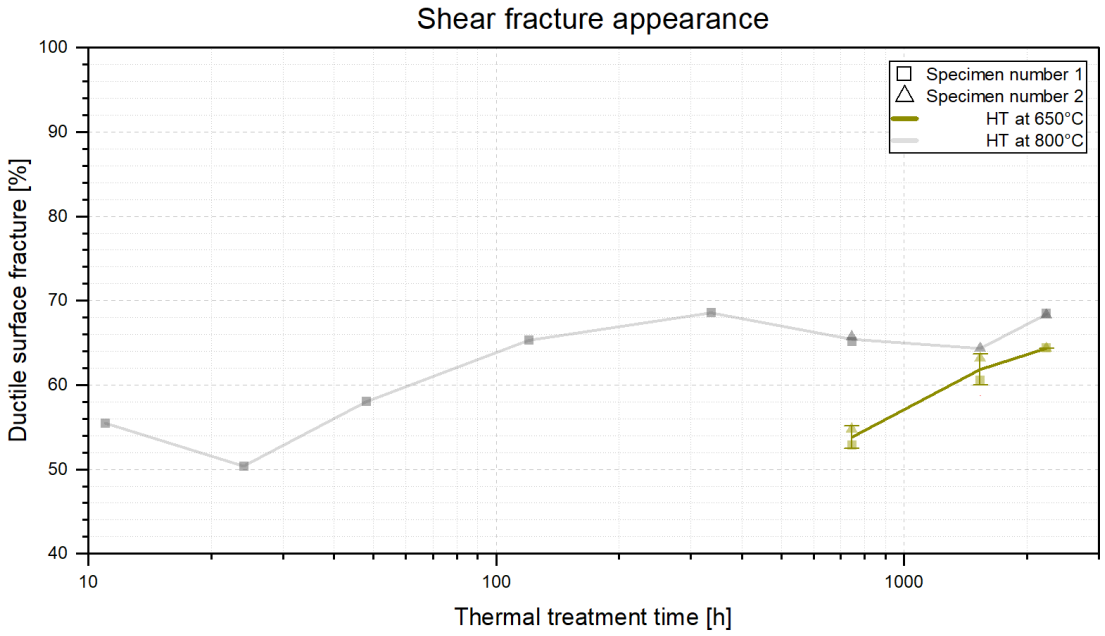

Fig. 10.37 Shear fracture appearance as a function of thermal treatment time at 650°C.

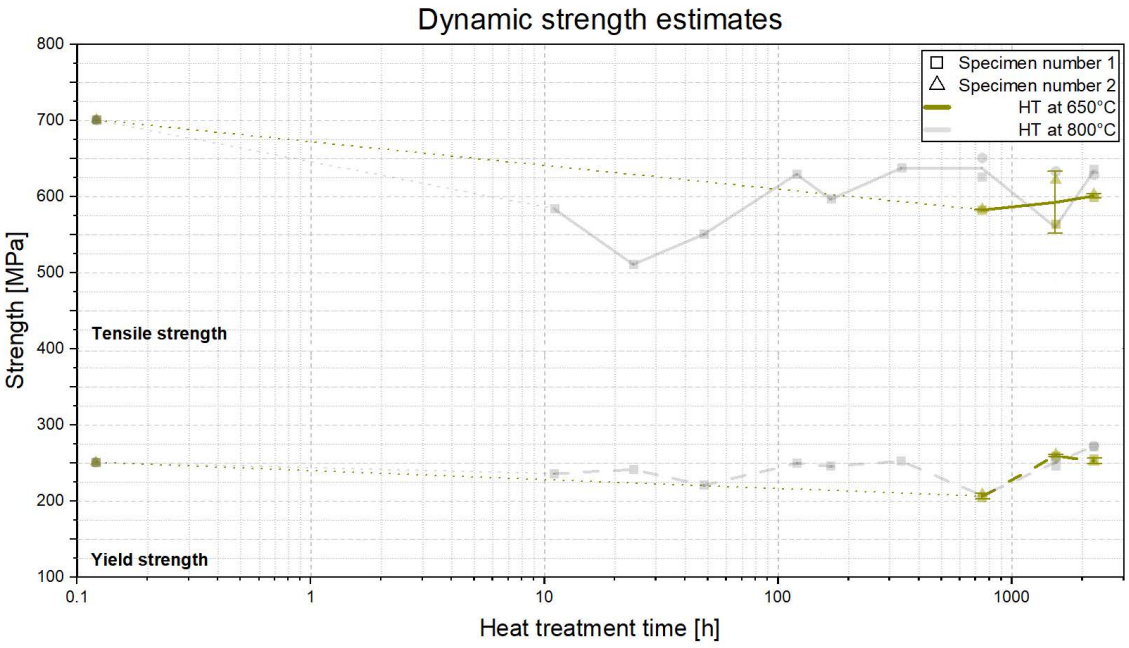

Fig. 10.38 Dynamic yield- and tensile strength estimates as a function of thermal treatment time at 650°C. The values are calculated from the instrumented Charpy test data.

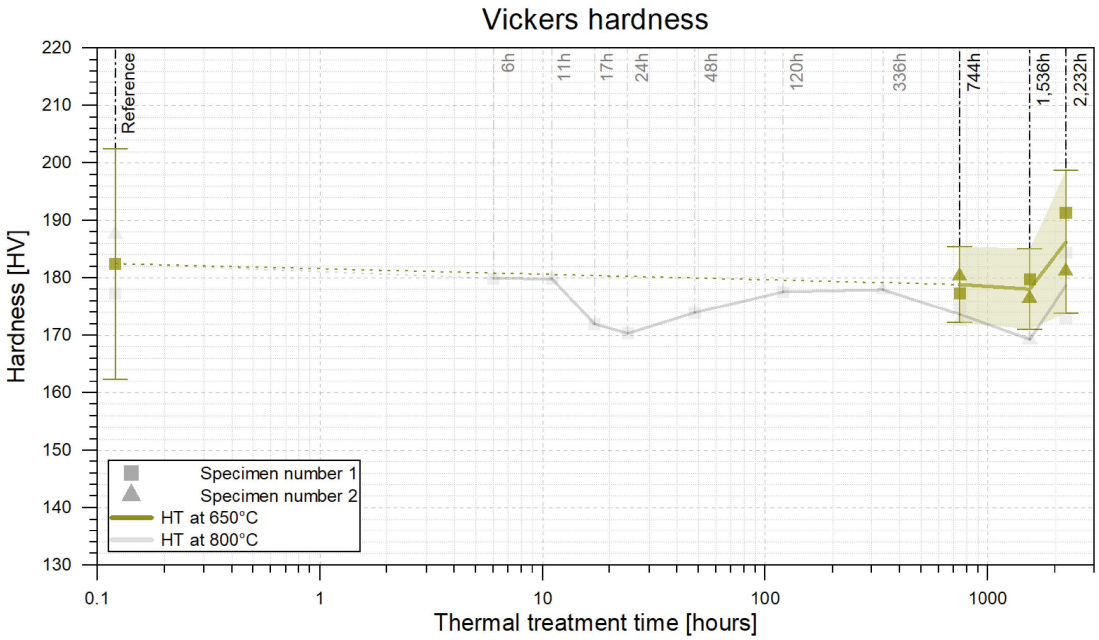

Fig. 10.39 Vickers hardness results as a function of thermal treatment time at 650°C. The average macro-hardness values are calculated from a set of 20 micro-indentations.

Chapter 11

Discussion

11.1 Inconsistencies Thermo-Calc, literature and observations

It is evident that there is a significant discrepancy between the computational thermodynamic results and the observed microstructure when simulation data from Thermo-Calc is combined with literature and microstructural observations. This is partially explained by the nature of the simulation, which computes a perfect thermodynamic equilibrium of a specific alloy at a given temperature, something that is not possible for a real alloy that has been thermally treated because diffusional processes take a long time before reaching their thermodynamic equilibrium, even without the interference of external influences. Thermo-Calc results, however, indicate a stable FCC Ni microstructure with a potentially very small fraction of carbides at 800°C. On the other hand, observations revealed that the microstructure of thermally treated MONICR did not contain any carbides, but rather a second-phase identified as Topologically Close-Packed (TCP), a phase that contains mainly Ni, Mo and Cr.

The initial observed MONICR microstructure is made up of the FCC Ni matrix (γ) combined with chromia and alumina inclusions, with a total volume fraction of about 0.06%, according to the SEM observations. After the first few hours of HT, molybdenum and chromium diffuse towards triple points and high-angle grain boundaries that are surrounded by primarily small grains. The second-phase precipitate nucleates and develops into an incoherent plate-like precipitate. Over time a large share of the grain boundaries are decorated by the TCP-phase as a result of the precipitates' tendency to grow on GBs. These precipitates have a width of 1-2 μm and a length of about 20 μm (along GB) after two-to-three months of thermal treatment at which the growth rate indicates stabilisation.

It is anticipated that the TCP precipitates, that were identified as NiMo by EBSD measurements, are a combination of the P-phase and NiMo because a high concentration of chromium was found in the precipitates. Both phases have an ordered orthorhombic phase with 56 atoms per unit cell and are part of the TCP crystal structure family. Their axial ratio and sub-lattice sites are the primary distinctions between the phases. While in the P-phase Ni, Mo, and Cr can occupy any of the sites, in NiMo specific sites are strictly occupied by Mo and Ni atoms [45]. This results in the P-phase being

energetically advantageous when chromium concentration is high.

It would be logical to assume that the thermodynamic simulation computes the stable presence of the phase given the relatively high fraction of TCP precipitation observed. However, due to some limitations of Thermo-Calc, and also other thermodynamic simulation tools, this is not the case. Nagashima *et al.* [45] state that commercially available databases for thermodynamic calculations of Ni-based alloys (including the used TTNI6 database) do not always simulate complex TCP phases correctly, in particular for Ni-Cr-Mo alloys. As a result, the stability of the TCP phase is not considered in these calculations, leading to the exclusion of these phases in the produced quasi-thermodynamic diagrams.

A study on the effect of TCP formation and its effect in nickel-based superalloys by Wilson [13] concluded similar problems surrounding the inaccurate results for TCP phase formation in these thermodynamic models, indicating that problems arise from incomplete databases as well as insufficient mathematical thermodynamic models used in these tools. Therefore, additional efforts are required to update the databases and thermodynamic models need to be adjusted.

11.2 Embrittlement

The mechanical behaviour of the material as a function of thermal treatment time was measured by instrumented Charpy, SFA and hardness testing and resulted in the characterisation of the dynamic yield and tensile strength, notch impact toughness, ductile fracture percentage and hardness. Of these values all but hardness and yield strength showed a similar trend during thermal treatment, hence substantiating the embrittlement trend.

Different measurements, observations, and findings are compared in order to understand the relationship between microstructural evolution and the observed mechanical-behaviour changes. The discussion of these connections is divided into three sections following the mechanical behaviour shift observed in MONICR during thermal treatment at 800°C. These sections discuss the observed embrittlement: (1.) decrease, (2.) recovery and (3.) stabilisation.

(1.) Embrittlement decrease

The first 24 hours of thermal treatment are characterised by a drastic decrease in toughness, as both the hardening ability (reflected in the difference between yield and tensile strength - work hardening) and ductility decline. The examined post-Charpy fracture surface of the 24h HT specimen showed a brittle fracture surface of 50%, a significant decrease from the fully ductile fracture of the reference sample. The changes in mechanical performance will be discussed following the two major microstructural processes in the material during the first 24 hours of thermal treatment, namely precipitation and grain growth combined with HAGB annihilation.

Precipitation Already in the first hours of thermal treatment at 800°C the alloy forms brittle TCP precipitates with a plate-like geometry. Between 11 hours and 24 hours these precipitates are primarily characterised by their small size of approximately 2 μm by 0.5 μm, their jagged tips and their nucleation location exclusively along high-angle grain boundaries, preferably surrounded by relatively small grains. After 24 hours of thermal treatment approximately 60 precipitates per mm^2 are observed, decorating most of the grain boundaries with small precipitates.

Formation of these precipitates indicate depletion of primarily molybdenum and chromium from the matrix because the measured chemical composition of the TCP phase revealed a Mo and Cr fraction three times that of the matrix. As a consequence this depletion reduces the concentration of solid solution strengtheners present in the matrix, hence reducing the material's strength. However, no significant trend in yield strength was observed and therefore the effects of the current amount depletion are seen as minimal. Nevertheless, further depletion of these strengtheners can potentially influence the tensile strength of the alloy.

From literature it is known that the formation of the TCP phase is detrimental to the mechanical performance of Ni-based alloys because of its brittleness and, in many cases, crack-inducing geometry. Due to their prevalent presence on grain boundaries, which already house many small oxide inclusions, the precipitates can form a so-called fracture chain along the GBs, hence reducing the toughness of the material drastically. This fracture behaviour is primarily driven by the high stress pile-ups around the sharp tips of the precipitates, consequently initiating cracks. When combined with a high density of brittle particles along the GBs these cracks can easily propagate and form a brittle fracture surface.

Grain growth and HAGB annihilation Next to precipitation, grain growth is observed in the material during the first 24 hours of HT. The average grain size increases and consequently the density of high-angle grain boundaries and twin boundaries decreases during this process, approximately a boundary-density decrease of 30%. This microstructural change is expected to increase dislocation hardening, consequently increasing the material's work hardening ability during deformation. This behavioural change, however, is not reflected in the yield strength and hardness trends as especially yield strength seems to be stable. Therefore the effect of grain growth combined with HAGB annihilation is assumed to relate with plastic deformation mechanisms.

Although this mechanism would increase the tensile strength a sharp decrease is measured. For that reason it is expected that precipitation of the detrimental TCP phase dominates the plastic deformation behaviour changes in the first 24 hours of thermal treatment by reducing the materials ductility.

(2.) Embrittlement recovery

After the first 24 hours of thermal treatment the alloy seems to recover from its loss in toughness in the following 312 HT hours (13 days). When comparing the toughness, tensile strength and fracture appearance results, two trends are observed. The first is a significant increase in ultimate

tensile strength between 24-to-120 HT hours that is also observed in all trend curves. Second is the deformation mechanism shift from primarily brittle fracture towards more ductile behaviour. This trend is observed in the HT period between 24 hours up to 336 hours. Due to this distinction the recovery mechanism can be split into two processes, namely the recovery in ductility and that of hardening.

Ductility recovery The recovery in ductility, as clearly seen in the SFA and toughness results, continues for aging periods up to approximately 336 hours (2 weeks). This period is associated with the growth of TCP precipitates in length and width. During the growth process many precipitate tips change geometry as the precipitate widens, replacing their initial jagged shape by a more globular (spherical/rounded) shape. This transformation is qualitatively observed at most precipitates and is able to explain the increased ductility during this microstructural evolution. The transformation in TCP precipitate tip geometry reduces the deformation-induced stress concentrations around these tips, consequently increasing the required stresses for crack initiation and propagation.

Hardening As discussed before, grain growth induced the decrease in density of high-angle grain boundaries and twin boundaries. With this microstructural process being most notable in the recovery period it is expected that it directly alters the strength of the material by influencing the work hardening ability. After approximately 48 hours of thermal treatment the observed grain growth rate, and related boundary annihilation, indicates a period of stability.

During grain growth two major processes influence the deformation mechanisms, namely the reduction in the density of high-angle grain boundaries and twin boundaries. Primarily the reduction in twin boundary density increases the strain hardening ability of the material during plastic deformation due to the decrease in dislocation slip barriers within the grain interior. Combined with the increased ductility the material's ability to allow for more dislocation hardening becomes more noticeable as the fracture toughness of the material is increased.

(3.) Embrittlement stabilisation

After two weeks of aging at 800°C the measured mechanical properties seem to be constant, indicating a period of microstructural stability. Despite this logical relation with stability, evolution of the microstructure is still observed in this period. Grain growth and the related density reduction of high-angle grain boundaries and twins is assumed to be stable because both trends indicated a significant reduction in growth and annihilation rate in the recovery period, suggesting stabilisation of these processes.

Precipitation on the other hand, does show signs of further microstructural evolution. Qualitative observations indicate an increase in precipitates along grain boundaries, combined with further coarsening. Both processes suggest a relation with the reduction and even stabilisation of grain growth, as the presence of incoherent precipitates, specifically at grain boundaries, can reduce GB migration by

pinning. This processes, also referred to as *Zener pinning*, restrict movement of grain boundaries at the particle-grain interface and thus restrain grain growth.

The increasing volume fraction of the TCP-phase observed during continued aging does not seem to influence the mechanical behaviour of the material any further. While this precipitate growth model based on diffusion rate predicts limited growth, additional increases cannot be excluded from long-term material employment in an MSR environment. An increase in the TCP phase could potentially lead to significant depletion of solid solution strengtheners in the matrix, consequently lowering its strength, while further decoration of grain boundaries with the phase can further influence intergranular deformation behaviour. For that reason microstructural and mechanical investigation of extended thermal treatment at 800°C is strongly recommended. The reduction in solid solution strengtheners in the current observations indicate an insignificant effect on the tensile strength.

11.3 Expected behaviour for continued thermal treatment

The current samples have been tested and investigated up to 2,232 hours, 3 months, of thermal treatment. Yet, components used in a generation IV MSR require an operational lifetime of more than 50 years at 700-750°C (MSR core vessel temperature), meaning microstructural and mechanical stability for approximately 400,000 hours is required.

Following the discussion in section 11.2 microstructural stability regarding grain growth and twin boundary density is assumed after the observed embrittlement recovery period. Nevertheless, precipitate coarsening is expected for continued aging. For that reason the estimated growth model for Mo-rich precipitation growth is extended to 400,000 hours. The resulting graph, given in figure 11.1, shows the molybdenum fraction of the measured TCP-phase (approximately, 42wt% Mo) and the simulated chemical composition fraction of molybdenum in NiMo (approximately, 40wt% Mo) and the P-phase (approximately, 50wt% Mo).

The qualitatively observed size of the precipitates was assumed to be approximately 15-20 µm (diameter) in the 2,232 hour HT sample. When comparing this size with the estimated size at 50 years of thermal treatment at 800°C this would mean a 10-fold increase. However, due to the limitations and simplicity of the mathematical diffusion model this behaviour is not expected. The current model excludes important factors that could reduce precipitation growth significantly when size increases, these factors include depletion of alloying elements, precipitate interaction, effects of interfacial energy, morphology and many more.

Nevertheless, further growth to some extent is expected in the material during continued aging. Primarily the depletion of important solid solution strengtheners molybdenum and chromium is expected to reduce the strength and creep resistance of the material. Further investigation of thermally treated MONICR at 800°C for longer periods is required to characterise continued microstructural evoluiton, depletion processes and extensive precipitation.

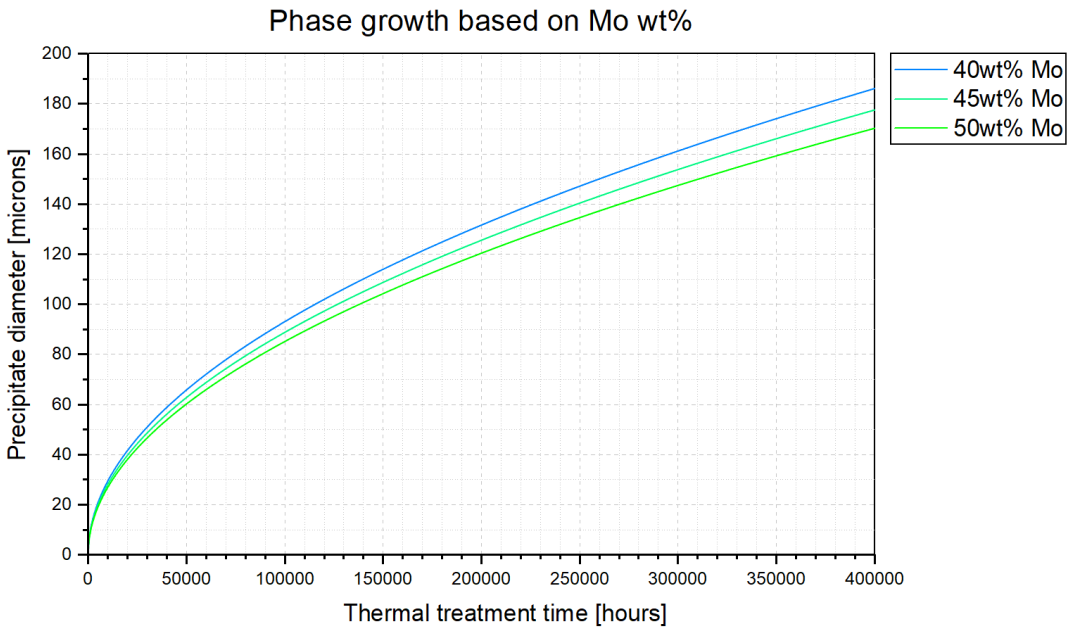

Fig. 11.1 Estimated Mo-rich volume growth as a function of thermal treatment time.

11.4 Expected behaviour during irradiation

Precipitation of the TCP-phase is observed to be detrimental to the mechanical performance of the material. After continued thermal treatment some of the toughness is restored but the alloy does not return to its as-received toughness. As discussed, multiple microstructural changes are likely related to these changes in mechanical behaviour, and for that reason the expected behaviour of the alloy during irradiation will be discussed. The discussion focuses on the likely mechanisms that are enhanced by thermal exposure.

Of the different irradiation degradation mechanisms two are seen as the most likely processes to further embrittlement of MONICR at MSR reactor conditions. These are recoil dissolution of precipitates and enhanced helium bubble formation. At last irradiation-enhanced diffusivity will be discussed.

Recoil dissolution The formation of plate-like TCP precipitates with jagged tips is suggested as the dominant contributor to MONICR embrittlement at elevated temperatures. Yet, when the material is exposed to a temperature of 800°C, and likely at MSR temperatures (700-750°C), precipitate growth is observed. This growth is accompanied by a transformation in the precipitate geometry, as a large share of the tips become more globular, hence restoring some ductility.

Nevertheless, when the material is irradiated displacement cascades can result in recoil dissolution. During this process a part of the precipitate is affected by the cascade, knocking many atoms out of

the precipitate volume. Following this cascade the size of the precipitate is reduced, in other words refining the particle. Therefore, the process can have a detrimental effect on the microstructure as it potentially reduces the ductility recovery mechanism observed in long-term HT samples. As a consequence, permanently reducing the ductility, and thus toughness, of the material.

Enhanced helium bubble formation Second the presence of precipitates along the grain boundaries can enhance the formation of voids and helium bubbles in the irradiated material. It is known that in particular incoherent precipitates attract a flux of point defects, so when these precipitates are close to a helium bubble this process can accelerate growth of helium bubbles, and to a lesser extent voids.

When these formed bubbles grow and become more stable along grain boundaries further embrittlement is expected as the newly formed bubbles can act as an additional crack initiation and propagation site. At this point the grain boundaries house oxide inclusions, detrimental TCP precipitates and bubbles that can form an interlinked brittle fracture chain.

Irradiation-enhanced diffusivity As discussed in section 8.4.3 irradiation can induce diffusivity due to the high vacancy concentration resulting from displacement-cascades. This additional atomic flux can significantly increase the diffusivity of alloying elements through the Ni matrix. When diffusion rates in the grain interior further increase the growth rate of Mo-rich precipitates such as the TCP-phase found along grain boundaries can also increase.

Enhancing the growth rate of the precipitates likely results in a rapid precipitate globular-transformation, hence increasing ductility at an accelerated rate after the embrittlement decrease. Nevertheless this process can also drastically increase the precipitate density in the system, potentially generating more fracture planes throughout the microstructure. Another consequence of increased diffusivity is further depletion of alloying elements from the matrix, reducing the density of solid solution strengtheners and thus lowering the strength of the matrix.

All by all, the effects of irradiation-enhanced diffusivity can further degrade the mechanical performance of the material, yet it can also shorten the embrittlement decrease period observed in MONICR.

11.5 Expected behaviour during HT at 650°C

A variety of tests, including Charpy, Vickers hardness, XRD, and SFA measurements, were carried out to analyse the mechanisms of degradation at a temperature of 650°C. As discussed in section 8.1 the ENICKMA project investigates the microstructural and mechanical behaviour of some selected alloys during irradiation at temperatures ranging from 650°C to 750°C, with most irradiation samples being subjected to the lower temperature limit. Six long-term thermally treated specimen at 650° (1,2 and 3 months) have been tested to further investigate the behaviour of MONICR under these elevated temperature conditions to support the ENICKMA project at NRG.

The results show similar mechanical behaviour changes to those seen in thermally treated specimens at 800°C, but at a lower rate. If similar microstructural mechanisms occur, then lower HAGB migration rates and lower diffusivity can account for the delay. Overall, similar microstructural processes are expected to play a significant role at MSR environment temperatures of 650°C, as embrittlement problems do not appear to be limited to 800°C. However, due to the small number of samples studied and the lack of microstructural analysis, these claims cannot be supported. Further research into the behaviour of MONICR at 650°C thermal treatment temperatures is therefore strongly advised. More detailed discussions on the long-term behaviour of the alloy at MSR temperatures can be made as more research is conducted.

Precipitation, similar to the 800°C samples, is expected to govern the microstructural evolution and mechanical behaviour changes during long-term thermal exposure. At a temperature of 650°C the solubility of the matrix is expected to be significantly lower than at 800°C, resulting in the likely stability of other second-phases, as seen in the quasi-phase diagram presented in figure 10.11. Yet, as discussed in section 11.1 the ThermoCalc results exclude the TCP phases that are observed to precipitate, as new thermodynamic models and an updated database are required to simulate a more accurate quasi-phase diagram of the system. Other TCP phases that are observed in Ni-Cr-Mo alloys are therefore potentially stable at a thermal treatment temperature of 650°, phases such as σ and μ could therefore form.

Based on the observations of 800°C samples the geometry of the precipitates suggest a significant role in the embrittlement of MONICR. When other second phases are preferred over NiMo or the P-phase this could potentially mean a change in precipitate geometry. Observations discussed by Wilson [13] state that intergranular precipitation of the σ-phase is known to promote transgranular fracture rather than intergranular fracture, hence changing the expected impact behaviour of the alloy. The formation of μ could also affect the expected behaviour of the material significantly as the phase is observed to precipitate along grain boundaries as needle-like volumes in some alloys, embrittling the material extensively. While in other alloys the phase precipitates with a more globular (rounded) and block-like morphology that is observed to have an insignificant effect on the tensile ductility of the material [13; 14].

At last it is important to discuss the diffusivity of molybdenum at 650°C as this could have a significant effect on the morphology of the precipitates. Figure 11.2 shows the estimated precipitate diameter based on its molybdenum fraction following the same model as discussed in section 10.2.1. Note, the diffusion rate of Mo through Ni used is based on a model that is proven for temperatures between 800-to-1200 °C, the following results are therefore seen as a rough estimate. Relative to the 800°C model the precipitate growth rate is significantly lower, as phases with an average TCP Mo fraction of 50wt% have an estimated diameter between 1 μm and 3 μm after three months of heat-treatment for grain interior and GB diffusion respectively. When compared to the observations of the 800°C samples this could indicate a higher fraction of jagged precipitates that are seen as detrimental for the mechanical properties of MONICR as they embrittle the material significantly.

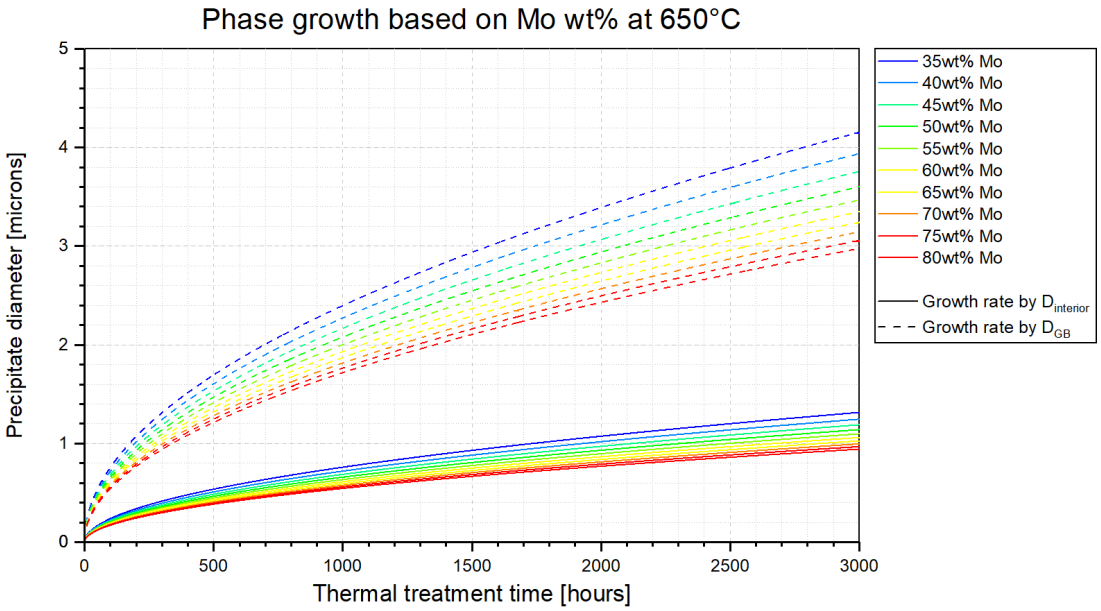

Fig. 11.2 Estimated Mo-rich volume growth as a function of thermal treatment time at 650°C.

Chapter 12

Conclusions and recommendations

12.1 Conclusions

The purpose of this research was to look into the microstructural and mechanical mechanisms of the MONICR (Mo-Ni-Cr) alloy at elevated Molten Salt Reactor (MSR) temperatures. A series of samples were thermally treated for a variety of hours at a thermal treatment temperature of 800°C. They were then investigated to determine the material's microstructural evolution and mechanical performance. Data from mechanical tests were compared to microstructural features characterised during SEM microscopy to correlate mechanical behaviour changes with microstructural evolution. These observations and findings lead to several conclusions regarding the main research focus of this thesis: the alloy's embrittlement problem under short-to-long thermal treatment. The conclusions are listed below:

(i.) During thermal treatment the detrimental Topologically Close-Packed (TCP)-phase forms as incoherent precipitates along high-angle grain boundaries. Due to their jagged morphology they promote intergranular fracture.

(ii.) Coarsening of the TCP-precipitates during continued thermal treatment tends to transform jagged tips to more rounded (globular) shapes, hence reducing the build-up of stress and consequently crack initiation/propagation.

(iii.) The presence of intergranular precipitates reduces grain growth and twin boundary annihilation by Zener pinning, consequently promoting microstructural stability.

(iv.) Reduction in the density of twin boundaries has a beneficial effect on the toughness of the material by allowing more strain hardening during deformation.

(v.) Oxide inclusions present from manufacturing, while stable during thermal treatment, promote brittle fracture.

12.2 Recommendations

This thesis contributes to the understanding of Ni-based alloys in MSR-like high temperature environments. Resulting from this research, several future studies are proposed to further promote the microstructural and mechanical characterisation of Ni-based alloys under these unique conditions. These suggestions could aid in the development of the Molten Salt Reactor while also investigating new innovative uses for the material. The following recommendations are proposed:

- Several samples were subjected to long-term heat treatment at 650°C in order to evaluate their mechanical behaviour. The data from these tests, as shown in figures 10.36-10.39, indicate that a similar performance evolution as at 800°C occurred somewhere during the first month of thermal treatment. Therefore, additional research into the mechanical behaviour and microstructural evolution of both short- and long-term HT samples at 650°C is proposed. The resulting data can be compared to the 800°C HT results to evaluate the microstructural changes and features, providing a more complete understanding of MONICR evolution at MSR temperatures.

- The limited operational lifetime of MSR materials as a result of mechanical deterioration is one of their major problems. Because of this, it is crucial to research how the material behaves and remains stable over even longer HT periods. This data can be combined with results from 650°C HT studies and extrapolated, so further characterisation at 800°C HT is proposed to refine the findings of this study.

- The inclusion distribution study included in this research made it clear that the processing procedure for MONICR components needs to be improved in order to guarantee highly homogeneous material quality. As a result, it is advised that the study concentrate on the distribution and origin of oxide (alumina and chromia) inclusions in the material.

- One of the most influential mechanisms observed in the HT MONICR specimen is precipitation. As a result, more research into the formation, geometry evolution and kinetics of these precipitates is suggested. An extensive EPMA study is proposed to understand the coarsening of the second phase. Transmission Electron Microscopy (TEM) combined with Atom Probe Tomography can be used to further characterise the phase and its crystallographic structure.

- Following the high fraction of brittle fracture in the HT material, further research into the material's fracture mechanics is suggested, emphasising the effect of grain boundary precipitation and preferred rupture surfaces. The significance of this research arises from the potential increased rate of helium bubble formation, consequently increased embrittlement, caused by incoherent precipitate defect trapping.

- The formation of some TCP-phase, as mentioned by Geddes *et al.* [10], Belan [12] and Nagashima *et al.* [45], may improve the material's creep-rupture strength. Therefore, it is suggested that more research be done on *grain boundary precipitation strengthening*.

- Smaller and larger grains seem to aggregate with grains of a similar size, according to both the EBSD mapping and the BEI images, which point to a potential preferred grain-size clustering. Further EBSD investigation into this potential phenomenon is advised because such preferred clustering combined with grain-boundary precipitation may have an impact on local and intergranular fracture behaviour.

References

1. Merle, E. *Concept of Molten Salt Fast Reactor* https://www.gen-4.org/gif/upload/docs/application/pdf/2017-05/07_elsa_merle_france.pdf.
2. European Atomic Energy Community (Euratom). *Final Report EVOL project* tech. rep. (European Atomic Energy Community, 2015). http://www.gen-.
3. Dolan, T. J. *Molten salt reactors and thorium energy* ISBN: 978-0-08-101126-3 (Woodhead Publishing, 2017).
4. NRG. *Molten Salt Reactor Research Program* https://www.ensuringnuclearperformance.com/en/nuclear-innovation/msr-research-program (2021).
5. Turchi, P. E., Kaufman, L. & Liu, Z. K. Modeling of Ni-Cr-Mo based alloys: Part I-phase stability. *Calphad: Computer Coupling of Phase Diagrams and Thermochemistry* **30,** 70–87. ISSN: 03645916 (Mar. 2006).
6. Naziris, F. *ENICKMA Reference Tensile Tests Pre-PIE characterization* tech. rep. (2022).
7. Guo, S., Zhang, J., Wu, W. & Zhou, W. Corrosion in the molten fluoride and chloride salts and materials development for nuclear applications. *Progress in Materials Science* **97,** 448–487. ISSN: 0079-6425. https://www.sciencedirect.com/science/article/pii/S0079642518300537 (2018).
8. Haynes International. *Alloy portfolio* https://haynesintl.com/alloys/alloy-portfolio_ (2022).
9. Wright, R. N. & Sham, T.-L. *Status of Metallic Structural Materials for Molten Salt Reactors* https://doi.org/10.2172/1467482 (Office of Scientific and Technical Information (OSTI), May 2018).
10. Geddes, B., Leon, H. & Huang, X. *Superalloys alloying and performance - Chapter 4: Phases and Microstructure of Superalloys* 25–57. ISBN: 978-1-62708-313-3 (2010).
11. Zhang, C., Zhang, L., Cui, Y., Feng, Q. & Cheng, C. Effects of High-Temperature Aging on Precipitation and Corrosion Behavior of a Ni-Cr-Mo-Based Hastelloy C276 Superalloy. *Journal of Materials Engineering and Performance* **29,** 2026–2034. ISSN: 15441024 (Mar. 2020).
12. Belan, J. *GCP and TCP Phases Presented in Nickel-base Superalloys* in *Materials Today: Proceedings* **3** (Elsevier Ltd, 2016), 936–941.

13. Wilson, A. Formation and effect of topologically close-packed phases in nickel-base superalloys. *Materials Science and Technology* **33,** 1108–1118 (2017).

14. Sun, F. & Zhang, J. *Topologically close-packed phase precipitation in Ni-based superalloys* in *Advanced Materials Research* **320** (2011), 26–32. ISBN: 9783037852118.

15. Liu, G., Zhang, X., Wang, X. & Qiao, Y. Precipitation behaviour of TPC in the DD5 superalloy during long-term HT aging. *Scanning* **2020.** https://doi.org/10.1155/2020/2569837 (2020).

16. Jin, Y. *et al.* Evolution of the annealing twin density during δ-Supersolvus grain growth in the nickel-based superalloy Inconel™ 718. *Metals* **6.** ISSN: 20754701 (Dec. 2015).

17. Manoharan, M., Natarajan, A. & Muktinutalapati, N. R. in *Superalloys* (InTech, Nov. 2015).

18. Gehlbach, R. E. & McCoy, H. E. Phase Instability in Hastelloy N. *Superalloys,* 348–366. https://doi.org/10.7449/1968%2FSUPERALLOYS_1968_346_366 (1968).

19. Was, G. S. *Fundamentals of radiation materials science: Metals and alloys* 2nd, 1–1002. ISBN: 9781493934386 (Springer New York, Jan. 2016).

20. Santofimia, M. & Sietsma, J. *Microstructure Control in Metals* ISBN: 978-94-640-3815-6 (Delft University of technology, 2020).

21. Gottstein, G. *Physical Foundations of Materials Science* (Springer Berlin Heidelberg, 2004).

22. *Structural Materials for Generation IV Nuclear Reactors* (ed Yvon, P.) 409. ISBN: 9781845699673 (Woodhead Publishing, 2017).

23. Royce, B. *Plastic deformation* https://www.princeton.edu/~maelabs/mae324/07/07mae_57.htm (2021).

24. Jeyaraam, R., Subramanya Sarma, V. & Vedantam, S. Phase field modelling of annealing twin formation, evolution and interactions during grain growth. *Computational Materials Science* **182,** 109787. ISSN: 0927-0256. https://www.sciencedirect.com/science/article/pii/S0927025620302780 (2020).

25. Grube, W. L. & Rouze, S. R. The Origin, Growth and Annihilation of Annealing Twins in Austenite. *Canadian Metallurgical Quarterly* **2,** 31–52. eprint: https://doi.org/10.1179/cmq.1963.2.1.31. https://doi.org/10.1179/cmq.1963.2.1.31 (1963).

26. Gao, Y. *et al.* Effect of twin boundaries on the microstructure and mechanical properties of Inconel 625 alloy. *Materials Science and Engineering A* **767.** ISSN: 09215093 (Nov. 2019).

27. Gladyshev, G. *Radiation Processes in Crystal Solid Solutions* tech. rep. (St. Petersburg State Technological Institute, St. Petersburg, 2012). http://ebookcentral.proquest.com','_blank'.

28. Knief, R. A. *Nuclear Engineering - Theory and Technology of Commercial Nuclear Power* 2nd ed. ISBN: 978-0-89448-458-2. https://app.knovel.com/hotlink/toc/id:kpNETTCNP1/nuclear-engineering-theory/nuclear-engineering-theory (ANS (American Nuclear Society), 2014).

29. Nordlund, K. *et al. Primary radiation damage: A review of current understanding and models* Dec. 2018.

30. Kirk, M. A. & Blewitt, T. H. Atomic Rearrangements in Ordered fcc Alloys During Neutron Irradiation. *Metallurgical and Materials Transactions A* **9A,** 1729–1737. ISSN: 0360-2133 (1978).

31. Ivanov, L. & Platov, Y. *Radiation Physics of Metals and its Applications* ISBN: 1-898326-8-35 (Cambridge International Science Publishing, 2004).

32. Janssen, M., Zuidema, J. & Wanhill, R. *Fracture Mechanics* ISBN: 90-407-2221-8. https://www.vssd.nl/hlf/m004.htm (VSSD, Delft, the Netherlands, 2004).

33. Royal Netherlands Standardization Institute. *Metallic materials - Charpy pendulum impact test - Part 1: Test method (ISO 148-1:2016,IDT)* en. Standard ISO 148-1:2016,IDT (Delft, the Netherlands, 2017).

34. *MTS Exceed E22 Series Pendulum Impact Test Systems for Metals* 100-308-285b ExceedE22Impact. MTS Systems Corporation (2018).

35. Royal Netherlands Standardization Institute. *Metallic materials - Vickers hardness test - Part 1: Test method (ISO 6507-1:2018,IDT)* en. Standard ISO 6507-1:2018,IDT (Delft, the Netherlands, 2017).

36. Chauhan, A. *Deformation and damage mechanisms of ODS steels under high-temperature cyclic loading* PhD thesis (Feb. 2018).

37. The California State University. *Scanning electron microscopy (SEM)* https://chem.libretexts.org/Courses/Franklin_and_Marshall_College/Introduction_to_Materials_Characterization__CHM_412_Collaborative_Text/Electron_and_Probe_Microscopy/Scanning_electron_microscopy_(SEM) (2022).

38. Raja, P. M. V. & Barron, A. R. *An Introduction to Energy Dispersive X-ray Spectroscopy* https://chem.libretexts.org/Bookshelves/Analytical_Chemistry/Physical_Methods_in_Chemistry_and_Nano_Science_(Barron)/01%5C%3A_Elemental_Analysis/1.12%5C%3A_An_Introduction_to_Energy_Dispersive_X-ray_Spectroscopy (2022).

39. Australian National University. *Electronic Backscatter Diffraction mapping* https://microscopy.anu.edu.au/highlights/electronic-backscatter-diffraction-mapping (2022).

40. Anton Paar. *X-Ray diffraction (XRD)* https://wiki.anton-paar.com/en/x-ray-diffraction-xrd/ (2022).

41. Cunningham, N. *Dynamic and Static Yield Stress* http://www.rheologyschool.com/advice/rheology-tips/29-dynamic-and-static-yield-stress (2022).

42. Lucon, E. Estimating dynamic ultimate tensile strength from instrumented Charpy data. *Materials and Design* **97,** 437–443. ISSN: 18734197 (May 2016).

43. Cronjé, S., Kroon, R., Roos, W. & Neethling, J. Twinning in copper deformed at high strain rates. *Bulletin of Materials Science* **36** (Feb. 2013).

44. Divya, V., Balam, S., Ramamurty, U. & Paul, A. Interdiffusion in the Ni–Mo system. *Scripta Materialia* **62,** 621–624 (Jan. 2010).

45. Nagashima, R., Yamagata R., Nakashima, H. & Takeyama, M. *Phase Equilibria Among A1/TCP/GCP Phases and Microstructure Formation in Ni-Cr-Mo System at Elevated Temperatures* in *Superalloys 2020* (eds Tin, S. *et al.*) (Springer International Publishing, Cham, 2020), 131–141. ISBN: 978-3-030-51833-2. https://link.springer.com/10.1007/978-3-030-51834-9.

46. Ashby, M. F., Shercliff, H. & Cebon, D. *Materials engineering, science, processing and Design* (Butterworth-Heinemann, 2007).

47. Yasnikov, I. S., Kaneko, Y., Uchida, M. & Vinogradov, A. The grain size effect on strain hardening and necking instability revisited from the dislocation density evolution approach. *Materials Science and Engineering A* **831.** ISSN: 09215093 (Jan. 2022).

Appendix A

A.1 Additional background information chapter 8

A.1.1 Diffusion

In a crystal system atoms are constantly moving around because of thermal vibrations, allowing movement throughout the bulk material. This means that even when a material is in equilibrium the atoms still move around. This type of diffusion is referred to as *self-diffusion* and does not alters the microstructure, in this situation there is no chemical potential gradient[1] [1, ch. 3.1]. In a real crystal most systems are not directly in chemical equilibrium due to the presence of external chemical potentials. These potentials can be a result of gravity, elastic fields, electrostatic interactions and many more potential force fields. Therefore, when this external chemical potential is added to the internal chemical potential (microstructure, temperature, etc) the total driving force for change is obtained. In many cases this results in atomic movement referred to as flux (J [#atoms/m^2s]), in its turn changing the microstructure [2, ch. 5.1].

An example of such a gradient can be a high local concentration of vacancies. In combination with the thermal vibrations these defects are able to diffuse, as atoms move towards the less dense (vacancy rich) area, while at the more concentrated area vacancies are created, thus smoothing the vacancy concentration over the system. This vacancy/atom diffusion is referred to as the *vacancy mechanism* and is the main diffusion mechanisms through the bulk[2]. Interstitial atoms have two ways of moving around the lattice, first being by the *interstitialcy mechanism* that describes the interstitial atom movement over vacant interstitial sites. As this process requires a significant energy it is mainly done by smaller interstitial atoms. Second is the *dumbbell interstitial mechanism*, a process that moves interstitial atoms towards a vacant lattice site, allowing the atoms to share the position, thus lowering the overall energy. It must be noted, that the mobility of interstitials is significantly higher compared to that of vacancies due to the available diffusion 'paths' [3, ch. 4.2; 2, ch. 5].

[1] The chemical potential (μ [J/atom]) is a quantity used in diffusivity and transformations to describe the tendency of matter to change its configuration [1, pp. 40-41].

[2] The bulk of a material is the structure that is most similar to a perfect crystal, in general has lower defect concentrations and can be found in the center of a crystal.

In a perfect crystal these imperfections will first try to annihilate themselves, if possible, or spread out over the crystal if recombination is not possible, thus lowering the internal energy and returning to a state of thermodynamic equilibrium. However, in a real structural metal this equilibrium is not always possible to achieve, as many barriers are present, such as complex boundaries and dislocations, that act as defect traps [3, p. 176]. These barriers specifically affect the diffusion character of the material at low temperatures, as atomic movement concentrates along *high-diffusivity paths*. Diffusion along these imperfections is faster compared to the bulk material, because the activation energy for movement is lower as the atoms are more loosely bound due to these defects [3, ch. 4.6; 2, ch. 5]. At higher temperatures, however, the thermal vibrations increase drastically, allowing for more energy intensive jumps, hence making high-diffusivity paths nearly obsolete (see figure 8.4). In this example the systems with a high grain density, and thus many grain boundaries, have many high-diffusivity paths. As expected at these temperatures diffusivity is accelerated due to its dependence on temperature and vacant neighbour probability (that is, in a perfect crystal that is only driven by thermal diffusion) [3, ch. 4.2; 2, ch. 5; 1, ch. 3.5], as seen in (reprinted from Santofimia & Sietsma [1, eq. 3.22]):

$$D = \frac{1}{6} z_v \nu_0 a^2 (1 + \frac{\partial \ln \gamma}{\partial \ln c}) \exp(-\frac{\Delta G_m}{kT}) = \frac{1}{6} z_v \nu_0 a^2 \chi \exp(-\frac{\Delta G_m}{kT}) \tag{A.1}$$

The diffusion coefficient D [m^2/s] depends on; neighbouring vacancy probability z_v (lattice structure dependent), atomic frequency ν_0 [s^{-1}], interatomic distance a [m], thermodynamic factor χ, activation free energy for diffusion ΔG_m [eV], temperature T [K], and the Boltzmann constant k [eV].

Multi-element systems

In an alloy many elements can be preset, and when an alloying element or impurity has a preferential association with the defect flux, referred to as *coupling*, it can generate a net flux towards (interstitials) or away (vacancies) from a defect sink such as GBs (section 8.3.1), see figure 8.5. This preferential association to a specific defect flux, referred to as the *Kirkendall effect*, is the result of a reduced activation energy over that specific solute element [4, ch. 7.2.3; 3, ch. 6].

Equation A.2, reprinted from Was [3, eq. 6.48], gives the total atom fluxes of a ternary alloy with respect to the crystal lattice using the different concentration gradients, diffusion coefficients and general alloy variables. The general alloy variables used are; the thermodynamic factor χ, the average atomic volume in the alloy Ω [m^3], the vacancy gradient C_v, and C_i the interstitial gradient. Atom (#) specific variables are; the total diffusion coefficient given by $D_\#$. $\nabla C_\#$ describes the concentration gradients, and the diffusivity coefficients for the conjugate atom-defect pairs are given as $d_{\#,v}$ (vacancy) & $d_{\#,i}$ (interstitial).

$$\begin{aligned}
J_A &= J_A^v + J_A^i = -D_A \chi \nabla C_A + d_{A,v} \Omega C_A \nabla C_v - d_{A,i} \Omega C_A \nabla C_i \\
J_B &= J_B^v + J_B^i = -D_B \chi \nabla C_B + d_{B,v} \Omega C_B \nabla C_v - d_{B,i} \Omega C_B \nabla C_i \\
J_C &= J_C^v + J_C^i = -D_C \chi \nabla C_C + d_{C,v} \Omega C_C \nabla C_v - d_{C,i} \Omega C_C \nabla C_i
\end{aligned} \tag{A.2}$$

Diffusion towards dislocations: *climb*

Another important diffusion mechanism is the point defect attraction to dislocations, supporting the mechanism of dislocation *climb*. Around dislocation cores a stress gradient is present as a result of the lattice mismatch. As a consequence, they act as sinks for self-interstitial atoms (SIAs) and vacancies to lower the systems free energy. Even though the dislocation sink attracts both point defects, it does prefer SIAs over vacancies because these interstitials at dislocations reduce overall strains around the dislocations at a higher rate. When a dislocation (excluding pure screw dislocations[3]) wants to leave its initial slip plane because of external shear stresses it needs to absorb or emit a vacancy or interstitial [3, p. 230; 2, p. 76].

A.1.2 Phase diagrams

To explain phase diagrams the following section describes the well-known steel phase diagram instead of Ni-Mo. Figure A.1 shows the thermodynamic equilibrium phase diagram of iron-carbon (steel). The diagram clearly shows the relation between the matrix (main lattice element) and the precipitate phase. For example an Fe matrix with 1.5wt%C at 1100°C will be *austenite*, or γ, in which the carbon is fully soluble with the Fe matrix. When quenching (rapidly cooling down) to 20°C the carbon becomes trapped in a metastable matrix known as *martensite* because diffusion is prevented due to the short cooling times. Because these new phases increase local strains because of their interface with the matrix the precipitates want to move towards defect sinks such as GBs to lower its overall energy.

[3] Pure screw dislocations do not have a defined slip plane and thus don't require the energy intensive climb mechanism to leave their current slip plane.

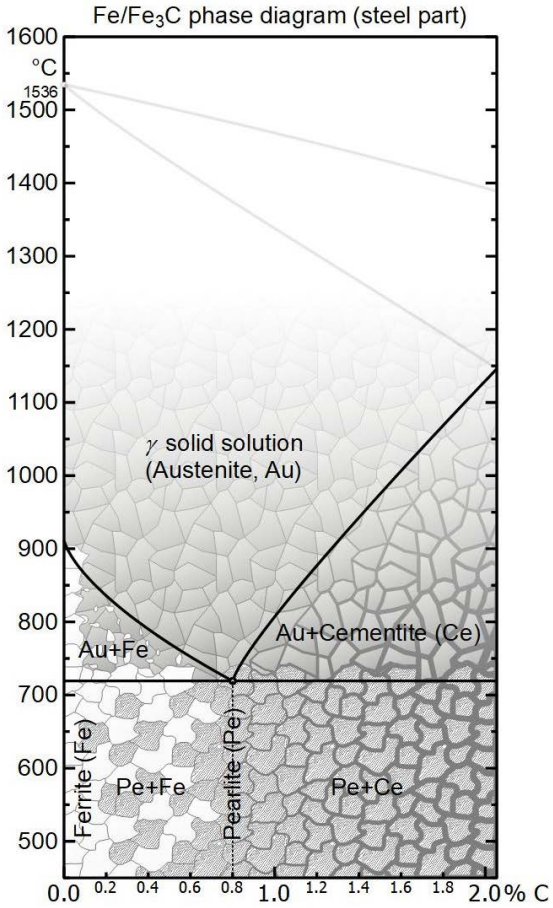

Fig. A.1 Phase diagram of iron-carbon (steel) at atmospheric pressure with illustrations of microstructure. Reprinted from tec-science [5].

A.1.3 Void- and bubble formation/growth

Resulting from the local characteristic of displacement cascades, the vacancies are fairly close together, making the growth of these voids at the affected area relatively easy, as it requires limited diffusion. In many cases the void is very unstable as the surface energy of the void increases the free energy, in a similar fashion as the free energy of precipitates discussed in 8.3.2. However, when the embryo reaches the critical size it can form into a void and start growing, this critical value of vacancies in the void is given as $n*$ in figure A.2.

At a certain vacancy supersaturation concentration the surface energy per area (γ) associated with the formation of a vacancy embryo becomes more favourable than other possible configurations such as a loop or SFT [3, p. 384]. As seen in equation A.3 reprinted from Was [3, eq. 8.19], the concentration of voids $\rho^0(n)$ increases when the temperature T [K] increases. Other variables are; number of possible void formation sites N_0, free energy of void formation ΔG_n^0 [eV], and the Boltzmann constant k [eV/K].

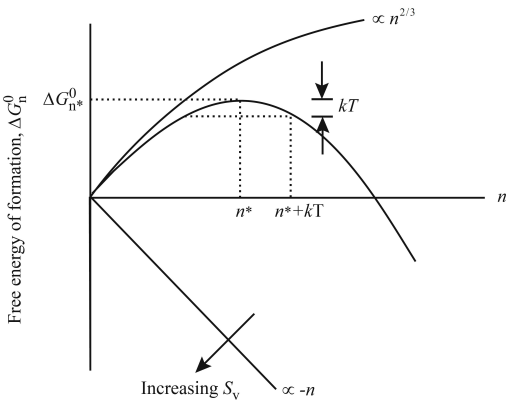

Fig. A.2 Free energy of formation for a void of n vacancies, with $n*$ representing the critical embryo size for void formation. The increase in interface energy is proportional to $n^{2/3}$ and the decrease of energy, related to the formation excess entropy, being proportional to $-n$. Reprinted from Was [3, ch. 384].

$$\rho^0(n) = N_0 \exp(-\frac{\Delta G^0_n}{kT}) \tag{A.3}$$

The free energy of formation, ΔG^0_n [eV], for these voids is given in equation A.4. The variables and constants are; the number of vacancies in the void n, temperature T [K], Boltzmann constant k [eV/K], entropy of void formation S_v [eV/K], atomic volume related to the vacancy defect Ω [m^3], and the interface surface area per unit area γ [eV/m^2].

$$\Delta G^0_n = -nkT \ln S_v + (36\pi\Omega^2)^{1/3}\gamma n^{2/3} \tag{A.4}$$

Combining these two equations and comparing them with figure A.2 it becomes clear that an increase in temperature results in a higher critical embryo size, thus making more smaller embryos unstable and nucleation more difficult. However, in radiated materials another factor greatly enhances the stability of those embryos, making the nucleation and growth more common in these high temperature irradiated materials.

Appendix B

B.1 Chapter 2

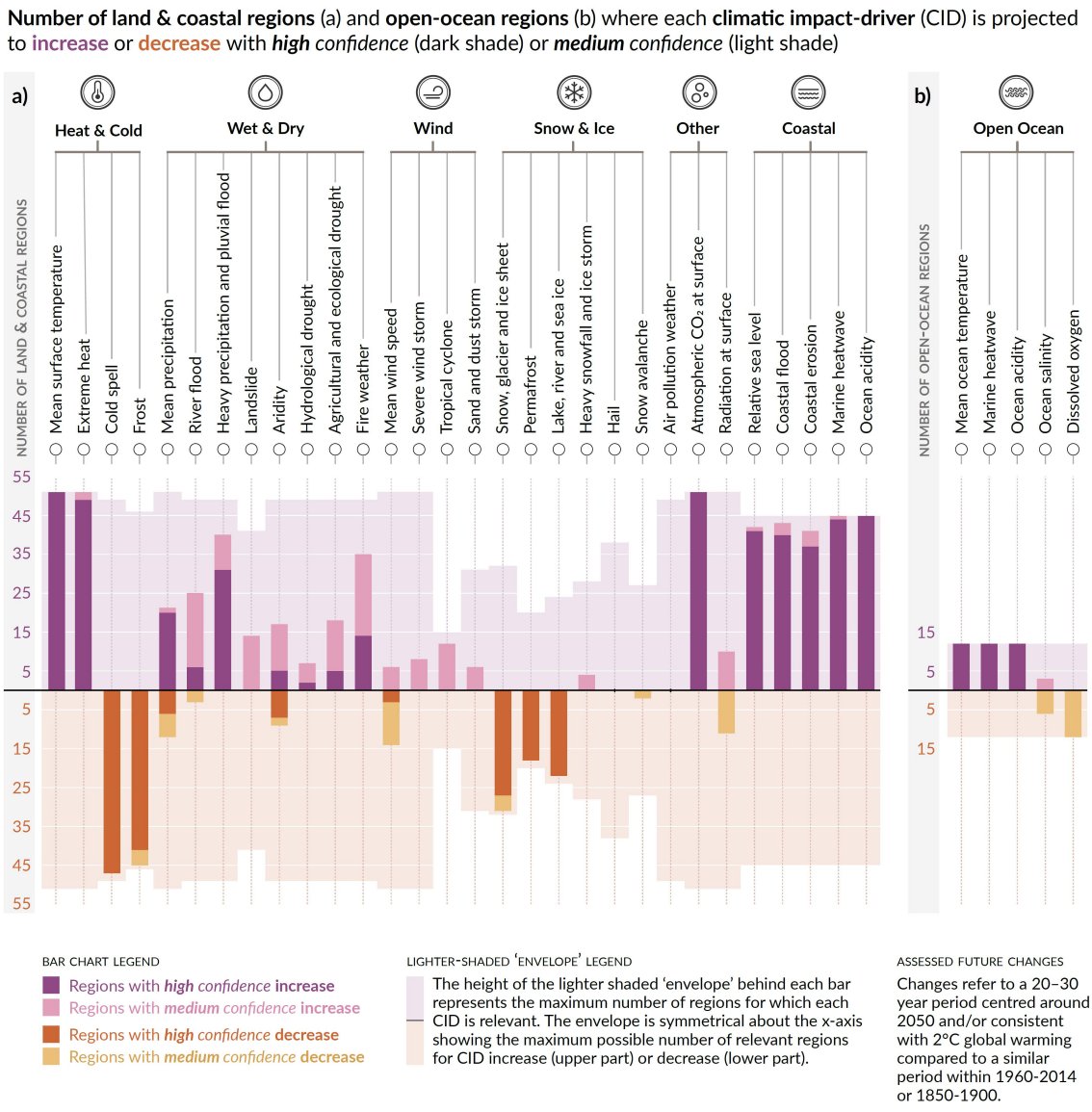

Fig. B.1 Synthesis of the number of *AR6 WGI* (IPCC climate predictions) reference regions where multiple climate impact drivers are projected to change. Reprinted from IPCC [6, p. C.2.7].

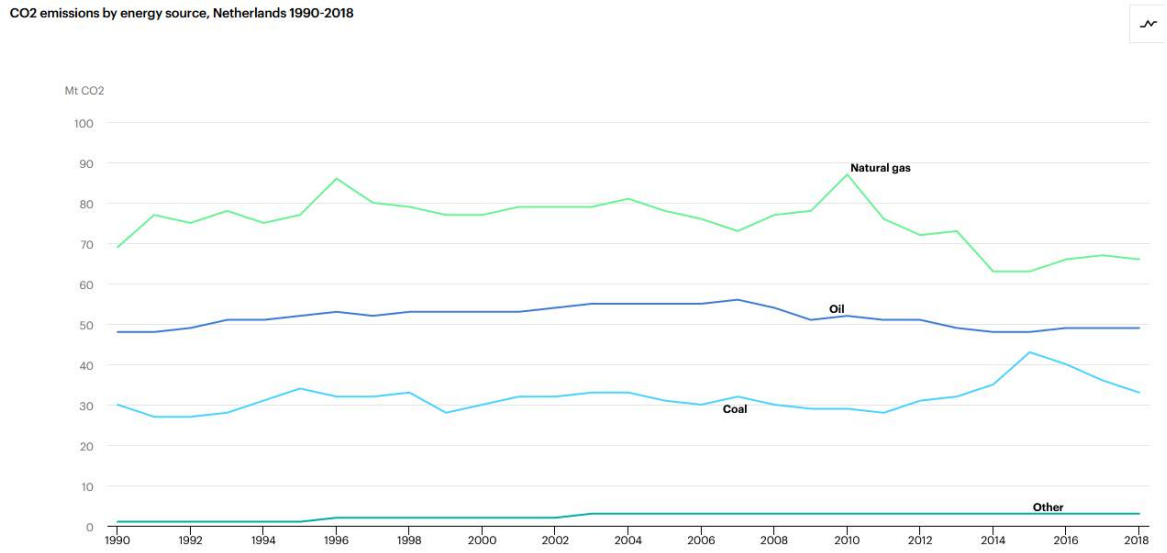

Fig. B.2 Total carbon dioxide emissions of different energy sources in the Netherlands over time. Reprinted from International Energy Agency (IEA) [7].

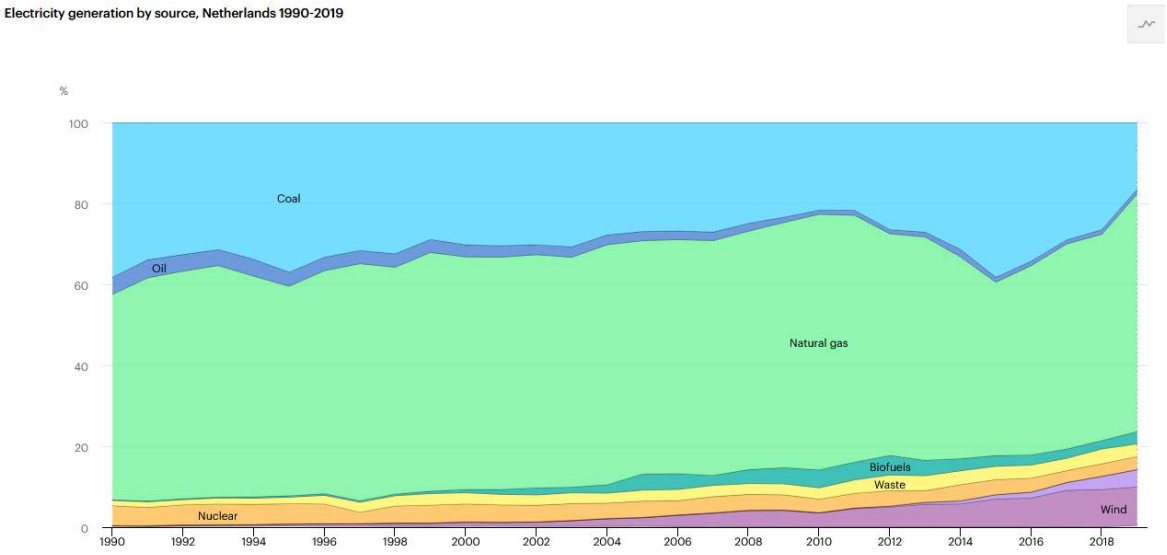

Fig. B.3 Share of electricity generation for different sources in the Netherlands over time. Reprinted from International Energy Agency (IEA) [7].

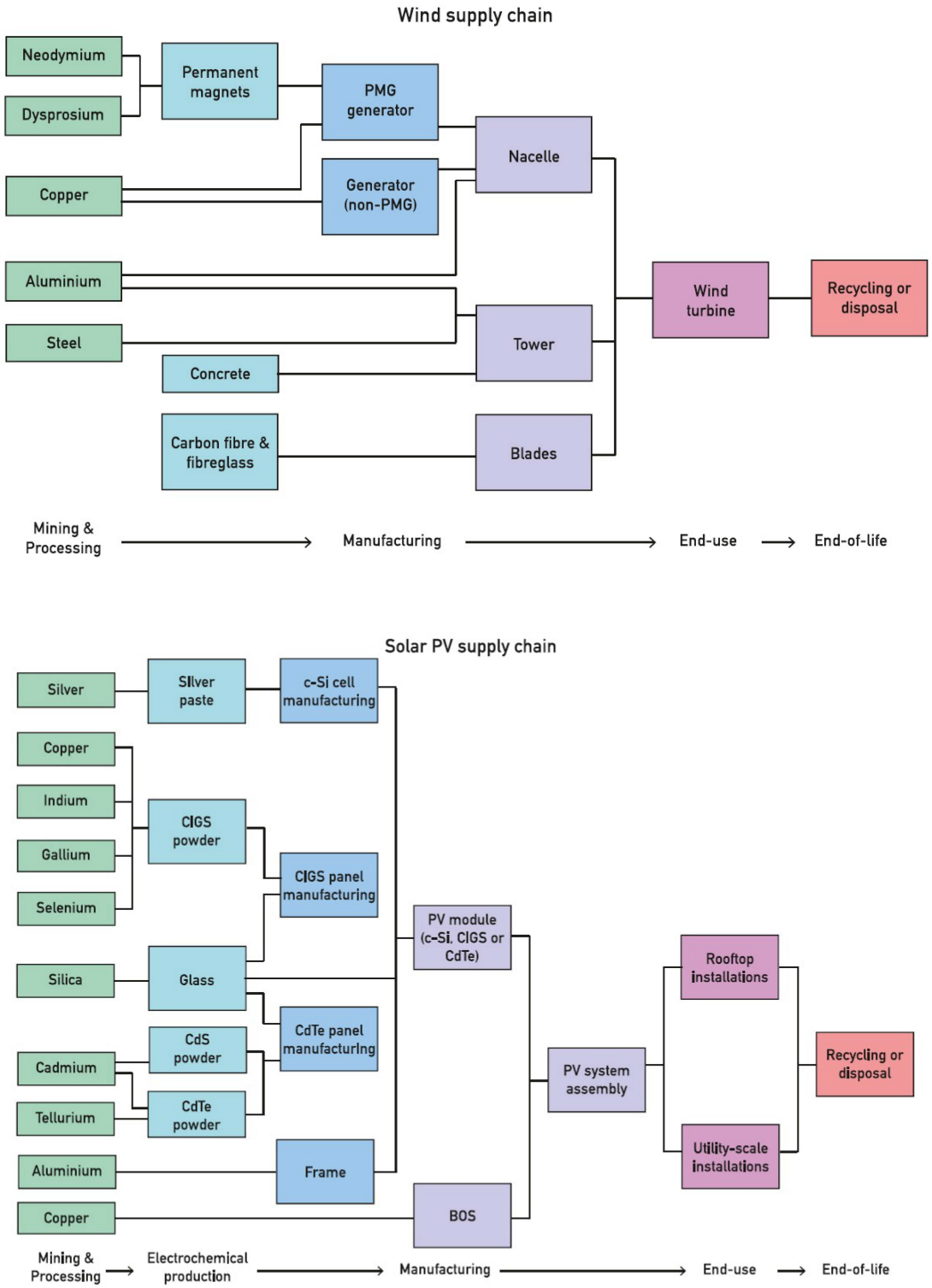

Fig. B.4 Simplified value chains for wind and solar PV materials. Reprinted from Carrara *et al.* [8, p. 6].

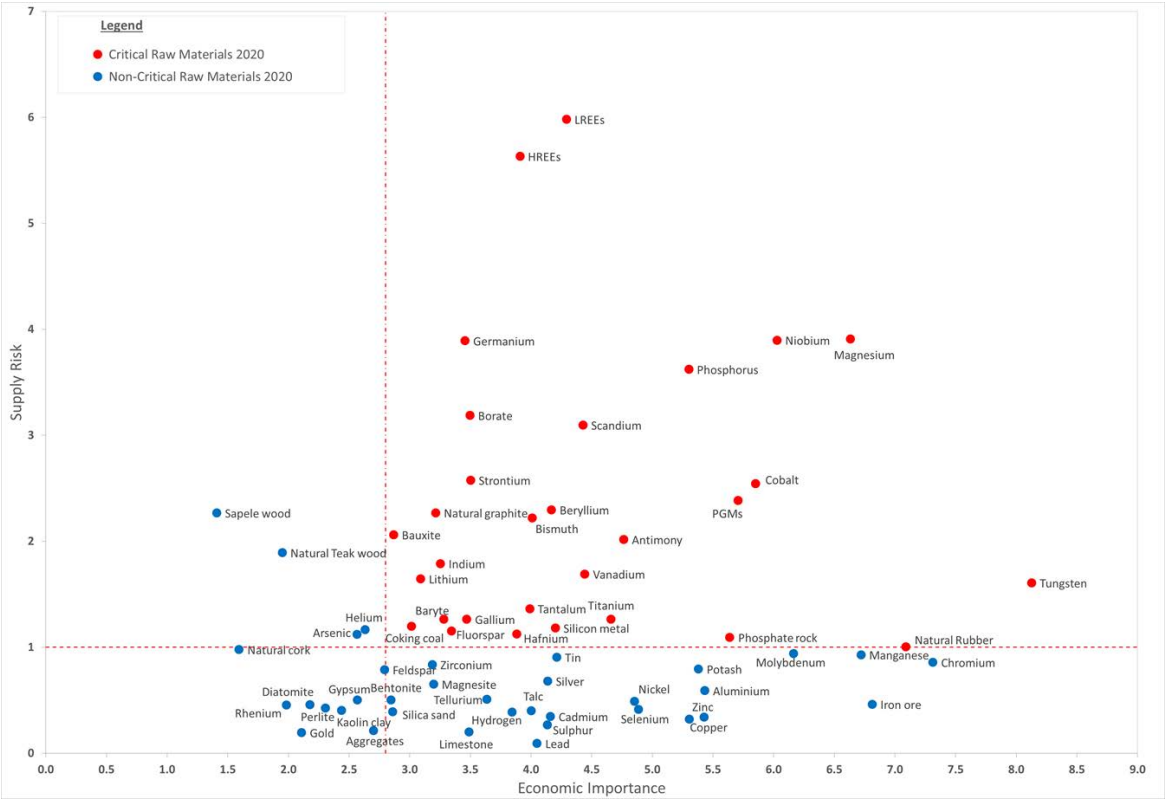

Fig. B.5 Critical raw materials for the European Union (2020). Reprinted from Joint Research Centre (JRC) [9].

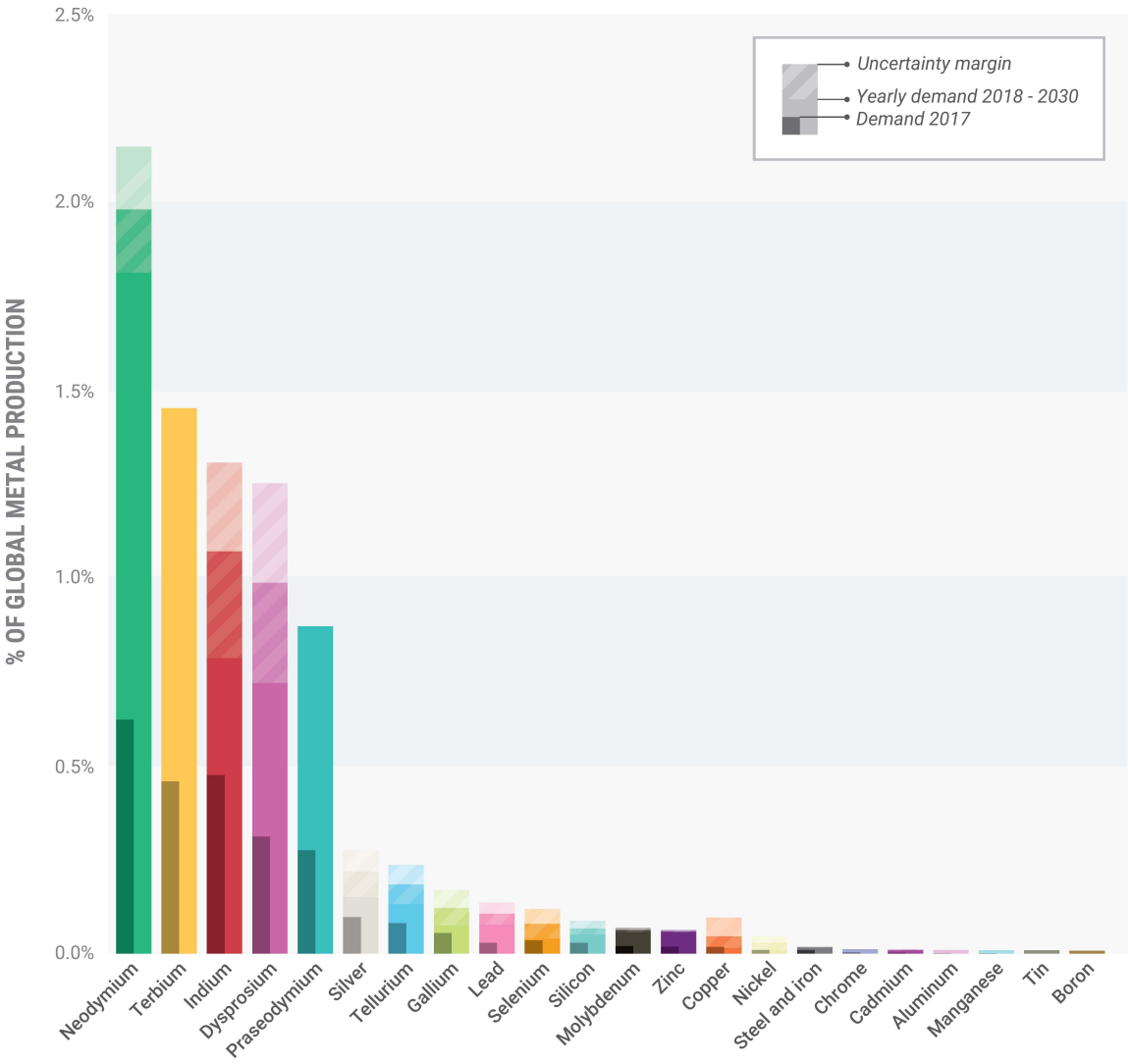

Fig. B.6 The average annual Dutch metal demand for wind turbines and solar panels for the period 2018-2030, compared to annual demand in 2017. Reprinted from van Exter *et al.* [10, p. 8].

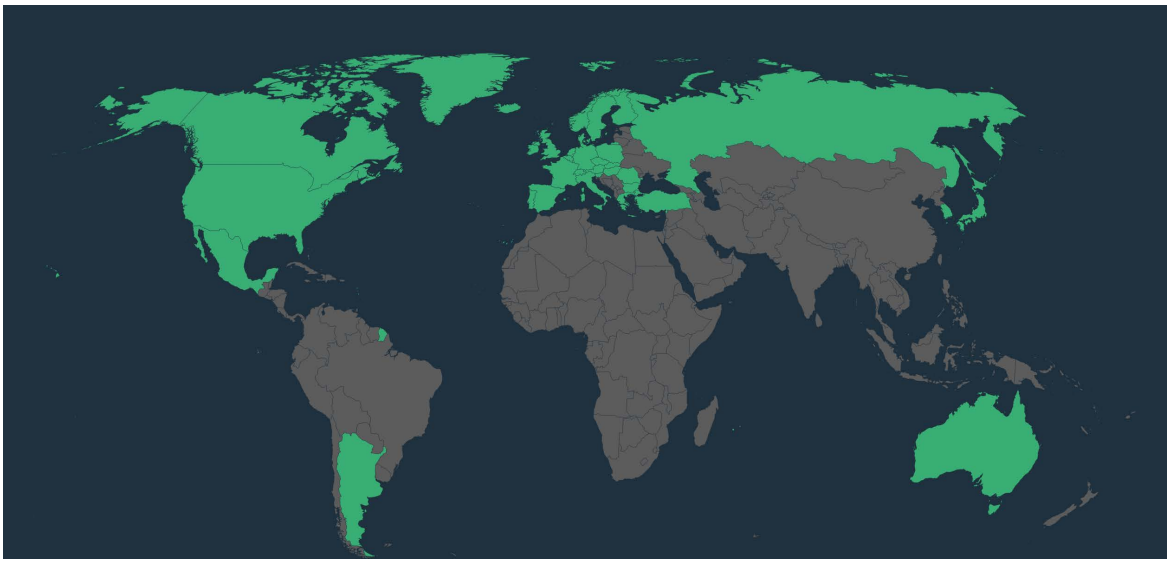

Fig. B.7 Map of member countries of the NEA as of 2021. Countries coloured as green are member states. Reprinted from NTI [11].

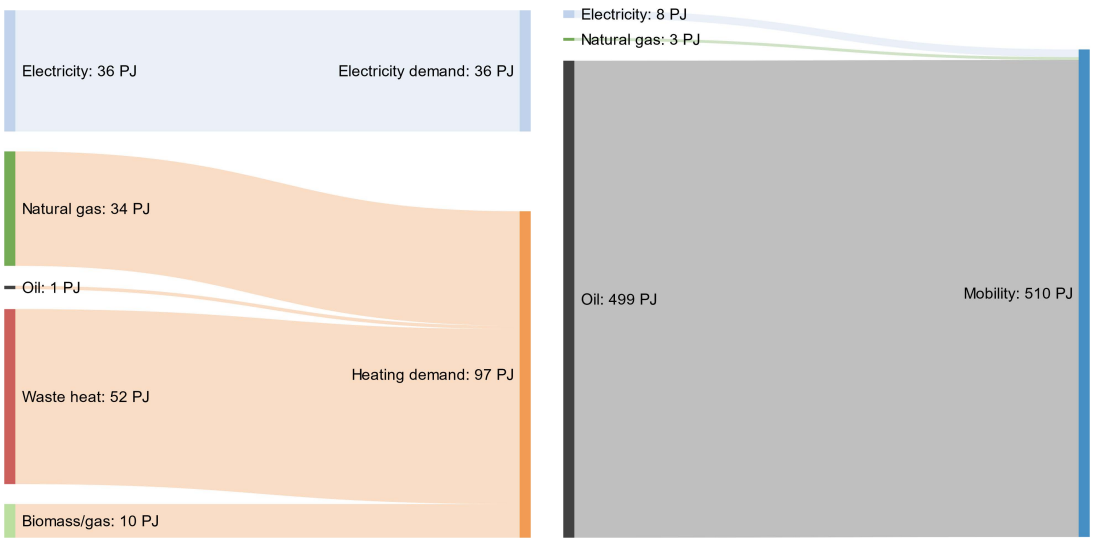

Fig. B.8 Sankey diagram of the 2019 Dutch agricultural (left) and mobility (right) sector energy mixs. The diagram excludes non-energy resource usage. Data from Energie Beheer Nederland [12] was used to create this overview diagram.

Fig. B.9 Overview of renewable electricity production of wind and solar PVs, for the seasonal days, March 21, June 21, September 21 and December 21. The graphs present the real production capacity. Retrieved from Energieopwek [13].

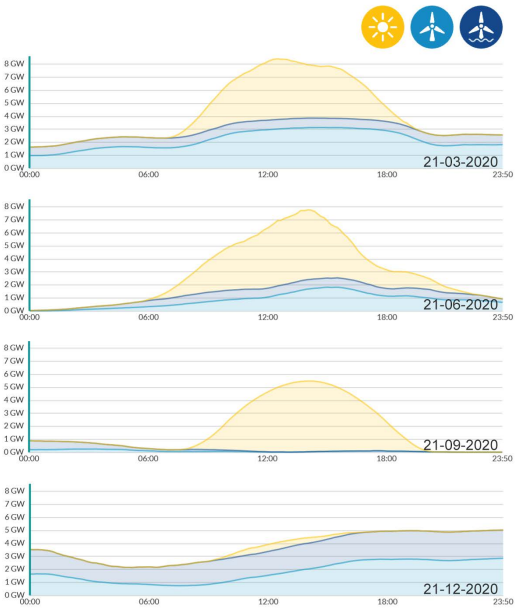

B.2 Chapter 8

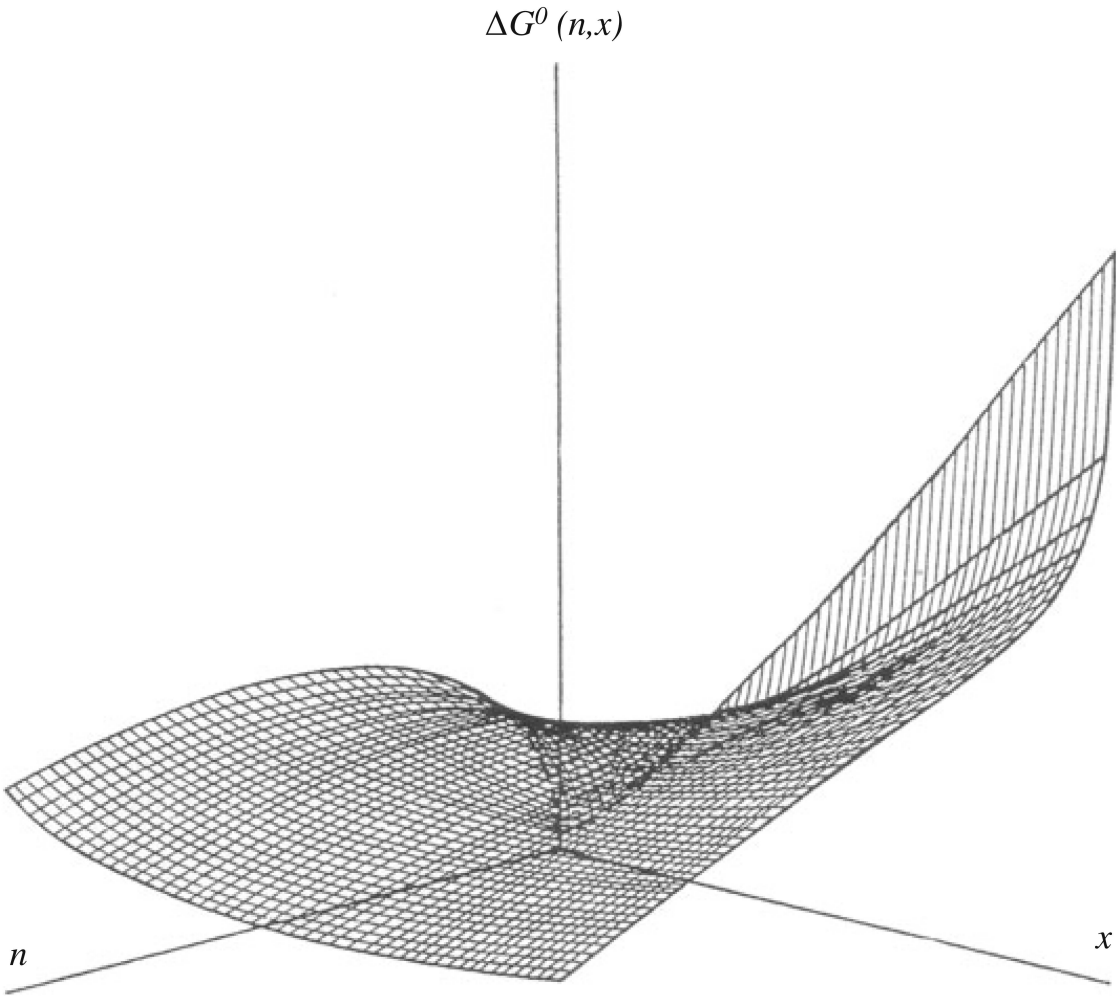

Fig. B.10 Plot of the free energy of void formation as a function of the number of vacancies (n) and the number of gas atoms (x) in the void. Conditions are as follows: S_v = 600, p_0 = 507 MPa, T = 500 °C, γ = 1 J/m^2. Reprinted from Was [3, p. 397].

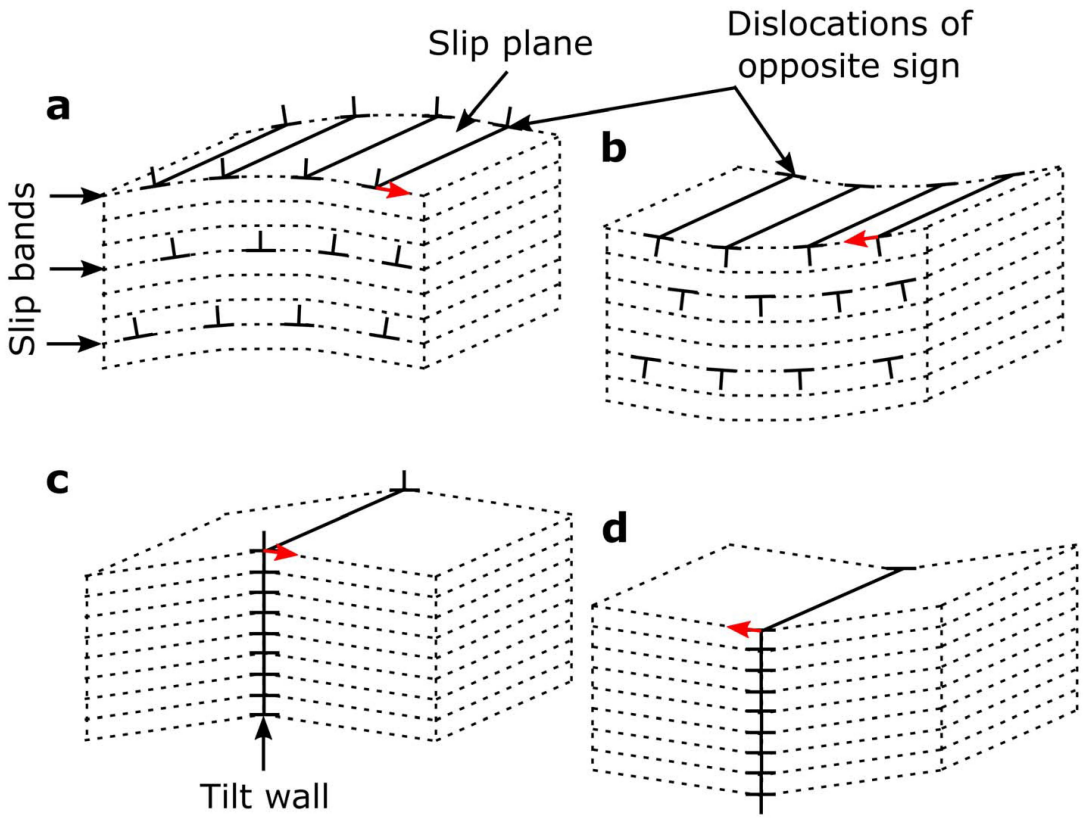

Fig. B.11 Recovery process of edge dislocations in a strained lattice crystal. (a) and (b) can annihilate, when annihilation is not possible they can form a tilt wall (low angle GB) (c-d). Reprinted from Wallis *et al.* [14, p. 7662].

B.3 Chapter 10

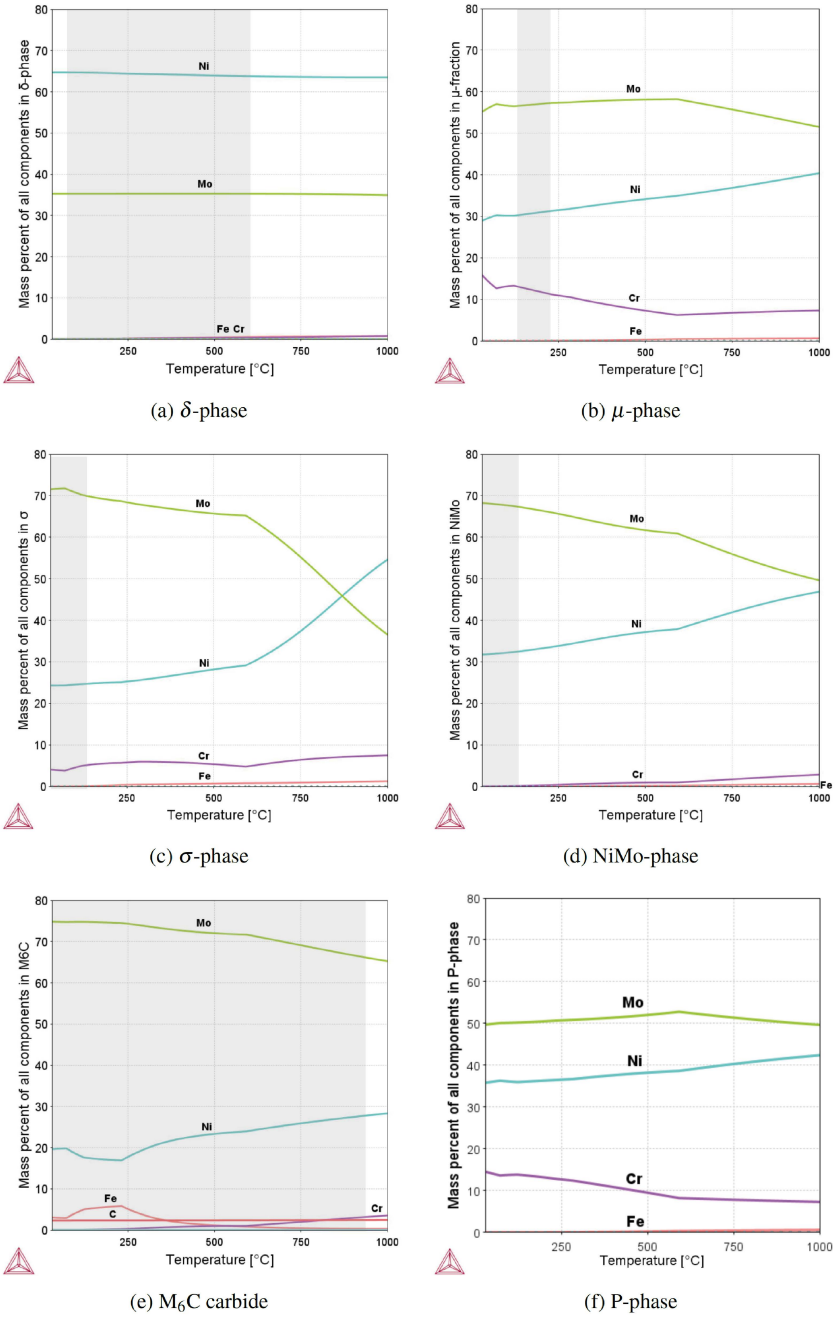

(a) δ-phase (b) μ-phase

(c) σ-phase (d) NiMo-phase

(e) M_6C carbide (f) P-phase

Fig. B.12 Chemical composition as function of temperature diagram of potential MONICR phases. The diagrams represent the chemical composition as a second-phase in the FCC Ni matrix. The grey gradient presents the calculated stable region of the phase.

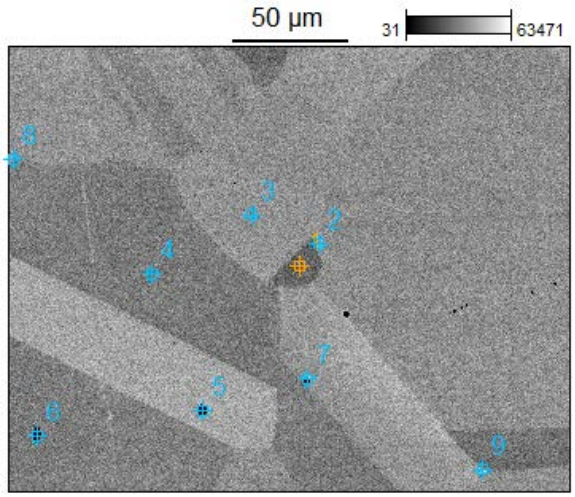

Fig. B.13 EDS measurement points for matrix and inclusion characterisation. Points 1-4 and 8-9 measure the matrix, points 5-7 the inclusions.

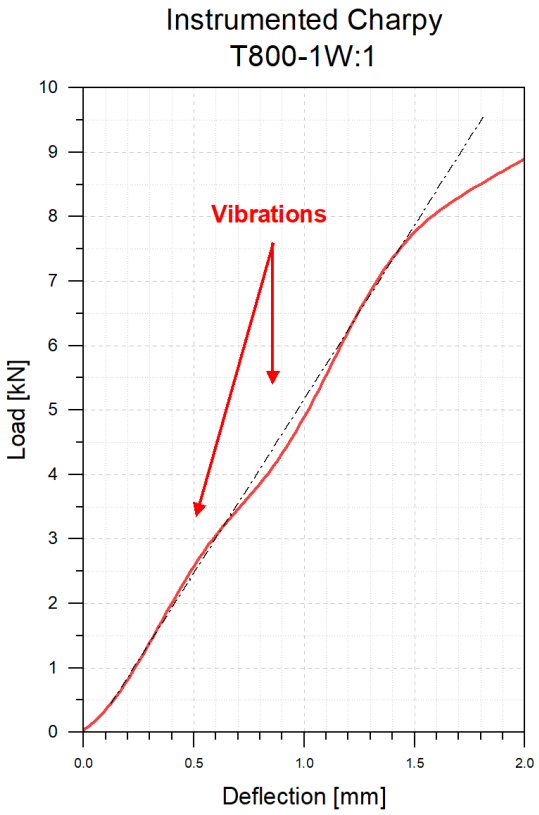

Fig. B.14 Measurement error during instrumented Charpy test. Deviation from normal trend indicate external vibrations.

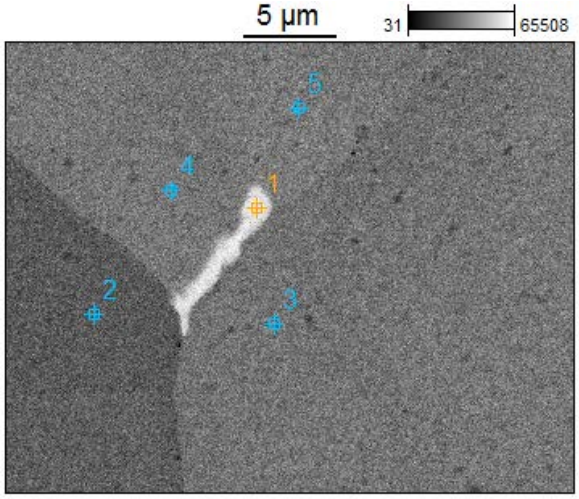

Fig. B.15 Example EDS measurement points for matrix and precipitate characterisation. Point 1 measures the precipitate, points 2-5 the matrix.

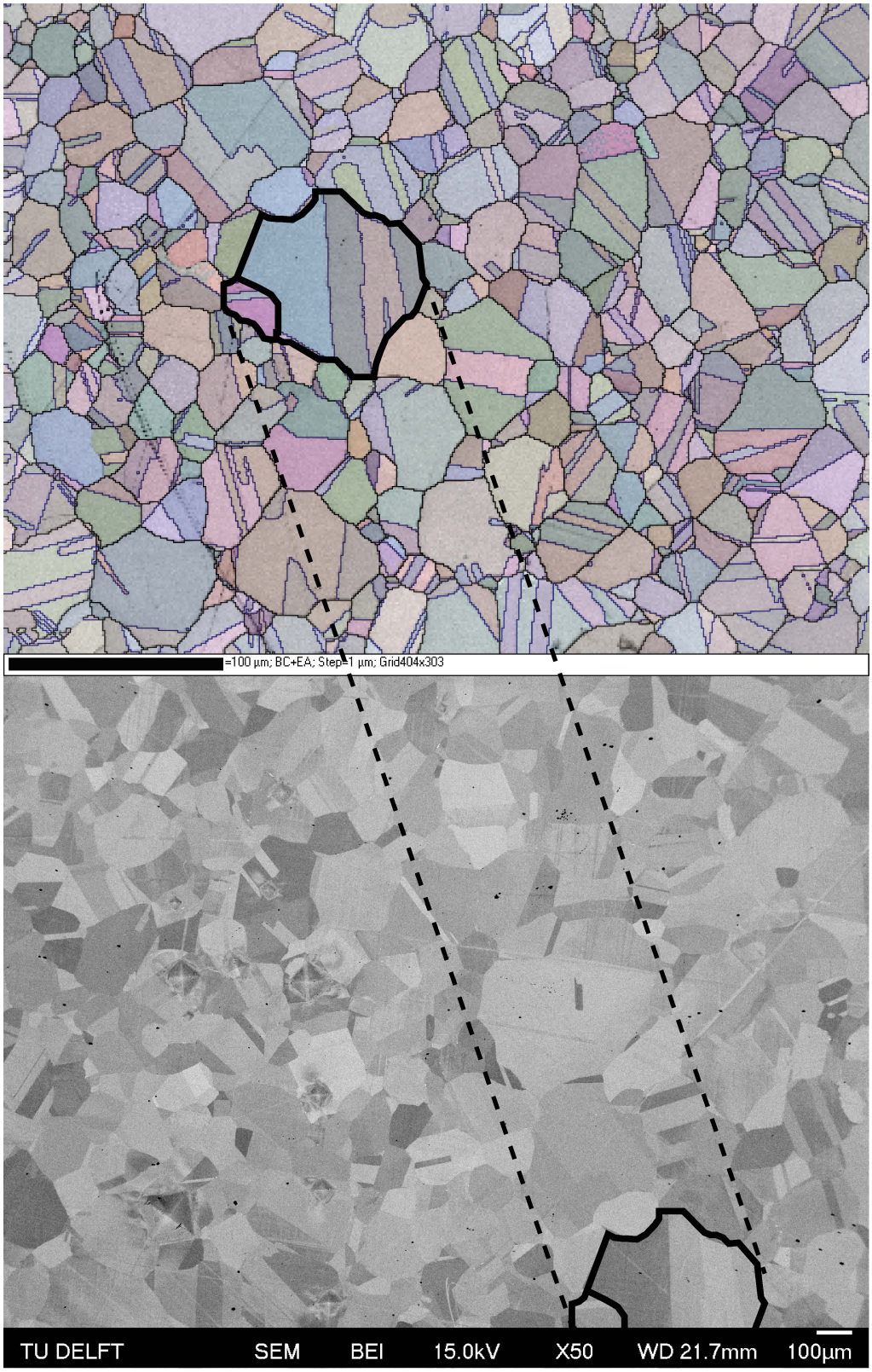

Fig. B.16 120h HT sample EBSD map (top image) and BEI image including precipitate locations (bottom).

Appendix C

C.1 Chapter 2

Table C.1 Generation IV nuclear system further properties. Reprinted and modified from Institut de radioprotection et de sûreté nucléaire (IRSN) [15, pp. 163-164].

System	Power Density [MW/m^3]	Fissile/fertile materials	Physical state fuel
Very High Temperature Reactor (VHTR)	5-10	$^{235}U/^{238}U$ $Pu/^{238}U$ $^{233}U/^{232}Th$	Particles
Gas-cooled Fast Reactor (GFR)	100	$Pu/^{238}U$	Pellets
Sodium-cooled Fast Reactor (SFR)	300	$^{235}U/^{238}U$ $Pu/^{238}U$	Pellets
Lead-cooled Fast Reactor (LFR)	100	$Pu/^{238}U$	Pellets
Molten Salt Reactor (MSR)	330 (only MSFR)	$^{233}U/^{232}Th$ $^{235}U/^{238}U$ $Pu/^{238}U$	Liquid
Supercritical Water-Cooled Reactors (SCWR)	100	$Pu/^{238}U$	Pellets

General assumptions LCOE assessment	Nuclear	VRE	Hydrogen P2P
WACC	7%	4,3%	4,3%
Technical Lifetime (years)	60	25	20, electrolysers limiting
Depreciation period	technical lifetime	technical lifetime	technical lifetime
Utilisation factor	100%	100%	50%
Decommissioning costs	15% of capital costs, discounted at 3%	5% of capital costs, discounted at 3%	5% of capital costs, discounted at 3%
Waste costs	Spent fuel disposal and storage, decomm. waste included in decomm. costs and operational waste in O&M costs	Decommissioning waste included in decomm. costs and operational waste in O&M costs	Decommissioning. waste included in decomm. costs and operational waste in O&M costs
Construction time (years)	7	0,5 – 1,5	3, CCGT limiting

Fig. C.1 LCOE calculation assumptions. Reprinted from ENCO [16, pp. 52].

Table C.2 Overview of the used wind turbine models in the MRDH, including their turbine count. The models and their share are based on a variety of information sheets from both government and electricity producer documentation. Turbine model information is retrieved at Lucas Bauer [17].

Model	Turbine count	Capacity [MW]	Rotor diameter [m]	Cut-in speed [m/s]	Cut-out speed [m/s]
Offshore					
Vestas V112/3000	43	3.0	112	3.5	25.0
Onshore					
AN Bonus 600/44 MK IV	7	0.6	44	5.0	25.0
Vestas V80-2.0	1	2.0	80	4.0	25.0
Enercon E-70 E4 2.300	1	2.3	71	2.5	34.0
Vestas V90-3.0	42	3.0	70	4.0	25.0
Envision EN140-3.0	6	3.3	90	3.0	20.0
Vestas V112-3.45	14	3.45	112	3.0	25.0
Average pre-2020 model	71	2.85	77.6	3.8	24.7

Table C.3 Overview of the included future wind turbine model in the MRDH. Turbine model information is retrieved at Lucas Bauer [17].

Model	Capacity [MW]	Rotor diameter [m]	Cut-in speed [m/s]	Cut-out speed [m/s]
Offshore				
SG 8.0-167 DD	8.0	167	3.0	25.0
Onshore				
SG 2.9-129	2.9	90	3.0	25.0

Table C.4 Information on a reference solar panel model and its properties in the Netherlands. Information is retrieved from LG model technical specifications sheets.

PV-model	Construction period	Capacity [W]	Area [m^2]	Efficiency [%]	Degradation loss start [%]	Performance decline [%/y]	Temperature loss coefficient	Transmittance value [W/m^2K]
LG255S1K-G3	≤ 2013	255	1.64	15.5	97.0	-0.007 (after year 1)	-0.45	1.22513
LG280S1K-L4	$2013 < y \leq 2016$	280	1.64	17.1	98.0	-0.006 (after year 2)	-0.39	1.17975
LG330N1C-A5	$2016 < y \leq 2017$	330	1.71	19.3	98.0	-0.005 (after year 1)	-0.37	1.13437
LG365Q1C-V5	$2017 < y \leq 2019$	365	1.73	21.1	98.0	-0.003 (after year 1)	-0.3	1.089
LG395A1C-A6	$y \geq 2020$	395	1.81	21.8	98.5	-0.0025 (after year 1)	-0.29	1.089

Table C.5 Information on the offshore wind parks close to the RES. Turbine count, distance to shore and average interior cable distance are calculated from GIS data on both the wind parks and sea cabling, data retrieved from Ministry of Infrastructure and Water Management [18; 19]. Calculations made using QGIS.

Wind park	Maximum turbine count	Distance to shore [km]	Average interior cable distance
HK-Z	350	43	7.14
HK-F	32	65	2.43
HK-W	216	6.72	
HK-D	347	115	15.86
IJmuiden ver	1175	146	15.15

References

1. Santofimia, M. & Sietsma, J. *Microstructure Control in Metals* ISBN: 978-94-640-3815-6 (Delft University of technology, 2020).
2. Gottstein, G. *Physical Foundations of Materials Science* (Springer Berlin Heidelberg, 2004).
3. Was, G. S. *Fundamentals of radiation materials science: Metals and alloys* 2nd, 1–1002. ISBN: 9781493934386 (Springer New York, Jan. 2016).
4. *Structural Materials for Generation IV Nuclear Reactors* (ed Yvon, P.) 409. ISBN: 9781845699673 (Woodhead Publishing, 2017).
5. tec-science. *Plastic deformation* https://www.tec-science.com/material-science/iron-carbon-phase-diagram/summary-of-phase-transformations/ (2021).
6. *The Physical Science Basis Summary for Policymakers Working Group I contribution to the Sixth Assessment Report of the Intergovernmental Panel on Climate Change* AR6 (eds Masson-Delmotte, V. *et al.*) (Cambridge University Press, Cambridge, Aug. 2021).
7. International Energy Agency. *The Netherlands - key energy statistics* https://www.iea.org/countries/the-netherlands (2021).
8. Carrara, S., Dias, A., Plazzotta, B. & Pavel, C. *Raw materials demand for wind and solar PV technologies in the transition towards a decarbonised energy system* EN 30095 EN. ISBN: 9789276162254. https://publications.jrc.ec.europa.eu/repository/handle/JRC119941 (Publication Office of the European Union, Luxembourg, 2020).
9. Joint Research Centre (JRC). *Raw Materials Information System (RMIS)* https://rmis.jrc.ec.europa.eu/?page=crm-list-2020-e294f6 (2022).
10. Van Exter, P., Bosch, S., Schipper, B., Sprecher, B. & Kleijn, R. *Metal demand for renewable electricity generation in the Netherlands: Navigating a complex supply chain* tech. rep. (METABOLIC, 2018). www.metabolic.nl.
11. NTI. *Nuclear Energy Agency (NEA)* https://www.nti.org/education-center/treaties-and-regimes/nuclear-energy-agency-nea/ (2021).
12. Energie Beheer Nederland. *Energie in Nederland in 2019* https://www.energieinnederland.nl/feiten-en-cijfers/uitgebreid/2019 (2021).

13. Energieopwek. *Energieproductie* https://energieopwek.nl/ (2021).

14. Wallis, D., Hansen, L., Britton, T. & Wilkinson, A. Dislocation Interactions in Olivine Revealed by HR-EBSD. *Journal of Geophysical Research: Solid Earth* **122,** 7659–7678. https://agupubs.onlinelibrary.wiley.com/doi/full/10.1002/2017JB014513 (2017).

15. Institut de radioprotection et de sûreté nucléaire (IRSN). *Review of Generation IV Nuclear Energy Systems* tech. rep. (Institut de radioprotection et de sûreté nucléaire, Apr. 2015).

16. ENCO. *Possible role of nuclear in the Dutch energy mix in the future* tech. rep. (ENCO, 2020).

17. Lucas Bauer, S. M. *Windturbines database* https://en.wind-turbine-models.com/turbines (2022).

18. Ministry of Infrastructure and Water Management. *Windparken Noordzee (Nederlands Continentaal Plat)* https://data.overheid.nl/en/dataset/12520-windparken-noordzee--nederlands-continentaal-plat- (2022).

19. Ministry of Infrastructure and Water Management. *Kabels en leidingen - pijpleidingen op de Noordzee* https://data.overheid.nl/en/dataset/9378-pijpleidingen-op-de-noordzee (2022).